



UNIVERSIDAD NACIONAL AUTÓNOMA DE
MÉXICO

POSGRADO EN CIENCIAS FÍSICAS

Measurement of the Transverse
Sphericity in Minimum Bias
proton-proton Collisions at $\sqrt{s} = 0.9$,
2.76 and 7 TeV with ALICE at the
LHC

T E S I S

QUE PARA OBTENER EL TÍTULO DE:

Doctor en Ciencias Físicas

PRESENTA:

Antonio Ortiz Velasquez

DIRECTOR DE TESIS: Dr. Guy Paić

MIEMBROS DEL COMITÉ TUTORIAL:

Dr. Eleazar Cuautle Flores

Dr. Luis Fernando Urrutia Ríos

pcf

posgrado en ciencias físicas
u n a m

Octubre, 2011



UNAM – Dirección General de Bibliotecas

Tesis Digitales
Restricciones de uso

DERECHOS RESERVADOS ©
PROHIBIDA SU REPRODUCCIÓN TOTAL O PARCIAL

Todo el material contenido en esta tesis está protegido por la Ley Federal del Derecho de Autor (LFDA) de los Estados Unidos Mexicanos (México).

El uso de imágenes, fragmentos de videos, y demás material que sea objeto de protección de los derechos de autor, será exclusivamente para fines educativos e informativos y deberá citar la fuente donde la obtuvo mencionando el autor o autores. Cualquier uso distinto como el lucro, reproducción, edición o modificación, será perseguido y sancionado por el respectivo titular de los Derechos de Autor.

*A Aranzazú mi compañera en esta aventura.
A Samuel mi apoyo incondicional.
A mi fuente de motivación: Yolanda, Dulce,
Gaby, Cynthia, Itzel, Karla, Aranza.*

Acknowledgements

The success of my project was possible thanks to the experience and the guidance of my supervisor Guy Paić. He involved me in the analysis group dedicated to the studies of high p_T physics in ALICE, and dedicated many hours to discussions. All the conversations with him were very motivating for my scientific career.

I want to thank Jean-Pierre Revol, who suggested me to investigate the event shapes. For his constant encouragement and interest.

I appreciate the time and good disposition of Andreas Morsch, Eleazar Cuautle and Alejandro Ayala to discuss the results and for all their suggestions to improve this analysis.

Special thanks to Arturo Fernández for inviting me to collaborate in ALICE during my bachelor studies at Universidad Autónoma de Puebla.

At the end of my Ph. D. I did a fruitful stay at CERN supported by Federico Carminati through the ALICE offline project. During this stay I presented my results in several conferences of 2011, and I concluded the work toward the final publication.

The excellent performance of our local cluster (Tochtli), its maintenance and technical support was provided by Luciano Díaz. His help and experience were crucial during the development of my project.

The discussions during the weekly meetings at ICN enriched my work with the interesting comments and suggestions of all my colleagues: Isabel Domínguez, Enrique Patiño, Ivonne Maldonado, Daniel Mayani, Xitzel Sánchez, Tonatiuh Bustamante and Edgar Pérez. And of course the professors: Guy Paić, Eleazar Cuáutle, Alejandro Ayala and Lukas Nellen.

Finally, I would like to express my gratitude to the mobility programs that allow me to visit with regularity CERN: the CERN-UNAM agreement, the HELEN program, the red FAE and the projects: DGAPA-UNAM under PAPIIT grants IN116008, IN115808 and IN116508 as well as by CONACyT grant 103735, 101597.

Contents

0.1	Modelo Estándar de las partículas elementales	i
0.2	La cromodinámica cuántica	ii
0.3	Componentes de los eventos QCD	iv
0.3.1	Interacciones Minimum Bias	v
0.4	Motivaciones físicas para estudiar eventos “Minimum Bias”	vi
0.5	Variables de forma del evento	xi
0.6	El experimento ALICE	xviii
0.6.1	Cámara de Proyección del Tiempo	xix
0.6.2	Sistema Interno de Rastreo	xxii
0.6.3	Detector VZERO	xxiii
0.7	Análisis de datos	xxiv
0.7.1	Descripción de la muestra MB	xxiv
0.7.2	Selección de trazas primarias	xxiv
0.7.3	Selección de eventos por su dureza	xxv
0.7.4	Correcciones aplicadas a los datos	xxv
0.7.5	Errores sistemáticos	xxviii
0.8	Resultados	xxix
0.8.1	$\langle S_T \rangle$ en datos a $\sqrt{s} = 0.9$ TeV	xxix
0.8.2	Resultados de $\langle S_T \rangle$ en datos a $\sqrt{s} = 7$ TeV	xxx
0.8.3	Momento transverso promedio	xxx
0.8.4	Espectros de S_T en contenedores de multiplicidad	xxxi
0.8.5	Evolución de la esfericidad transversa con la multiplicidad a 0.9, 2.76 y 7 TeV	xxxi
0.9	Discusiones y Conclusiones	xxxi

1 Theoretical Framework	1
1.1 The standard model	1
1.2 Perturbative and non-perturbative QCD aspects in high energy collisions . .	3
1.3 Environment of the High Energy Hadron Collisions	4
1.3.1 Minimum Bias Interactions	4
1.3.2 Underlying Event	8
1.4 Event Generators	8
2 The ALICE experiment	11
2.1 Role of ALICE in the LHC program	11
2.2 The proton proton program in ALICE	12
2.3 The Central Tracking Detectors of ALICE	13
2.3.1 The Inner Tracking System (ITS)	15
2.3.2 Time-Projection Chamber (TPC)	16
2.4 Minimum Bias triggers in proton-proton collisions	17
3 Event Reconstruction with the central tracking detectors.	20
3.1 Primary vertex reconstruction with the SPD	20
3.2 3D reconstruction of the vertex position using tracks.	21
3.3 Track Reconstruction	23
4 The Event Shape Analysis, MC Study	25
4.1 Event Shapes	25
4.1.1 Study of τ and r for 2-particle events.	27
4.1.2 Event Shapes in the case of an isotropic phase-space (PS) model. . .	31
4.2 Sensitivity of the Event Shape with respect to different PYTHIA parameters.	35
4.2.1 Parameters related to the Underlying Event Activity	36
4.2.2 Intrinsic transverse momentum: k_{\perp}	45
4.2.3 Effect of the PDF on the ES.	47
4.3 ESA and the jet structures.	51
4.3.1 Description of the procedure.	51
4.3.2 Results in simulated pp collisions at 10 TeV.	53

5 Technical details of the analysis	72
5.1 Linearization of the transverse sphericity	72
5.2 Event and Track Selection.	73
5.3 Separation in “soft” and “hard” events	74
5.4 Multiplicity estimator	75
5.5 Correction of $\langle S_T \rangle$ vs N_{ch}	76
5.5.1 Extrapolation of the sphericity response matrices	78
5.5.2 Test of the method	83
5.6 Average transverse momentum versus multiplicity	86
5.6.1 Sphericity spectra in bins of multiplicity	87
6 Analysis in real data	92
6.1 Data Analysis	92
6.1.1 Off-line physics selection	93
6.1.2 Selection of events due to their hardness	94
6.1.3 Systematic uncertainties on $\langle S_T \rangle(N_{ch})$	94
6.1.4 Systematic uncertainties on the sphericity spectra	101
6.1.5 Systematic uncertainties on the mean p_T	101
6.2 Results	103
6.2.1 $\langle S_T \rangle$ in 0.9 TeV data	103
6.2.2 Results on $\langle S_T \rangle$ in 7 TeV data	108
6.2.3 Mean transverse momentum	108
6.2.4 S_T spectra in multiplicity bins	113
6.2.5 Evolution of the transverse sphericity with multiplicity at 0.9, 2.76 and 7 TeV	113
6.3 Discussion	122
7 Conclusions	124

Introducción

El Gran Colisionador de Hadrones (LHC, por sus siglas en inglés) tiene un ambicioso programa, este incluye: la verificación del Modelo Estándar (SM) através del descubrimiento del bosón de Higgs, seguido de estudios más allá del SM como la supersimetría y dimensiones extra, así como estudios de violación de CP, hasta la creación del estado que se formó microsegundos después del Big-Bang, es decir, el plasma de quarks y gluones.

Para lograr estos objetivos es necesario entender detalladamente las colisiones y por supuesto un profundo conocimiento de los detectores usados para registrar los eventos. En particular, el estudio de señales raras necesita de un casi perfecto entendimiento del fondo de las colisiones entre constituyentes de los hadrones. Esto incluye el entendimiento de los espectros de momento y multiplicidad, abundancia de partículas así como las correlaciones entre las observables. Mucha de la información que se puede extraer de estas estan contenidas en las variables de estructura del evento (event shapes). Estas mediciones en p-p son requeridas por todos los experimentos y también como referencia para la correcta interpretación de los resultados provenientes de colisiones entre iones pesados que se producen en el LHC.

Las mediciones que reporto se llevaron a cabo en el gran experimento colisionador de iones (ALICE, por sus siglas en inglés) que esta situado en el punto dos del LHC. ALICE esta optimizado para colisiones de iones pesados con el objetivo de estudiar la materia que interactúa de manera fuerte, especialmente el plasma de quarks y gluones y la transición de fase asociada. Dadas las características únicas de ALICE, este es un experimento que se espera contribuya de manera importante en el programa de física protón protón en el LHC.

Mi trabajo consistió en estudiar las variables de estructura de los eventos, a saber: esfericidad, thrust, thrust menor y recoil. Estas observables fueron ampliamente explotadas en experimentos de colisiones electrón-positrón así como de dispersión inelástica profunda. En colisiones de hadrones el ambiente que acompaña al proceso de dispersión entre constituyentes esta muy nutrido de radiación de bajo momento; por ello, realicé un estudio detallado de los cortes que se debían implementar tanto a nivel partícula como a nivel evento con el fin de minimizar la contribución aleatoria a la estructura del evento y asegurar una buena resolución de la variable al momento de ser medida usando los detectores de ALICE. Una vez que demostré que era viable hacer un análisis de este tipo en ALICE, procedí a estudiar posibles aplicaciones usando simulaciones Monte Carlo. Demostré que con el simple cálculo de thrust y recoil, era posible discriminar eventos con topologías específicas de jets. Luego, varié los

modelos para hacer la generación de eventos y demostré que estas observables eran sensibles al modelo. Más aún, varié los parámetros de MC que regulan la actividad “underlying” de las colisiones y demostré que eran muy sensibles respecto a esta componente no perturbativa de la cromodinámica cuántica (QCD). Finalmente, desarrollé las herramientas computacionales para llevar a cabo el análisis en datos reales usando una estadística importante. En la tesis, reporto las mediciones de esfericidad transversa contra multiplicidad, con la intención de hacer un test de pQCD en la alta multiplicidad. Los estudios sistemáticos son reportados, así como la comparación de las mediciones con diferentes modelos.

La tesis está organizada de la siguiente manera. En el Capítulo 1 se presenta el marco teórico de la física de colisiones de hadrones a altas energías. El Capítulo 2 está dedicado a la descripción del experimento ALICE, junto con su programa de física que espera cubrir. El Capítulo 3 discute la manera en la que se lleva a cabo la reconstrucción de los eventos en el sistema de rastreo central. El Capítulo 4 presenta las bases del análisis de la estructura de eventos (Event Shape Analysis, ESA) junto con sus aplicaciones potenciales en colisiones minimum bias protón-protón. El Capítulo 5 discute el procedimiento para hacer la deconvolución de las mediciones y poder llevar a cabo una comparación directa de los resultados con los distintos modelos. En el Capítulo 6 se muestra el análisis aplicado a datos reales junto con los estudios de los errores sistemáticos. Finalmente se presentan las conclusiones.

Resumen Amplio

0.1 Modelo Estándar de las partículas elementales

Una fuerza fundamental es el mecanismo responsable de la interacción entre partículas, y que no puede ser explicada en términos de otra interacción. Todos los fenómenos físicos observados pueden ser entendidos en términos de éstas. La aparente naturaleza irreducible de estas interacciones, es lo que motiva a los físicos a estudiar a detalle, las propiedades de dichas fuerzas. Por el momento, hay cuatro interacciones fundamentales conocidas: gravitatoria, electromagnética, nuclear fuerte y nuclear débil.

El modelo estándar (MS) [JFD92] de física de partículas es la teoría que describe tres de las cuatro interacciones fundamentales. Es una teoría cuántica del campo[aDVS95] que fue desarrollada entre 1970 y 1973 y que incorpora tanto a la mecánica cuántica como a la relatividad especial. El modelo estándar esta basado en el principio de invariancia de norma local del grupo $SU(3) \times SU(2) \times SU(1)$. $SU(3)$ representa el grupo de simetría de la interacción fuerte, mientras que $SU(2) \times SU(1)$ representa el grupo de simetría de la interacción electro-débil unificada.

La gravedad no esta incluida en el modelo, pero sabemos que a escala nuclear su magnitud es muy pequeña. Se podría hacer una discusión más detallada del MS, sin embargo el objetivo de esta sección es presentar los aspectos más relevantes del modelo en la física de colisiones de hadrones.

Todas las partículas descritas por el Modelo Estándar son fermiones que tienen un espín intrínseco igual a $1/2$. Por lo tanto ellas obedecen el principio de exclusión de Pauli de acuerdo con el teorema de estadística de espín [Pau40]. Además de sus anti-partículas, hay 12 tipos diferentes de partículas fundamentales que son conocidas y consideradas por el Modelo Estándar. Seis de ellas son clasificadas como quarks: up (u), down (d), strange (s), charm (c), top (t) bottom (b). Y las otras seis son clasificadas como leptones: electrón (e), muón (μ), tau (τ), y sus correspondientes neutrinos (ν_e, ν_μ, ν_τ). Estas partículas llevan cargas que las hacen susceptibles a las fuerzas fundamentales. Los pares de cada grupo (por ejemplo: un quark-u y un quark-d) forman una generación. Las propiedades de los quarks y leptones están resumidas en la Tabla 1.1.

Todas las partículas mediadoras de las fuerzas (bosones) que son descritas por el Modelo

Estándar tienen un espín intrínseco cuyo valor es 1. Los fotones son los mediadores de la fuerza electromagnética entre partículas eléctricamente cargadas. El fotón no tiene masa y es descrito por la electrodinámica cuántica. Todos los fermiones conocidos interactúan de forma débil. Ésta es mediada por el intercambio de los tres bosones de norma: W^+ , W^- y Z^0 . Z^0 es más masivo que los W , más aún, los W s llevan carga eléctrica y se acoplan a la interacción electromagnética. Estos tres bosones de norma junto con los fotones se agrupan y colectivamente son los mediadores de las llamadas interacciones electrodébiles.

Cada quark lleva alguna unidad de las tres cargas de color: -rojo, vede o azul, lo que les permite participar en interacciones fuertes a través del intercambio de alguno de los ocho gluones no masivos. Dado que los gluones tienen una carga efectiva de color, también puede haber interacciones entre ellos. Los gluones y sus interacciones son descritas por la teoría de la cromodinámica cuántica [Fie89] (QCD, por sus siglas en inglés). Las propiedades de los bosones de norma están resumidas en la Tabla 1.2.

La única partícula predicha por el Modelo Estándar que aún no ha sido descubierta es el bosón de Higgs (H). Dicho bosón juega un rol clave que explica el origen de la masa de otras partículas elementales, en particular la diferencia entre los fotones sin masa y los bosones pesados W y Z . También es necesario para dar la masa a los fermiones. Las masas se producen por medio de una invariancia de norma, debido al proceso conocido como mecanismo de Higgs [Hig64]. En este mecanismo, la simetría local de $SU(2) \times SU(1)$ de las interacción electrodébil se rompe espontáneamente. Este aspecto de la teoría acierta en la predicción de la existencia de los bosones de norma de la interacción débil así como la razón de sus masas. También predice la existencia de una partícula de espín 0: el bosón de Higgs.

A la fecha, casi todas las pruebas experimentales de las tres fuerzas descritas por el Modelo Estándar han estado en buen acuerdo con sus predicciones. Quizá la más impresionante es el excelente acuerdo entre los valores predichos y medidos para las masas de los bosones W y Z . Las predicciones han conducido también al descubrimiento del quark top en el Tevatron. A pesar del éxito de la teoría, aún no puede considerarse como una teoría completa de las interacciones fundamentales, principalmente porque falta incluir a la gravedad, pero también por el gran número de parámetros libres (como las masas y las constantes de acoplamiento) que deben ser puestas “a mano” en lugar de que sean derivados de primeros principios.

0.2 La cromodinámica cuántica

La cromodinámica cuántica, es la teoría de la interacción fuerte, que es la fuerza que describe la interacción entre quarks y gluones en los hadrones. Con la invención de las cámaras de burbujas y las cámaras de chispas en los años cincuentas, se descubrió un gran número de partículas llamadas hadrones. Parecía que este gran número de partículas no podrían ser todas fundamentales. Primero, las partículas fueron clasificadas de acuerdo a su carga e iso-espín; luego en 1953, de acuerdo a la extrañeza por Murray Gell-Mann y Kazuhiko Nishijima. Para extraer más información, los hadrones fueron puestos en grupos con propiedades

similares y masas usando “octupletes” inventados en 1961 por Gell-Mann y Yuval Neeman. Gell-Mann y George Zweig propusieron en 1963 que la estructura de los grupos podría ser explicada por la existencia de tres sabores de partículas pequeñas dentro de los hadrones: los quarks [GM64]. En ese tiempo la partícula Δ^{++} permanecía como un misterio en el modelo de quarks, pues esta compuesta de tres quarks up con espín paralelo, y esto es inaceptable por el principio de exclusión de Pauli. En 1965 este problema fue resuelto proponiendo que los quarks poseen un grado de libertad mas, posteriormente llamado carga de color y que los quarks interactúan vía un octeto de bosones de norma vectoriales: los gluones.

Una constante de acoplamiento g , es un número que determina la intensidad de una interacción. En teoría cuántica del campo, una función beta, $\beta(g)$ lleva la variación de una constante de acoplamiento y esta definida por la relación:

$$\beta(g) = \mu \frac{\delta g}{\delta \mu} \quad (1)$$

donde μ es la escala de energía de un proceso físico dado. Como un resultado, la constante de acoplamiento de QCD decrece logarítmicamente a altas energías:

$$\alpha_s(Q^2) = \frac{4\pi}{\beta_0 \ln(\frac{Q^2}{\Lambda_{QCD}^2})} \quad (2)$$

donde Λ_{QCD} es la escala de energía a la que el acoplamiento QCD diverge. Este comportamiento de la constante de acoplamiento implica dos propiedades muy importantes de QCD. Es fácil darse cuenta que a altos valores de Q^2 , la constante de acoplamiento se hace pequeña, esto da la propiedad llamada “libertad asintótica”. Básicamente, ésta implica que en colisiones a alta energía los quarks se mueven casi libremente en los nucleones. A baja Q^2 , la constante de acoplamiento diverge. Esta propiedad es conocida como “confinamiento de color” y es la razón por la cual nunca podemos observar quarks y gluones libres en la naturaleza. En lugar de esto, ellos forman “singletes” de color conocidos como hadrones.

Hay diferentes métodos teóricos que pueden ser usados para describir cada uno de los dos dominios de QCD. A pequeñas distancias (altos valores de Q^2) pueden ser aplicados los métodos perturbativos de QCD (pQCD), mientras que los modelos fenomenológicos son usados a largas distancias (pequeña Q^2). El comportamiento (variativo) del acoplamiento QCD es principalmente debido a la presencia de auto interacciones de los bosones de norma.

El parámetro Λ_{QCD} depende del esquema de normalización y del número de sabores activos (número de quarks con masa $m_q < Q$). Su valor fue determinado experimentalmente y es aproximadamente de 200 MeV. Por tanto, la aproximación perturbativa falla en escalas comparables con las masas de los hadrones ligeros ($Q \sim 1$ GeV/c).

0.3 Componentes de los eventos QCD

En esta tesis la medición que presento fue hecha en colisiones protón-protón. Como sabemos, la naturaleza de este tipo de colisiones entre hadrones es mucho más complicada que la de los choques electrón-positrón. Pues los protones no solo consisten de los quarks de valencia, si no también de un “mar” de quarks y gluones que constantemente se están produciendo y aniquilando. Cada uno de estos partones lleva una fracción de la energía total de un hadrón. De hecho las colisiones a alta energía no son entre protones si no entre los partones. Las funciones que describen la probabilidad de encontrar un cierto constituyente que lleva una fracción de la energía del hadrón son las funciones de distribución partónica (PDFs, Parton Distribution Functions).

La sección transversal inelástica de las colisiones entre hadrones esta muy dominada por una componente “suave”, lo que significa que solo una pequeña fracción de momento es transferida para formar nuevas partículas. Sin embargo, algunas veces una dispersión “dura” puede ocurrir. En este caso hay partones de alto momento transverso que son creados en las colisiones. Estos partones radian gluones suaves creando las llamadas lluvias de partones. La probabilidad de que un gluón con momento k y momento transverso k_T sea emitido por un quark con momento p es:

$$d\omega^{q \rightarrow q+g} = 2C_F \frac{\alpha_s(k_T)}{4\pi} [1 + (1 - \frac{k}{p})^2] \frac{dk}{k} \frac{dk_T^2}{k_T^2} \quad (3)$$

donde

$$\alpha_s(k_T) = \frac{2\pi}{\beta_0} \ln\left(\frac{k_T}{\Lambda}\right) \quad (4)$$

C_F es el factor de Casimir, en este caso vale $4/3$. Es fácil ver que la evolución del jet es determinada por la emisión de gluones suaves y colineales [YLD91], es decir, $\omega \sim \alpha_s \ln^2 p$ siempre que $k \ll p$. La emisión de un partón a un ángulo grande es también posible, sin embargo esta suprimida por $\omega \sim \alpha_s/\pi \ll 1$ cuando $k \sim p$. En la práctica no podemos ver la lluvia de partones (partones de estado final), por ello decimos que es un proceso a “nivel partónico”. Debido al confinamiento del color, los partones en el chubasco tienen que hadronizar. Un jet es un estrecho cono de hadrones y otras partículas producidas por la hadronización de un quark o gluón. El contenido de partículas de un evento después de la hadronización es referido como “nivel hadrónico”. La hadronización es descrita por las funciones de fragmentación (FF, Fragmentation Functions) ellas son relevantes para todo sistema de colisión. Estas representan la probabilidad de que un partón se confine con otros para formar un hadrón particular que lleve una fracción de la energía del partón. Las FFs incorporan efectos de largo alcance (baja Q^2), es decir, física no perturbativa de los procesos de hadronización en la que los hadrones observados se forman de partones de estado final del proceso de dispersión dura.

Intuitivamente podríamos pensar que los procesos de producción inclusivos de un hadrón pueden ser predichos, si primero se calcula el proceso equivalente a nivel partónico (es decir, remplazando el hadrón producido por un partón final y la suma inclusiva sobre todos los hadrones finales por partones finales), luego permitir que estos hadronicen.

La descripción general de la producción de hadrones finales (X) se logra por medio del teorema de factorización de QCD[Alb10], el cual puede resumirse así:

$$\frac{d\sigma}{dX} = \sum_{j,k} \int_{\hat{X}} f_j(x_1, Q_i) f_k(x_1, Q_i) \frac{d\hat{\sigma}_{jk}(Q_i, Q_j)}{d\hat{X}} F(\hat{X} \rightarrow X; Q_i, Q_f) \quad (5)$$

Note que la sección eficaz esta separada en dos partes: la sección eficaz partónica $\frac{d\hat{\sigma}_{jk}(Q_i, Q_j)}{d\hat{X}}$, que incorpora los procesos de corto alcance que son calculables en pQCD. Y las funciones universales que describen los procesos no perturbativos (PDFs, FFs). La Fig.1.1 muestra un esquema histórico usado por Feynman *et al.* para explicar la producción de partículas de alto momento. En estos trabajos por primera vez se incorporan los conceptos de funciones de distribución partónica, fragmentación y de jets [FFF78].

La detección de los hadrones en un experimento se hace usando su interacción con el material de un detector. Los objetos analizados típicamente son trazas, esto ocurre en el llamado “nivel detector”. En general, la dispersión dura principal va acompañada por otras interacciones dentro del mismo choque protón-protón, este proceso es llamado interacción múltiple de partones (MPI, Multi Parton Interaction¹). Dicho MPI junto con los remanentes del haz y la radiación de estado final e inicial constituyen el llamado “underlying event” (UE). La presencia del UE complica las mediciones en el ambiente de las colisiones hadrónicas porque uno tiene que descomponer el evento en las contribuciones de partículas de la dispersión dura y del UE. Dada la complejidad descrita, no es posible corregir por este efecto en las bases evento-por-evento, pero en su lugar uno puede calcular el factor de corrección promedio.

0.3.1 Interacciones Minimum Bias

QCD es una teoría muy exitosa en describir dispersiones partónicas en las que hay una transferencia de momento transverso grande. Sin embargo, las colisiones hadrónicas a alta energía están dominadas por colisiones partónicas suaves, estos eventos son conocidos como “minimum bias” (MB).

La sección eficaz total de la dispersión hadrón-hadrón, σ_{TOT} puede dividirse en procesos elásticos (σ_{ELAS}) y procesos inelásticos. Una clasificación común de las interacciones inelásticas $p - p$ es [ea08a]:

¹Las interacciones multipartónicas han sido indirectamente observadas experimentalmente: en distribuciones de multiplicidad de partículas cargadas en eventos “minimum bias” [SGM99], en mediciones de sección eficaz de jets de baja energía transversa [Col03]. También hay evidencia de ellas en estudios del UE asociado a eventos con jets [Col02a].

- eventos no difractivos (σ_{ND})
- eventos de una difracción (σ_{SD})
- eventos con doble difracción (σ_{DD})

La sección eficaz total en términos del cuadrado de la energía en el centro de masa de la colisión, s , puede ser expresada como:

$$\sigma_{\text{TOT}}(s) = \sigma_{\text{ELAS}}(s) + \sigma_{\text{SD}}(s) + \sigma_{\text{DD}}(s) + \sigma_{\text{ND}}(s) \quad (6)$$

Un evento difractivo es aquel en el cual uno (o ambos) proyectiles permanece(n) intacto(s). Entre los eventos sin difracción están las interacciones partónicas con transferencia de momento en algunos GeV/c. La Figura 1.3 muestra un esquema de las interacciones hadrónicas en el espacio η - ϕ para los distintos procesos discutidos.

Entre las características de estas clases de eventos, la distribución de partículas en pseudo-rapidez muestra que los procesos no difractivos tienen muchas partículas en la región central y abruptamente cae a más grande rapidez. En colisiones con una difracción, solo una de las partículas del haz se divide y produce partículas a alta rapidez en un solo lado. En una colisión con doble difracción ambos haces se dividen y producen partículas a valores altos de rapidez positiva y negativa con un hueco en la región central.

Las mediciones de los eventos minimum bias muestran una estrecha similaridad con las interacciones sin un sistema difractivo creado (NSD). La interpretación es basada en el sistema de disparo usado por ejemplo en los experimentos que hicieron tales mediciones CERN-ISR [ea84], CERN-SPS UA5 [ea87a], hasta la era del Tevatron: CDF [ea90] y E735 [ea98, ea99]. Estos experimentos favorecieron la detección de eventos NSD. Desde el punto de vista teórico, algunos modelos pudieron satisfactoriamente describir las interacciones suaves y los procesos difractivos a través de la identificación de los eventos MB con las interacciones no difractivas (ND). En términos prácticos, la elección experimental de los eventos minimum bias no difiere considerablemente. Por ejemplo las secciones eficaces a $\sqrt{s} = 900$ GeV/c para interacciones ND es ~ 34.9 mb mientras que para NSD es ~ 40.8 mb. Estos valores fueron obtenidos de PYTHIA6. En general, a las energías de colisión actuales, las secciones eficaces (NSD y ND) difícilmente podrían diferir en más del 15 %.

0.4 Motivaciones físicas para estudiar eventos “Minimum Bias”

Como vimos en las secciones anteriores, hay objetos muy pequeños que constituyen a la materia, estos son las partículas elementales: quarks, leptones y bosones de norma. La rama de la física que se encarga de estudiarlas se llama física de altas energías, el nombre viene del hecho de que estas no se producen en condiciones normales de la Tierra si no mediante

colisiones a muy altas energías. Es por ello que se construyen los grandes aceleradores de partículas. Actualmente, la máquina más poderosa construida en la Tierra para producir choques de protones con energía en centro de masa de hasta 14 TeV es el LHC (Large Hadron Collider). Esta en un túnel circular de 27 km de circunferencia, y enterrado entre 50 y 175 m bajo la superficie de la tierra [ea08c]. El LHC se encuentra entre la frontera de Suiza y Francia a las afueras de la Ciudad de Ginebra. Las primeras colisiones a una energía de 3.75 TeV por haz ocurrieron el 30 de Marzo del 2010. Los cuatro grandes experimentos del colisionador comenzaron a tomar datos y han dado los primeros resultados.

Los experimentos ATLAS [GAea08] y CMS [SCea08] fueron diseñados principalmente para buscar al bosón de Higgs, esta es una tarea fundamental del programa del LHC. Al verano de 2011, con una luminosidad integrada de más de 1 fb^{-1} (ya sensible al Higgs del Modelo Estándar) de datos a 7 TeV han excluido amplios rangos para la masa del Higgs². Por lo tanto hasta el momento el Higgs permanece como la única partícula del MS que no ha sido descubierta.

Otras búsquedas de física más allá del MS se están llevando a cabo, entre ellas SUSY (supersimetría) y dimensiones extra a la escala de TeV. Estos ambiciosos proyectos requieren de un buen entendimiento del fondo que acompaña a las señales de interés, pues por ejemplo en ATLAS se reporta que cada evento potencialmente interesante está acompañado por más de 20 eventos MB, por lo tanto la física de colisiones MB adquiere importancia!

Además, en el LHC se lleva a la materia a condiciones extremas de temperatura y densidad con el objetivo de entender como fenómenos colectivos y propiedades macroscópicas que involucran varios grados de libertad, emergen de leyes microscópicas de la física de partículas elementales. Tal medio se crea mediante colisiones de iones pesados y el experimento ALICE (A Large Ion Collider Experiment) fue diseñado para eso. ALICE [ea04b, ea06] fue optimizado para trabajar en ambientes en los cuales se esperaba que se producirían hasta 8000 partículas por unidad de rapidez, eso condujo a construir un detector de respuesta lenta (TPC, Time Projection Chamber), que exige trabajar a baja luminosidad. La colaboración ALICE ha analizado cerca de 20 millones de eventos de colisiones plomo-plomo ($\text{Pb} - \text{Pb}$) a energía en centro de masa por par de núcleo de $\sqrt{s_{NN}} = 2.76 \text{ TeV}$. Entre las primeras mediciones reportadas está la densidad de partículas producidas a rapidez media (centralidad hasta de 5%) el resultado no es muy espectacular, pues la medición da 1584 (menos del 20% de lo esperado hace varios años).

El medio “caliente y denso” se puede estudiar mediante las llamadas pruebas duras, esto se refiere a estudiar sus propiedades a través de procesos duros que ocurren en la colisión. Uno espera que como resultado de los choques, exista la posibilidad de que se de una dispersión dura entre partones, los partones finales atraviesan el medio, que en principio está formado por quarks y gluones desconfinados que conforman el plasma de quarks y gluones (QGP). Al interactuar los partones con el medio, estos experimentan una pérdida de energía por colisión o por radiación inducida del medio, el resultado final es que el partón dispersado se absorba, o bien, salga en forma de un jet pero con una energía menor a la que tendría si

²Europhysics Conference on High-Energy Physics: <http://eps-hep2011.eu/>

hubiera fragmentado en el vacío. Lo que se hace para extraer las propiedades del medio, es entender el proceso en $p - p$ y compararlo con mediciones análogas en choques de núcleos pesados. Como ejemplo, discutámos el factor de modificación nuclear R_{AA} , que sirve para cuantificar los efectos del medio a alto p_T . Éste esta definido como la razón de la producción de partículas cargadas en $\text{Pb} - \text{Pb}$ respecto a $p - p$, escalado al número de colisiones binarias nucleón-nucleón $\langle N_{coll} \rangle$:

$$R_{AA}(p_T) = \frac{(1/N_{ev}^{AA}) \frac{d^2N_{ch}^{AA}}{d\eta dp_T}}{\langle N_{coll} \rangle (1/N_{ev}^{pp}) \frac{d^2N_{ch}^{pp}}{d\eta dp_T}} \quad (7)$$

La medición de R_{AA} se reporta en [KAea10a] para p_T hasta de 20 GeV/c, alrededor de 1 GeV/c el R_{AA} alcanza su máximo y comienza a decrecer hasta más o menos 5-6 GeV/c y luego muestra una tendencia creciente. Si no existiera un medio creado, el resultado sería un $R_{AA} = \text{constante}$. A resaltar es el hecho de que al igual que en las mediciones de CMS y ATLAS, en ALICE, para hacer una correcta interpretación de los resultados de iones, los estudios en $p - p$ MB son de gran envergadura.

ALICE tiene todo un programa dedicado a física de colisiones $p - p$, entre ellos se encuentran: espectros de partículas identificadas, producción de extrañeza, correlaciones, producción de sabores pesados, estudios con jets, física difractiva. Sin embargo, podemos ir más allá aprovechando algunas cualidades que posee ALICE, que consiste en hacer reconstrucción de trazas de partículas con momento muy bajo ~ 100 MeV/c y hasta 100 GeV/c. Además de los sistemas que posee para hacer identificación de partículas mediante el uso de varias tecnologías: TRD, TOF, HMPID, TPC.

La física de choques $p - p$ MB no creo que pueda reducirse a proporcionar señales de referencia para entender los procesos “interesantes”. Pues hay resultados que llaman la atención porque son inesperados, por ejemplo, consideremos la multiplicidad de partículas cargadas a $\sqrt{s} = 7$ TeV reportada por ALICE [KAea10b]. La Figura 1 muestra la distribución de multiplicidad en $|\eta| < 1$, para procesos inelásticos. Las mediciones hechas por ALICE son comparadas con las predicciones de los generadores Monte Carlo, vemos que PYTHIA6 versión 6.4.21 [Sjo94] con el modelo ATLAS-CSC [Mor] es el que más se acerca a reproducir las mediciones, esto lo hace sin mucho éxito, pues como podemos ver para multiplicidades más grandes que 40 las diferencias son hasta de un 30 %. Los demás modelos difieren en más de un 50 % respecto a las mediciones observadas. Si miramos el espectro de momento transverso de partículas primarias cargadas para procesos inelásticos, vemos de la Fig. 2 que PHOJET[Eng95] reproduce mejor esta observable que la multiplicidad, de hecho es de los modelos más exitosos para el espectro de p_T .

El mensaje que se lee de los resultados es muy claro, no es posible describir con un conjunto de parámetros las mediciones hechas en colisiones MB $p - p$, pues por ejemplo por un lado un generador puede ser exitoso en describir una observable pero no en describir otra.

Al parecer la descripción de los eventos MB va más allá de ese cuadro que hemos pintado

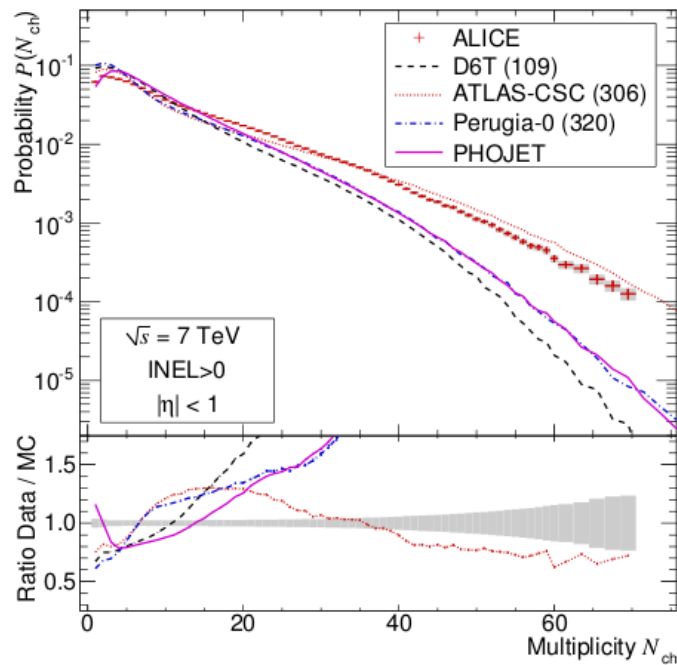


Figure 1: Medición de la distribución de multiplicidad en $|\eta| < 1$ para eventos inelásticos. Las barras de error de los datos representan el error estadístico mientras que las zonas sombreadas representan la incertidumbre sistemática. Los datos a $\sqrt{s} = 7 \text{ TeV}$ son comparados con los generadores Monte Carlo PHOJET y PYTHIA.

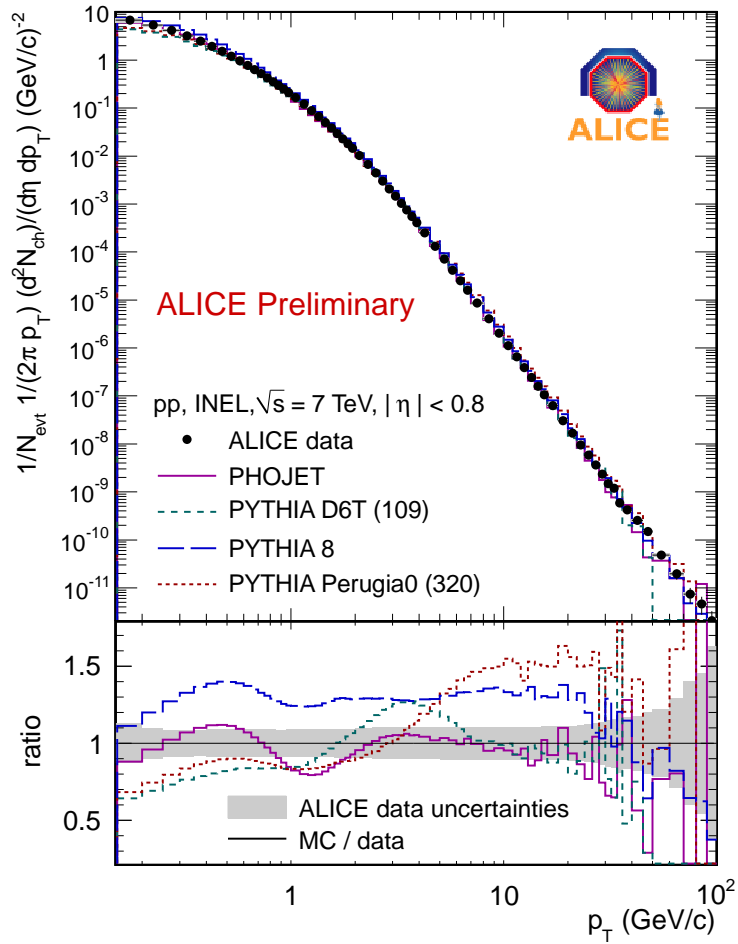


Figure 2: Espectro de momento transverso de partículas primarias cargadas en colisiones $p - p$ a $\sqrt{s} = 7$ TeV medido con ALICE en el LHC. La figura muestra el espectro en el rango de 0.15 a 100 GeV/c además de la comparación con los generadores de eventos Monte Carlo PYTHIA y PHOJET así como la razón MC/Datos.

basado en la interacción múltiple, la radiación de estado final e inicial, los remanentes del haz y el proceso inelástico o difractivo. Quizás estos eventos son un conjunto de modos diferentes de colisiones incluso basados en la centralidad de la colisión. Por ejemplo, si una colisión se da de manera muy central, lo más probable es que la multiplicidad final sea muy grande, esto no esta fuera de los modelos MC, pues por ejemplo en PYTHIA hay parámetros que regulan el traslape de materia hadrónica, el efecto de incrementar la densidad en el centro del hadrón es un ensanchamiento de la distribución de multiplicidad. En esta lógica, las colisiones más periféricas son las que se asociarían a eventos de menor multiplicidad. Además de esto, en los generadores las multiplicidades grandes son logradas haciendo más violenta la colisión a nivel de partones. Parecen muchos los elementos que entran en este juego!

La alta multiplicidad resulta interesante, pues de hecho el rango medido a 7 TeV se traslapa con mediciones hechas en colisiones CuCu a energías ultra-relativistas de $\sqrt{s_{NN}} = 62$ y 200 GeV en RHIC (Relativistic Heavy Ion Collider). Esto abre la posibilidad de comparar observables entre $p - p$ e iones pesados al mismo estado final de multiplicidad. La cuestión interesante a atender es si las colisiones $p - p$ a alta multiplicidad se parecen a las colisiones entre iones pesados.

Esta pregunta ha adquirido más relevancia con la reciente observación hecha por la colaboración CMS en la que reportan correlaciones en rapidez de largo alcance en eventos de alta multiplicidad $p - p$ [Col10]. Hay varios intentos por explicar el fenómeno en el marco del CGC (Color Glass Condensate) o como un flujo elíptico. Este descubrimiento es muy relevante, pues un fenómeno similar es observado en colisiones de iones pesados, y casualmente el efecto es más evidente en el rango intermedio de momento transverso similar al que se observa en choques de núcleos pesados ($1 < p_T^{trig} < 3$ GeV/c y $1 < p_T^{assoc} < 3$ GeV/c). En este tipo de estudios, se seleccionan partículas “trigger” en ciertas ventanas de momento transverso y se mide su correlación transversal ($\Delta\phi = \phi^{trig} - \phi^{assoc}$) y longitudinal ($\Delta\eta = \eta^{trig} - \eta^{assoc}$) con partículas llamadas “asociadas” en otra ventana de p_T . La Figura 3 ilustra claramente el resultado, la estructura de “ridge” se observa a $\Delta\phi \approx 0$ y se extiende hasta valores de $|\Delta\eta|$ en al menos cuatro unidades. Ningún generador de eventos da un efecto similar, pues incluso es difícil alcanzar tales multiplicidades.

Las líneas anteriores soportan la idea de que el tema de la alta multiplicidad es interesante y física nueva podría ser descubierta. Es por ello que esta tesis se enfoca en caracterizar las colisiones MB $p - p$ por medio de las observables de forma. Se propone estudiar la evolución de los eventos desde la multiplicidad más baja hasta las más altas que se puedan colectar en el experimento ALICE.

0.5 Variables de forma del evento

Las variables de forma caracterizan la estructura global de las colisiones a alta energía. Especialmente en el caso de las colisiones electrón-positrón y dispersión inelástica profunda (DIP) estas observables fueron de las más usadas para probar QCD perturbativa conforme

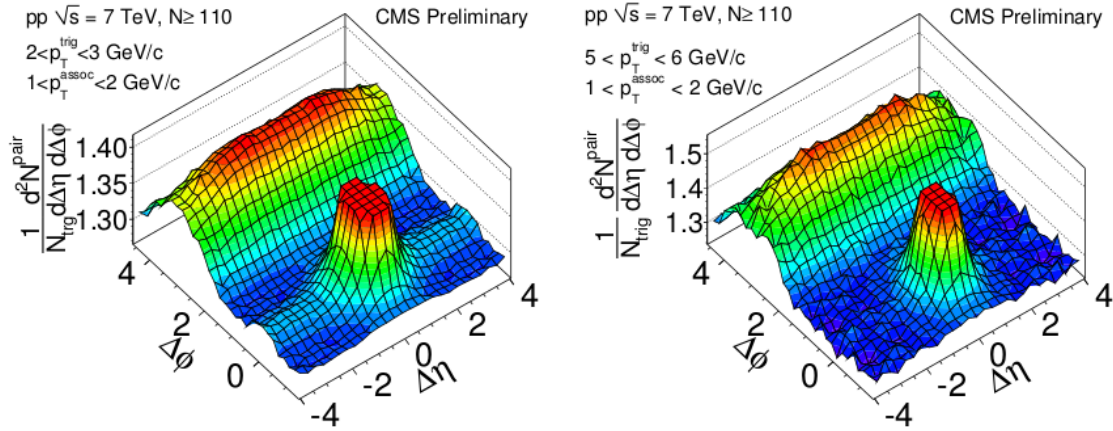


Figure 3: Distribución en dos dimensiones del número de pares de hadrones cargados correlacionados por trigger en función de $\Delta\eta$ y $\Delta\phi$ con un corte en el pico del jet para una mejor visibilidad del “ridge”. El estudio se hace para eventos de multiplicidad mayor a 110 hadrones cargados en colisiones $p - p$ a $\sqrt{s} = 7$ TeV. Dos casos son mostrados: (a) $2 < p_T^{\text{trig}} < 3$ GeV/c y $1 < p_T^{\text{assoc}} < 2$ GeV/c, (b) $5 < p_T^{\text{trig}} < 6$ GeV/c y $1 < p_T^{\text{assoc}} < 2$ GeV/c.

se incrementaba la energía del sistema de colisión. Hay un amplio número de trabajos que se han reportado tanto en los frentes teórico como experimental, una revisión se puede encontrar en [DS04]. La prueba experimental que sirvió para aceptar la existencia de los jets, es quizás, una de las aplicaciones más importantes en las que las observables de estructura jugaron un rol clave. Por ejemplo, la esfericidad fue usada en SLAC (Stanford Linear Accelerator Center) para demostrar la existencia de jets en procesos de aniquilación e^+e^- a energías hasta de 7.4 GeV en centro de masa [ea75]. Más tarde en 1979 la colaboración MARK-J usó la variable “oblateness” para describir procesos en los que tres jets prolongados se producen a energía hasta de 31.5 GeV, no fue el único trabajo reportado, hubo otros que usaron observables tales como el “thrust” y la “aplanarity”; aportando más evidencia para revindicar el descubrimiento del gluón [Col79a, Col79b, Col79c, Col80]. Dado que estas variables son calculables en términos de partones finales y medidas usando los hadrones observados asimismo es posible usarlas para estudiar la hadronización [SK01, PA96]. También se han reportado varias mediciones de la constante de acoplamiento [Bet03].

En el caso de los colisionadores de hadrones, resulta un poco difícil extraer la estructura de los eventos dado que hay una gran componente de procesos suaves que no forma parte del proceso de interés, ya hemos referido a esta como UE. Recientemente ha aparecido en la literatura una modificación a la definición de las observables de tal manera que sean medibles en colisiones de hadrones, lo que se hace es restringir el análisis a la componente perpendicular a la dirección del haz [BSZ]. Sin ésta, la esfericidad tendría una componente longitudinal muy grande asociada a la fragmentación de los remanentes del haz. Típicamente las mediciones

reportadas así como los estudios fenomenológicos [aPS11] se basan en analizar eventos en los que hay jets de alta energía transversa, por ejemplo recientemente las colaboraciones CDF [Col11a] y CMS [Col11b] han medido las observables “thrust” transversal y “thrust” menor usando eventos con jets. Y han encontrado un buen acuerdo con cálculos perturbativos de QCD.

La idea de este trabajo es caracterizar los eventos MB usando este tipo de observables pero ahora en función de la multiplicidad. La variable propuesta para ser estudiada es la esfericidad transversa, sin embargo en [OP, COP] hemos hecho estudios a nivel MC usando observables como “thrust” transversal, “thrust menor” y “recoil”.

Comúnmente la esfericidad transversa esta definida en términos del los auto-valores $\lambda_1 > \lambda_2$ que resultan de diagonalizar la matriz de momento transversal del evento en cuestión:

$$\mathbf{S}_{\mathbf{x}\mathbf{y}}^{\mathbf{Q}} = \sum_i \begin{pmatrix} p_{xi}^2 & p_{xi}p_{yi} \\ p_{xi}p_{yi} & p_{yi}^2 \end{pmatrix}$$

donde $\vec{p}_{Ti} = (p_{xi}, p_{yi})$ es el momento transverso de la partícula i en la aceptancia fijada por el experimento. La esfericidad transversa queda definida como:

$$S_T \equiv \frac{2\lambda_2}{\lambda_2 + \lambda_1} \quad (8)$$

Dado que $\mathbf{S}_{\mathbf{x}\mathbf{y}}^{\mathbf{Q}}$ es cuadrática en el momento de las partículas, ésta es altamente afectada por las divergencias colineales. Por ejemplo, si un momento “duro” a lo largo de la dirección x se divide en dos iguales en momento y colineales, entonces su contribución combinada a $\sum_i p_{xi}^2$ será la mitad de lo que daría el momento original. Estas divisiones colineales cambian la esfericidad! Para librarnos de este tipo de divergencias, la matriz puede ser linealizada de la siguiente manera:

$$\mathbf{S}_{\mathbf{x}\mathbf{y}}^{\mathbf{L}} = \frac{1}{\sum_i p_{Ti}} \sum_i \frac{1}{p_{Ti}} \begin{pmatrix} p_{xi}^2 & p_{xi}p_{yi} \\ p_{xi}p_{yi} & p_{yi}^2 \end{pmatrix}$$

Y la esfericidad linealizada puede ser definida igual que (8). En ambos casos, los límites de la esfericidad transversal son:

$$S_T = \begin{cases} = 0 & \text{“estructura de lápiz”} \\ = 1 & \text{“estructura isotrópica”} \end{cases}$$

La Figura 4 muestra un evento real de choque protón-protón a $\sqrt{s} = 7$ TeV reconstruido por ALICE. Para calcular la esfericidad se usaron trazas primarias cargadas con momento transverso mayor que 500 MeV/c en la aceptancia $|\eta| < 0.8$. El evento es de alta multiplicidad y tiene una esfericidad cercana al límite de estructura de lápiz. Dada la multiplicidad, es claro ver que hay dos máximos tanto en la distribución de densidad de partículas (“Entries”) como

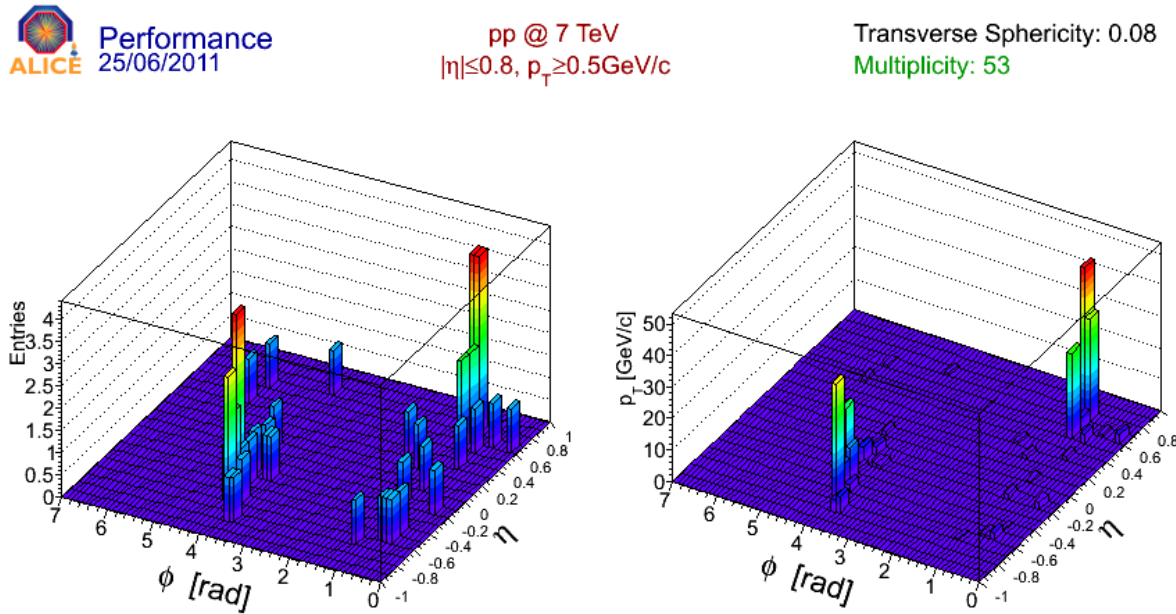


Figure 4: Estructura de un evento de alta multiplicidad y baja esfericidad transversal en el espacio η - ϕ . El evento corresponde a una colisión de protones a $\sqrt{s} = 7$ TeV reconstruida por ALICE. Las trazas usadas para el cálculo son de partículas primarias con momento transverso mayor que 500 MeV/c en $|\eta| < 0.8$.

en la de momento transverso; ambas están en función de η - ϕ . Los máximos difieren en ángulo azimutal por π . Los picos pueden ser asociados con dos jets producidos por una dispersión dura. Para comparar, la Figura 5 muestra otro evento extremo de alta multiplicidad pero ahora con esfericidad cercana a uno. Las trazas están uniformemente distribuidas en el espacio η - ϕ y el momento transverso no muestra una estructura definida. En este sentido decimos que podemos clasificar eventos de acuerdo a su dureza.

Las variables de forma son una herramienta muy poderosa, pues por ejemplo, podríamos identificar fácilmente eventos con estructura poco usual. Imaginemos un evento de muy alta multiplicidad y con alto momento isotrópicamente distribuido, en principio haciendo cortes en p_T , los eventos deberían de ser más duros y por lo tanto con menor esfericidad. Si estos eventos especiales existieran, serían fácilmente detectables pues aparecerían como una señal perfectamente definida en la alta esfericidad. Para clarificar esta idea consideraremos el caso de la variable τ (límite isotrópico: ~ 0.3634 , límite de estructura de lápiz: 0). En la Figura 6 (tomada de [ftAC11]) se encuentra un estudio de la variable τ en eventos generados con PYTHIA6 (modelo ATLAS-CSC [Mor]), la observable fue calculada usando partículas primarias cargadas con $p_T \geq 0.5$ GeV/c y los eventos tienen más de 2 partículas primarias. Se señalan tres casos: (izquierda) se consideran todos los eventos, (centro) eventos con al menos una partícula con $p_T > 2$ GeV/c y (derecha) eventos con al menos una partícula con

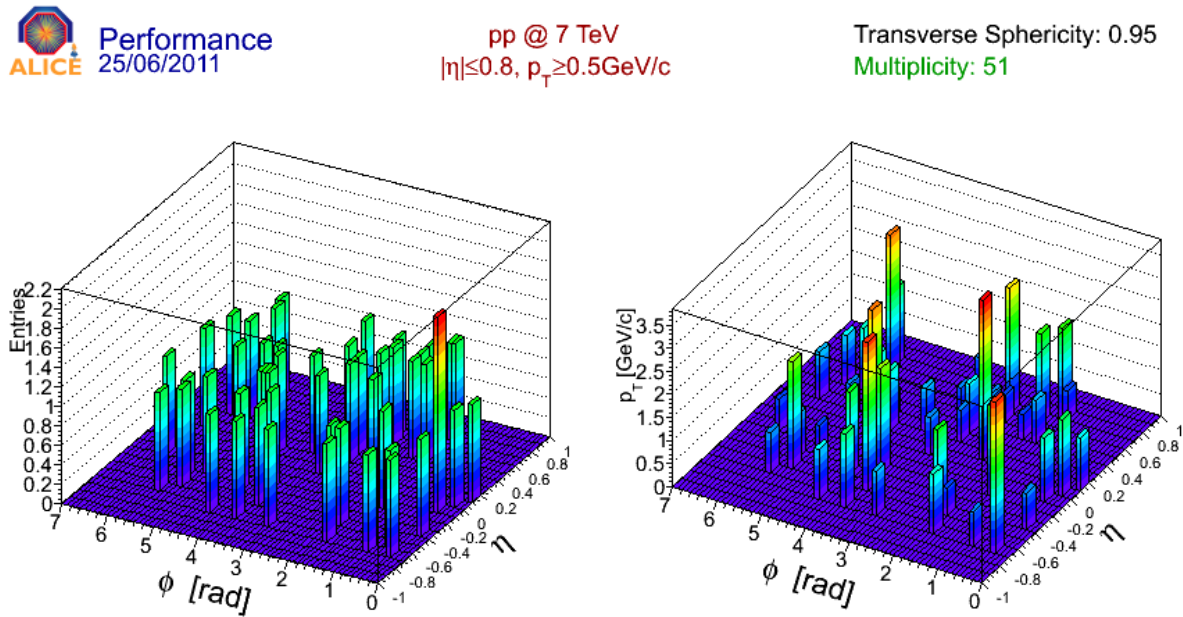


Figure 5: Estructura de un evento de alta multiplicidad y alta esfericidad transversal en el espacio η - ϕ . El evento corresponde a una colisión de protones a $\sqrt{s} = 7$ TeV reconstruida por ALICE. Las trazas usadas para el cálculo son de partículas primarias con momento transverso mayor que 500 MeV/c en $|\eta| < 0.8$.

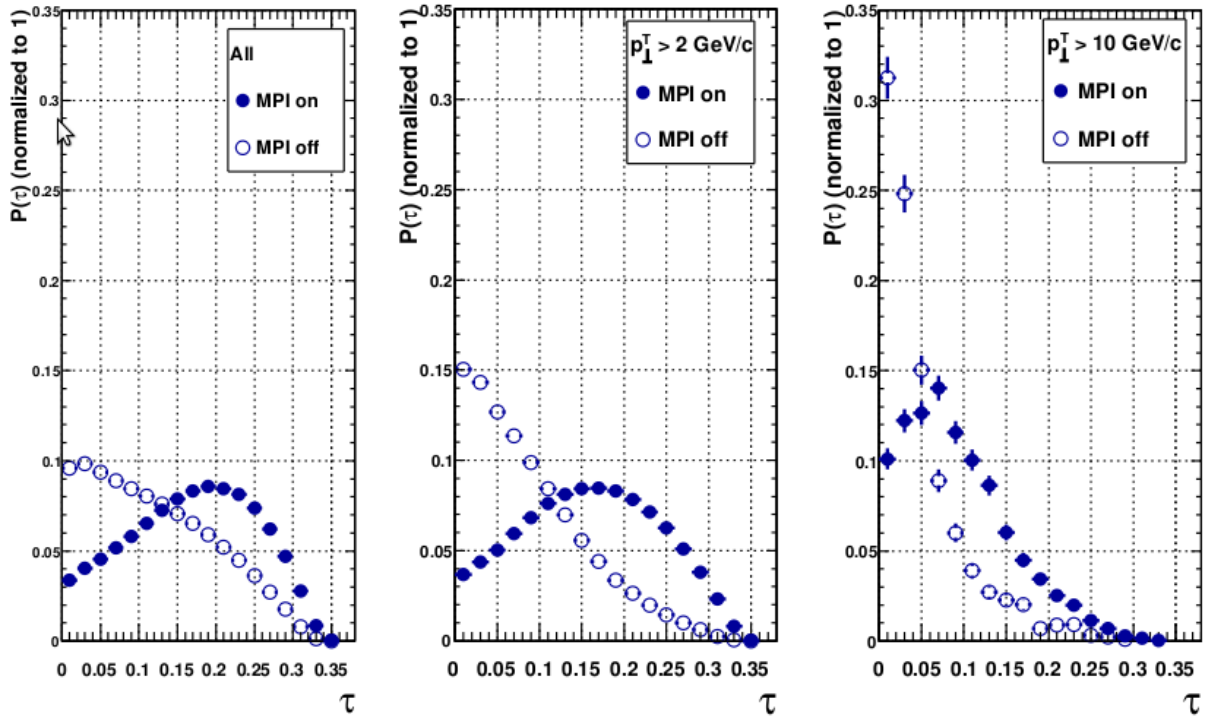


Figure 6: Distribución de la observable τ para eventos generados con PYTHIA6 modelo ATLAS-CSC[Mor] en los que se hacen diferentes cortes en la partícula de más alto momento transverso del evento.

$p_T > 10 \text{ GeV}/c$. En las gráficas también se muestra los casos en el que se incluye (o no) la múltiple interacción de partones. Con el corte más alto en la partícula líder, la estructura del evento es mayormente dominada por el proceso duro. Además el bin asociado a los eventos más esféricos comienza a despoblararse conforme el corte en p_T líder se incrementa, es en ese bin en el que se deberían de encontrar los eventos raros al aplicar cortes más duros en p_T .

Otro aspecto interesante de las observables es su alta sensibilidad a los aspectos no perturbativos de la colisión. Como ejemplo consideremos la Figura 7 en la cual se muestra la correlación a dos hadrones cargados primarios normalizada al número de partículas líder (“trigger”), la partícula líder es la que posee el máximo momento transverso del evento, en este caso se considera una ventana de $2 \leq p_T^{trig} \leq 15 \text{ GeV}/c$. Si consideramos todos los eventos con más de dos partículas primarias cargadas en $|\eta| \leq 0.8$ y $p_T \geq 0.5 \text{ GeV}/c$, el panel izquierdo muestra la correlación para tres casos: todos los parámetros activados de PYTHIA6 modelo ATLAS-CSC, modelo ATLAS-CSC sin radiación de estado inicial y el caso en el que se desactiva la radiación de estado final. Para el primer caso, el fondo sobre el que descansan el pico del lado cercano a la líder ($|\Delta\phi| \leq 1 \text{ rad.}$) y del lado lejano esta a un nivel alto, ~ 0.2 , el efecto de la radiación de estado final es clave en el ancho del pico del lado lejano. Si consideramos eventos con esfericidad muy baja, por ejemplo menor que 0.1

(gráfica del centro), vemos que es el proceso duro el que define la estructura del evento, pues los diferentes modos que hemos activado producen la misma señal, además el nivel del fondo es prácticamente cero. Por otro lado si vemos la figura del lado derecho en la que se considera una esfericidad intermedia entre 0.5-0.6, notamos que aparecen estructuras interesantes en el lado lejano para cada uno de los modos activados; la radiación de estado inicial y final producen estructuras diferentes, si no se incluye la primera, aparece una estructura de doble pico en el lado lejano de la distribución. Podemos decir que cada bin de esfericidad, esta asociado con una estructura global definida por las partículas primarias que emergen de la colisión.

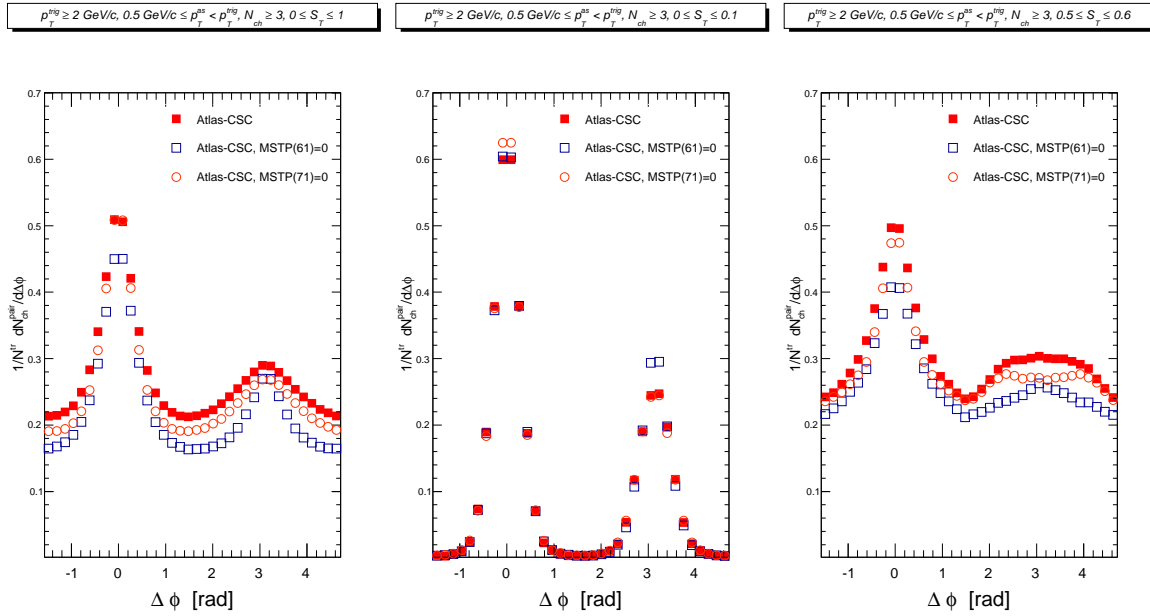


Figure 7: Correlación a dos hadrones normalizada al número de partículas líder en el rango: $2 \leq p_T \leq 15$ GeV/c. Los eventos son generados con PYTHIA6 modelo ATLAS-CSC. Se muestran tres casos: todos los parámetros del modelo están activados, sin radiación de estado inicial (MSTP(61)=0), sin radiación de estado final (MSTP(71)=0). Los eventos tienen una multiplicidad mayor de dos partículas primarias cargadas con $p_T \geq 0.5$ GeV/c en $|\eta| \leq 0.8$. Para ver la estructura de los eventos de acuerdo al valor de su esfericidad, se muestran tres tipos de selección: (izquierda) todo el rango de S_T , (en medio) $0 \leq S_T \leq 0.1$ y (derecha) $0.5 \leq S_T \leq 0.6$

Tomando como base los estudios hechos en MC, se puede concluir que el análisis de estructuras de eventos puede ser usado para:

1. Seleccionar eventos con estructura suave y dura. Los eventos de estructura dura se localizan a baja esfericidad.
2. Hacer una rápida identificación de eventos con estructuras inusuales, por ejemplo los llamados eventos “erizo” que consistirían en aquellos que tienen un alto momento isotrópicamente distribuido.

3. Las variables de forma son altamente sensibles a los parámetros de PYTHIA que regulan la componente UE, por ejemplo vimos el efecto de la radiación de estado final e inicial. Además en [COP] se reporta como varían las observables de forma y su correlación con otras observables si se cambian los parámetros de la interacción múltiple de partones. Por ello es posible hacer una afinación o “tune” de los modelos a fin de reproducir mejor las mediciones.
4. Son observables que nos ayudan a caracterizar los eventos de alta multiplicidad, nos dan los elementos para responder a la pregunta: Cómo es la presencia de jets (“jetness”) en los eventos de alta multiplicidad? En ALICE resulta particularmente importante usar este tipo de aproximación, pues el experimento no cuenta con un calorímetro lo suficientemente extendido para hacer identificación y reconstrucción de jets.

0.6 El experimento ALICE

El experimento ALICE es un experimento de propósito general cuyos detectores miden e identifican hadrones, leptones y fotones a rapidez media producidos en la interacción. Su diseño es único, pues posee una optimización muy diferente a la que tienen los experimentos dedicados a física $p - p$ en el LHC. Éste es resultado de los requerimientos para hacer identificación de partículas desde el bajo (~ 100 MeV/c) hasta alto (~ 100 GeV/c) p_T , para reconstruir partículas de tiempo de vida corta como los hiperones, mesones D y B , y para llevar a cabo estas tareas en un ambiente con muy alta multiplicidad de partículas primarias cargadas. La detección e identificación de muones son llevadas a cabo con un espectrómetro dedicado, que incluye un gran dipolo magnético y cubre un dominio de rapidez desde -4.0 hasta -2.4. Los hadrones, electrones y fotones son detectados en la región de rapidez central ($|\eta| \leq 0.8$) por un sistema complejo de detectores inmerso en un campo magnético moderado de 0.5 T. La reconstrucción de trazas es posible debido a un conjunto de detectores de alta granularidad: un sistema de reconstrucción de trazas interno (ITS, Inner Tracking System) que consiste en tres tecnologías diferentes de detectores de silicio, una cámara de proyección del tiempo de gran volumen (TPC) y un detector de transición de radiación (TRD, Transition Radiation Detector) de alta granularidad. La identificación de partículas se lleva a cabo a través de medir la pérdida de energía en los detectores de trazas, transición de la radiación en el TRD, tiempo de vuelo con el TOF (Time Of Flight) con un arreglo de alta resolución, detector de radiación Cherenkov con un detector de identificación de trazas de alto momento (HMPID. High Momentum Particle Identification Detector), y fotones con el PHOS (PHoton Spectrometer). Otros detectores adicionales localizados a alta rapidez completan el sistema de detección para caracterizar al evento y dar la señal de disparo cuando hay una interacción interesante. Ellos cubren una amplia aceptancia ($-3.4 < \eta < 5.1$) para la medición de partículas cargadas y dar la señal de disparo (Forward Multiplicity Detector-FMD, VZERO y T0), y un dominio estrecho a alta rapidez ($2.4 < \eta < 3.5$) para la medición de multiplicidad de fotones (Photon Multiplicity Detector-PMD), y la cobertura de la rapidez de los haces para medir nucleones espectadores en colisiones entre iones pesados (Zero-Degree

Calorimeters-ZDC). La Figura 2.1 muestra un esquema del sistema de detectores de ALICE.

Para el análisis que se reporta en esta tesis, los detectores relevantes en la medición son: TPC e ITS para la reconstrucción de trazas, SPD para la reconstrucción del vértice primario y VZERO+SPD para el disparo. A continuación se presenta una descripción de su funcionamiento.

0.6.1 Cámara de Proyección del Tiempo

Dado que la TPC es el principal dispositivo que usamos para la reconstrucción de las trazas, vale la pena hacer una pequeña revisión del funcionamiento de los detectores de gas. Los puntos clave para entender el funcionamiento de éstos se listan a continuación:

- **Ionización de gas por partículas cargadas** Una partícula que atraviesa la materia interactúa con electrones y con núcleos, posiblemente también con el medio como un todo (radiación Cherenkov, Bremsstrahlung). Las pérdidas de energía son descritas por la fórmula de Bethe-Bloch. Mucha de la energía perdida se convierte en excitación de moléculas/átomos y en ionización. Al pasar por ejemplo un kaón a través del medio, el proceso va a lucir como $K A \rightarrow K A^+ + e^-$, donde A está cargado positivamente, por lo tanto es un ión positivo del medio y e^- es un electrón libre. La energía perdida promedio por ionización es cerca del doble que el potencial de ionización. Por ejemplo, para el Argón, el potencial de ionización es de 15 eV, pero la energía promedio requerida para producir un par ion/electrón es de 26 eV.

- **Arrastre de electrones e iones en gases** Si aplicamos un potencial eléctrico estático en el detector los electrones de ionización primaria, e^- , se van a arrastrar hacia el electrodo con carga +, ánodo. Los iones positivos, A^+ , se moverán al cátodo. Así, se obtienen dos nubes cargadas moviéndose en direcciones opuestas. Debido a la baja masa de los electrones, éstos se mueven con mayor velocidad de arrastre que los iones. El valor de la velocidad de arrastre depende de la forma del campo, \vec{E} , las propiedades de las moléculas del gas, la densidad o presión, P , y la temperatura. Para una mezcla particular de gas, típicamente la velocidad de arrastre *vs.* E , donde E está en kVolts/cm, luce como en la Figura 8.

Lo deseable es garantizar que la velocidad de arrastre sea estable con pequeñas variaciones de la intensidad del campo. Esta es la razón por la que en cámaras de arrastre se usa un campo eléctrico $\lesssim 1-1.1$ kV/cm. En este caso la velocidad de arrastre es alrededor de 50 micrones por nanosegundo.

- **Amplificación de la ionización** Si un campo eléctrico es suficientemente grande, los electrones se aceleran a tal grado que tienen suficiente energía cinemática para liberar electrones en colisiones con otros átomos o moléculas: $e^- A \rightarrow e^- e^- e^- A^{++}$. De esta manera se puede tener alto campo eléctrico si el ánodo es un cable delgado. Como un electrón se arrastra a través del cable este viaja en un campo eléctrico que se incrementa,

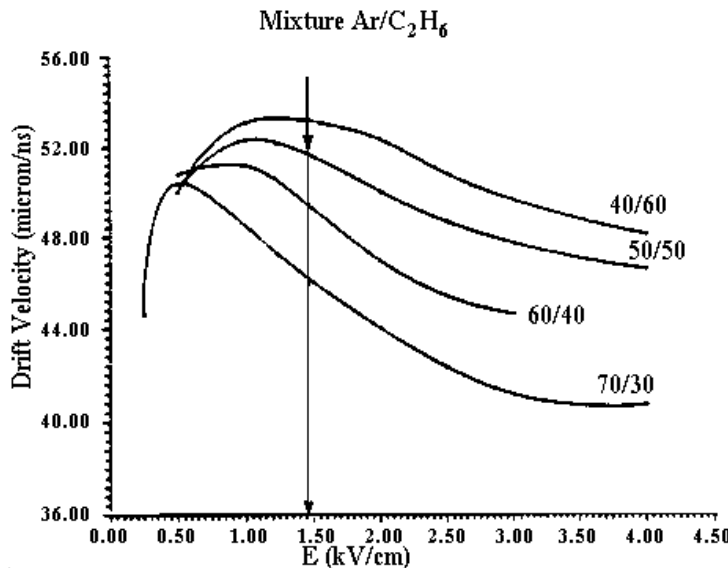


Figure 8: Velocidad de deriva *vs.* intensidad del campo eléctrico en un detector de gas.

\vec{E} . En la vecindad del ánodo de alambre este campo a un radio r , esta dado por la densidad de carga lineal, λ :

$$E \sim \lambda/r \quad (9)$$

Para describir el factor de multiplicación del gas, esta el coeficiente de Townsend, $\alpha(E)/\text{cm}$, que determina la multiplicación del gas por unidad de longitud a una intensidad particular del campo E . En campo variable la ganancia del gas M puede ser descrita por la integración desde un radio al cual inicia la ganancia del gas hasta el radio del alambre del ánodo:

$$M = \exp\left[\int_{r_1}^{r^2} \alpha(x)dx\right] \quad (10)$$

El coeficiente de Townsend depende significativamente de la composición del gas. Por ejemplo para las cámaras de arrastre la ganancia del gas es el orden de 10^4

- **Creación de la señal** Para simplificar la descripción del proceso de creación de la señal, consideremos un detector de alambre cilíndrico:

1. Una carga se mueve en un campo eléctrico que produce trabajo o energía eléctrica:

$$dW = qEdr = qdp \quad (11)$$

donde q es la carga, E es la intensidad del campo eléctrico, p es el potencial y r la distancia. Esto significa que para producir energía, la carga debe cruzar

potenciales diferentes, haciendo un trabajo por lo que podemos ver la señal (voltaje inducido) mientras la carga se mueve, no cuando la carga llega al ánodo! La energía producida por el movimiento de la carga es alimentada por el circuito eléctrico, que suministra una carga dQ al ánodo para mantener el voltaje aplicado constante. Así tenemos:

$$qdp = V_0 dQ \quad (12)$$

y la señal de voltaje inducida en el ánodo con capacitancia C al cátodo:

$$dV_a = \frac{dQ}{C} = q \frac{dp}{V_0} \frac{1}{C} \quad (13)$$

De este modo en cada momento la señal del voltaje es proporcional a la diferencia de potencial entre los puntos iniciales y finales, y para obtener la señal completa de la carga en movimiento ésta debe pasar por todo el V_0

2. En un detector cilíndrico donde la mayor parte de la carga es producida en la vecindad del ánodo, los electrones pasan a través de una muy pequeña diferencia de potencial eléctrico y producen un pequeño trabajo (negativo inducido). En contraste, los iones positivos cruzan casi el potencial completo V_0 y producen un voltaje inducido mucho más grande. Pero usamos señales de electrones en nuestros detectores. La movilidad de los electrones e iones son muy diferentes, los electrones se mueven mucho más rápido. Así que usamos detectores como una fuente de corriente. Las avalanchas próximas al cable del ánodo toman algunos nanosegundos, mientras que los iones se mueven al cátodo en algunos microsegundos, incluso casi algunos milisegundos. Si la capacitancia del detector es C , las cargas inducidas en el cátodo (o ánodo) es $Q = V(t)/C$ y la corriente inducida sería $i = dQ/dt = 1/CdV/dt$. Así, podemos usar electrónica rápida sensible a la corriente para detectar la señal. Durante 5-10 nanosegundos se colecta un muy pequeño porcentaje de la carga total integrada pero el pulso de corriente más largo.

Recordemos, que el ánodo y cátodo son idénticos para la formación de señal: en el ánodo hay una señal negativa de electrones que se aproximan y se alejan de los iones positivos; con la misma amplitud y forma una señal positiva es inducida en el cátodo. Debido a las cargas que se mueven en el campo formado por extensos y espaciados electrodos, por ejemplo por el cátodo, la señal inducida luce como distribuida en la superficie del cátodo con máximo justo donde se localiza la avalancha en el alambre del ánodo [Fer92, aLR].

- **Cámara Multi-alambre** La cámara proporcional de multi-alambre (MWPC, Multi-Wire Proportional Chamber) es un plano de alambres de ánodo entre dos planos de cátodos. Cada alambre de ánodo actúa como un contador proporcional individual. La resolución espacial es determinada por el espaciamiento entre los alambres del ánodo. Lecturas simultáneas de los electrodos ánodo y cátodo son posibles.

Una cámara de proyección del tiempo consiste de una cámara cilíndrica rellena de gas con MWPC como “tapas”. Una TPC es el principal dispositivo de ALICE para hacer la reconstrucción de las trazas, este cubre el ángulo azimutal completo y un rango de pseudorapidez $|\eta| < 0.8$ para reconstruir trazas con longitud radial completa. Para colisiones $p - p$, el tiempo de memoria de la TPC es un factor de limitación para la luminosidad dado el tiempo de arrastre de $\sim 94 \mu s$. La TPC tiene una membrana central mantenida a alto voltaje ~ 100 kV y dos planos de lectura en las capas finales (ve Figura 2.3). Su volumen activo esta limitado a $85 < r < 247$ cm y $-250 < z < 250$ cm en las direcciones radial y longitudinal, respectivamente. El material entre el punto de interacción y el volumen activo de la TPC corresponde a 11% de una longitud de radiación promediada en $|\eta| < 0.8$. La membrana central divide el volumen en dos partes. El campo de arrastre homogéneo de 400 V/cm en la mezcla de gas Ne-CO₂-N₂ (85.7%-9.5%-4.8%) origina un máximo tiempo de arrastre de $94 \mu s$. Los electrones de ionización producidos por las partículas cargadas que atraviesan la TPC se arrastran hasta las capas finales de lectura compuestas de 72 MWPC con cátodo para lectura.

0.6.2 Sistema Interno de Rastreo

El sistema interno de rastreo (ITS, por sus siglas en inglés) consta de seis capas de detectores de silicio localizadas a radios entre 3.9 y 43 cm (ver Figura 2.2) y que son coaxiales al tubo del haz. Sus principales tareas son: localizar y reconstruir el vértice primario con una resolución mejor que 100 μm , reconstruir los vértices secundarios de decaimientos de hiperones y mesones D y B, rastrear e identificar partículas con momento abajo de 200 MeV/c, mejorar la resolución angular y de momento para partículas reconstruidas en la TPC y reconstruir partículas que atraviesan por las regiones muertas de la TPC. Hay tres tecnologías que son implementadas en el ITS.

- **Detector Pixelar de Silicio (SPD).** Debido a la alta densidad de partículas en colisiones de iones pesados y para garantizar la resolución requerida en el parámetro de impácto, los detectores SPD se usan para las dos capas más internas del ITS. El SPD cubre un rango de pseudorapidez de $|\eta| < 2$ y $|\eta| < 1.4$, respectivamente. Y tiene un total de 9.8 millones de pixeles: 50×425 . La resolución espacial de diseño ($\sigma_{r\phi} \times \sigma_z$) es $12 \times 100 \mu m^2$. El SPD también es usado como nivel cero de disparo L0. Para este propósito cada uno de los 1,200 chips de lectura dan una señal rápida llamada “fast OR” que indica que al menos un pixel de un chip dado produjó una señal. Estas señales son enviadas a un FPGA³ que es capaz de implementar funciones lógicas Booleanas. Esto permite desarrollar “disparos” que van desde los MB hasta los más complejos, como el disparo de alta multiplicidad (HM).

³Un FPGA (del inglés Field Programmable Gate Array) es un dispositivo semiconductor que contiene bloques de lógica cuya interconexión y funcionalidad puede ser configurada mediante un lenguaje de descripción especializado.

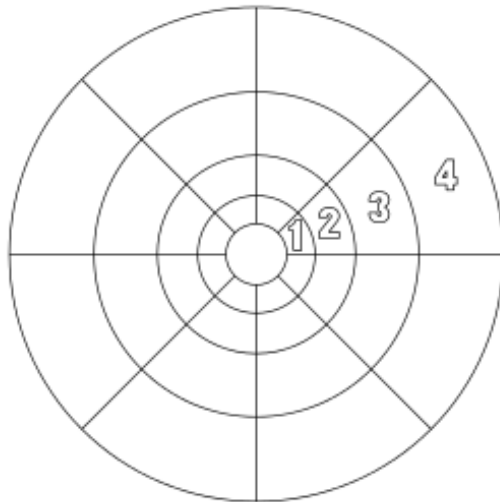


Figure 9: Segmentación de los arreglos V0A/V0C.

- **Detector de Arrastre de Silicio (SDD)** Son dos capas de SDD con un total de 133,000 canales de lectura. El SDD es operado con un campo de deriva de 500 V/cm que resulta en una velocidad de arrastre de cerca de $6.5 \mu\text{m}/\text{ns}$ en un tiempo máximo de arrastre de al rededor de $5.3 \mu\text{s}$. Su resolución espacial de diseño es de cerca de $35 \times 25 \mu\text{m}^2$.
- **Detector de Tiras de Silicio (SSD)** Con esta tecnología están diseñadas las dos capas externas del ITS. El SSD consiste de sensores de micro-tiras de silicio de doble cara, comprende un total de 2.6 millones de canales de lectura. Su resolución espacial es de $20 \times 830 \mu\text{m}$.

0.6.3 Detector VZERO

El detector VZERO esta hecho de dos arreglos (V0A y V0C) localizados asimétricamente en cada lado del punto de interacción. El primero a 340 cm desde la posición nominal del vértice en el lado opuesto al espectrómetro de muones. El segundo esta fijo a la cara frontal del absisor a 90 cm de la posición nominal del vértice. Ambos están segmentados en 32 contadores elementales distribuidos en cuatro sectores (ver Figura 9). Cada anillo cubre 0.4-0.6 unidades de pseudorapidez. Los anillos son divididos en ocho sectores de $\pi/4$. El contador elemental consiste de material centellador con fibras inmersas. La luz de las fibras es colectada por fibras claras y transportada a tubos foto-multiplicadores instalados a 3-5 m desde los detectores. La resolución temporal de cada contador es mejor que 1 ns.

Este detector se usa como “disparo” de los eventos MB, así como para rechazar ruido relacionado con interacciones del haz.

0.7 Análisis de datos

El objetivo del trabajo es medir la esfericidad y momento transverso promedio en función de la multiplicidad. La multiplicidad es definida como el número de partículas primarias cargadas con $p_T \geq 0.5$ GeV/c en $|\eta| \leq 0.8$. Además se estudiaron los espectros de esfericidad en bines de multiplicidad. En los siguientes párrafos se describen los aspectos más esenciales del análisis. Las gráficas sobre las que se hace la discusión están en los capítulos que vienen en el cuerpo oficial de la tesis, pues éste es solo un resumen.

0.7.1 Descripción de la muestra MB

En 2010, ALICE grabó eventos de interacciones MB a las energías en centro de masa: 0.9 y 7 TeV, en 2011 el LHC corrió a $\sqrt{s} = 2.76$ TeV. La estadística de eventos analizados es de ~ 40 millones de eventos a 7 y a 2.76 TeV, mientras que a 0.9 TeV solo 3.6 millones. La posición del vértice de interacción fue reconstruida correlacionando señales en las dos capas del SPD. La resolución del vértice lograda depende de la multiplicidad de trazas, y es típicamente de 0.1-0.3 mm en la dirección longitudinal y de 0.2-0.5 mm en la dirección transversa. El evento es aceptado si la posición longitudinal del vértice, z_v satisface $|z_v - z_0| < 10$ cm, donde z_0 es la posición nominal. Para obtener una buena resolución de la esfericidad[COP], solo eventos con más de dos trazas primarias en $|\eta| < 0.8$ y $p_T > 0.5$ GeV/c son considerados. Estos cortes reducen la estadística a ~ 9.1 , ~ 4.2 y ~ 0.42 millones de eventos para datos a 7, 2.76 y 0.9 TeV, respectivamente.

0.7.2 Selección de trazas primarias

Solo trazas de partículas cargadas son seleccionadas en el rango de pseudorapidez $|\eta| < 0.8$. En este rango, las trazas en la TPC pueden ser reconstruidas con máxima longitud y mínima pérdida de eficiencia debido a las fronteras del detector [KAea10c]. Además se requieren cortes de calidad para asegurar alta resolución en el rastreo y baja contaminación debido a trazas de partículas secundarias. Una traza es aceptada si tiene al menos 70 puntos espaciales reconstruidos en la TPC, y una χ^2 por punto espacial usada para el ajuste del momento menor que 4. Las trazas son rechazadas como no asociadas al vértice primario si su distancia de acercamiento más próxima al vértice reconstruido del evento en el plano perpendicular a la dirección del haz, d_0 , satisface: $d_0 > 7(0.0350 + 0.042/p_T^{0.9})$ (con p_T en GeV/c). Éste corte es ajustado para seleccionar partículas primarias cargadas con alta eficiencia y minimiza la contribución de decaimientos débil, conversiones e interacciones hadrónicas en el material del detector.

0.7.3 Selección de eventos por su dureza

Antes de describir el método y los resultados es bueno justificar el porque de una selección basada en la dureza del evento, en particular tomando como referencia el máximo p_T de eventos individuales. Se trata de usar un método que ha sido implementado a menudo para tratar de caracterizar los eventos en el sentido de separar los modos de producción. Éste consiste en dividir la muestra en eventos “suaves” y “duros”. Varios experimentos han mostrado interesantes diferencias entre los dos regímenes [Col02b, Hua]. En la aproximación que proponemos, los eventos “suaves” están definidos como aquellos que no tienen una traza con p_T más allá de 2 GeV/c, mientras que los eventos “duros” son del resto de la muestra. En el análisis también se considera el bullo que corresponde a considerar ambas muestras. La Tabla 6.1 muestra la razón de eventos “suaves” a “duros” para los datos de ALICE y los generadores: PYTHIA6 (modelos ATLAS-CSC[Mor] y PERUGIA-0[Ska]), PHOJET[Eng95] y PYHIA8[eab]. Sumado a ésto, la Figura 5.1 muestra la correlación entre el máximo p_T del evento y la esfericidad promedio para datos reconstruidos de ALICE y MC (PERUGIA-0). Podemos ver que la esfericidad promedio alcanza un máximo en $p_T \sim 1.8$ GeV/c, antes de ese máximo la tendencia es creciente y después la esfericidad decrece al incrementar el p_T . Es como si ese valor marcará la transición de los procesos suaves a los duros, es claro que nuestra elección no es tan arbitraria.

0.7.4 Correcciones aplicadas a los datos

El método usado para corregir las distribuciones de esfericidad medida por eficiencia, aceptancia y otros efectos del detector esta basada en una deconvolución que consiste en minimizar la función χ^2 con un término de regularización [COP].

$$\chi^2(\mathbf{U}) = \sum_m \left(\frac{\mathbf{M}_m - \sum_t \mathbf{R}_{mt} \mathbf{U}_t}{e_m} \right)^2 + \beta P(\mathbf{U}) \quad (14)$$

donde \mathbf{M} es el espectro medido con error en la medición e_m ; \mathbf{R}_{mt} es la matriz de respuesta; \mathbf{U} es el espectro deconvolucionado. Para prevenir las soluciones fluctuantes se agrega un término de regularización $P(\mathbf{U})$ pesado por el parámetro β .

El procedimiento es aplicado en bins de multiplicidad. Una vez que se tiene el espectro deconvolucionado en un bin de multiplicidad medida, N_m , se extrae el promedio de la distribución, $\langle S_T \rangle^m$, dicho promedio se corrige por la multiplicidad siguiendo la apoximación:

$$\langle S_T \rangle(N_t) = \sum_m \langle S_T \rangle^m(N_m) \mathbf{R}(N_t, N_m) \quad (15)$$

donde $\mathbf{R}(N_t, N_m)$ es la matriz de respuesta de la multiplicidad y N_t es la multiplicidad real, que a partir de ahora llamamos N_{ch} . Se usaron diferentes simulaciones para probar el método, todas producen el mismo resultado con una discrepancia mínima (< 1%). La Figura 5.12

muestra un ejemplo de la matriz de respuesta de esfericidad a multiplicidad medida 27. El MC usado para calcular las correcciones es PYTHIA6 con el modelo ATLAS-CSC, los eventos son generados con una distribución de multiplicidad plana. La Figura 5.3 muestra la matriz de respuesta de multiplicidad que fue usada para el cálculo de los factores de corrección, el comportamiento es muy bueno, pues la correlación no muestra “no linealidades” severas.

Para determinar $\langle p_T \rangle(N_t)$, calculamos el promedio de p_T contando todas las trazas que pasan los cortes de selección que ya fueron discutidos. Este procedimiento es aplicado en bins de multiplicidad medida, N_m .

$$\langle p_T \rangle(N_m) = \frac{1}{N_m} \sum_i p_{T,i} \quad (16)$$

Una vez que se tiene el promedio en función de la multiplicidad, $\langle p_T \rangle^{\text{raw}}(N_m)$, seguimos la siguiente aproximación:

$$\langle p_T \rangle(N_t) = \sum_m \langle p_T \rangle^{\text{raw}}(N_m) R(N_t, N_m) \quad (17)$$

Note que en este caso no implementamos alguna deconvolución del promedio de p_T . La Figura 10 ilustra el buen funcionamiento de este procedimiento. Para llegar a esa gráfica, se usaron las matrices de respuesta discutidas previamente y calculadas usando PYTHIA6 como generador. Los datos MC reconstruidos (generados con PHOJET) fueron corregidos con dichos factores y el resultado después de la corrección se compara con los puntos que se obtienen directamente del generador (puntos verdaderos). Las diferencias entre los puntos verdaderos y los corregidos casi en todo el rango de multiplicidad considerada alcanza a lo más $\sim 1.5\%$, dicha diferencia se mantiene estable.

Finalmente para obtener los espectros normalizados de esfericidad en contenedores de multiplicidad, se aplica una corrección en cada bin. De este modo, la probabilidad de encontrar un evento con esfericidad S_T^{corr} en un bin dado de multiplicidad (N_{ch}) se obtiene de la siguiente manera:

$$P(S_T^{\text{corr}}) |_{atN_{ch}} = P(S_T^{\text{raw}}) |_{atN_{raw}} \times C_1 \times C_2 \quad (18)$$

donde $P(S_T^{\text{raw}}) |_{atN_{raw}}$ es la probabilidad (usando la información de la reconstrucción) de encontrar un evento con esfericidad S_T en un bin de multiplicidad reconstruida, N_{raw} . Esta probabilidad se corrige por C_1 y C_2 que se calculan usando MC. C_1 es la corrección del espectro en función de la multiplicidad medida.

$$C_1 = \frac{P(S_T^{\text{unf}})}{P(S_T^m)} |_{atN_m} \quad (19)$$

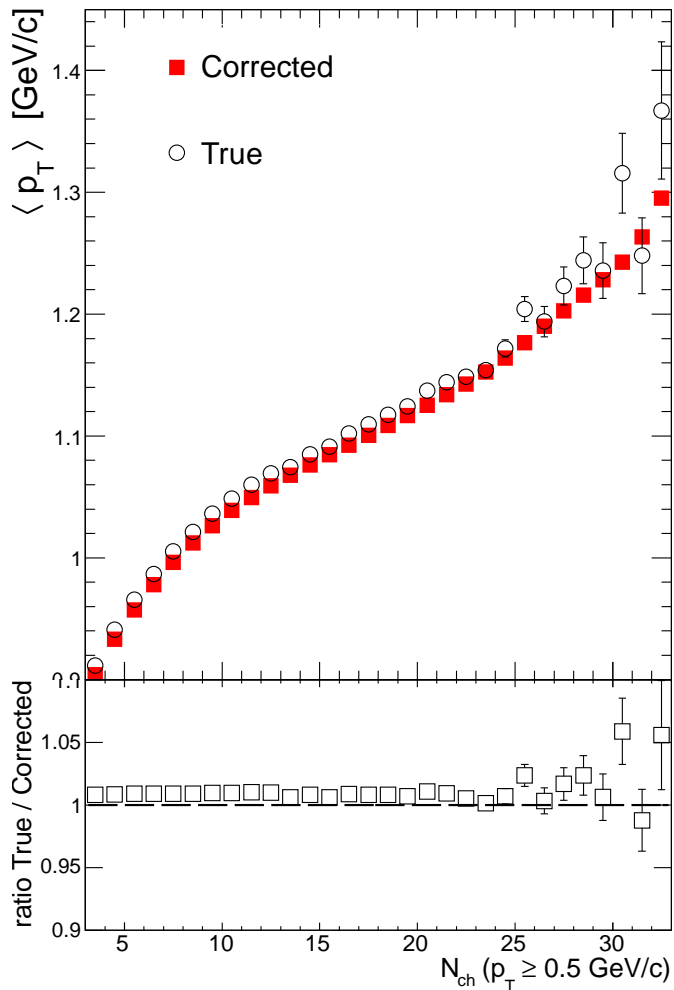


Figure 10: Prueba del funcionamiento del procedimiento de corrección del momento transverso promedio en función de la multiplicidad para los eventos “bulto”. En esta prueba, datos MC reconstruidos generados con PHOJET son corregidos usando PYTHIA6. En la gráfica se muestran los puntos corregidos y los puntos obtenidos directamente del generador (TRUE).

Por otro lado C_2 corrige la probabilidad por la fuga de multiplicidad, es decir la filtración de eventos que poseen una multiplicidad verdadera mayor a la especificada por el contenedor.

$$C_2 = \frac{P(S_T^t) |_{atNt}}{P(S_T^t) |_{atNm}} \quad (20)$$

En la expresión, $P(S_T^t)$ es la probabilidad de encontrar un evento con esfericidad verdadera S_T^t , los símbolos N_m y N_t son las multiplicidades medida y verdadera. S_T^t y S_T^{unf} son los espectros de esfericidad verdadera y deconvolucionada, respectivamente. La última es el resultado de deconvolucionar la medición simulada, *i.e.* PYTHIA6 corregida por PHOJET y viceversa.

0.7.5 Errores sistemáticos

Para estimar los errores sistemáticos en la esfericidad promedio, el análisis fue aplicado en diferentes condiciones experimentales de tal manera que fuese posible ver su influencia en los resultados finales.

La contribución que preocupa en este tipo de análisis es el “pile up” o efecto de reconstruir dos eventos al mismo tiempo y grabarlo como uno solo. Como ya discutimos, en ALICE debido a la TPC se trabaja a baja luminosidad, esto origina que la probabilidad de tener eventos amontonados sea muy pequeña. Sin embargo, como medida de control, a la muestra de datos se le aplica un corte de tal manera que todos aquellos eventos con más de un vértice primario reconstruido por el SPD son rechazados. El error sistemático fue estimado usando la fracción de eventos con el máximo amontonamiento de la muestra. El efecto en el resultado para los eventos del bullo es menor al 0.2 %.

El error debido al rechazo de secundarios fue estimado incrementando la contribución de secundarios en la muestra hasta un $\sim 8\%$. Esto se logra variando N de $d_0 > N(0.0350 + \frac{0.0420}{pt^{0.9}})$ (pt in GeV/c), donde d_0 es la distancia de acercamiento más próximo de la traza al vértice primario en el plano perpendicular al haz.

La dependencia en el modelo fue determinada por medio de una comparación de los resultados corregidos con PYTHIA6 o PHOJET.

En este análisis la contribución a los errores sistemáticos, quizás la más importante, es la debida al método de corrección. Por ejemplo, la incertidumbre más grande es a baja multiplicidad ($N_t \sim 3$) para la muestra de eventos duros. Ésta alcanza hasta un 11% en el bin de multiplicidad más baja.

Se probaron diferentes conjuntos de cortes razonables para estimar el error sistemático debido a la selección.

La Tabla 6.2 muestra un resumen con las incertidumbres sistemáticas que fueron analizadas para $\langle S_T \rangle$.

Table 1: Incertidumbres sistemáticas en los espectros de esfericidad

Rango de Multiplicidad	3-9	10-19	20-29
Método	< 0.1%	< 2.0%	< 5.0%
Dependencia en el Modelo	< 5.0%	< 1.0%	< 1.0%
Eventos Amontonados	< 1.0%	< 1.0%	< 4.0%
Total	< 5.1%	< 2.4%	< 6.5%

Además de estas pruebas, hubo otras verificaciones para asegurar la calidad de los resultados, por ejemplo se usaron eventos mezclados para demostrar que la señal obtenida realmente corresponde a la estructura del evento y no a combinaciones aleatorias de trazas. También, el análisis fue aplicado a eventos con eje de esfericidad en diferentes regiones de la TPC, los resultados no son sensibles a estas variaciones.

En el caso del promedio del momento transverso en función de la multiplicidad los errores sistemáticos son tomados de [KAea10c], la única diferencia esta en el método usado para corregir. Para los eventos del bulto el error alcanza $\sim 1.5\%$, mientras que para los suaves y duros los errores son hasta de $\sim 1.0\%$ y $\sim 5.1\%$, respectivamente.

Para los espectros de esfericidad en contenedores de multiplicidad, las principales incertidumbres sistemáticas están listadas en la Tabla 6.3. Las estimaciones fueron hechas siguiendo un procedimiento similar al que fue explicado. En la Figura 6.12 se muestra un resumen con los errores sistemáticos que fueron analizados.

0.8 Resultados

En esta sección se presentan los resultados del análisis aplicado en datos reales así como la comparación con diferentes modelos de interacciones MB: PYTHIA6 [Sjo94] (modelos: ATLAS-CSC [Mor] y PERUGIA-0 [Ska]), PHOJET [Eng95] y PYTHIA8 [eab].

0.8.1 $\langle S_T \rangle$ en datos a $\sqrt{s} = 0.9$ TeV

La esfericidad transversa promedio en función de la multiplicidad para colisiones $p - p$ a $\sqrt{s} = 0.9$ TeV esta mostrada en las Figuras: 6.13, 6.14 6.15 para eventos del bulto, suaves y duros, respectivamente.

Con la estadística disponible de datos reales la máxima multiplicidad alcanzada es 20. Los eventos del bulto exhiben un buen acuerdo con los modelos: PHOJET y los modelos de PYTHIA6. Pero los puntos de ALICE van $\sim 10\%$ arriba de PYTHIA8 para $N_{ch} > 10$. Si miramos a los eventos suaves, los cuatro modelos están en buen acuerdo con las mediciones

de ALICE para las multiplicidades hasta 13, pero PYTHIA8 esta $\sim 5\%$ por debajo de los datos. Para los eventos duros, hay una notable diferencia entre ALICE y los otros modelos. Las diferencias son más grandes que las incertidumbres sistemática y estadística.

0.8.2 Resultados de $\langle S_T \rangle$ en datos a $\sqrt{s} = 7$ TeV

Las Figuras 6.16, 6.17 y 6.18 muestran la esfericidad promedio en función de la multiplicidad para eventos del bullo, suaves y duros, respectivamente. El comportamiento de los eventos del bullo esta en desacuerdo con los modelos, excepto en el rango $N_{ch} = 3 - \sim 10$, en el que ATLAS-CSC reproduce muy bien las mediciones. Sin embargo, para multiplicidades más altas, las simulaciones basada en PYTHIA alcanzan un valor $\langle S_T \rangle \sim 0.7$ y luego al rededor de $N_{ch} \sim 25$ muestran una ligera caída. Para PHOJET se observa una caída más dramática para una multiplicidad de al rededor de 25. El resto de los modelos luce similar a ambas energías. En contraste ALICE exhibe un comportamiento más isotrópico para eventos con multiplicidad mayor que 20. Para los eventos suaves, los cuatro modelos describen razonablemente bien las tendencias de los datos; en el rango completo de multiplicidad hay un pequeño “offset” menor al 10% en las razones. De esta manera, las diferencias observadas en los eventos del bullo son causadas por eventos de naturaleza dura. Mirando a los eventos duros, la esfericidad promedio predicha por los modelos es más pequeña que la medida en el rango completo de multiplicidad. La caída en esfericidad promedio observada en PHOJET para eventos del bullo es recuperada en los eventos duros.

0.8.3 Momento transverso promedio

La Figura 6.19 muestra $\langle p_T \rangle$ como función de la multiplicidad. Para eventos del bullo, a 0.9 TeV, la Figura 6.19 muestra que PERUGIA-0 reproduce mejor los datos, mientras que PYTHIA8 esta en buen acuerdo para multiplicidades hasta 12, más allá su pendiente se incrementa notablemente comparada con las mediciones. PHOJET y ATLAS-CSC son más suaves que los datos. Para los datos a 7 TeV la pendiente de los datos es más pequeña que la de MC a excepción de ATLAS-CSC. De manera general observamos que la pendiente de las tendencias de los generadores se incrementan significativamente al rededor de 30. Este comportamiento es consistente con nuestras observaciones de esfericidad dado que a esas multiplicidades, el $\langle S_T \rangle$ de los generadores alcanza su máximo y luego decrece fuertemente a altos valores. En contraste, para las multiplicidades más bajas, PHOJET esta más próximo a los datos. El comportamiento indica que PERUGIA-0 pudiera contener más jets que los datos de ALICE.

Considerando los eventos suaves, a 0.9 TeV PERUGIA-0 y PYTHIA8 describen bien los datos. A 7 TeV para multiplicidades más pequeñas que 20, PERUGIA-0, PHOJET y PYTHIA8 están en buen acuerdo con los datos mientras que a más alta multiplicidad se observan diferencias. Para los eventos duros la diferencia con generadores arriba de $N_{ch} = 20$ es aún más notable. Las mediciones implican que los generadores parecen construir los

eventos de alta multiplicidad incrementando el $\langle p_T \rangle$ de los eventos.

0.8.4 Espectros de S_T en contenedores de multiplicidad

Para tratar de entender los resultados observados en $\langle p_T \rangle$, $\langle S_T \rangle$ y multiplicidad hemos extraído el espectro normalizado de esfericidad en diferentes bins de multiplicidad: $N_{ch} = 3 - 9$, $10 - 19$, $20 - 29$ y > 30 . Estos están mostrados en las Figuras 6.20, 6.21, 6.22 y 6.23 junto con las razones a sus correspondientes MC. En el primer bin de multiplicidad, el acuerdo entre datos y MC es bueno, pero en el siguiente bin ($N_{ch} = 10 - 19$) la razón datos a MC alcanza 0.3. En el último bin de multiplicidad la sobre producción de eventos con jets alcanza un factor 3, y la subestimación de los eventos isotrópicos es hasta de un factor 2.

0.8.5 Evolución de la esfericidad transversa con la multiplicidad a 0.9, 2.76 y 7 TeV

La última parte de esta tesis está dedicada a la comparación de la esfericidad promedio a las tres energías disponibles. Las Figuras 6.25, 6.26 y 6.27 muestran los resultados para eventos del bullo, suaves y duros, respectivamente. Los datos de ALICE son comparados con PYTHIA8 y PHOJET. La esfericidad promedio de los datos parece indicar una única función de multiplicidad, excepto quizás para el último bin. Por otro lado MC exhibe una dependencia diferente de los datos e incluso entre ellos también difieren.

0.9 Discusiones y Conclusiones

Por primera vez se presenta un estudio de la esfericidad transversa en eventos minimum bias. La observable fue linealizada para que sea libre de divergencias colineales y de este modo calculable en el marco de QCD perturbativa. Asimismo se midió el momento transverso en función de la multiplicidad. El análisis se hizo en eventos minimum bias reconstruidos en ALICE. La muestra fue dividida en dos categorías: eventos suaves (sin p_T por arriba de 2 GeV/c), duros (los eventos restantes). Además se analizó la mezcla de ambos que llamamos bullo. Una división similar fue hecha por CDF [Col02b] y STAR [Hua] mostrando que el p_T no cambia mucho desde la energía de RHIC de 0.2 TeV hasta las energías de CDF para los eventos suaves, mientras que la parte dura muestra una evolución en momentos altos. Esta información fue la inspiración para nuestra separación. A través de esta tesis hemos visto que las diferencias entre los datos de ALICE y los generadores son en general más pequeñas para los eventos suaves lo cual sugiere que al considerar los eventos del bullo podríamos ocultar las diferencias de los generadores entre ellos y también respecto a los datos.

Los resultados apuntan a lo siguiente:

1. A nivel de eventos suaves/duros vemos un notable desacuerdo entre los generadores, quizá solo PERUGIA-0 esta más próximo a describir los datos.
2. El análisis de la esfericidad transversa fue estudiado de dos maneras: extrayendo $\langle S_T \rangle$ en función de la multiplicidad y graficando el espectro de esfericidad en bins de multiplicidad, lo cual mostró diferencias sustanciales entre los datos y en general todos los modelos MC analizados. Observamos, esencialmente que a alta multiplicidad, hay una diferencia cuantitativa y cualitativa entre todos los generadores y los datos. Principalmente, mientras que un valor sistemáticamente menor y una tendencia que apunta a un ligero descenso en $\langle S_T \rangle$ para los generadores a las multiplicidades más altas, los datos muestran una dependencia opuesta. El estudio del espectro de S_T en bins de multiplicidad muestra un comportamiento muy interesante. Principalmente, mientras que a baja esfericidad los generadores sobre predicen la producción, a alta esfericidad la situación esta invertida. Por supuesto, esto significa que los espectros de los generadores y del experimento se han cruzado en cierto valor de esfericidad, así que el promedio de S_T podría dar un buen acuerdo ficticio con datos mientras que de hecho el acuerdo es resultado del promedio de las contribuciones a la esfericidad. Esto es lo que aparentemente da el buen acuerdo a baja multiplicidad porque esencialmente se ocultan las diferencias al promediar. Este descubrimiento permite evidenciar mucho más grandes diferencias entre los datos y los generadores que las que son observadas cuando se toma el promedio.
3. A pesar de que hasta hace poco se pensaba que la física de colisiones MB estaba completamente entendida, vemos que no es así. La cuestión es qué tanto influye nuestra ignorancia en las propiedades del bulto cuando hacemos mediciones tomando cantidades promediadas. Dada la rica variedad de topologías diferentes de los eventos que encontramos, se sugiere explorar las observables hasta ahora reportadas: j_T , k_T , producción de extrañeza, correlaciones a dos hadrones, etc., en función de la esfericidad.

Chapter 1

Theoretical Framework

In this chapter the reader can find a brief description of the theoretical background related with the high energy hadronic collisions. The goal is to understand the collisions as complex processes which involve the interaction of the hadron constituents. So, measurements like the event shapes are important to extract information about the inner structure of the hadron and they teach us how the constituents interact and fragment.

First of all, the Standard Model is presented as the most successful theory of the fundamental forces and the composition of matter. Then, the Quantum Chromodynamics (QCD) is introduced to be the framework which describes the phenomena of hadron physics. The most relevant components of the hadron-hadron collisions are reviewed. Finally the Monte Carlo event generators are discussed.

1.1 The standard model

The $SU(3) \times SU(2) \times SU(1)$ Standard Model[JFD92]¹ (SM) describes the fundamental forces and the composition of matter. In this framework, the matter is constituted out of point-like particles which have a spin $\frac{1}{2}$ and are grouped into three families, each family has two quarks and two lepton members (see Table 1.1).

The Quantum Chromodynamics[Fie89] (QCD) is one of the components of the SM ($SU(3)$); it is a gauge theory which describes the strong interactions of colored quarks and gluons (q, g). The color is a property which plays a role similar to that of the charge in strong interactions. A quark of specific flavor comes in one of three different colors (red, green and blue). The quarks are always confined and appear in the form of hadrons that are colorless (white). Hadrons are grouped into baryons and mesons. Baryons consist of three quarks, *i.e.* qqq , while mesons consist of two quarks, *i.e.* $q\bar{q}$. The gluons are the mediators of the strong force, for example, a blue quark may convert into a red quark (flavor is not affected).

¹Note that gravity is not part of the Standard Model.

Table 1.1: Basic blocks of matter (quarks and leptons) in the Standard Model [ea08b].

Family	Quarks				Leptons		
	Name	Charge	Mass		Name	Charge	Mass
1	u	$2/3 e$	$1.5 - 3.3 \text{ MeV}/c^2$		e^-	$-e$	$0.511 \text{ MeV}/c^2$
	d	$-1/3 e$	$3.5 - 6.0 \text{ MeV}/c^2$		ν_e	0	$< 2 \text{ eV}/c^2$
2	c	$2/3 e$	$1.27^{+0.07}_{-0.11} \text{ GeV}/c^2$		μ^-	$-e$	$106 \text{ MeV}/c^2$
	s	$-1/3 e$	$104^{+26}_{-34} \text{ MeV}/c^2$		ν_μ	0	$< 0.19 \text{ MeV}/c^2$
3	t	$2/3 e$	$171.2 \pm 2.1 \text{ GeV}/c^2$		τ^-	$-e$	$1.78 \text{ GeV}/c^2$
	b	$-1/3 e$	$4.20^{+0.17}_{-0.11} \text{ MeV}/c^2$		ν_τ	0	$< 18.2 \text{ MeV}/c^2$

Table 1.2: Fundamental forces [Per00]. All forces, except gravitation, are described by the Standard Model. Their strength is given relative to the strength of the strong force for two protons at a distance of about 0.5 fm. The gravitons, the gauge bosons of gravity, are postulated but have not been found yet.

Force	Strength	Gauge Boson(s)
Strong force	1	8 Gluons (g)
Electromagnetic force	10^{-2}	Photon (γ)
Weak force	10^{-7}	W^\pm, Z^0
Gravitational force	10^{-39}	Gravitons

Since color (like electric charge) is always conserved, this means that the gluon must carry away the difference, in this instance, one unit of blueness and minus one unit of redness. So, gluons come in eight different “bi-colored” combinations.

On the other hand, the electro-weak interaction is based on the gauge group $SU(2) \times SU(1)$. There are two kinds of electro weak interactions: charged (mediated by W^{+-}) and neutral (mediated by Z^0). The first one is the only which changes flavor. The Quantum Electrodynamics (QED) describes the electromagnetic interactions mediated by the exchange of photons (γ). Leptons are affected by the weak force and the charged ones in addition by the electromagnetic force.

Table 1.2 shows the gauge bosons together with their relative coupling strengths ².

In spite of its success, the SM is incomplete. From the theoretical point of view, the theory can not tell us how to calculate the quark and lepton masses. Also, the SM takes as empirical inputs over 20 arbitrary parameters, and this is unacceptable in any “final” theory. On the experimental side, the most conspicuous missing link is the Higgs particle, which is

²The “strength” of a force is an intrinsically ambiguous notion -after all, it depends on the nature of the source and on how far away you are [Gri08].

necessary in the Standard Model to account for the masses of the W and Z . Like the top quark, the predicted mass of the Higgs has increased with time, as each new experiment failed to discover it. However we expect that the puzzle about the existence of the Higgs boson may soon be resolved by the ATLAS and CMS experiments at the LHC.

1.2 Perturbative and non-perturbative QCD aspects in high energy collisions

Today, most of us will agree that all the phenomena of hadron physics should be described in the framework of QCD. There are two areas where the theory has been successful:

- In short distance phenomena, where due to asymptotic freedom perturbation theory can be applied.
- In hadron spectroscopy and other long distance phenomena, where numerical, non-perturbative methods can be applied.

There is a third class of phenomena which are neither pure short distance or pure long distance: high energy hadron-hadron collisions.

By now, it is accepted that the hadronic reactions involving large transfers of transverse momentum (“hard” processes) are controlled by the direct collision of constituents (quarks and gluons) within the colliding hadrons. Also, it is well known that high energy hadronic interactions are dominated by the production of a large number of particles, mostly confined to the nearly forward direction, *i. e.* dominated by events in which the produced secondaries have small p_\perp leading to the conclusion that strong interactions at high energies are generally rather “soft.” In the QCD language, these are the so called non-perturbative effects.

Where there is a better chance of detecting the basic dynamic properties of the interactions is in those events occurring at large p_\perp values. It is hoped that such events will allow an unravelling of the inner structure of the hadrons and will teach us how the constituents interact. Note that the partons involved are scattered through large p_\perp and are supposed to materialize as a set of fairly well collimated hadrons called a “jet.”

Fig. 1.1 displays the historical scheme used by Feynman *et al.* to explain the large p_\perp particle production and jets [FFF78]. It shows that the simplest configuration of a large p_\perp hadronic process implies the existence of at least four jets; two of these, the beam and target jets. In the picture the terminology is self-explanatory. The inclusive hadronic reaction:

$$A + B \longrightarrow h_1 + h_2 + X \tag{1.1}$$

can be expressed in terms of:

- The elementary quark-quark cross section $\frac{d\hat{\sigma}}{dt}$ for the reaction:

$$q_a + q_b \longrightarrow q_c + q_d \quad (1.2)$$

- The density function $G_{B \rightarrow b}(x_b, k_{\perp b})$ which is the probability for finding a quark of flavor a in hadron A .
- The fragmentation function $D_c^{h_1}(z_c, k_{\perp c})$ for quark c to produce hadron h_1 [Alb10].

The quantities x_a , x_b , $k_{\perp a}$ and $k_{\perp b}$ are the longitudinal fraction of the incoming hadrons A , B momentum and perpendicular momentum of constituents a and b , respectively. z_c , z_d , $k_{\perp c}$ and $k_{\perp d}$ are the fractions of the outgoing constituents longitudinal and perpendicular momentum carried by the detected hadrons h_1 and h_2 .

1.3 Environment of the High Energy Hadron Collisions

In a high-energy collision the two colliding particles have an energy much larger than their rest mass. At the moment of the collision the transferred momentum can be very small and essentially just change the configuration of the incoming particles. The transferred momentum can also be so large that the particles do not act as compound objects, instead the constituent partons participate in the collision (hard scattering).

As we have mentioned, QCD has been very successful in describing parton scatterings involving large amount of transverse momentum. However the high energy hadron collisions are dominated by partonic soft collisions, the so called “minimum bias” (MB) events. Attained to the main physics process at parton level, the underlying event (UE) is an important element of the hadronic environment within all physics at the LHC. The underlying activity may include initial- and final-state radiation, beam remnants and multiple parton interactions; its final result is the multi-particle production mostly at low p_{\perp} . Fig. 1.2 illustrates the structure of a high-energy physics collision, in the example there is the process $p + p \rightarrow \text{jet1} + \text{jet2} + \text{UE}$. The understanding of the UE component is quite important in the sense that such background must be well understood in studies which will be done at LHC like the search for the Higgs boson.

1.3.1 Minimum Bias Interactions

The total collision cross section for hadron-hadron scattering, σ_{TOT} can be divided into elastic (σ_{ELAS}) and inelastic processes. A common classification of inelastic $p + p$ interactions is into: non-diffractive (σ_{ND}), single-diffractive (σ_{SD}) and double-diffractive (σ_{DD}) events [ea08a]. The total cross-section in terms of the square of the total centre of mass energy (s), can thus be written as:

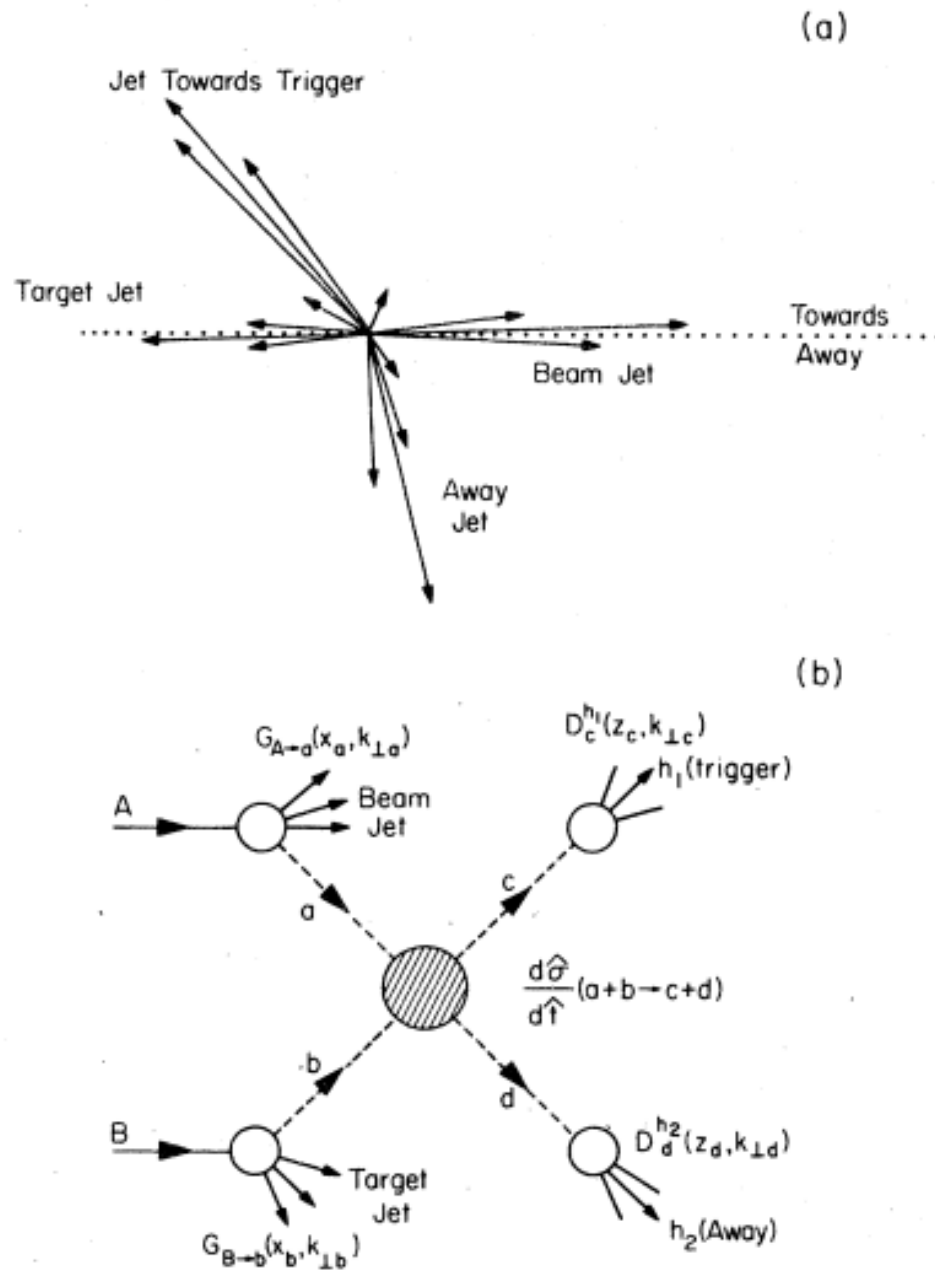


Figure 1.1: Idealization of a large p_{\perp} hadronic interaction producing four jets.

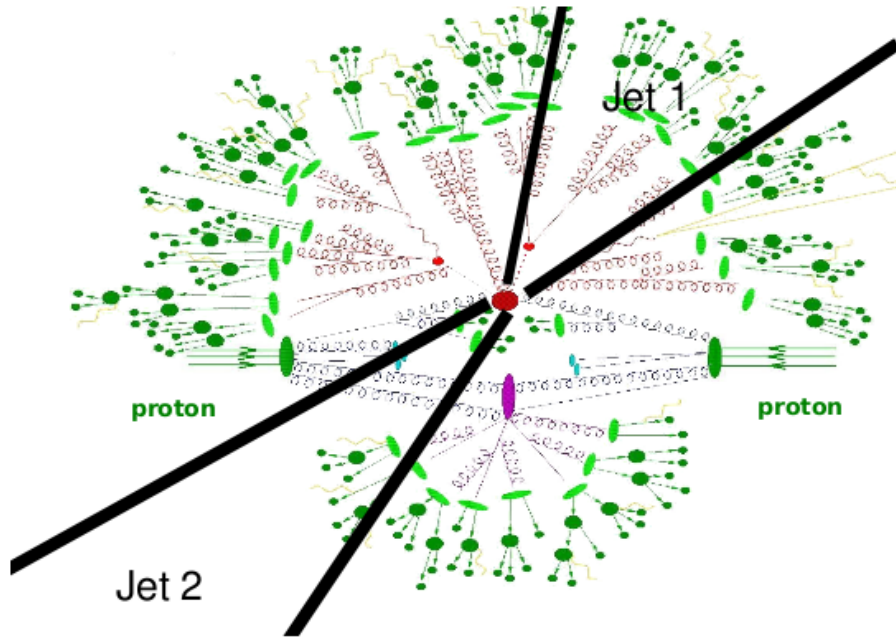


Figure 1.2: Environment of the high energy hadron collisions.

$$\sigma_{\text{TOT}}(s) = \sigma_{\text{ELAS}}(s) + \sigma_{\text{ND}}(s) + \sigma_{\text{SD}}(s) + \sigma_{\text{DD}}(s) \quad (1.3)$$

The so-called diffractive system is created carrying the quantum numbers of the respective incoming particle (except possibly the spin). Subsequently it evolves and decays. In single-diffractive events only one such system is created and the second particle remains intact; double-diffractive events feature two of them. Among the non-diffractive events are parton-parton interactions with medium-to-large momentum transfers of a few GeV/c. Fig. 1.3 shows a schematic view of the elastic (Fig. 1.3a), single-diffractive (Fig. 1.3b), double diffractive (Fig. 1.3c) and non-diffractive inelastic hadron interactions (Fig. 1.3d) in the $\eta - \phi$ space.

Among the characteristics of these event classes, the distributions of the particles in pseudo-rapidity show: non-diffractive collisions have many particles in the central region, steeply falling to higher rapidities. In a single-diffractive collision only one of the beam particles breaks up and produces particles at high rapidities on one side. In a double-diffractive collision both beam particles break up and produce particles at positive and negative high rapidities. A dip can be seen in the central region.

The measurements of the minimum-bias events show a close similarity with non-single diffractive inelastic interactions (NSD). The interpretation is based on the triggering system used for example in the historical experiments which performed such measurements: CERN-ISR [ea84], CERN-SPS UA5 [ea87a], up to the Tevatron era CDF [ea90] and E735 [ea98, ea99].

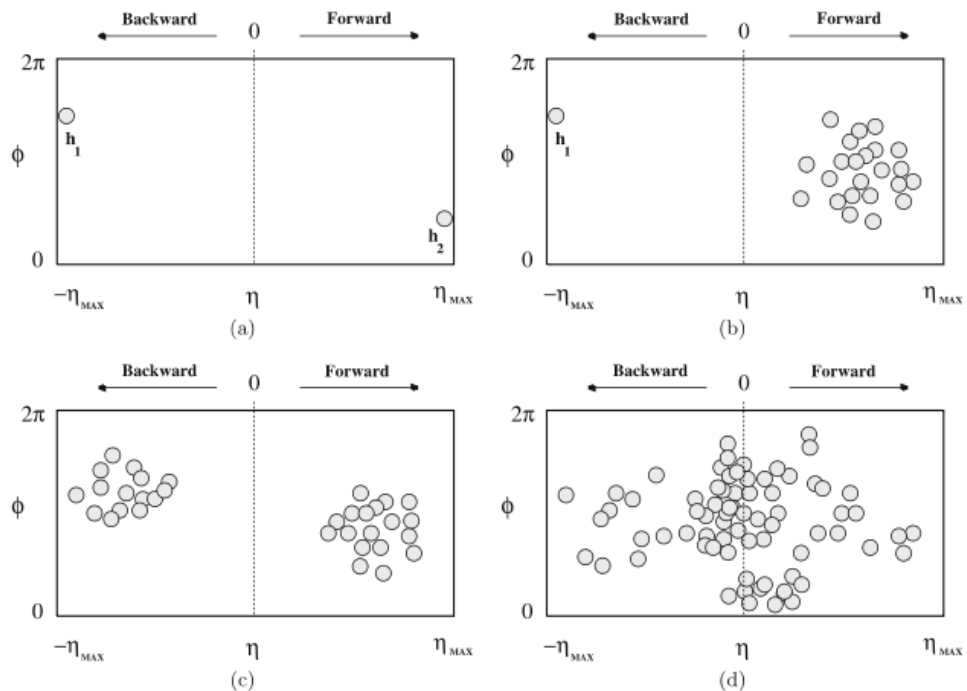


Figure 1.3: Schematic view of: a) elastic, b) single-diffractive, c) double-diffractive and d) non-diffractive hadron interactions in the $\eta - \phi$ space.

Such experiments favored the detection of the non-single diffractive events. On the theoretical front, some models could satisfactorily describe the soft interactions and diffractive processes by the identification of MB events with ND interactions [ea94]. In practical terms, the experimental choice of the minimum bias events does not differ considerably. For example the cross-sections at $\sqrt{s} = 900$ GeV/c for non-diffractive interactions is ~ 34.9 mb while the non-single diffractive one is ~ 40.8 mb. These values were gotten using PYTHIA event generator [Sjo94] version 6.4.214. In general, at current collider energies, the cross sections (NSD and ND) would hardly differ by more than $\sim 15\%$.

As it was mentioned, the processes which involve a large transfer of transverse momentum are the so-called “hard” processes, and of course pQCD can be applied with success to describe them. However an important component in high-energy hadronic collisions are of soft nature (*e.g.* Underlying Event), the momentum transfer is small and the strong coupling constant accordingly too large to apply pQCD for their description. The Quark-Gluon String Model (QGSM) [Kai94] and the Dual Parton Model (DPM) [CSTV94] describe high-energy collisions by combining the topological expansion in QCD with Regge Field Theory ([Col77]) making use of the parton structure of hadrons. In the calculations of physical observables, QGSM and DPM deviate because they use different sets of diagrams as well as different parameterizations for the structure and fragmentation functions.

1.3.2 Underlying Event

The Underlying Event (UE) is everything in the event except the hard scattering, including Initial State Radiation (ISR), Final State Radiation (FSR), beam remnants and the so-called multiple parton interactions (MPI). From an experimental point of view, it is impossible to separate these two things; however, topological properties of the event can be used to define a set of physics observables which are sensitive to different aspects of the UE [ea08a]. Studying the UE is important for understanding the evolution of QCD with collision energy as well as understanding the systematic corrections, from basic detector calibrations to physics analyses such as mass measurements.

1.4 Event Generators

The complexity of the high energy hadron-hadron collisions requires models which describe the processes to be formulated as MC event generators. Event generators provide simulated events that are as close as possible to real interactions as occur at the collision point. Normally, the event generators combine the information of pQCD for well-understood areas and phenomenological approaches mostly to simulate the soft component of the collisions (UE, low p_t production).

For the description of a typical high-energy event, an event generator should contain a simulation of several physics aspects. If we try to follow the evolution of an event in some

semblance of a time order, one may arrange these aspects as follows:

- Initially two beam particles are coming in towards each other. Normally each particle is characterized by a set of parton distributions, which defines the partonic substructure in terms of flavour composition and energy sharing.
- One shower initiator parton from each beam starts off a sequence of branchings, such as $q \rightarrow qg$, which build up an initial-state shower.
- One incoming parton from each of the two showers enters the hard process, where then a number of outgoing partons are produced, usually two. It is the nature of this process that determines the main characteristics of the event.
- The hard process may produce a set of short-lived resonances, like the Z^0/W^\pm gauge bosons, whose decay to normal partons has to be considered in close association with the hard process itself.
- The outgoing partons may branch, just like the incoming did, to build up final-state showers.
- In addition to the hard process considered above, further semi-hard interactions may occur between the other partons of two incoming hadrons.
- When a shower initiator is taken out of a beam particle, a beam remnant is left behind. This remnant may have an internal structure, and a net colour charge that relates it to the rest of the final state.
- The QCD confinement mechanism ensures that the outgoing quarks and gluons are not observable, but instead fragment to colour neutral hadrons.
- Normally the fragmentation mechanism can be seen as occurring in a set of separate colour singlet subsystems, but interconnection effects such as colour rearrangement or Bose-Einstein may complicate the picture.
- Many of the produced hadrons are unstable and decay further.

In the present work, the predictions of PYTHIA6[Sjo94], PYTHIA8 [eab] and PHOJET[Eng95] event generators were compared with the ALICE results. In the case of PYTHIA6, the tunes ATLAS-CSC[Mor] and PERUGIA-0[Ska] were used.

PHOJET is based on the Dual Parton Model (DPM) and it also uses two-component approach that describes high-energy collisions with a soft and a hard component. While the starting point for the event generation in PYTHIA is the description of possible hard interactions in $e^+ - e^-$, $p - p$, $p - \bar{p}$ or $e - p$ colliders. combining sophisticated models to treat the soft hadronic interactions [Sjo94, SLM01]. PHOJET, on the other hand, initialises the event generation by describing the soft component of hadron-hadron, photon-hadron or

photon-photon interactions at high energies. The hard component, calculated by pQCD at the partonic level, is then introduced to complete the event simulation. Due to the different underlying theoretical models used in the physics simulation by these two event generators, PYTHIA presents the user with hundreds of settings that can be adjusted in order to better reproduce the data while PHOJET is relatively more tightly restricted.

Chapter 2

The ALICE experiment

ALICE (A Large Ion Collider Experiment) is a general-purpose heavy-ion experiment designed to study the physics of strongly interacting matter and the quark-gluon plasma in nucleus-nucleus collisions at the LHC (Large Hadron Collider). The detailed description of ALICE is summarized in the Physics Performance Report [ea04b, ea06].

High energy physics has established and validated the Standard Model (SM). The aim of ultra-relativistic heavy-ion physics is to apply and extend the SM to complex and dynamically evolving systems of finite size. The idea is to study and understand how collective phenomena and macroscopic properties, involving many degrees of freedom, emerge from microscopic laws of elementary-particle physics. The most interesting bulk phenomenon predicted by the SM is the occurrence of phase transitions in quantum fields at characteristic energy densities.

2.1 Role of ALICE in the LHC program

The LHC is a two-ring-superconducting-hadron collider installed in the existing 26.7 km tunnel constructed for the CERN LEP machine [ea08c]. The aim of the LHC is to reveal the physics beyond the SM with center of mass collision energies of 0.9, 7 and up to 14 TeV. One of the fundamental problems addressed at LHC is the connection between phase transitions involving elementary quantum fields, fundamental symmetries of nature and the origin of the mass.

- ATLAS [GAea08] and CMS [SCea08] search for the Higgs which is the particle that generates the mass of the electroweak gauge bosons and the bare mass of elementary fermions through spontaneous breaking of the electro-weak gauge symmetry. They will also search for super-symmetric particles which are manifestations of a broken intrinsic symmetry between fermions and bosons in extensions of the SM.
- LHCb [AAAJea08] focus on the precision measurements with heavy b quarks and on the studies of the CP-symmetry-violating processes.

- ALICE studies the role of chiral symmetry in the generation of mass in composite particles (hadrons) using heavy-ion collisions to attain high-energy densities over large volumes and long timescales. ALICE investigates equilibrium as well as non-equilibrium physics of strongly interacting matter in the energy density regime $\epsilon \sim 1 - 1000$ GeV/fm³. In addition, the aim is to gain insight into the physics of parton densities close to phase-space saturation, and their collective dynamical evolution towards hadronization in a dense nuclear environment.

2.2 The proton proton program in ALICE

The successful completion of the heavy-ion program requires the study of p-p, p-A and lighter A-A collisions in order to establish the benchmark processes under the same experimental conditions. But also, the ALICE capabilities will permit to explore the p-p physics in a new energy domain. In the list below there are some aspects which will be covered by the study of p-p collisions.

- **Proton proton measurements as benchmark for heavy-ion physics.**

Most of the heavy-ion observables require pp measurements of the same observable for comparison. This is important to identify the genuine collective effects in A-A collisions and to separate them from phenomena present already in p-p collisions. Among such studies are: particle multiplicities, jet fragmentation functions, slopes of the transverse-mass distributions, particle yields and ratios of momentum spectra, strangeness enhancement, heavy-quark and quarkonium production cross sections, dilepton spectra and photon spectra.

- **Specific aspects of proton-proton physics in ALICE**

Among the important aspects of p-p physics is the exploration of a novel range of energies and of Bjorken-*x* values accessible at LHC. More generally, in ALICE the p-p program aims at studying non-perturbative strong-coupling phenomena related to confinement and hadronic structure.

ALICE was designed to allow particle identification over a broad momentum range tracking with good resolution from 100 MeV/c up to 100 GeV/c, and excellent determination of secondary vertices. Combined with its low material thickness and low magnetic field, ALICE is an important contributor in the low momentum domain in p-p physics at LHC. Some specific studies are listed below.

1. **Particle spectra.** ALICE measures charged-particle spectra in rapidity and transverse momentum for a wide variety of particle species including: π , p , \bar{p} , Λ , K , etc.
2. **Strangeness production.** It is interesting to measure the energy dependence of strange-particle production, the suppression factor for strange quark production

with respect to u and d quarks, on the other hand, the correlation between the mean kaon-transverse momentum and the charged-particle multiplicity.

3. **Baryon-number transfer in rapidity.** ALICE with its particle-identification capability, is ideally suited to clarify the rapidity distribution of baryon number in hadronic collisions. Recently, the collaboration has reported the measurement of the ratio: $p/p\bar{p}$ at 0.9 [KAea10d]. But of course, this kind of studies will be done with abundant baryon statistics in other channels (Λ , $\bar{\Lambda}$) in the central rapidity region.
4. **Correlations.** Two particle correlations have been traditionally studied in pp multi-particle production in order to gain insight into the dynamics of high-energy collisions via a unified description of correlations and multiplicity distributions.
5. **Heavy-flavor production.** The b -production cross section measured at the CERN-SPS collider and the Fermilab Tevatron lies about a factor 2 above the predictions in both cases. Also, data taken at HERA and LEP require better understanding. ALICE can measure heavy-flavor production down to very low p_\perp this can be achieved by using inclusive large impact-parameter lepton-detection, and by reconstructing exclusive charm-meson decays at relatively low p_\perp .
6. **Jet studies.** The goal of ALICE is to characterize events with several jets at relatively low p_\perp . Among the observables of interest are the following.
 - The semi-hard cross sections, measured by counting all events with at least one jet produced above some given E_\perp .
 - The relative rates of production of 1, 2 and 3 jets as a function of the lower E_\perp cutoff.
 - The measurement of double-parton collisions and their distinction from the leading QCD $2 \rightarrow 4$ process.
7. **Diffractive physics.** Interest in diffractive physics ranges from understanding Pomeron exchange within Regge theory to small- x phenomena. Observables at the LHC which could improve our understanding of diffractive physics include the study of the elastic and total proton-proton cross section, multi-particle production.
8. **Double-parton collisions.** Increasing the center-of-mass energy increases the parton fluxes in pp collisions. Therefore at very high energies, multiple parton collisions become increasingly important.

2.3 The Central Tracking Detectors of ALICE

ALICE consists of central sub-detectors (see Fig. 2.1) which measure event-by-event hadrons, electrons and photons; and of a forward spectrometer to measure muons.

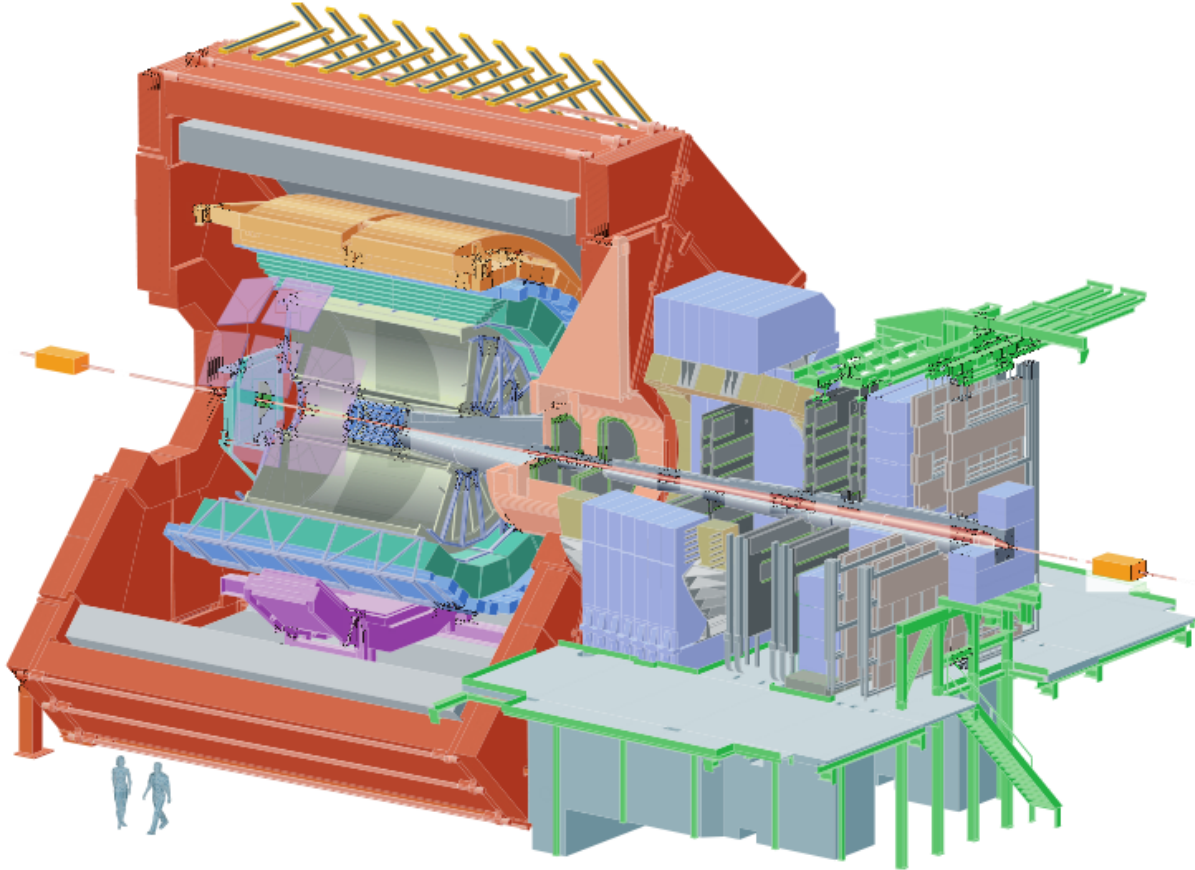


Figure 2.1: ALICE schematic view.

The central part which covers polar angles from 45° to 135° over the full azimuth, is embedded in the large L3 solenoidal magnet. It consists of: an Inner Tracking System (ITS); a cylindrical Time-Projection Chamber (TPC); three particle identification arrays, of Time-Of-Flight (TOF) detector, a single arm electro magnetic calorimeter (PHOS) a Transition-Radiation Detector (TRD) and a single-arm ring imaging Cherenkov detector (HMPID).

The forward muon arm (covering polar angles $180^\circ - \theta = 2^\circ - 9^\circ$) consists of a complex arrangement of absorbers, a large dipole magnet, and fourteen planes of tracking and triggering chambers. Several smaller detectors (ZDC, PMD, FMD, T0 and V0) for global event characterization and triggering are located at forward angles. An array of scintillators (ACORDE) on top of the L3 magnet is used to trigger on cosmic-rays.

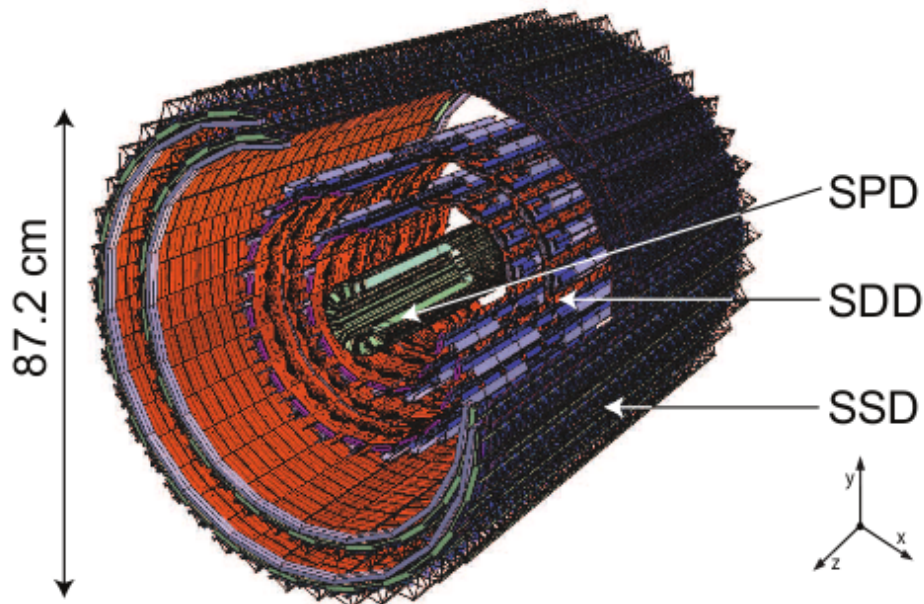


Figure 2.2: Layout of the ITS and his orientation with respect to the ALICE global reference system.

2.3.1 The Inner Tracking System (ITS)

The ITS consists of six cylindrical layers of silicon detectors located at radii between 3.9 and 43 cm (see Fig. 2.2). Its alignment was done using cosmic rays [KAea10e]. The main tasks of the ITS are to localize the primary vertex with a resolution better than $100 \mu\text{m}$, to reconstruct the secondary vertices from the decays of hyperons and D and B mesons, to track and identify particles with momentum below 200 MeV/c, to improve the momentum and angle resolution for particles reconstructed by the TPC and to reconstruct particles traversing dead regions of the TPC. The ITS surrounds the beam pipe which is $800 \mu\text{m}$ -thick beryllium cylinder of 3 cm outer radius, coaxial with the ITS layers. Three different technologies are employed in the ITS.

- Due to the high-particle density in heavy-ion collisions at LHC¹ and in order to achieve the required impact parameter resolution, Silicon Pixel Detectors (SPD) have been chosen for the innermost two layers. The SPD layers cover a range in pseudorapidity of $|\eta| < 2$ and $|\eta| < 1.4$, respectively. And it has a total of 9.8 million 50×425 pixels. Its design spatial resolution ($\sigma_{r\phi} \times \sigma_z$) is $12 \times 100 \mu\text{m}^2$. The SPD can also be used as L0 trigger. For this purpose each of the 1,200 readout chips provides a so-called fast OR signal indicating that at least one pixel of a given chip produced a signal. These

¹ At center-of-mass energy per nucleon pair of $\sqrt{s_{NN}} = 2.76 \text{ TeV}$, ALICE measured ~ 1580 for the primary charged particle pseudo-rapidity density for the most central events 5% [KAea10a].

signals are sent to an FPGA which is able to implement Boolean logic functions upon them. This allows trigger possibilities that ranges from a minimum-bias trigger up to very complex trigger patterns.

- The next two layers conform the Silicon Drift Detector (SDD). It consists of a total of 133,000 readout channels. The SDD is operated with a drift field of 500 V/cm resulting in a drift speed of about $6.5 \mu\text{m}/\text{ns}$ and in a maximum drift time of about $5.3 \mu\text{s}$. Its design spatial resolution is about $35 \times 25 \mu\text{m}^2$.
- The outermost layers conform the Silicon Strip Detector (SSD). It consists of double-sided silicon micro-strip sensors with $95 \mu\text{m}$ pitch, comprising a total of 2.6 million readout channels. Its spatial resolution is $20 \times 830 \mu\text{m}$.

The SDD and SSD have analogue readout; therefore they can be used to measure ionization. With a minimum thickness of approximately $300 \mu\text{m}$ they provide acceptable signal-to-noise ratio. The detectors effective thickness amounts to 0.4 % of χ_0 .

2.3.2 Time-Projection Chamber (TPC)

The TPC is the main tracking detector of the central barrel, it covers the full azimuth and a pseudorapidity range of $|\eta| < 0.8$ for tracks with full radial track length; for reduced track length an acceptance up to about $|\eta| < 1.5$ is accessible. A large p_\perp range is covered from low p_\perp of about 0.1 GeV/c up to 100 GeV/c with good momentum resolution. TPC was designed to cope with particle multiplicity density of $dN_{ch}/d\eta = 8000^2$ which would result in 20,000 charged primary and secondary tracks in the TPC acceptance.

For proton proton runs, the memory time of the TPC is the limiting factor for the luminosity due to the $\sim 94 \mu\text{s}$ drift time. For instance, at a $p - p$ luminosity of about $5 \times 10^{30} \text{ cm}^{-2}\text{s}^{-1}$, with a corresponding interaction rate of about 350 kHz, “past” and “future” tracks from an average of 60 $p - p$ interactions are detected together with the trigger event; the detected multiplicities correspond to about 30 minimum bias $p - p$ events. Since the total occupancy is lower by more than an order of magnitude than in $\text{Pb} - \text{Pb}$ collisions, tracks from pile-up events can be eliminated because they point to the wrong vertex.

The shape of the TPC is cylindrical, it has a central high voltage membrane maintained at $\sim 100\text{kV}$ and two readout planes at the end-caps (see Fig. 2.3). Its active volume is limited to $85 < r < 247 \text{ cm}$ and $-250 < z < 250 \text{ cm}$ in the radial and longitudinal directions respectively. The material budget between the interaction point and the active volume of the TPC corresponds to 11% of a radiation length averaged in $|\eta| < 0.8$. The central membrane at $z = 0$ divides the nearly 90 m^3 active volume into two halves. The homogeneous drift field of 400 V/cm in the $\text{Ne}-\text{CO}_2-\text{N}_2$ (85.7%-9.5%-4.8%) gas mixture leads to a maximum drift

²The design of TPC was based in the better extrapolation to LHC energy for $\text{Pb} - \text{Pb}$ collisions before of the RHIC data.

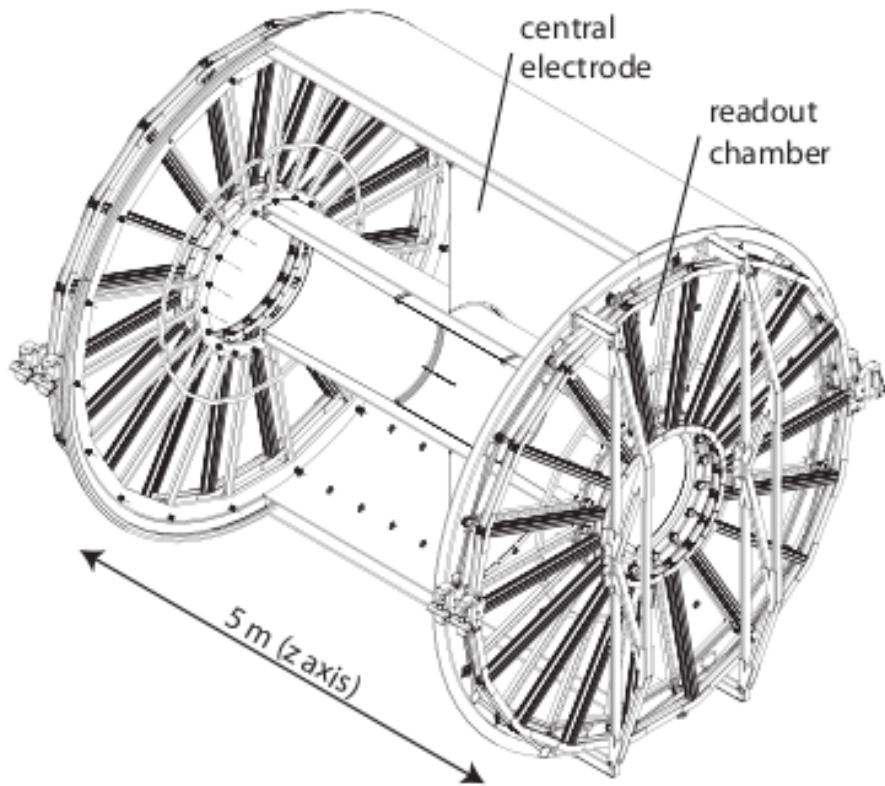


Figure 2.3: Schematic view of the TPC.

time of $94 \mu\text{s}$. Ionization electrons produced by charged particles traversing the TPC drift towards the readout end-caps composed of 72 multi-wire proportional chambers with cathode pad readout. The typical gas gain is 10^4 . Signals induced on the segmented cathode planes, comprising a total of 557,568 readout pads, are transformed into differential semi-gaussian signals by a charge-sensitive shaping amplifier (PASA). This is followed by the ALICE TPC ReadOut (ALTRO) chip, which employs a 10 bit ADC at 10 MHz sampling rate and four digital filtering circuits. These filters also perform tail cancellation and baseline restoration. They are optimized for precise position and dE/dx measurements in the high track density environment of the heavy-ion collisions.

2.4 Minimum Bias triggers in proton-proton collisions

Various triggers can be configured simultaneously and more complex trigger patterns can be implemented in the ALICE High Level Trigger (HLT). Minimum-bias triggers are designed to trigger on all inelastic interactions occurring in the detector, even when the momentum transfer between the incoming particles is small or when only very few final-state particles

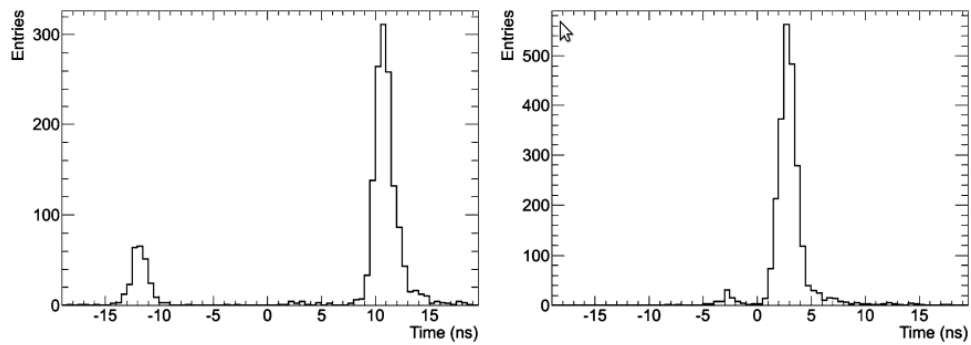


Figure 2.4: Arrival time of particles in the V0 detectors relative to the beam crossing time. A number of beam-halo or beam-gas events are visible as secondary peaks in V0A (left panel) and V0C (right panel). This is because particles produced in back-ground interactions arrive at earlier times in one or the other of the two counters. The data correspond to the first $p - p$ collisions reconstructed by ALICE at $\sqrt{s} = 900$ GeV/c on November 2009 [KAea10f].

are produced. These triggers combine the information provided by the detectors: V0 and the SPD.

The V0 detector is a small angle detector consisting of two arrays of scintillator counters, called V0A and V0C. The first one is located 340 cm from the vertex on the side opposite to the muon spectrometer while V0C is placed in the front face of the hadronic absorber, 90 cm from the vertex. They cover the pseudo-rapidity ranges: $2.8 < \eta < 5.1$ and $-3.7 < \eta < -1.7$ respectively. They are segmented into 32 individual counters each distributed in four rings. The V0 detector uses the time of hits produced by charged particles to distinguish and trigger events from $p - p$ or beam-background interactions. In practice and during normal operation, both arrays are required (`VZERO.AND`³) to provide the so-called triggers: Minimum Bias (MB), Multiplicity (MT), semi-Central (CT1) and Central (CT2). And the `VZERO.OR`⁴ mode can be also adopted. For instance, Fig. 2.4 shows the arrival times of particles at the detector relative to the beam crossing time (“time zero”). The data correspond to the first $p - p$ collisions reconstructed by ALICE at $\sqrt{s} = 900$ GeV/c on November 2009 [KAea10f].

On the other hand, the 1,200 readout chips of the SPD produce the same number of signals which are logically combined to form the global fast-OR (`GLOB.OR`) trigger element.

Using logical combinations of the different trigger elements there is the foloowing set of MB triggers.

³It requires at least one hit in one counter on both sides.

⁴It requires at least one hit in one counter on one sides.

- MB1 = (GLOB.F0 or VZERO.OR) and not V0_BG.⁵
- MB2 = (GLOB.F0 and VZERO.OR) and not V0_BG.
- MB3 = (GLOB.F0 and VZERO.AND) and not V0_BG.

The table 2.1 compare the efficiencies of the three minimum bias triggers at a fixed $\sqrt{s} = 10$ TeV using Pythia [Sjo94] event generator. Also shown are the trigger efficiencies for beam-gas and beam-halo events.

Trigger	ND	SD	DD	NSD	INEL	Beam-gas	Beam-halo
MB1	100.0	71.6	86.2	97.9	93.0	7.7	2.3
MB2	99.2	57.5	66.3	94.2	87.4	2.0	0.3
MB3	99.1	53.7	61.5	93.4	86.0	< 0.01	< 0.01

Table 2.1: Trigger efficiency in percent at $\sqrt{s} = 10$ TeV (Pythia) (see [GO09]).

In the practice, for real data, the off-line triggers are combined with the information provided by the LHC bunch-crossing signals.

⁵It indicates that a beam-gas or beam-halo collision was detected by the V0 which utilizes the timing of the collision

Chapter 3

Event Reconstruction with the central tracking detectors.

In this section, the reconstruction procedures of tracks and vertex are explained. The main challengers are:

1. Determine the momentum of particles as close as possible to the point of their generation (main interaction point or secondary decay vertices).
2. The track reconstruction procedure should be capable of a precise extrapolation of the tracks to the detectors providing the particle identification information (TOF, HMPID, PHOS) that are, in the case of ALICE, situated far away from the main interaction point.

3.1 Primary vertex reconstruction with the SPD

The algorithm starts by looking at the distribution of the z coordinates of the reconstructed space points ¹ in the first pixel layers. At a vertex z coordinate $z_{true} = 0$ the distribution is symmetric and its centroid (z_{cen}) is very close to the nominal vertex position. For primary vertex locations not too far from $z_{true} = 0$ (up to about 12 cm), the centroid of the distribution is still correlated to the true vertex position. The saturation effect at large z_{true} values of the vertex position ($z_{true} = 12 - 15$ cm) is, however, not critical, since this procedure is only meant to find a rough vertex position, in order to introduce some cut along z .

A monotonic relationship, through a polynomial fit, is used to evaluate a first approximated value (z_v^0) of z_v from the centroid of the z coordinate distribution of the reconstructed space points. Then, a confidence region around z_v^0 is determined (z_v^{min}, z_v^{max}). To find the

¹This is the estimation of the position where a particle crossed the sensitive element of a detector

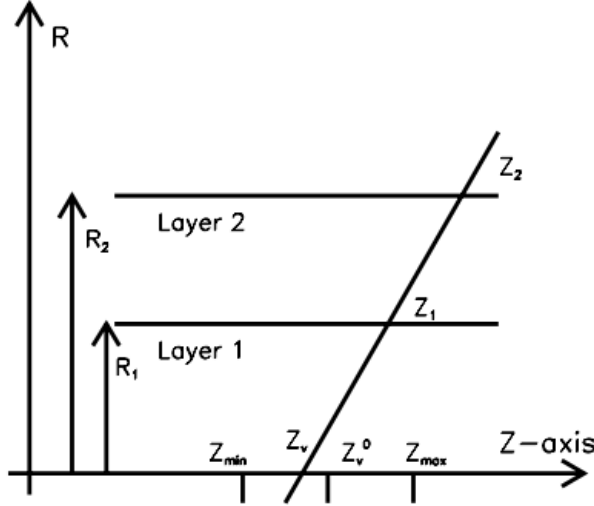


Figure 3.1: Geometrical sketch of the algorithm used to correlate the points in the two pixel layers.

final vertex position, the correlation between the points z_1 , z_2 in the two SPD layers is considered (see Fig. 3.1).

Leaving only those points z_1 , for each point z_2 , which give a z_v between z_v^{\min} and z_v^{\max} , the correlation between z_1 and z_2 results in a z_v spectrum. A similar approach can be applied to the reconstruction of the vertex position in the transverse plane. Fig. 3.2 shows the resolution and efficiency of the vertex reconstruction along the beam direction using the SPD, note that the efficiency saturates at 100% for $dN_{ch}/dy \sim 6$, where the resolution is $155\mu m$.

Precision of about 1 mm is enough for reconstruction purposes. However specific analysis like the detection of open charm and open beauty particles like $D0$ ($c\tau \sim 123\mu m$) or B mesons ($c\tau \sim 500\mu m$) requires the primary vertex position to be reconstructed with a precision better than $50\mu m$ in the bending plane. So, a 3D vertex reconstruction is necessary for such purposes.

3.2 3D reconstruction of the vertex position using tracks.

Each track, reconstructed in the TPC and in the ITS, is approximated with a straight line at the position of the closest approach to the nominal primary vertex position (the nominal vertex position is supposed to be known with a precision of $100 - 200\mu m$). Then, all possible track pairs (i, j) are considered and for each pair, the centre $C(i, j) \equiv (x_{ij}, y_{ij}, z_{ij})$ of the segment of minimum approach between the two lines is found. The coordinates of the primary vertex are determined as

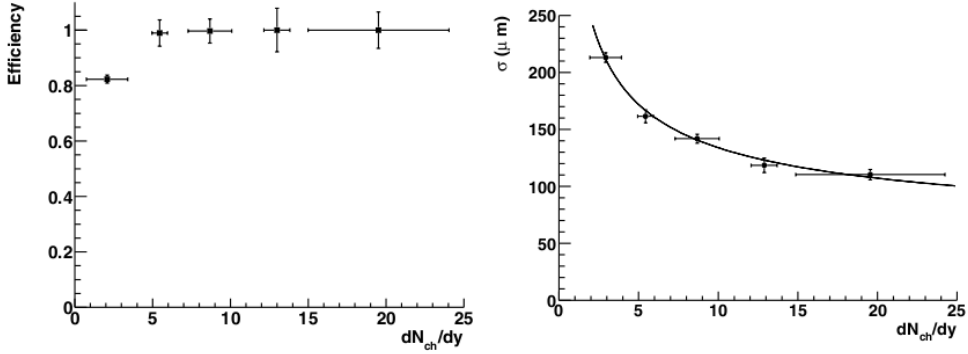


Figure 3.2: Resolution and efficiency of the vertex reconstruction along the beam direction using the SPD as a function of dN_{ch}/dy for the case of pp interactions.

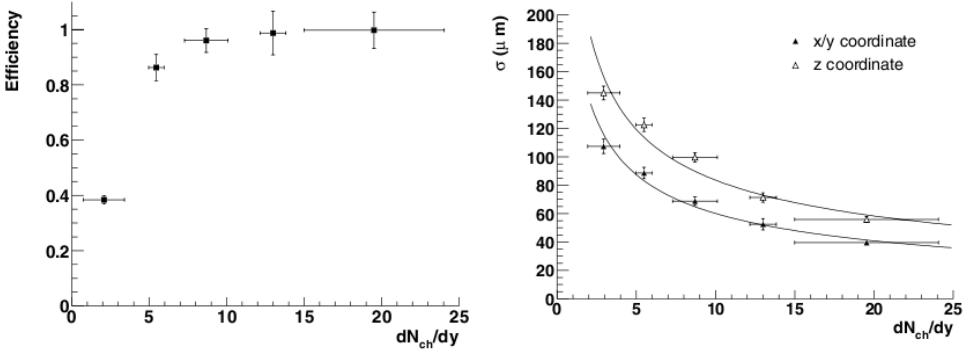


Figure 3.3: Efficiency and resolutions for the primary vertex reconstructed in 3D from tracks as a function of dN_{ch}/dy for the case of pp events.

$$\vec{r}_v = (x_v, y_v, z_v) = \left(\frac{1}{N_{pairs}} \sum_{i,j} x_{ij}, \frac{1}{N_{pairs}} \sum_{i,j} y_{ij}, \frac{1}{N_{pairs}} \sum_{i,j} z_{ij} \right) \quad (3.1)$$

where N_{pairs} is the number of track pairs. This gives an improved estimate of the vertex position. Finally, the position \vec{r}_v is reconstructed minimizing the χ^2 :

$$\chi^2(\vec{r}_v) = \sum_i (\vec{r}_v - \vec{r}_i)^\top V_i^{-1} (\vec{r}_v - \vec{r}_i) \quad (3.2)$$

where \vec{r}_i is the global position of the track i (*i.e.* the position assigned at the step above) and V_i is the covariance matrix of the vector \vec{r}_i .

Fig.3.3 shows the resolution of the vertex as a function of dN_{ch}/dy .

3.3 Track Reconstruction

The Kalman-filtering [P.84] approach has been chosen for the offline track reconstruction. Among the attractive properties of such approach are:

- It is a method for simultaneous track recognition and fitting.
- There is a possibility to reject incorrect space points “on the fly,” during the only tracking pass.
- In the case of substantial multiple scattering, track measurements are correlated and therefore large matrices (of the size of the number of reconstructed points) need to be inverted during a global fit. In the Kalman-filter procedure we only have to manipulate up to 5×5 matrices (although as many times as we have reconstructed space points), which is much faster.
- One can handle multiple scattering and energy losses in a simpler way than in the case of global methods.
- It is a natural way to find the extrapolation of a track from one detector to another (for example from the TPC to the ITS or to the TRD).

The reconstruction begins with cluster finding in all of the ALICE central detectors (ITS, TPC, TRD, TOF, HMPID and PHOS). Using the clusters reconstructed at the two pixel layers of the ITS, the position of the primary vertex is estimated and the track finding starts.

The procedure starts in the outer radius of the TPC. First, the track candidates (“seeds”) are found. Because of the small number of clusters assigned to a seed, the precision of its parameters is not sufficient to safely extrapolate it outwards to the other detectors. Instead, the tracking stays within the TPC and proceeds towards the smaller TPC radii. Whenever possible, new clusters are associated with a track candidate in a “classical” Kalman-filter way and the track parameters are more and more refined. When all of the seeds are extrapolated to the inner limit of the TPC, the tracking in the ITS takes over. The ITS tracker tries to prolong the TPC tracks as close as possible to the primary vertex. On the way to the primary vertex, the tracks are assigned additional, precisely reconstructed ITS clusters, which also improves the estimation of the track parameters.

After all the track candidates from the TPC are assigned their clusters in the ITS, a special ITS stand-alone tracking procedure is applied to the rest of the ITS clusters. This procedure tries to recover the tracks that were not found in the TPC because of the p_t cut-off, dead zones between the TPC sectors, or decays.

At this point the tracking is restarted from the vertex back to the outer layer of the ITS and then repeated towards the outer wall of the TPC. For the track that was labeled by the ITS tracker as potentially primary, several particle-mass-dependent, time-of-flight hypotheses are calculated. These hypotheses are then used for the particle identification

(PID) with the TOF detector. Once the outer radius of the TPC is reached, the precision of the estimated track parameters is sufficient to extrapolate the tracks to the TRD, TOF, HMPID and PHOS detectors. Tracking in the TRD is done in a similar way to that in the TPC. Tracks are followed till the outer wall of the TRD and the assigned clusters improve the momentum resolution further. Next, the tracks are extrapolated to the TOF, HMPID and PHOS, where they acquire the PID information. Finally, all the tracks are refitted with the Kalman filter backwards to the primary vertex (or to the innermost possible radius, in the case of the secondary tracks). The tracks that passed the final refit are used for the secondary vertex (V0 , cascade, kink) reconstruction. There is also an option to reconstruct the secondary vertices “on the fly” during the tracking itself. The potential advantage of such a possibility is that the tracks coming from a secondary vertex candidate are not extrapolated beyond the vertex, thus minimizing the risk of picking up a wrong track prolongation. This option is currently under investigation. The reconstructed tracks (together with the PID information), kink, V0 and cascade particle decays are then stored in the Event Summary Data (ESD).

Normally the real data are re-processed due to the calibration of the detectors, in the practice there are the so-called “passes of the reconstruction.”

Chapter 4

The Event Shape Analysis, MC Study

In this chapter I present a MC study of the observables: thrust, thrust-minor, recoil and quadratic transverse sphericity. I discuss the potential physics which can be extracted from an analysis like this applied in minimum bias $p - p$ interactions.

4.1 Event Shapes

The event shapes characterize the global structure of the high energy collisions. They are among the simplest experimental measurements sensitive to the parameters of perturbative QCD and fragmentation models. They were widely studied in $e^+ e^-$ and DIS, both theoretically and experimentally [DS04]. More recently a modification of the concept (reducing the parameters to the transverse plane) has been studied in hadronic interactions [BSZ]. The studies currently available applying this approach to hadronic collisions utilize datasets triggered on high energy jets.

In this section we present the event shape variables: Thrust (T), Thrust-Minor (T_{min}), Sphericity (S_\perp) and the recoil (r) term recoil. All these variables are defined in the transverse plane in order to avoid the contribution of the forward radiation. At hadron colliders they are defined over particles within the acceptance of the detector. The thrust (T) is defined as [ea04a]:

$$T \equiv \underbrace{\max}_{\vec{n}_t} \frac{\sum_i |\vec{p}_{t,i} \cdot \vec{n}_t|}{\sum_i |\vec{p}_{t,i}|} \quad (4.1)$$

Now, let's consider the limit case where the event is of high multiplicity and isotropic. We can compute T^{iso} ¹ as follows:

¹iso: isotropic limit

$$\sum_i |\vec{p}_{\perp,i}| \rightarrow \int |p_{\perp}| d|p_{\perp}| d\phi \quad (4.2)$$

Due to the isotropy, \vec{n}_{\perp} can be fixed in whatever direction, for simplicity it is placed parallel to the x-axis, in this case:

$$|\vec{p}_{t,i} \cdot \vec{n}_t| = |\vec{p}_{t,i}| |\cos \phi| \quad (4.3)$$

Combining Eq. 4.2 and Eq. 4.3 in Eq. 4.1 the final expression for T^{iso} is:

$$T^{iso} = \frac{\int \int |p_{\perp}|^2 |\cos \phi| d|p_{\perp}| d\phi}{\int |p_{\perp}|^2 d|p_{\perp}| d\phi} = \frac{2}{\pi} \quad (4.4)$$

It is easy to show that in the “pencil-like” limit, i.e when the particles are perfectly aligned, $T=1$.

In the literature it is more common to find the following definition:

$$\tau \equiv 1 - T \quad (4.5)$$

The variable τ is related with the Sphericity of the event, with the limits:

$$\tau = \begin{cases} = 0 & \text{“pencil-like” limit} \\ = 0.3633 & \text{“isotropic” limit} \end{cases}$$

In the following we will use τ instead of T .

For a given thrust axis (\vec{n}_t), we can also define Thrust-minor (T_{min}) as:

$$T_{min} \equiv \frac{\sum_i |\vec{p}_{t,i} \times \vec{n}_t|}{\sum_i |\vec{p}_{t,i}|} \quad (4.6)$$

T_{min} is a measure of the importance of the out-of-plane components of the transverse momentum.

A further event shape variable is the transverse Sphericity: S_{\perp} , is defined in terms of the eigenvalues $\lambda_1 \geq \lambda_2$ of the transverse-momentum tensor:

$$\mathbf{S}_{xy} = \sum_i \begin{pmatrix} p_x^{(i)2} & p_x^{(i)} p_y^{(i)} \\ p_x^{(i)} p_y^{(i)} & p_y^{(i)2} \end{pmatrix}$$

According to:

$$S_{\perp} \equiv \frac{2\lambda_2}{\lambda_2 + \lambda_1} \quad (4.7)$$

Finally, an useful extra term is the recoil r . The recoil is simply the normalized transverse momentum balance:

$$r \equiv \frac{1}{\sum_i |\vec{p}_{t,i}|} \left| \sum_i \vec{p}_{ti} \right| \quad (4.8)$$

For example if we would have only one jet in the acceptance the value of r would be high, while in the case of both jets entering in the acceptance the recoil value will be small.

$$r = \begin{cases} = 0 & \text{"balanced momentum"} \\ = 1 & \text{"unbalanced momentum"} \end{cases}$$

4.1.1 Study of τ and r for 2-particle events.

To illustrate the main elements of an event shape in the r and τ space we present the simplest case where events with only two particles in the acceptance are analyzed. From the definitions of r and T , there is a general relation between r and τ :

$$1 - T + R = 1 - \frac{\sum_i |\vec{p}_{\perp,i} \cdot \vec{n}_{t0}|}{\sum_i |\vec{p}_{\perp,i}|} + \frac{|\sum_i \vec{p}_{\perp,i}|}{\sum_i |\vec{p}_{\perp,i}|} \quad (4.9)$$

Now, using the fact that:

$$\left| \sum_i \vec{p}_{\perp,i} \right| \leq \sum_i |\vec{p}_{\perp,i}| \quad (4.10)$$

Then:

$$1 - T + r \leq 1 - T + 1 \quad (4.11)$$

But we know that $T \leq 1$, so we find the following restriction:

$$1 - T + r \leq 1 \quad (4.12)$$

in terms of τ

$$\tau + r \leq 1 \quad (4.13)$$

Let's consider the limiting case, *i. e.*, $\tau + r = 1$, this means: $r(\tau) = 1 - \tau$. Note that this is an upper limit extracted from the Eq. 4.8 and it is always valid.

Now, we consider the case where there are only two particles. For simplicity, we place the leading particle at 0 rad (on x axis). So, the vectorial expression of the transverse momentum of the leading particle is:

$$\vec{p}_{\perp}^l = (p_{\perp}^l, 0) \quad (4.14)$$

where, of course $|\vec{p}_{\perp}^l| = p_{\perp}^l$

The azimuthal angle of the associated particle (ϕ) is measured with respect to the leading one, so $\phi \in (0, 2\pi)$. Thus, the vectorial transverse momentum of the associated particle is:

$$\vec{p}_\perp^a = (p_\perp^a \cos(\phi), p_\perp^a \sin(\phi)) \quad (4.15)$$

On the other hand, a generic unitary vector in the transverse plane is expressed as:

$$\vec{n}_\perp = (\cos(\phi_n), \sin(\phi_n)) \quad (4.16)$$

In this case, the expression of thrust is:

$$T = \underbrace{\max_{\vec{n}_\perp}}_{\vec{n}_\perp} \frac{|\vec{p}_\perp^l \cdot \vec{n}_\perp| + |\vec{p}_\perp^a \cdot \vec{n}_\perp|}{p_\perp^l + p_\perp^a} \quad (4.17)$$

Now, we define α as:

$$\alpha \equiv \frac{|\vec{p}_\perp^l|}{|\vec{p}_\perp^a|} = \frac{p_\perp^l}{p_\perp^a} \quad (4.18)$$

So, for a system of two particles, thrust reduces to a expression:

$$T = \underbrace{\max_{\phi_n}}_{\phi_n} \frac{\alpha |\cos(\phi_n)| + |\cos(\phi - \phi_n)|}{1 + \alpha} \quad (4.19)$$

Before performing the computations, it is interesting to look at the behavior of the function $f(\phi_n)$ given by:

$$f(\phi_n) = \frac{\alpha |\cos(\phi_n)| + |\cos(\phi - \phi_n)|}{1 + \alpha} \quad (4.20)$$

Note that the absolute maximum of this function with respect to ϕ_n is exactly the so called Thrust.

Fig. 4.1 (left) shows the function $f(\phi_n)$ for the case where $\alpha = 1$. Four different cases are analyzed,

- (black) The associated particle is very close to the leading one ($\phi \sim 0$). Note that in this case, two symmetrical maximum are reached, at $\phi_n = 0, \pi/2$. This is expected, because the thrust axis is defined by the direction of the leading particle, so the projection of the transverse momentum of the leading and the associated particles on the thrust axis is the total transverse momentum of the event. So, $T = 1$.
- (blue) The associated particle is at $\pi/2$ with respect to the leading one ($\phi = \pi/2$). This is a symmetrical case, because four possible directions maximize $f(\phi_n)$. Of course the maximum are reached at $\phi_n = \pi/4, 3\pi/4, 5\pi/4, 7\pi/4$. Note also, that the value of thrust is $T \sim 0.7$.

- (red) The associated particle is at $\pi/4$ with respect to the leading one ($\phi = \pi/4$). This is an “intermediate”-case between the first and second. Note that local maximum appear, the directions are perpendicular with respect to the thrust axis. The module of the projections of the transverse momenta of the particles on such new vector is by construction, smaller than the projections on the thrust axis.
- (green) The associated particle is at $3\pi/4$ with respect to the leading one ($\phi = \pi/2$). The pattern is reproduced.

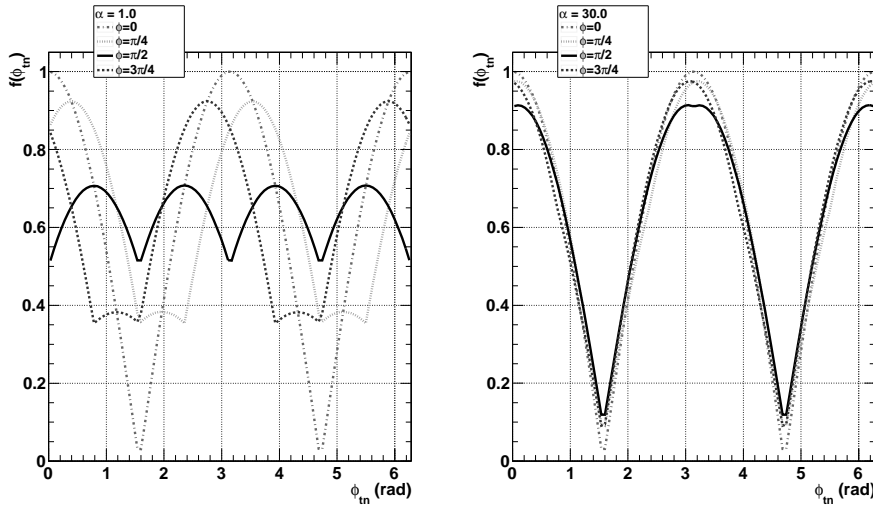


Figure 4.1: For events with $\alpha = \frac{p_\perp^l}{p_\perp^a}$ equal to 1 (left) and 10 (right). The function $f(\phi_n)$ is shown for different configurations given in terms of ϕ .

As we increase the value of α , the maxima of the different configurations converge to 1 (see Fig. 4.1 (right)).

Using Eq. [14], by trivial optimization procedure we can get the following solutions for which the maximum of Eq. [14] is attained:

- If $\pi/2 < \phi < 3\pi/2$:

$$\phi_n^* = \arctan \left(\frac{\sin(\phi)}{\cos(\phi) - \alpha} \right) \quad (4.21)$$

- If $\phi < \pi/2$ or $\phi > 3\pi/2$:

$$\phi_n^{**} = \arctan \left(\frac{\sin(\phi)}{\cos(\phi) + \alpha} \right) \quad (4.22)$$

In order to get the relation between thrust and recoil, we proceed as follows.

For the first solution:

- The recoil for the present system is:

$$r = \frac{\sqrt{1 + \alpha^2 + 2\alpha \cos \phi}}{1 + \alpha} \quad (4.23)$$

- Using the facts: $\alpha \geq 1$ (by definition) and $\cos \phi < 0$, the expression of thrust is:

$$T = \frac{\sqrt{(1 + \alpha^2) - 2\alpha \cos \phi}}{1 + \alpha} \quad (4.24)$$

- From Eq. [18] we extract $\cos \phi$ in terms of r , thus we can get $r(\tau)$:

$$r = \sqrt{\frac{2(1 + \alpha^2)}{(1 + \alpha)^2} - (1 - \tau)^2} \quad (4.25)$$

The beauty of the last expression is that given configurations of particles, governed by α , it is possible to identify them in a map formed by the variables thrust and recoil.

Following the same procedure we can get the expression for the second solution.

$$r = T \quad (4.26)$$

In summary, if the $\Delta\phi$ between the leading particle is in the range: $\pi/2 < \Delta\phi < 3\pi/2$, then the variables $\tau \equiv 1 - T$ and r are related as follows (see Fig. 4.2):

$$r = \sqrt{\frac{2(1 + \alpha^2)}{(1 + \alpha)^2} - (1 - \tau)^2} \quad (4.27)$$

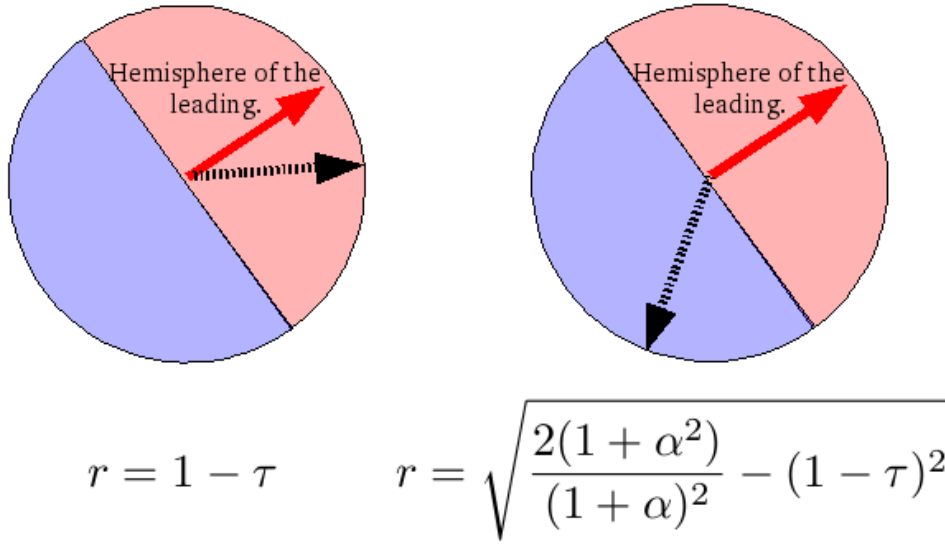


Figure 4.2: The function $r(\tau)$ for two classes of events: when the associated particle is in the hemisphere of the leading (left) and when the associated particle is in the away hemisphere (right).

When the associated particle is in the same hemisphere as the leading particle (see Fig. 4.2) $\Delta\phi > 3\pi/2$ or $\Delta\phi < \pi/2$:

$$r = 1 - \tau \quad (4.28)$$

The function $r(\tau)$ for different values of α is shown in the left panel of Fig. 4.3. The upper black line of this panel shows the behavior of the function $r(\tau)$ for limit case $r = 1 - \tau$. The right panel of Fig. 4.3 shows τ vs. r weighted by $\langle\alpha\rangle$, for proton-proton collisions² obtained with PYTHIA events at 0.9 TeV. This analysis is restricted to $|\eta| \leq 0.8$, a cut in the transverse momentum was applied: $p_{\perp} \geq 0.5$ GeV/c. Only events with multiplicity 2 were selected.

4.1.2 Event Shapes in the case of an isotropic phase-space (PS) model.

In the present section we compare the event shapes obtained with a phase space model to physics events using proton-proton collisions at 7 TeV.

A PYTHIA6 model which includes the soft and hard processes and special input parameters (see the section 3) based on the tune ATLAS-CSC[Mor] was used. In order to study

²From the early physics simulations in ALICE at 0.9 TeV (run LHC10a8).

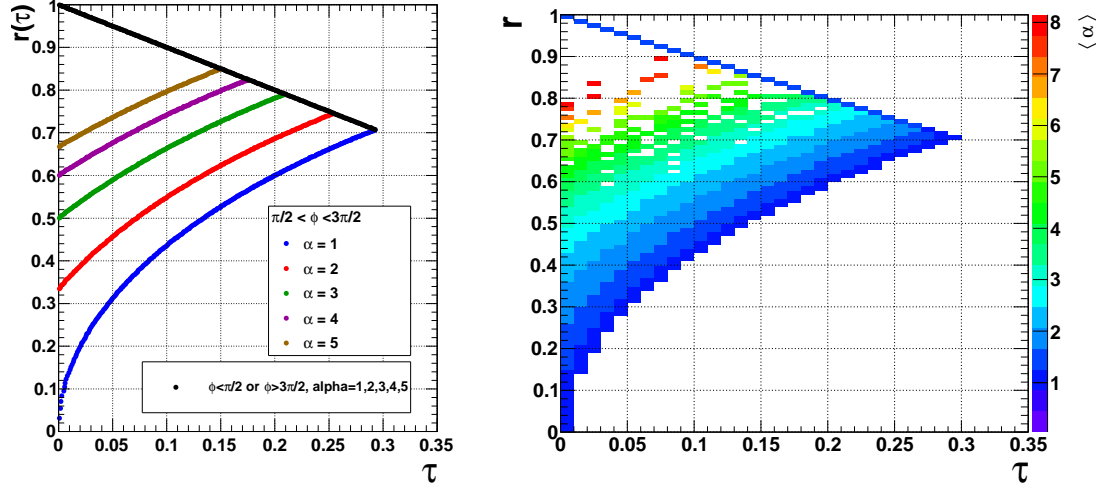


Figure 4.3: Left panel corresponds to $r(\tau)$ function for different values of α . Right panel, shows τ vs. r weighted by $\langle \alpha \rangle$, for p-p collisions at 0.9 TeV simulated with PYTHIA. Only events with two charged particles in $|\eta| \leq 0.8$ and $p_{\perp} \geq 0.5$ GeV/c were considered.

the event shapes at high multiplicity, the analysis was done using the ALICE Monte Carlo production LHC10b6³.

The PS model is based on the n-body phase-space integral which is defined as:

$$R_n = \int^{4n} \delta^4 \left(P - \sum_{j=1}^n p_j \right) \prod_{i=1}^n \delta(p_j^2 - m_i^2) d^4 p_i \quad (4.29)$$

where: P is the total four-vector of the n-body system, p_i are the four-vectors of the individual particles and m_i are the masses of the particles. For a given kinematic parameter: β of the system, its spectrum will be given by:

$$f(\beta) = \frac{d}{d\beta} (|M.E.|^2 \cdot R_n) \quad (4.30)$$

where M.E. is the scattering matrix element describing the interactions between the particles. If there is no interaction between the outgoing particles: M.E. = 1, and we say that the spectra are given by phase-space considerations alone. The simulations of the phase-space have been done using the tool TGenPhaseSpace provided by ROOT. This class generates an n-body event with constant cross section. The code is based on the GENBOD function (W515 from CERNLIB) using the Raubold and Lynch method [Jam68]. In the present analysis, events with $n = 200$ charged pions were generated.

³Early physics-2, measured SPD mean vertex and spread, pp, ATLAS-CSC, flat multiplicity distribution 0.5T, 7 TeV, ID #170.

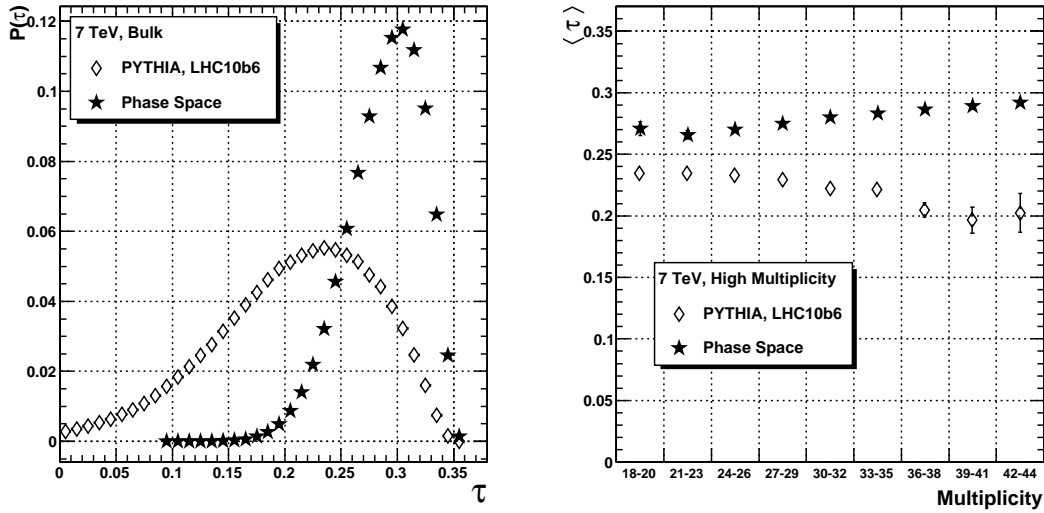


Figure 4.4: τ spectra for simulations based on an isotropic phase-space and PYTHIA models (left). Mean τ as a function of the multiplicity for both models (right).

In the analysis only primary charged particles in the acceptance: $|\eta| \leq 0.8$ and with $p_{\perp} \geq 0.6$ GeV/c were considered. Fig.4.4 shows the τ spectra for PYTHIA and phase-space models (left). In order to study the high multiplicity, the sample was divided in different multiplicity bins and plotted versus the mean τ (right side Fig. 4.4). Similar plots for the case of the transverse Sphericity are shown in Fig. 4.5

One interesting feature is that at high multiplicity, the Sphericity of the events decreases with respect to the low multiplicity ones. This behavior is different in the PS events where the jets are absent. The ‘bulk’ distribution shows that the PS events populate the isotropic region of the Sphericity, while the PYTHIA ones are distributed in the full range of Sphericity.

On the other hand, we can do a similar study but now using the recoil variable (see Fig. 4.6). From the present study we conclude that the PS events show marked differences with respect to the case of PYTHIA events.

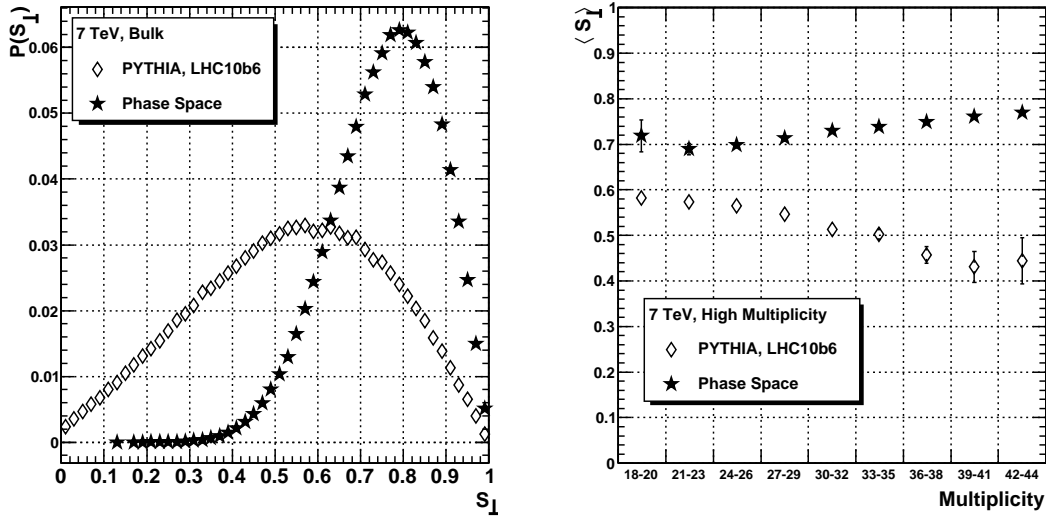


Figure 4.5: S_{\perp} spectra for simulations based on an isotropic phase-space and PYTHIA models (left). Mean S_{\perp} as a function of the multiplicity for both models (right).

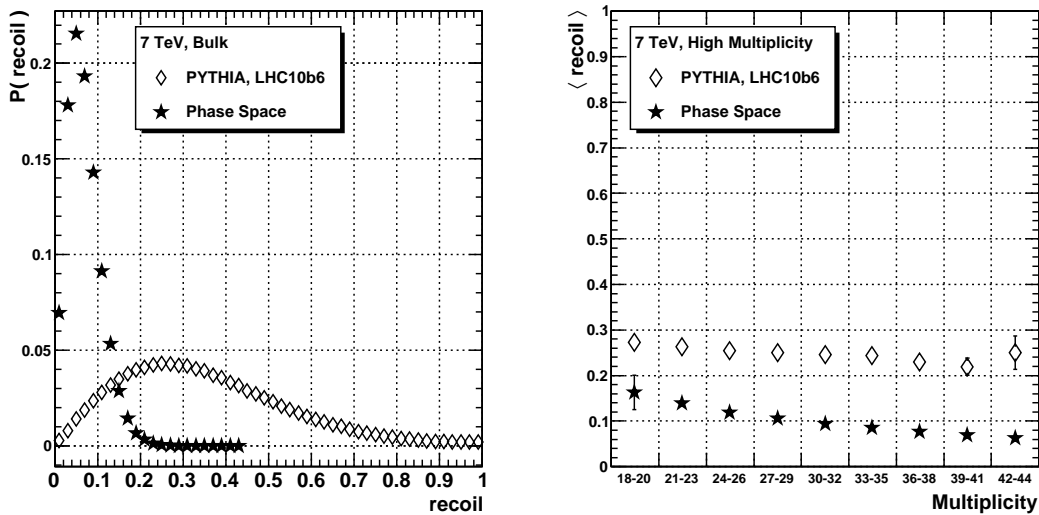


Figure 4.6: r (recoil) spectra for simulations based on an isotropic phase-space and PYTHIA models (left). Mean r as a function of the multiplicity for both models (right).

4.2 Sensitivity of the Event Shape with respect to different PYTHIA parameters.

At LHC energies, the processes which involve parton-parton scattering with high transverse momentum transfer (“hard processes”) are copiously produced. Although these processes are well described in terms of QCD, the environment of the hadron collider is dominated by soft interactions (minimum bias events) which are not associated to hard processes. It is well established that a good understanding and adequate simulation of minimum bias events is crucial for LHC experiments. Beyond the numerous exclusive parameters it is interesting to identify an overall behavior of the events and to compare them in the first instance to the results of generators with default parameters, something of exceptional importance for the correction and analysis of data. Comparison of the data with the existing event generators gives rise to the so called “tuning” activity [Ska, Fie]. In the present section we investigate the bulk behavior of the minimum bias events as present in the event generators in use at LHC (mostly the ATLAS PYTHIA tune) using a convenient approach namely the Event Shape Analysis (ESA). As we will see, the method, adopted from electron colliders and modified to be applicable in hadron hadron collisions [ea04a] represents an elegant way to study bulk properties of events.

In the present work we have used proton-proton collisions simulated with the PYTHIA [Sjo94] event generator. The events which were reconstructed in ALICE correspond to inelastic interactions, *i. e.* the processes which produce new particles, in this framework: the single-diffractive (SD), double-diffractive (DD) and non diffractive processes were taken into account. The way in which PYTHIA simulates the collisions is through the incorporation of two components. The first is associated to the inelastic processes including the SD, DD and ND corresponding, in the language of PYTHIA, to the minimum-bias (MB) events. The second is related to the underlying event (UE) activity. Mostly, the UE are formed of beam remnants, initial state radiation, and, visualizing the hadrons as a beam of partons, multiple-parton interaction (MPI). The latter has been proposed and supported by many experimental measurements[ea87b, ea91, ea97]. The inclusion of MPI solves the problem which arises from considering momentum transfer of \sim few GeV, where σ_{QCD} for a $2 \rightarrow 2$ parton scattering exceeds the $p p$ or $p \bar{p}$ cross section. In this context, there are several free parameters which control the different ingredients, the goal is to tune them in order to describe in the best way the experimental data.

The following simulations were done starting from the set of parameters which defines the ATLAS-TDR tune[ea08a]. This tune reproduces the event shape spectra at 0.9 TeV recorded by ALICE but fails in the description of the multiplicity and transverse momentum spectra. In the table 4.3 are listed the values of the parameters of the tune corresponding to MPI that were considered in the present work.

Table 4.1: Parameters of tune ATLAS-TDR.

Parameter	Description	ATLAS TDR
PDF	Partonic function	CTEQ5L
MSTP(2)	First-order running α_s	1
MSTP(33)	Factors $K = 1$	0
MSTP(81)	Switch-on for MPI	1
MSTP(82)	Structure of multiple interactions	4
PARP(82)	$p_{\perp 0}$	1.8 GeV
PARP(83)	Fraction of the total hadronic matter	0.5
PARP(84)	Core radius	0.5
PARP(85)	Related to gluon production	0.33
PARP(86)	Related to gluon production	0.66
PARP(89)	Reference energy scale	1.0 TeV
PARP(90)	Power of the energy-rescaling term.	0.16

4.2.1 Parameters related to the Underlying Event Activity

Effect of varying $p_{\perp min}$.

For *parton-parton* interactions the differential cross section is divergent for $p_{\perp} \rightarrow 0$, so that a lower cut-off has to be introduced in order to regularize it. In PYTHIA the parameter which regularizes the divergence is given by $p_{\perp 0}$, we can interpret such parameter as follows. For a given reference energy scale (PARP(89)= E_{ref}), we have:

$$p_{\perp 0}(s) = p_{\perp min} \times \left(\frac{\sqrt{s}}{E_{ref}} \right)^{2 \times pow} \quad (4.31)$$

where $pow=PARP(90)$, $p_{\perp min}=PARP(82)$ is the minimum p_{\perp} at reference energy, and \sqrt{s} is the energy in the center of mass of the collision.

In this context, as the value $p_{\perp min}$ is increased the *parton-parton* interaction rate is reduced. This implies a reduction in the multiplicity and particle density at central rapidity. In Fig. 4.7 Sphericity distribution and the mean multiplicity of primary charged particles in function of Sphericity are shown.

Although the range of variation of $p_{\perp min}$ (which corresponds to the range used by different tunes) is small one does observe in the Sphericity spectrum and in the mean multiplicity distribution differences.

We also present the correlation between the Sphericity and the mean transverse momentum of the particles for a given event. Fig. 4.8 shows in the left panel such distributions. We observe a major sensitivity to the PARP(82) at low Sphericities. To complete the discussion,

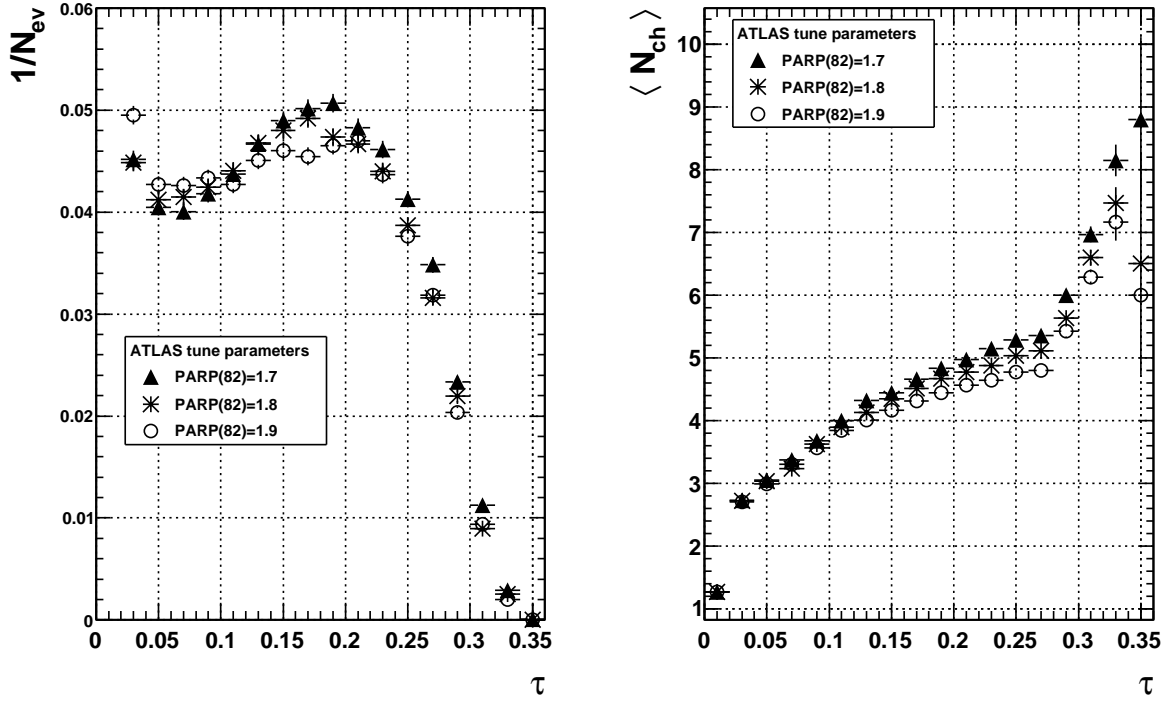


Figure 4.7: τ spectra as a function of $p_{\perp min}$ (left). Mean multiplicity of primary charged particles versus τ for different cuts on $p_{\perp min}$ (right).

the right panel of Fig. 4.8 shows the Thrust Minor spectrum, where we observe a small but observable effect in the range $0.4 < T_{min} < 0.5$. Next, we have split the sample into high and low transverse momentum samples. Figs. 4.9 and 4.10 show the behavior of the Sphericity spectrum and the averaged multiplicity versus Sphericity, both of them as function of $p_{\perp min}$ for the so called “soft” and hard components, respectively.

Finally, Fig. 4.11 shows the same type of analysis, for the case of T_{min} .

Varying the core size of the hadronic matter

Keeping in mind that hadrons have a matter distribution it is necessary to consider the possibility of Multiple Interaction (MI) in simulations. Then, each collision is characterized by its impact parameter b , which is the distance of closest approach of the colliding nuclei. A small b is associated to a large overlap between the two colliding hadrons, so the probability of Multiple Interactions is increased. On the other hand, a large b value corresponds to a low probability of MI. In PYTHIA, to quantify the concept of hadronic overlap matter, a spherically symmetric distribution of matter inside the hadron is assumed, $\rho(x)d^3x =$

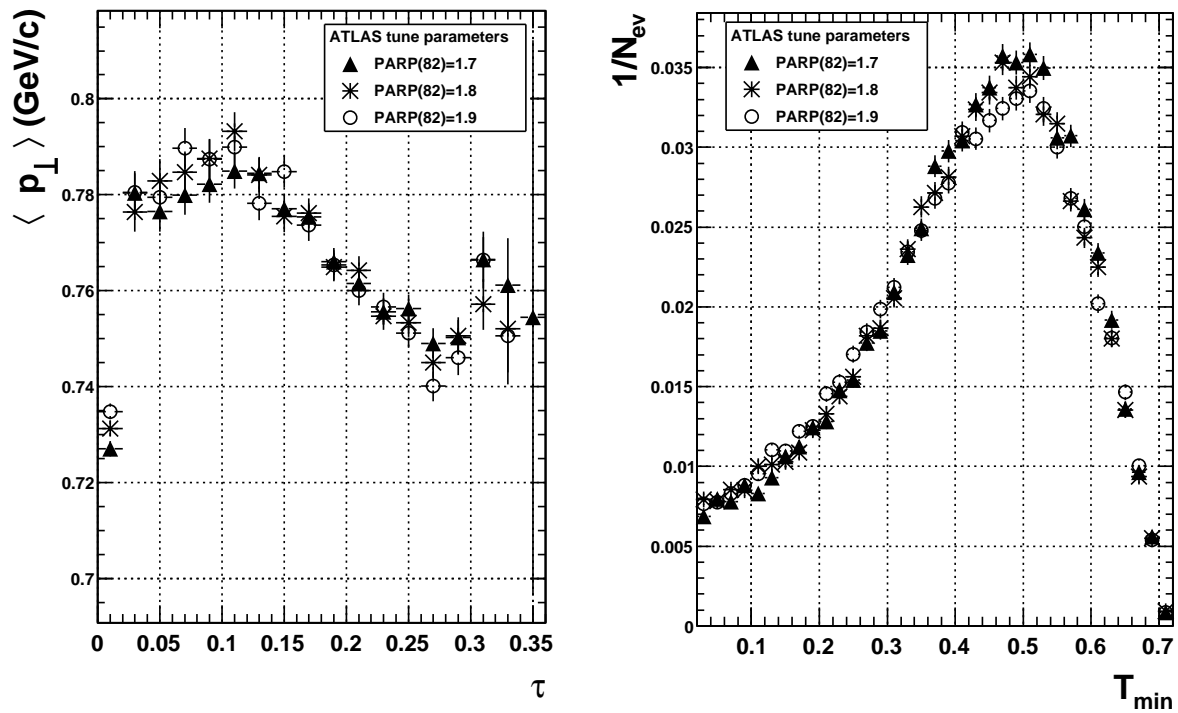


Figure 4.8: τ versus mean transverse momentum for different values of $p_{\perp min}$ (left). Thrust minor spectra as a function of $p_{\perp min}$ (right).

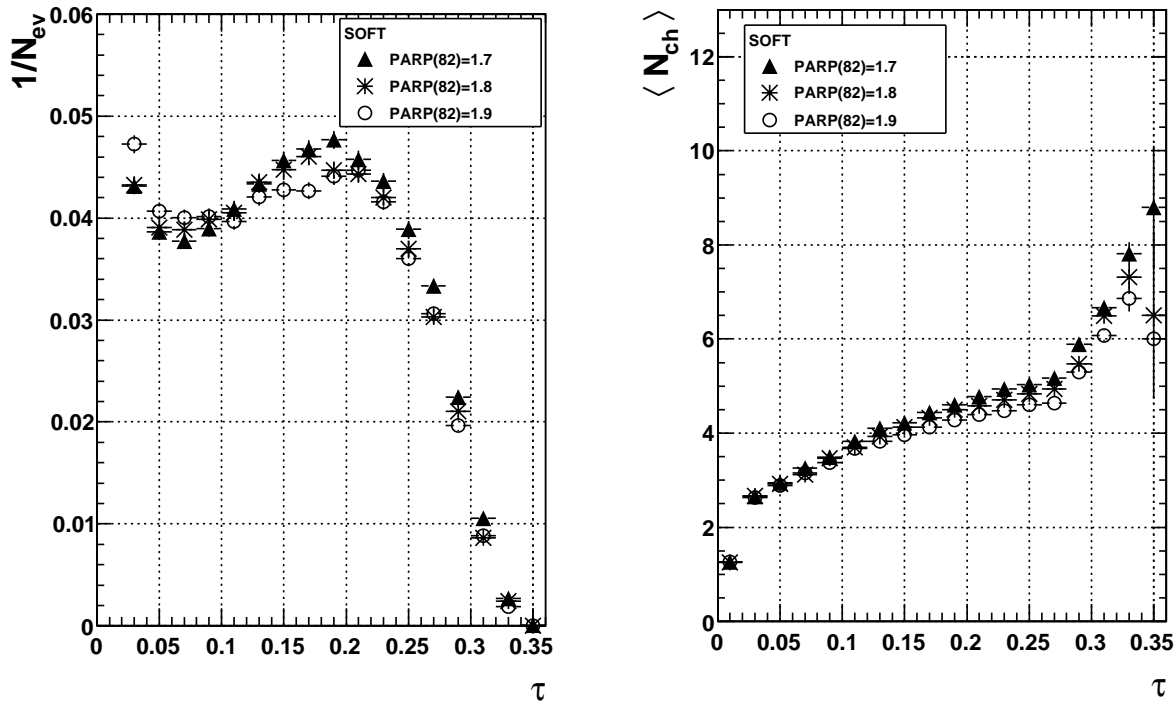


Figure 4.9: Analysis of the “soft” component of the sample, *i. e.*, events with leading particle with $p_{\perp} < 2$ GeV/c. (τ spectra as a function of $p_{\perp min}$ (left). Mean multiplicity of primary charged particles versus τ for different cuts on $p_{\perp min}$ (right)).

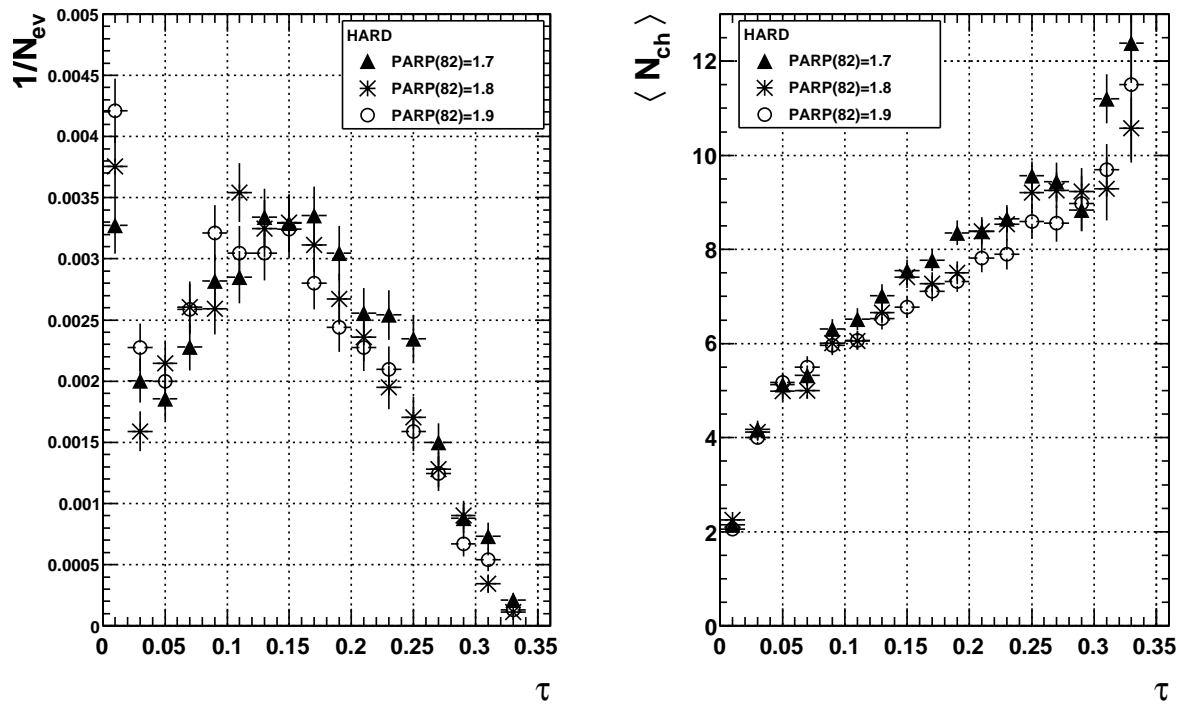


Figure 4.10: Analysis of the “hard” component of the sample, *i. e.*, events which leading particle has $p_\perp \geq 2$ GeV/c. τ spectra as a function of $p_{\perp min}$ (left). Mean multiplicity of primary charged particles versus τ for different cuts on $p_{\perp min}$ (right).

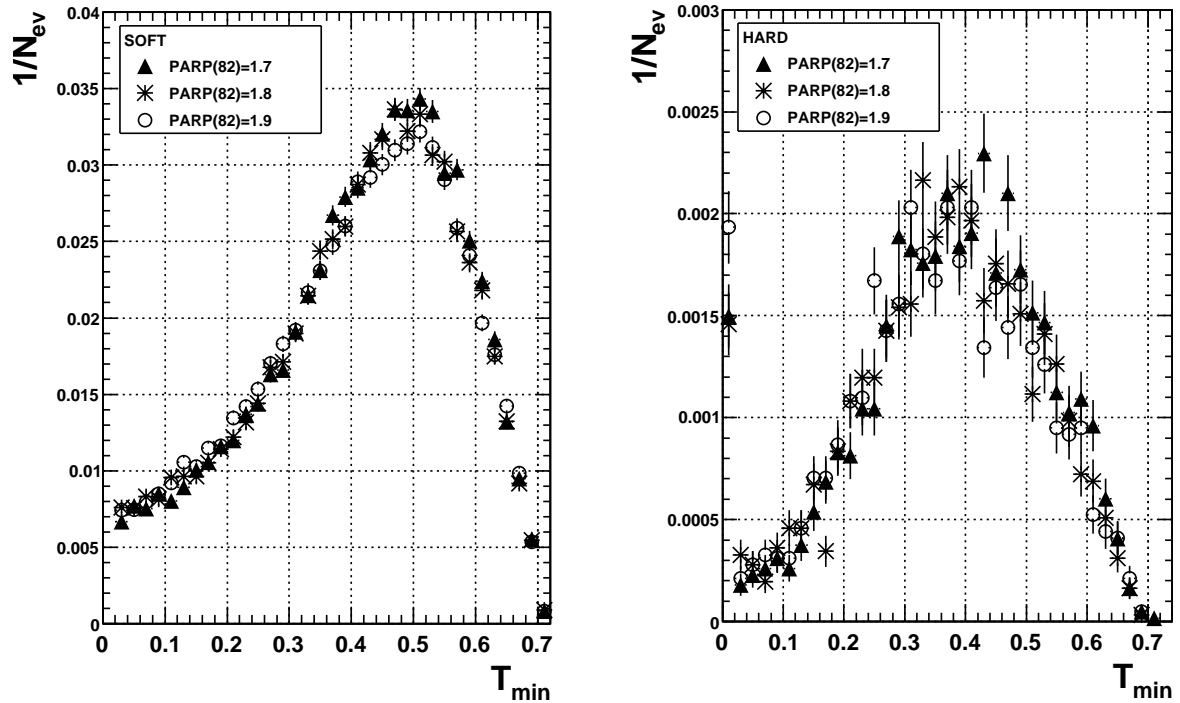


Figure 4.11: Thrust minor spectra for the “soft” (left) and “hard” (right) samples. The value of $p_{\perp min}$ was varied starting from 1.7 up to 1.9.

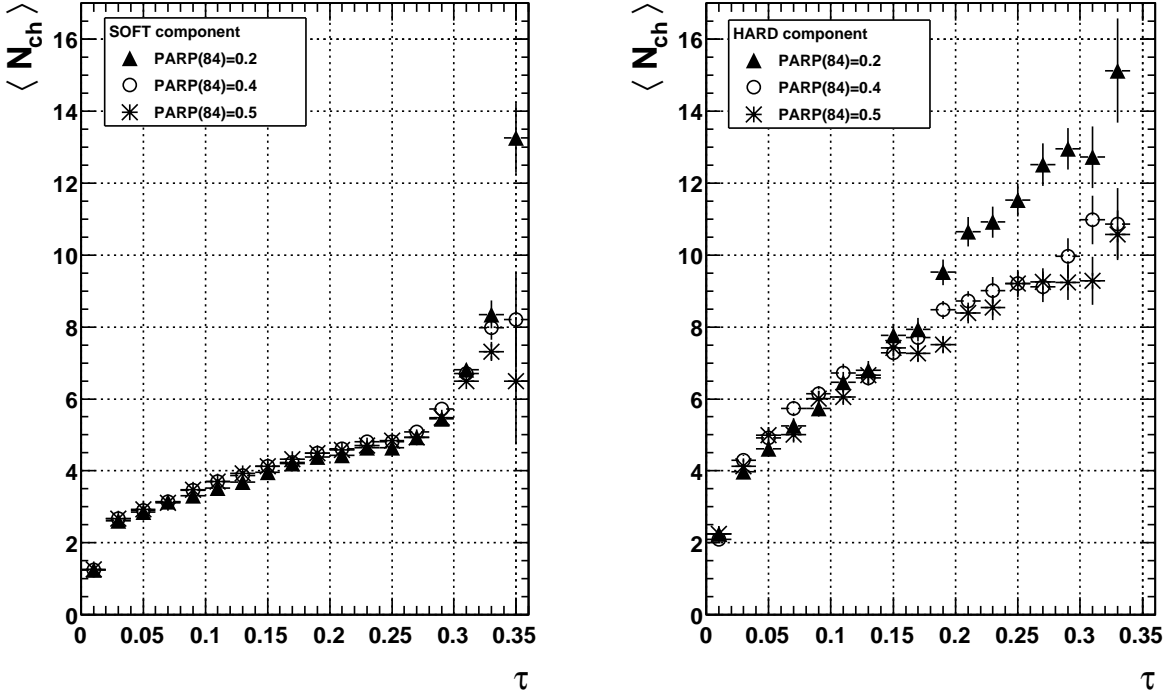


Figure 4.12: Average multiplicity of primary charged particles as a function of τ . The analysis was done in the central barrel of rapidity $|\eta| \leq 0.9$, and using particles with $p_T \geq 500$ MeV/c. “soft” component (left) with $p_T^l \leq 2$ GeV/c of the leading particle, while “hard” component with $p_T^l \geq 2$ GeV/c (right). Different values of core size: $a_2/a_1 = 0.2$, 0.4 and 0.5 (default value for the ATLAS-TDR tune). The core density is fixed at $\beta = 0.5$.

$\rho(r)d^3x$. and the overlap of hadronic matter distributions is described by a double Gaussian distribution, given by

$$\rho \propto \frac{1-\beta}{a_1^3} \exp\left\{-\frac{r^2}{a_1^2}\right\} + \frac{\beta}{a_2^3} \exp\left\{-\frac{r^2}{a_2^2}\right\} \quad (4.32)$$

where $\text{PARP(84)}=a_2/a_1$ and $\text{PARP(83)}=\beta$. The following results are for $\beta = 0.5$ which corresponds to the fraction of total hadronic matter inside a core region of radius a_2 which is embedded in a larger hadron of radius a_1 . In Fig. 4.12 is shown the averaged multiplicity as a function of Sphericity for: $a_2/a_1 = 0.2$, 0.4 and 0.5. We show the results for the split samples

Note that the value of $a_2/a_1 = 0.5$ is the value given by the ATLAS-TDR tune. As in the previous cases, the total sample of 100 000 events was divided into “soft” and “hard” components according with the criterion of the transverse momentum of the leading particle.

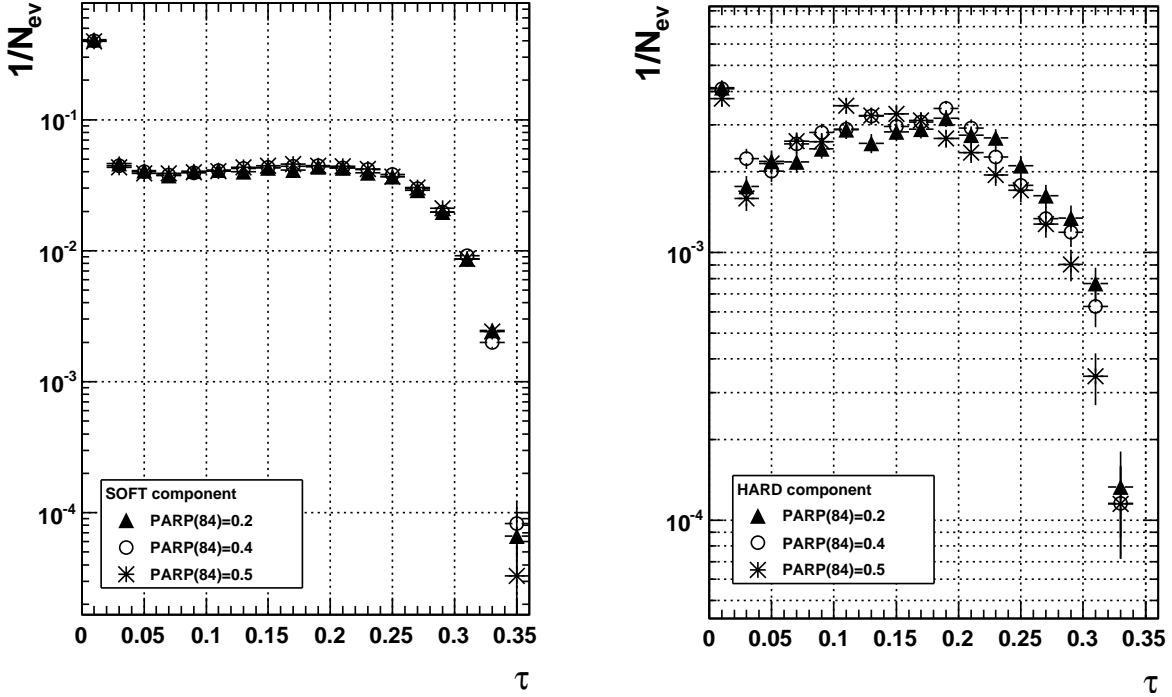


Figure 4.13: τ spectra as a function of the core size. The analysis was done in the central barrel of rapidity $|\eta| \leq 0.9$, and using particles with $p_{\perp} \geq 500$ MeV/c. “soft” component (left) with momentum of the leading particle $p_{\perp}^l \leq 2$ GeV/c, while “hard” component (right) with $p_{\perp}^l \geq 2$ GeV/c are shown. Different values of core size: $a_2/a_1 = 0.2, 0.4$ and 0.5 (default for ATLAS tune).

In the left side of Fig. 4.12 is the result for the “soft” component, where no substantial differences among the three different cases are observed. However the right side of the figure where the “hard” component case is plotted, we can see a specific behavior. The core densities given by $a_2/a_1 = 0.4$ and 0.5 look similar in the description of the event shape in the full range. Both show a saturating trend at $\tau \geq .25$. But if the core size is drastically reduced, *i. e.* $a_2/a_1 = 0.2$, the MPI is increased and the effect in the multiplicity is large. In order to complete this part, the Fig. 4.13 shows the τ distribution for the three different sets of MI. As we noted in the precedent analysis, the main differences appear at high momentum. While in the range $\tau \leq 0.25$ the three spectra intersect in many points, at high Sphericities the probability of finding an event with an isotropic distribution of transverse momentum is higher when $a_2/a_1 = 0.2$ than in the other two cases.

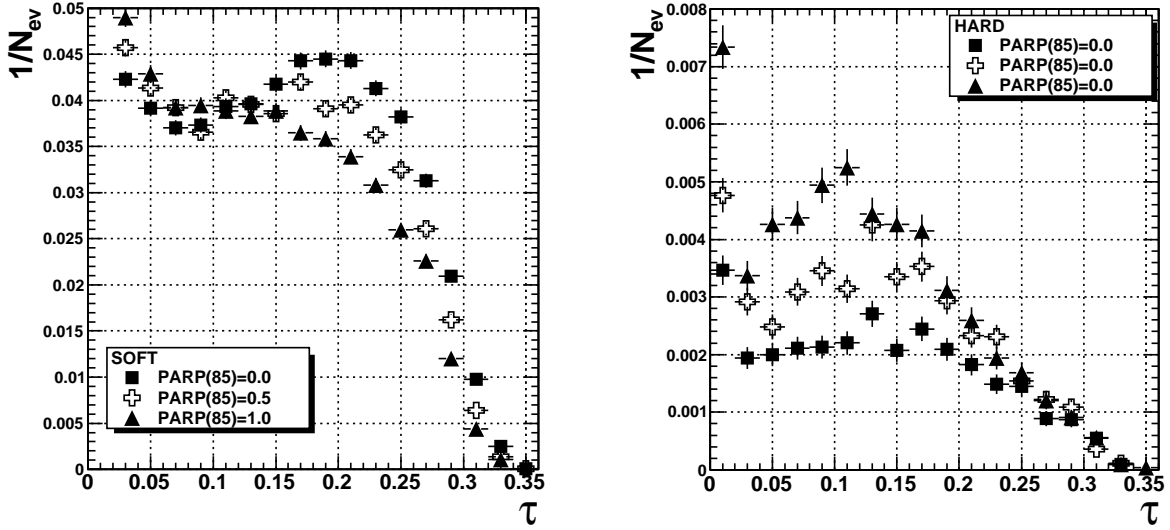


Figure 4.14: τ at 900 GeV for two cases. “soft” (left) events, with leading particle $p_t < 2$ GeV/c, and “hard” (right) events, with leading $p_t \geq 2$ GeV/c. The τ spectrum is shown for different values of PARP(85), which is associated with the probability that an additional interaction in the old multiple- interaction formalism that gives two gluons(see text).

Varying the Gluon Production Mechanisms

In the old model of MPI, the gluon production mechanisms are governed by PARP(85) and PARP(86). The first one gives the probability that an additional interaction in the old multiple-interaction formalism gives two gluons, with colour connections to “nearest neighbours” in momentum space. The other parameter gives the probability that an additional interaction in the same formalism gives two gluons, either as described in PARP(85) or as a closed gluon loop. The remaining fraction is supposed to consist of quark-antiquark pairs (See [Sjo94]).

In Fig. 4.14 the Sphericity spectra are shown considering three values of PARP(85) ($= 0.0, 0.5, 1.0$), as in the previous sections the result is shown for the different components. Note that there is a strong dependence at intermediate Sphericities with respect to the gluon-production in the MPI context at low momentum. On the other hand, the production of the hardest hadrons is also increased. There is a clear change in both, shape and number of events for the “HARD” component. A similar behavior is observed in T_{min} .

But even more interesting is what is happening if we look at other correlations. For example in the left panel of Fig. 4.15 there is the correlation between the average transverse momenta per event and the Sphericity. Note that as the production of the gluon-pairs from MPI is increased the average momentum per event grows in a monotonous way with respect to the Sphericity of the event. On the other hand (right panel) the mean multiplicity

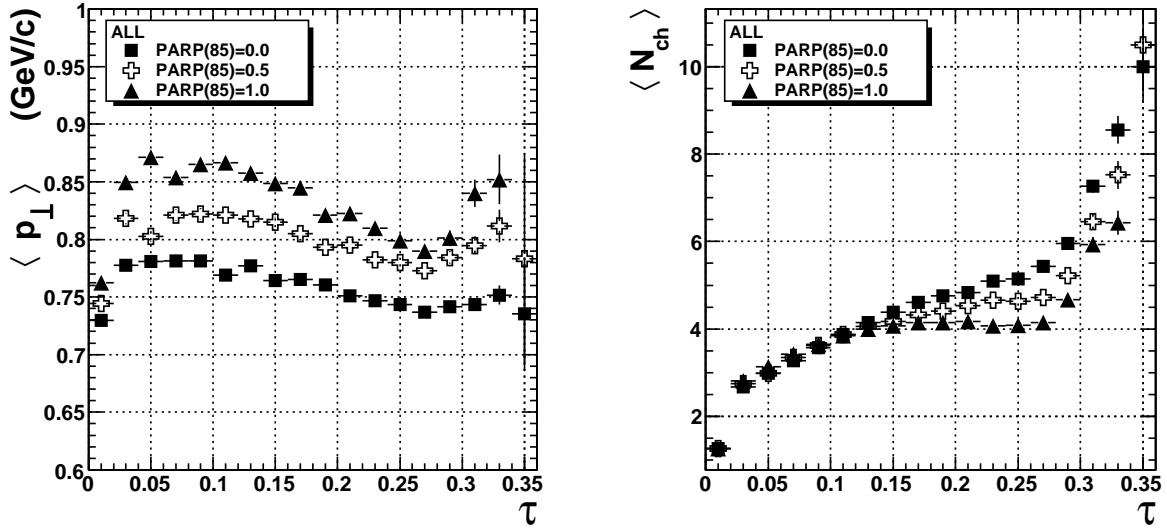


Figure 4.15: Correlations on Sphericity at 900 GeV. Average transverse momentum per event versus τ (left); the average multiplicity per bin of τ (right). Both cases are shown for different values of PARP(85), which is associated with the probability that an additional interaction in the old multiple- interaction formalism gives two gluons.

versus Sphericity has an evident sensitivity to PARP(85). At highest Sphericities the mean multiplicity is increased when the probability of gluon production decreases.

So, this parameter looks like an excellent candidate to tune the UE activity, it is at the moment the most sensitive one of all parameters reviewed here.

4.2.2 Intrinsic transverse momentum: k_{\perp} .

Now is the turn to present the effect of the primordial transverse momentum distribution (k_{\perp}). The usual way to introduce it is through a Gaussian distribution inside hadrons⁴, given by $\exp(-k_{\perp}^2/\sigma^2)k_{\perp} d k_{\perp}$. Where $\langle k_{\perp}^2 \rangle = \text{PARP}(91)^2$ and $\sigma = \text{PARM}(91)$. In this section we vary this parameter starting from 1 to 5. Of course we have changed also the parameter associated with the upper cut-off of the Gaussian, so, in all the cases PARP(93)=15. Fig. 4.16 shows the behavior of the τ for five different values of k_{\perp} .

We observe that the effect is almost exclusively limited to the “hard” component, due to the increase of k_{\perp} , the region of the intermediate and low Sphericity suffers a notable change. As the value of the intrinsic momentum is increased the “dip” at $0.02 < \tau < 0.09$ looks more modulated. This can be understood in terms of the shape of the events, because

⁴Well known as the primordial k_{\perp} distribution, in PYTHIA there are several options to model it.

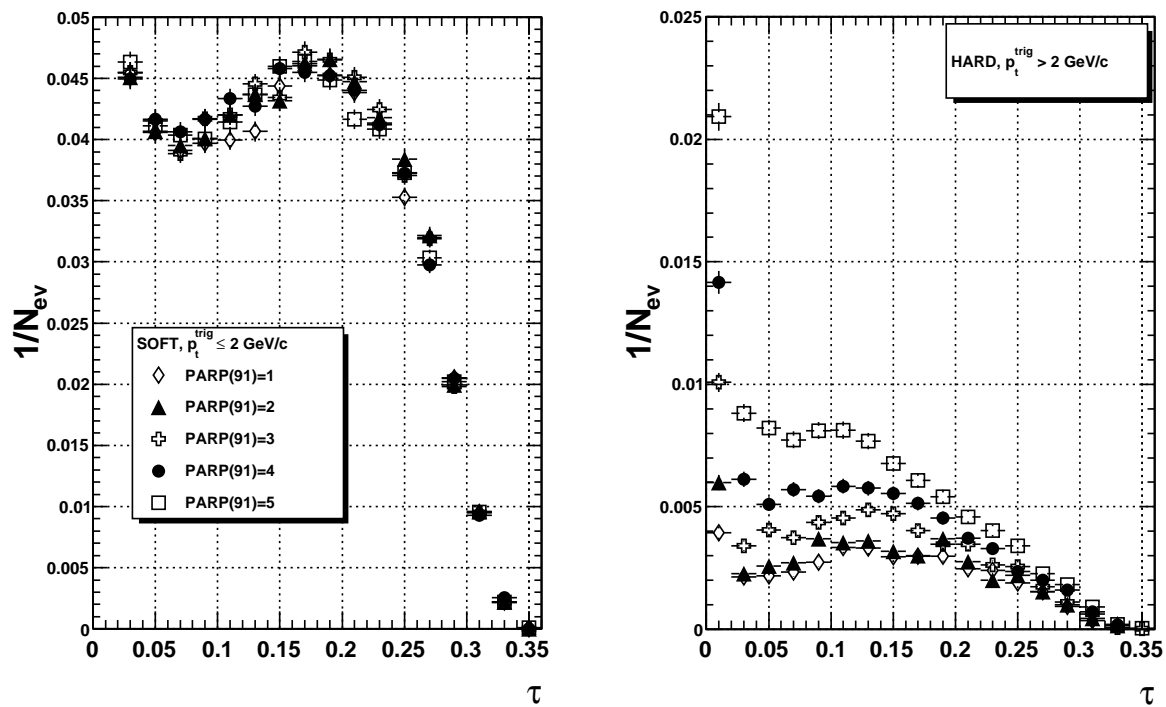


Figure 4.16: Sphericity at 900 GeV for the cases: “soft” events (left), leading particle has $p_t < 2 \text{ GeV}/c$ and “Hard” events, with leading $p_t \geq 2 \text{ GeV}/c$ (right).

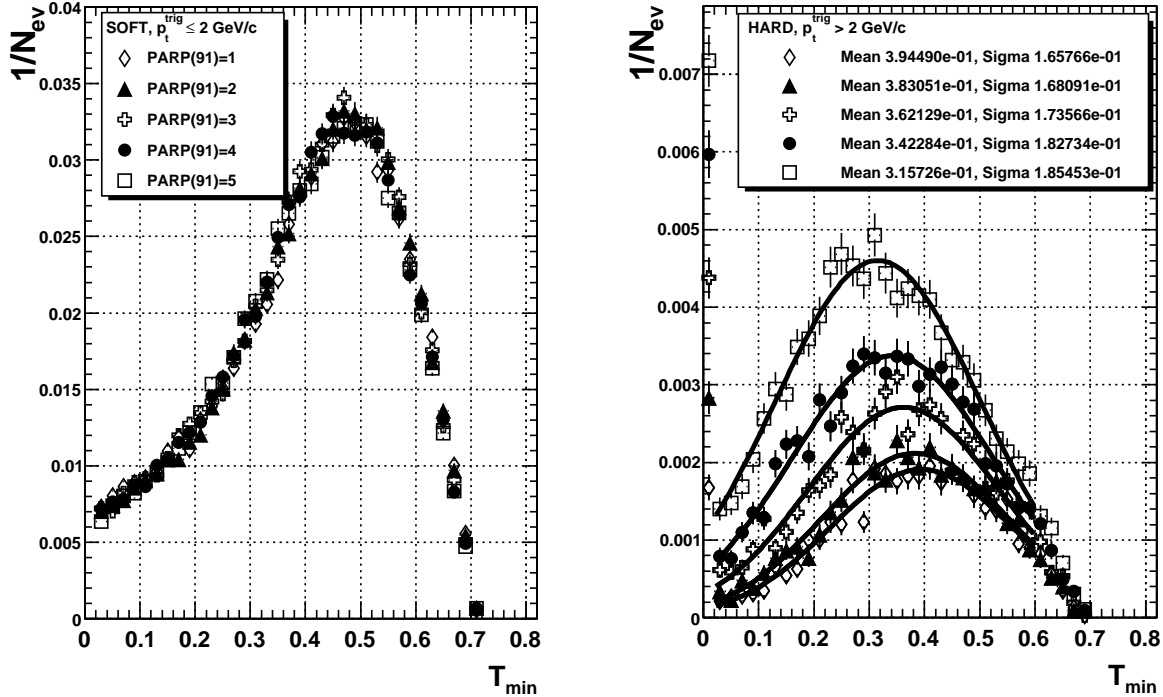


Figure 4.17: T_{min} at 900 GeV for the cases: “soft” events, leading particle has $p_t < 2 \text{ GeV}/c$ (left); “Hard” events, with leading $p_t \geq 2 \text{ GeV}/c$ (right).

at τ very close to zero there are events with back-to-back jet-like shape. However we expect that increasing the k_{\perp} value, many of such events will suffer a “broadening”, in the language of the event shapes this means that the “dip” region will be more populated.

Taking into account that the k_{\perp} essentially affects the out-of-plane component it seems indicated to see the effect of this variable in the T_{min} behavior. We show the effect of changing the k_{\perp} from 1 to 5 in the T_{min} distribution in Fig. 4.17.

Again we see the maximum effect in the hard sample. where the mean of the distribution starts from $\tau = 0.31$ (for $k_{\perp} = 5$) to reach 0.39 (for $k_{\perp} = 1$). At first glance the result seems counter intuitive but the fact is that a higher k_{\perp} means that less events “fit” into the acceptance.

4.2.3 Effect of the PDF on the ES.

The study of the sensitivity of the event shapes variables with respect to the parton distribution function used in the simulation of minimum bias events at different energies has been investigated [eaa]. A strong dependence of correlations like the mean multiplicity versus τ on

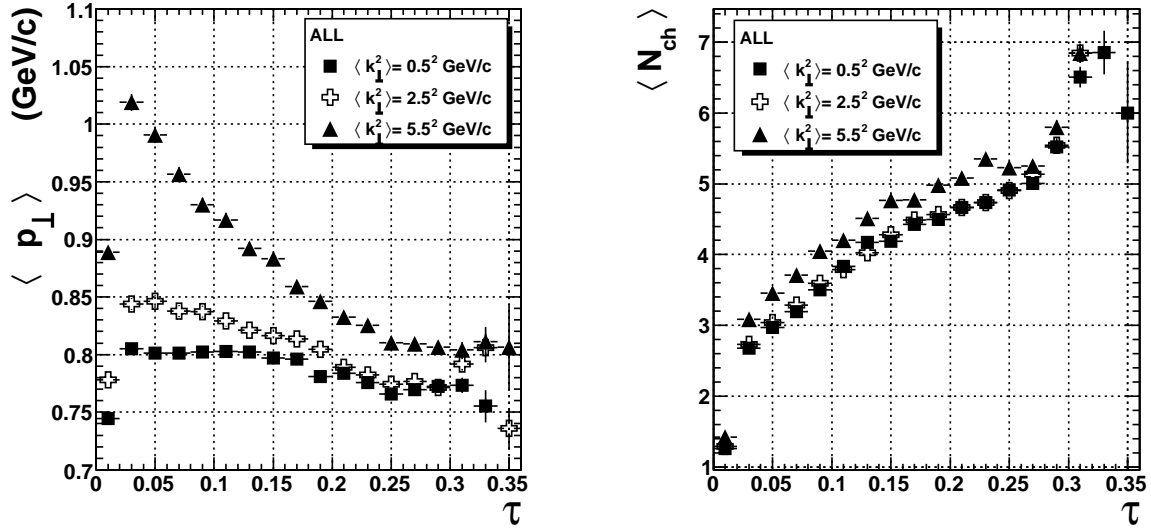


Figure 4.18: Some correlations at 900 GeV: mean transverse momentum of the charged particles per event as a function of the Sphericity (left). Mean multiplicity as a function of Sphericity (right). Three different values of k_\perp were considered: 0.5, 2.5 and 5.5 GeV/c.

PDF was found. In the study two PDF's of different groups were used: CTEQ5L [ea00] and ZEUS2005_ZJ [eaZC05]. Each function was merged to the ATLAS-TDR tune parameters. In this section we compare the effect of changing the PDF in the context of the ES, choosing 3 functions of the same family: CTEQ4L [ea96], CTEQ5L (default of ATLAS tune) and CTEQ6L [ea02]. In Fig. 4.19 we show the average multiplicity as function of Sphericity, for the three PDF's. Note that the main difference with respect to the other parameters which we varied in previous sections, is that we observe a sensitivity in the behavior of the distribution also in the “soft” component; CTEQ6L that is the most recent PDF, produces higher multiplicity events with isotropic distribution in the transverse plane than the other two. This behavior is observed also for high p_\perp events. As well, in the Sphericity distributions (Fig. 4.20), one observes that the effect of changing the PDF is more pronounced for the sample with a hard cut on p_\perp . Actually, both the CTEQ5L and CTEQ6L are crossing the CTEQ4L prediction at $\tau \sim 0.1$.

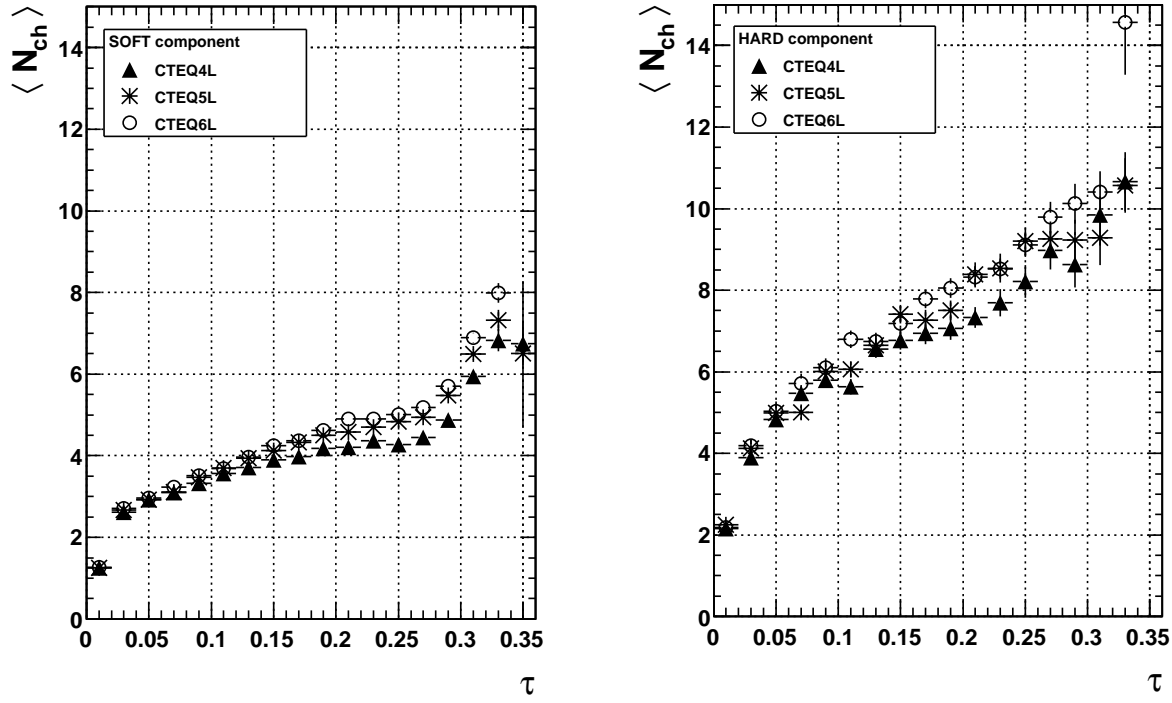


Figure 4.19: Average multiplicity of primary charged particles as a function of Sphericity. The analysis was done at $|\eta| \leq 0.9$, and using particles with $p_T \geq 500$ MeV/c. “soft” component (left), leading particle with $p_T^l \leq 2$ GeV/c and “hard” (right) component, $p_T^l \geq 2$ GeV/c. Different Parton Distribution Functions were used: CTEQ4L, CTEQ5L (default of ATLAS tune) and CTEQ6L.

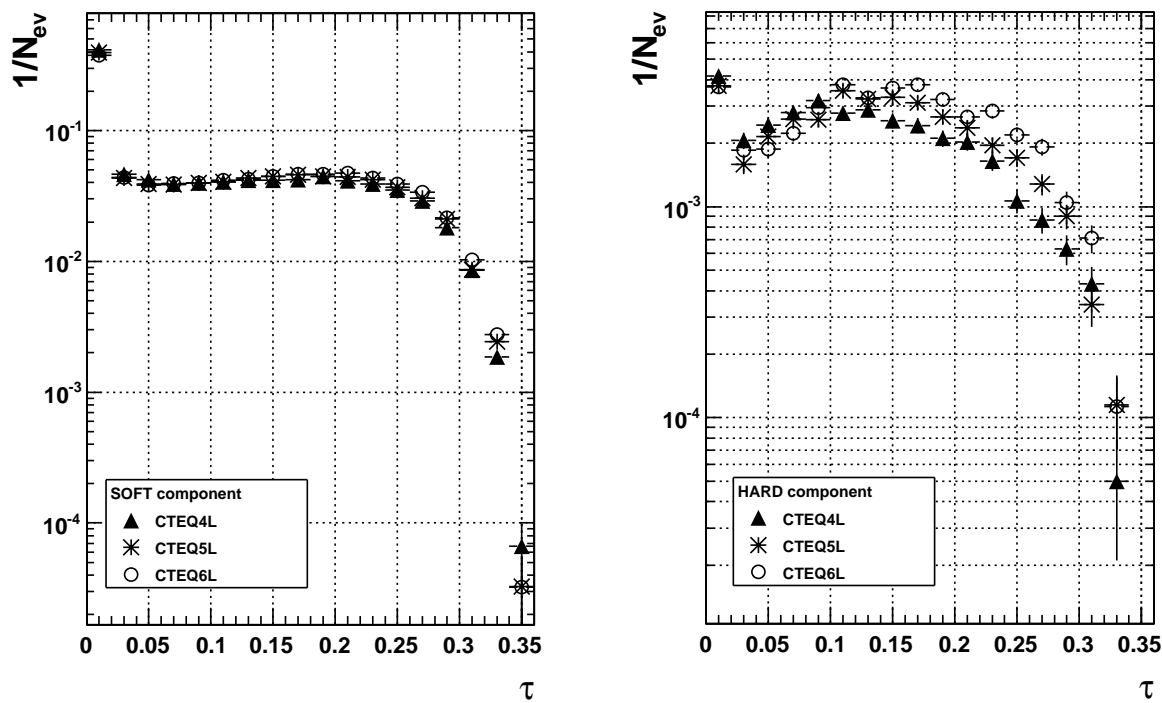


Figure 4.20: Sphericity spectra for different PDF's: CTEQ4L, CTEQ5L and CTEQ6L.
“soft” (left) component and “hard” (right) component.

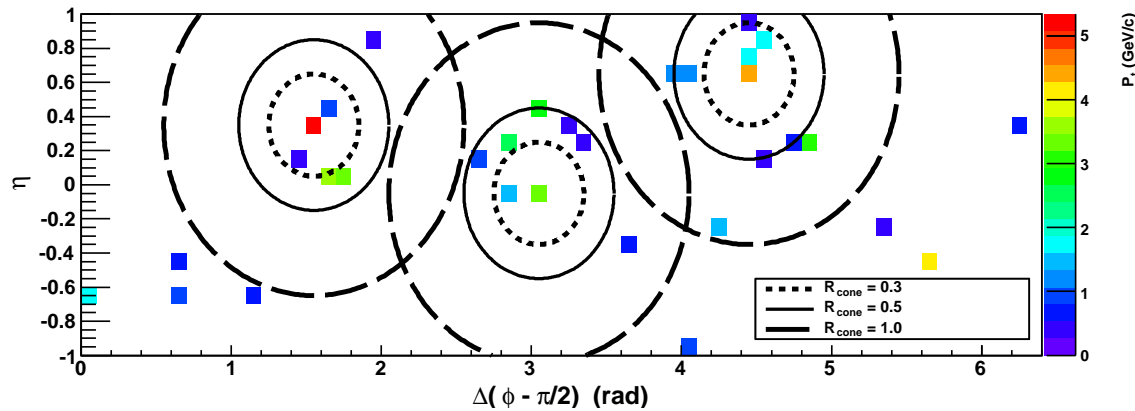


Figure 4.21: Plot: η vs. $\Delta(\phi - \pi/2)$ vs. p_t for a typical event. The leading particle is placed at $\pi/2$ rad. Different radii are shown.

4.3 ESA and the jet structures.

This section is based on [OP]. The goal is to show that using the variable thrust (related with the sphericity) and the term recoil, it is possible to construct a map where a fast identification of specific jet topologies can be done.

The main problem we will face at LHC is the big number of jets overlapping one another. This makes all analysis subject to numerous cuts which do increase the systematic uncertainties of the results. A typical events represented in the eta-phi plane is shown in Fig. 4.21. To guide the eye the contours of jets with $R_{cone}=0.3$, 0.5 and 1.0 are shown for the ALICE acceptance. However we would like to emphasize the fact that there is a possibility, using the event shapes, to identify painlessly events where the topology is much simpler than shown in Fig. 4.21.

4.3.1 Description of the procedure.

We have computed the shape variables at level generator and reconstruction. Note that in both cases MC simulations were used. The participants in the computations are primary charged particles ⁵ in the generation case, and tracks associated with primary particles in the reconstruction one. In both cases events are selected using the MB1[ea06] trigger criteria and we restrict the analysis for events with primary vertex in z direction: $|v_z| \leq 10$ cm.

⁵Primary particles are defined as particles produced in the collision, including products of strong and electromagnetic decays, but excluding feed-down products from strange weak decays and particles produced in secondary interactions. In the simulation these are the final state particles created by the event generator, which are then propagated (and decayed) by the subsequent detector simulation.

The requirements to perform the computation are:

1. Generation level:

Event level: the first step is for selecting hard events: $p_t^{leading} \geq 3$ GeV/c and $|\eta^{leading}| \leq 0.5$.

This requirement guarantees that the leading jets are contained within the ALICE acceptance with a $\Delta R_{cone} = \sqrt{\Delta\eta^2 + \Delta\phi^2} \leq 0.7$

Particle level: for primary charged particles in the acceptance: $|\eta| \leq 1$ and $p_t \geq 1.5$ GeV/c, the shape variables are computed. The cut in p_t eliminates the mostly soft underlying component.

2. Reconstruction level: In the present analysis we used tracks reconstructed by the TPC and ITS. The event cuts described above are applied.

Track level: tracks associated to primary particles in the acceptance: $|\eta| \leq 1$ and with $p_t \geq 1.5$ GeV/c. To select this class of tracks we applied the following cuts.

- (a) TPC refit.
- (b) At least 50 clusters in TPC.
- (c) Covariance matrix cuts.
- (d) Reject kink daughters.
- (e) Maximum DCA (in xy and z) to vertex 3 cm.

For more details see [GOE].

In Fig. 4.22 we show a picture of two classes of candidate events: di-jet and mono-jet (to separate these events we used their values of shape variables according with the discussion in the next paragraphs). For a given event we have taken the projection of the particles momentum in the transverse plane. It is well visible that the thrust axis is very close to the direction of the transverse momenta of the leading particle (particle with the highest p_t in the event).

The method starts by plotting a two-dimensional distribution (“thrust map”), with τ (one minus thrust) in the horizontal axis and r (recoil) in the vertical axis. This plot allows to identify different classes of events according with their location in the thrust map.

1. **Region A.** Suppose a di-jet event which occurs completely inside the ALICE acceptance ($|\eta| \leq 1$). In this case, we have in the transverse plane; the thrust axis (\vec{n}_t) almost collinear to the direction of the leading particle. So, the region A is characterized by events with small values of $1 - T$ and R , corresponding to di-jet events.
2. **Region B.** Events with only one jet in the acceptance of the detector will have small values of τ and due to the absence of vectorial cancellations in the numerator of the recoil term, these classes of events will have the biggest values R . So, the region B is populated by monojet events.

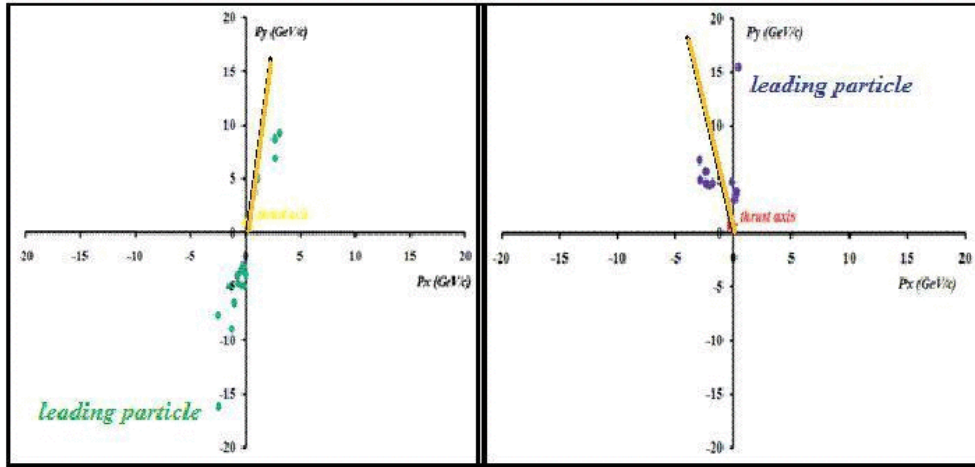


Figure 4.22: Illustration of the distribution of the momenta in the transverse plane for two classes of events. (left) Dijet event, (right) monojet event. In both cases the thrust axis is very close to the direction of the leading particle.

3. **Region C.** The most isotropic events (with high $1-T$ and small R) of the sample have to compensate the transverse momentum. This zone of the thrust map is characterized by the presence of multi-jet events.

The intermediate region between A and B is populated by the combination of mono-jets and “incomplete di-jets”; di-jets are incomplete due to their high R , many particles are outside of the acceptance.

The intermediate region between B and C is populated by events where 3 or more jets are emitted but at small angles with respect to the direction of the leading jet.

In the present note we will not deal with these cases which will be the subject of a special study at later time.

4.3.2 Results in simulated pp collisions at 10 TeV.

The present analysis uses the standard simulated samples staged on alice⁶. The production corresponds to PDC09, minimum bias simulations of proton-proton collisions at 10 TeV in the center of mass, the events were generated with PYTHIA. The simulation of the detector included a magnetic field of 0.5 T. The results were obtained through the analysis of 1,200,000 events. In figure 4.23 the thrust map is shown for generated (upper) and reconstructed (bottom) data. In both histograms two interesting regions are exhibited (A and

⁶The CERN Analysis Facilities for ALICE (alicecaf) is a cluster at CERN running PROOF (Parallel ROOT Facility) which allows interactive parallel analysis on a local cluster.

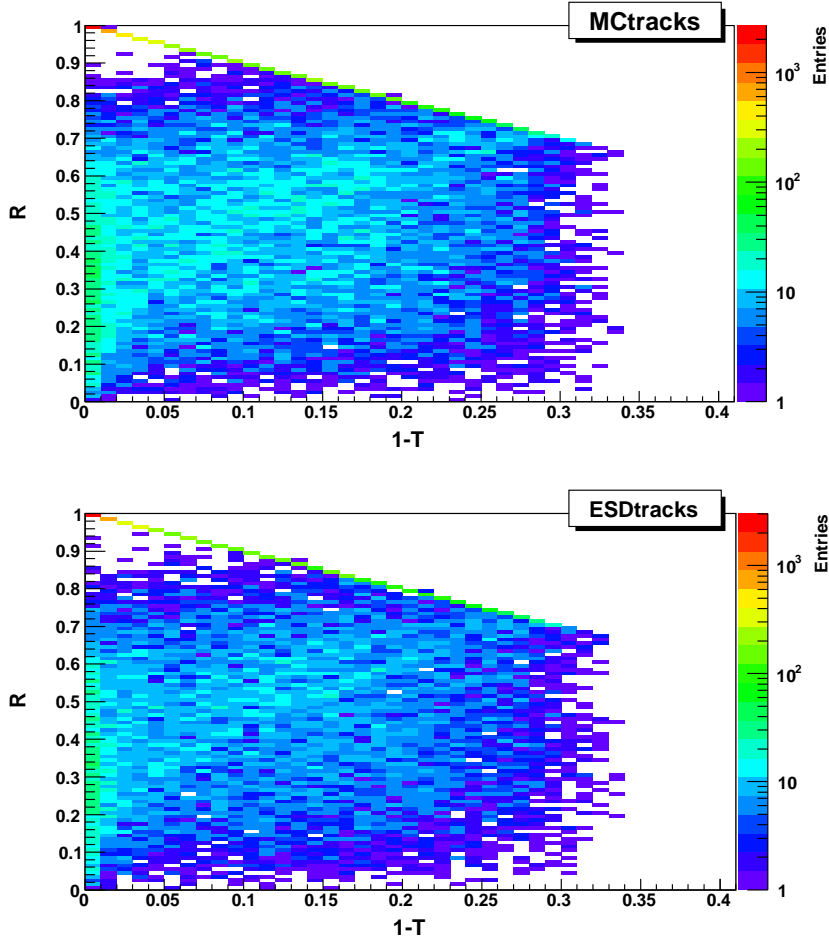


Figure 4.23: Thrust map: a) generator level (upper), in this case we use primary charged MC particles; and b) reconstruction level (bottom), in this case we used tracks associated to primaries from TPC+ITS information.

B regions described before). Note, that any exceptional event with an azimuthally uniform distribution would be immediately “detected” in the area: $\tau \geq 0.34$.

In Fig. 4.24 there is a plot which shows the correlation of the τ values computed from the generator information and from the reconstruction. Note that there is a small leakage of events with $\tau_{mc} \geq 0.03$ to the reconstructed zone associated to events with 2 back-to-back jet structure. This can be understood in terms of the reconstruction effects. For example a generated event with three primary charged particles ($p_t \geq 1.5$ GeV/c) distributed isotropically in the azimuth could be reconstructed as a event with a structure of two jets.

In Fig. 4.25, we show the analogous plot for the variable r .

For describing the topology of the events we performed an azimuthal correlation. The

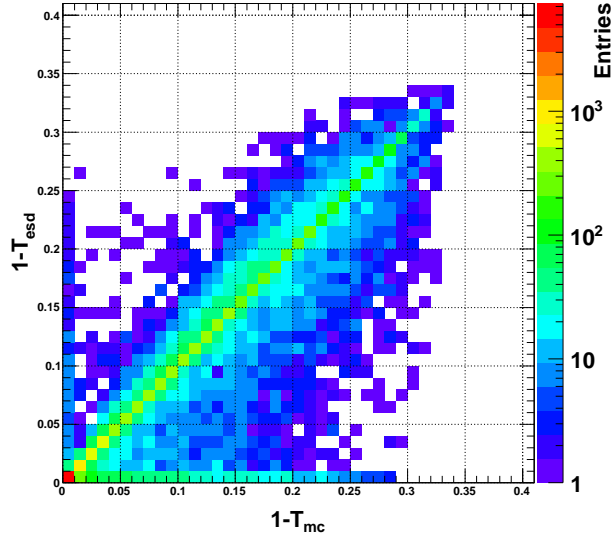


Figure 4.24: Correlation between the quantity τ computed from MC information and from TPC+ITS information.

idea is to select the leading particle, and apply a rotation placing it at $\pi/2$ rad. After that, we plot the azimuthal distribution of the associated particles with respect to the leading one. In the following our convention about the azimuthal correlation it will be referred as $\Delta\phi$ and it refers to: $\Delta(\phi - \pi/2)$.

If we concentrate ourselves to events in the region $\tau \leq 0.03$, and small $r \leq 0.35$ values. The azimuthal correlation of the Fig. 4.26 (right panel) shows that the width of the away side peak does not change if we modify the cut in the r range. This is in agreement with our assumption which suggests that r is important to select complete events in the acceptance. On the other hand, if we select events with small value of r ($r \leq 0.35$) and modify the range of τ (Fig. 4.26 (left panel)) there is a clear evolution in the structure of the away side peak. If we increase the value of τ the selected events include different configuration multijets (split jets) which are manifested in the azimuthal distribution behavior. This suggests that the cut $\tau \leq 0.03$ is almost equivalent to select particles inside a cone radii $R_c = \sqrt{(\Delta\phi)^2 + (\Delta\eta)^2} = 1$.

In the following we will concentrate on particular parts of the map, plotting the azimuthal correlations encountered.

The procedure is:

- Select events according to their values of shape variables as shown in table 4.2

The azimuthal correlations of events sited at different regions of the thrust map are plotted

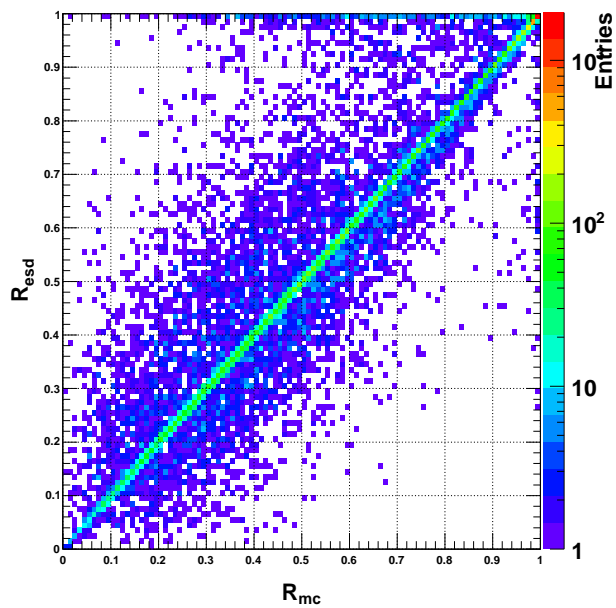


Figure 4.25: Correlation between the quantity r computed from MC information and from TPC+ITS information.

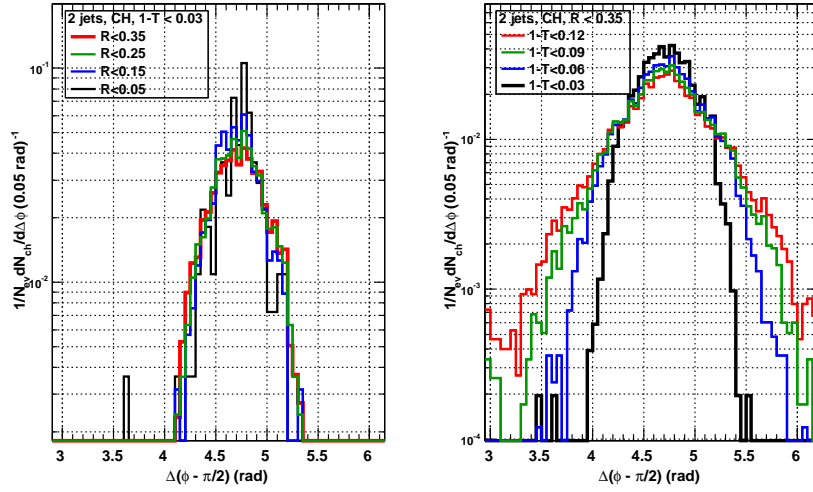


Figure 4.26: Sensitivity of the azimuthal correlation of the away side peak on the thrust variable range. Fixed τ interval and variation of the r range (right panel). Fixed r and modification of the range τ (left panel)

Region	Kind of event	Variables
A	Dijets	$r \leq 0.35, \tau \leq 0.03$
B	Monojets	$r \geq 0.9, \tau \leq 0.03$
C	Mercedes	$r \leq 0.4, \tau \geq 0.25$

Table 4.2: τ and r parameters used for the present analysis.

in Fig. 4.27. The evolution of the away peak (formed by particles with $\pi \leq \Delta\phi \leq 2\pi$) is interesting.

As predicted, the events of region B really have a monojet topology in the azimuth. One can see there are associated particles which go near to the leading particle (peak in the toward side: $0 \leq \Delta\phi \leq \pi$) but in the away side there is no corresponding jet. In contrast, for events of the region A the peak of the away side is located at $\Delta\phi \sim 3\pi/2$, so, in the transverse plane we have 2 back-to-back jets. In the case of the events of region C we found a multi-jet structure, in the green distribution we observe three peaks in the spectrum: the first (associated to the leading jet) at $\Delta\phi \sim \pi/2$ and the others at $\Delta\phi \sim 7\pi/6$ and $\Delta\phi \sim 11\pi/6$ respectively. The result bears some resemblance with the away side structure observed at RHIC e.g. PHENIX collaboration in heavy-ion collisions [eaPC08]. This observation brought us to study the presence of the same double hump structure at RHIC energies [ACD⁺09]

In Fig. 4.28 we show for the different regions of the thrust map, a two-dimensional

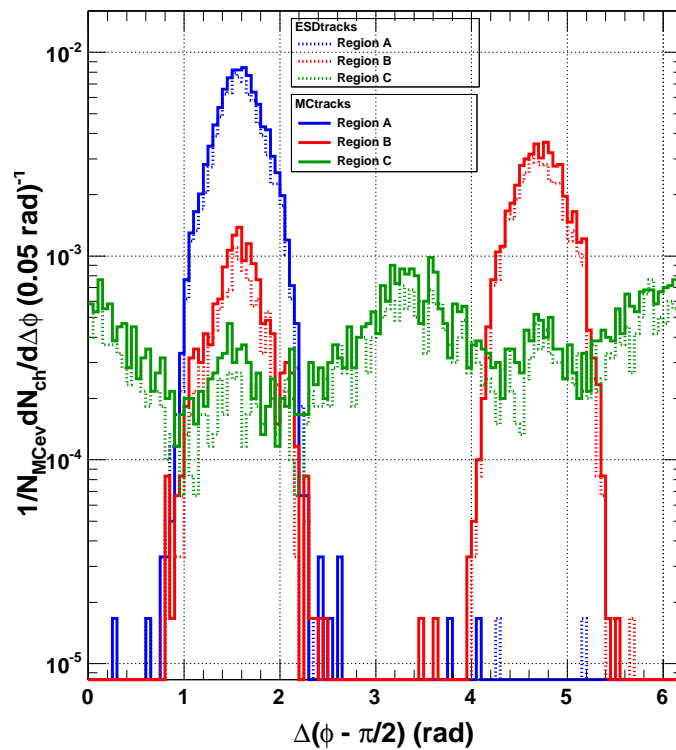


Figure 4.27: Azimuthal correlation for particles with $p_t \geq 1.5$ GeV/c: dijets (red-region A), monojets (blue-region B) and the mercedes events (green-region C). True spectrum (solid line), measured spectrum (dotted line). The leading particle is not shown.

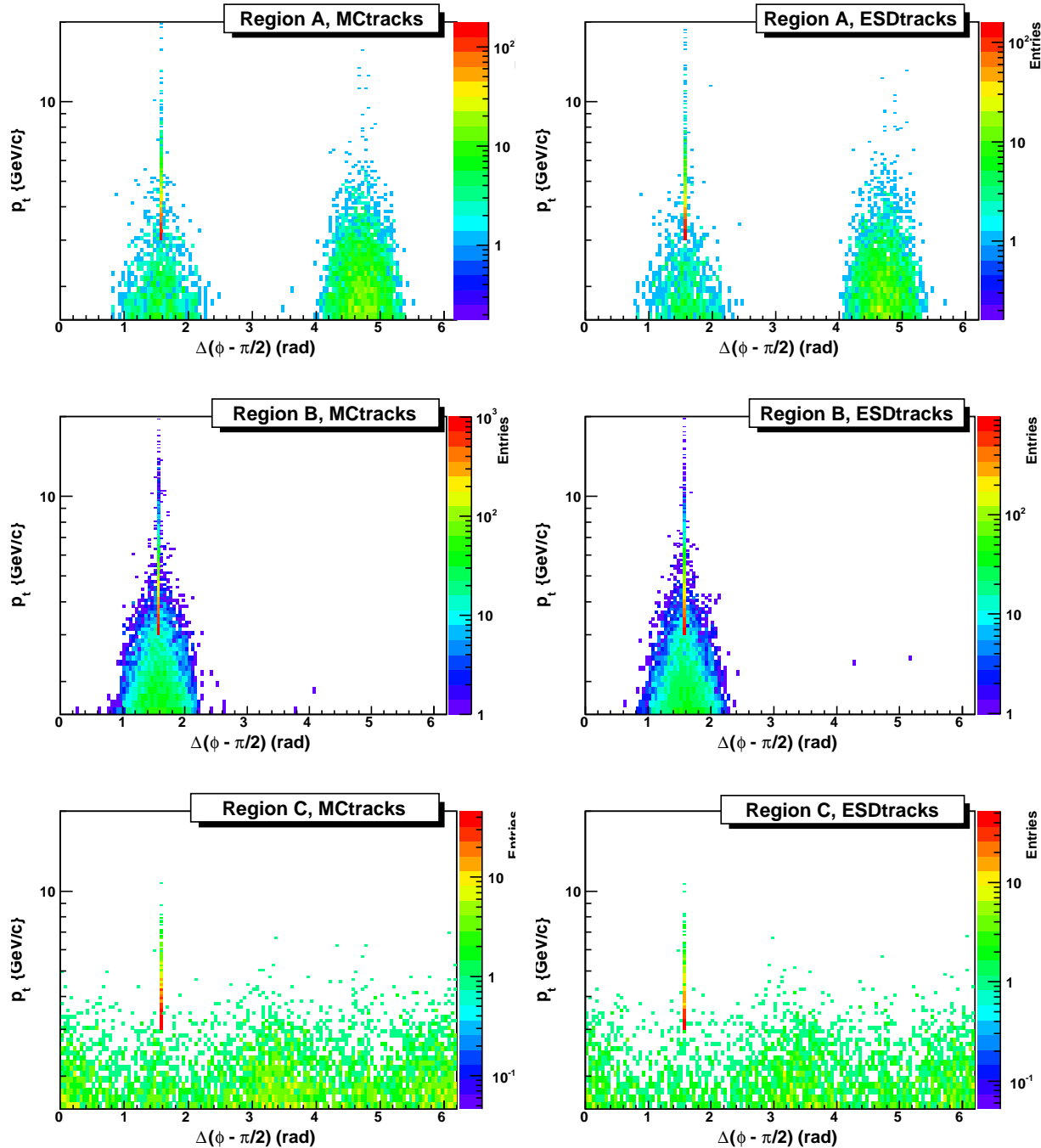


Figure 4.28: Transverse momentum vs. $\Delta(\phi - \pi/2)$ for the associated particles: dijets (top), monojets (middle) and the mercedes events (bottom). True distribution (left plots), measured distribution (right plots). The leading particle is shown, and you can note the cut $p_t \geq 1.5$ GeV/c which we imposed.

distribution: p_t vs. $\Delta\phi$ for the associated particles.

The table 4.3 shows a summary of the analyzed events.

Event	MCtracks	ESDtracks	Efficiency	τ (τ) cuts	r cuts
With T	28920	24960	86%	no	no
Dijet	1503	1316	67%	$\tau \leq 0.03$	$r \leq 0.35$
Monojet	8903	8329	79%	$\tau \leq 0.03$	$r \geq 0.9$
Mercedes	523	439	62%	$\tau \geq 0.25$	$r \leq 0.4$

Table 4.3: Number of events with particular topologies in the analyzed sample of 1.2 million of events.

The efficiency represents the number of reconstructed events of given topology with respect to the generated events.

One observes a $\sim 70\%$ efficiency with respect to the MC. This may indicate that due to reconstruction and/or absorption of particles one relocates events in other parts of the thrust map as shown in Figs. 4.24-4.25.

Note that, out of the 1200000 events only 2.4% (with given T) of them pass the cuts imposed (at least 1 particle with $p_t \geq 3$ GeV/c and $|\eta^{leading}| \leq 0.5$). The dijets in acceptance reach about $\sim 0.125\%$ of the total, and about 0.04% belong to mercedes event types. About 37.8% of the accepted events belong to clearly identifiable categories, while the others correspond to events with multi-jets closer to the leading jet.

In the next section we will study each one of the topologies selected. That study includes a visualization of the events through the use of the tools of AliRoot.⁷

Dijets and monojets

In the present section we are investigating the p_t spectra and the multiplicities of the jets in various configurations. As a first step we turn to the visualization tool of events in ALICE. We selected events located in the region A and scanned them. Due to their small r values, they should be inside the acceptance. Fig. 4.29 shows the visualization of one of them. This particular event has $r = 0.00132$ and $\tau = 0.0000896$. The lines are primary monte carlo tracks with $p_t \geq 0.5$ GeV/c. The figure clearly shows the whole event contained inside the TPC.

Looking at more events shows always the same structure in the visualization.

Further we computed the total transverse momenta in each jet (here we used all events of the region A). In order to do it, we divided the event into two parts: toward and away. The

⁷AliRoot is the name of ALICE Off-line framework for simulation, reconstruction and analysis. It uses the ROOT system as a foundation on which the framework and all applications are built.

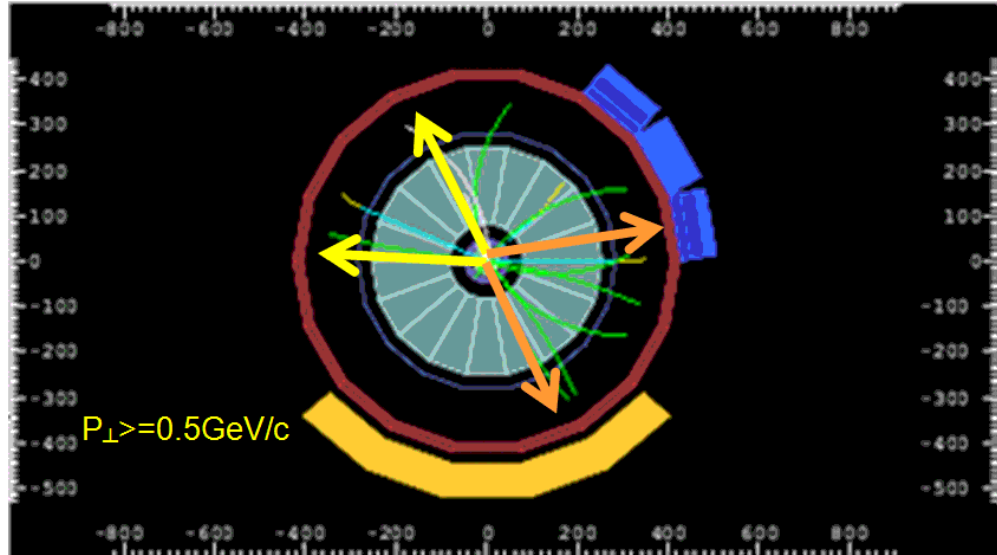


Figure 4.29: Visualization of one dijet event from the region A. The lines are primary Monte Carlo tracks with $p_t \geq 0.5$ GeV/c. The superimposed arrows separate each jet for a better visualization.

first (near side) contains the leading particle and it is formed by all particles in the interval: $\pi/4 \text{ rad} \leq \Delta\phi \leq 3\pi/4 \text{ rad}$. The away side is formed by particles in the interval: $5\pi/4 \text{ rad} \leq \Delta\phi \leq 7\pi/4$.

Fig. 4.30 shows the distribution of the transverse momentum spectrum of each jet (sum in each azimuthal region of the transverse momentum of all the participants with $p_t \geq 0.3$ GeV/c) for generation and reconstruction. The away side distribution is left shifted ~ 1 GeV/c with respect to the near side one. This can be understood in terms of the fluctuation of the neutral component of the associated jet and also as effects from the acceptance in the associated jet. In order to illustrate this arguments we plotted the distribution of the ratio: total transverse momenta in the “toward” side over the total transverse momenta in the “away” side for the generation case. Fig. 4.31 (right panel) shows the behavior of such distribution (red line). The distribution manifest a clear peak at 1, this fact is in agreement with our assumption about the dijet structure. However the distribution shows many events where the near side jet represent up to 5 times the energy of the away side jet. In this respect the role of the value r is important, because as you can see the width of the distribution decreases as the r interval is decreased. The same analysis can be performed including the neutral component (left panel). The away side jets with a low transverse momentum correspond to events where the away jet is not completely contained.

We checked also the multiplicity distributions for the dijets events. In Fig. 4.32, we show the multiplicity distribution for the away and toward sides.

A mono-jet event taken from region B of the ESA map is shown in Fig. 4.33.

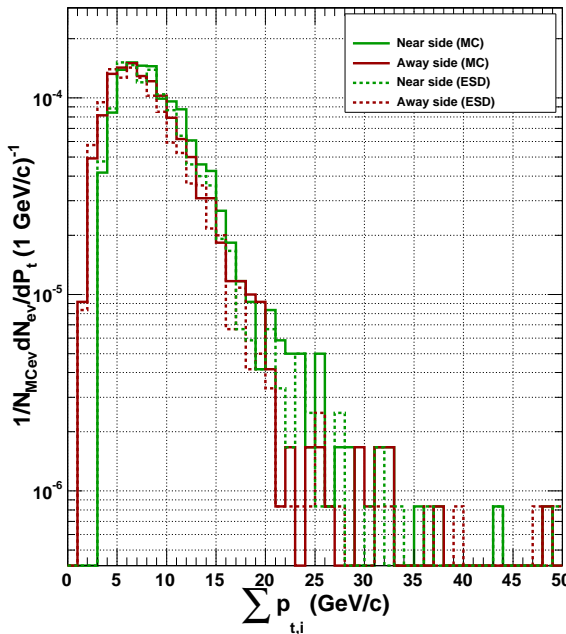


Figure 4.30: Distribution of the sum of the transverse momenta of particles with $p_t > 0.3$ GeV/c in the toward and away regions for dijet events. The toward region (black, leading jet) is formed by primary charged particles in the azimuthal range: $\pi/4 \text{ rad} \leq \Delta\phi \leq 3\pi/4 \text{ rad}$ while the away region (red line) corresponds to particles with: $5\pi/4 \text{ rad} \leq \Delta\phi \leq 7\pi/4 \text{ rad}$. The plot shows two cases: reconstruction (dotted line) and generation (solid line).

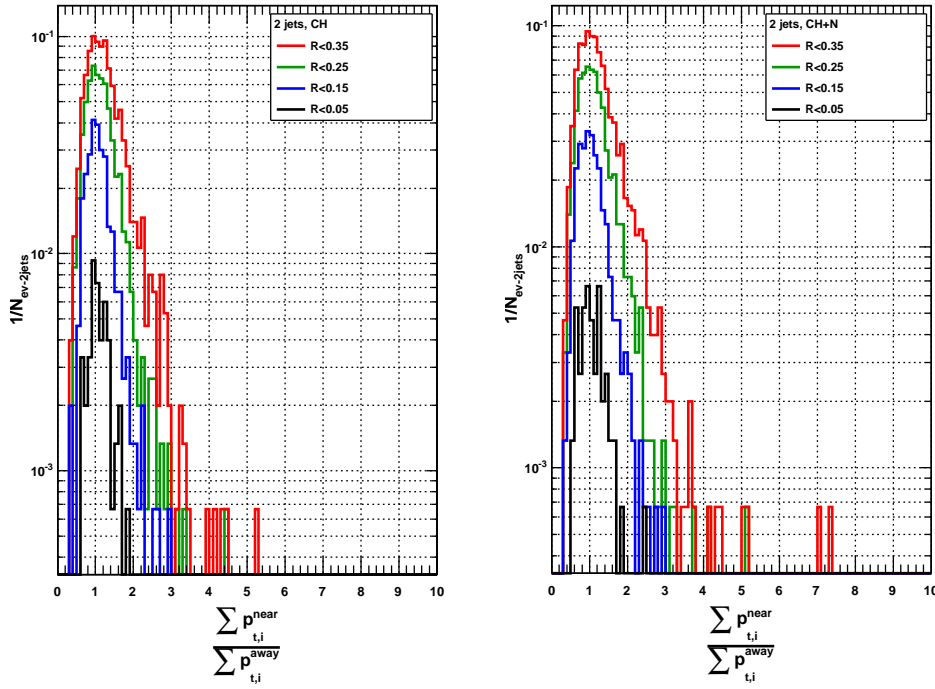


Figure 4.31: Ratio of the transverse momenta of the toward jet over transverse momenta of the away jet as a function of r for dijet events. The participants have $p_t \geq 0.3$ GeV/c. The near side corresponds to the azimuthal range: $\pi/4 \text{ rad} \leq \Delta\phi \leq 3\pi/4 \text{ rad}$. For the away side: $5\pi/4 \text{ rad} \leq \Delta\phi \leq 7\pi/4$. Charged component (right), (left) including the neutral component.

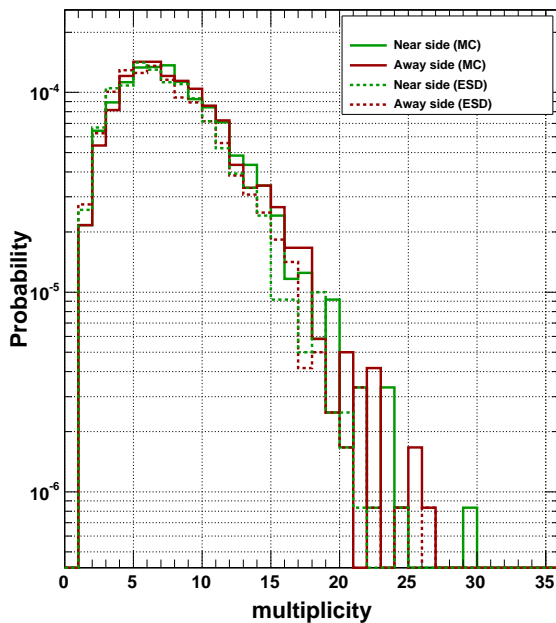


Figure 4.32: Multiplicity distribution of particles with transverse momenta: $p_t > 0.3$ GeV/c for dijet events. The particles belonging to the leading jet (black line) consist of primary charged particles in the azimuthal range: $\pi/4 \text{ rad} \leq \Delta\phi \leq 3\pi/4 \text{ rad}$. The away side (red line) corresponds to particles with: $5\pi/4 \text{ rad} \leq \Delta\phi \leq 7\pi/4 \text{ rad}$. The plot shows two cases: reconstruction (dotted line) and generation (solid line).

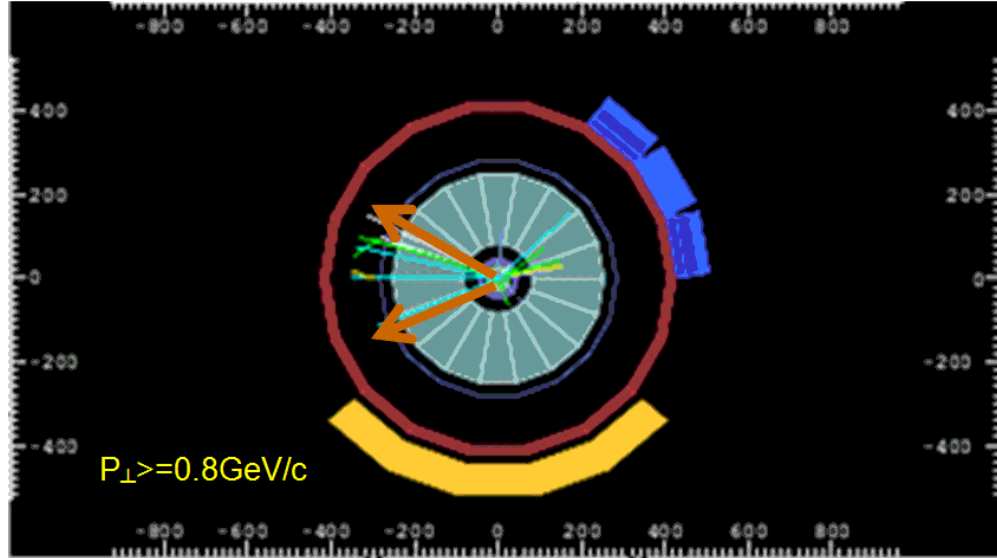


Figure 4.33: Visualization of a mono-jet event. The lines are mctracks with $p_t \geq 0.8 \text{ GeV}/c$. The arrows contain the particles associated with the jet.

The lines correspond to mctracks with $p_T \geq 0.8 \text{ GeV}/c$. For this event: $\tau = 0.00216$ and $r = 0.99874$. Again, by counting primary charged particles within the azimuthal range: $\pi/4 \text{ rad} \leq \Delta\phi \leq 3\pi/4 \text{ rad}$, we estimate the total transverse momentum of the jet. In Fig. 4.34, is the distribution of the total transverse momenta for events of region B. Note that the peak of this distribution is at $\sim 6 \text{ GeV}/c$, in the case of di-jet events this peak is also located at $\sim 6 \text{ GeV}/c$.

The multiplicity distribution for mono-jet events is in Fig. 4.35.

The conclusion of this part of the analysis is, that according with the results of the visualization and the behavior of the multiplicity and transverse momentum spectra ESA works fine for discriminating the di-jet events from the mono-jet ones. Using the event shape analysis the signals can be cleaned in order to improve the jet studies.

Multi-jet events

The green distributions of Fig. 4.27 allows to observe a double hump structure in the away side of the azimuthal distribution. They look like if the three particles with the highest p_t in each event were distributed in the transverse plane according to: the leading particle at $\pi/2$ radians, and the others at: $7\pi/6$ radians and $11\pi/6$ radians, respectively.

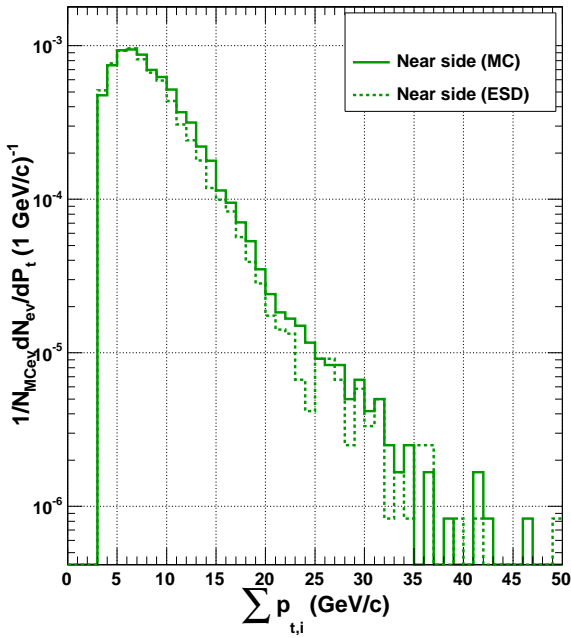


Figure 4.34: The distribution of the total charged transverse momenta of the identified mono-jets. The particles which were counted are within the azimuthal range: $\pi/4 \text{ rad} \leq \Delta\phi \leq 3\pi/4 \text{ rad}$; and they have: $p_t > 0.3 \text{ GeV}/c$. The generated (solid line) and the reconstructed (dotted line) are shown.

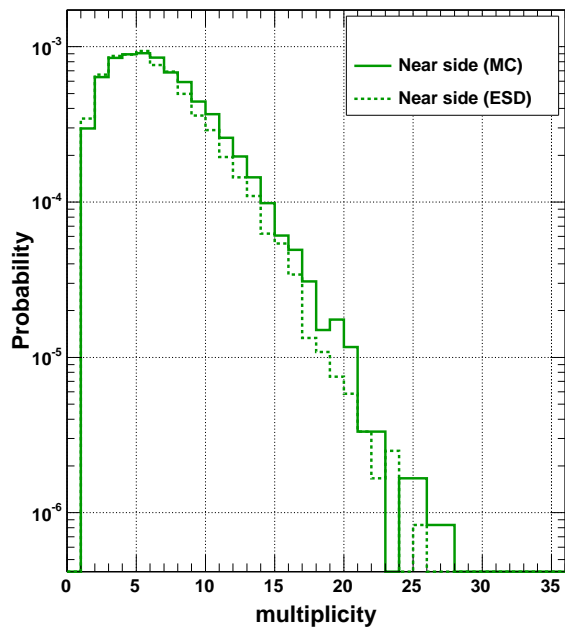


Figure 4.35: Multiplicity of primary charged particles ($p_t > 0.3$ GeV/c) of mono-jet events. The azimuthal range is: $\pi/4 \text{ rad} \leq \Delta\phi \leq 3\pi/4 \text{ rad}$. The results of generation (solid line) and the reconstruction (dotted line) are compared.

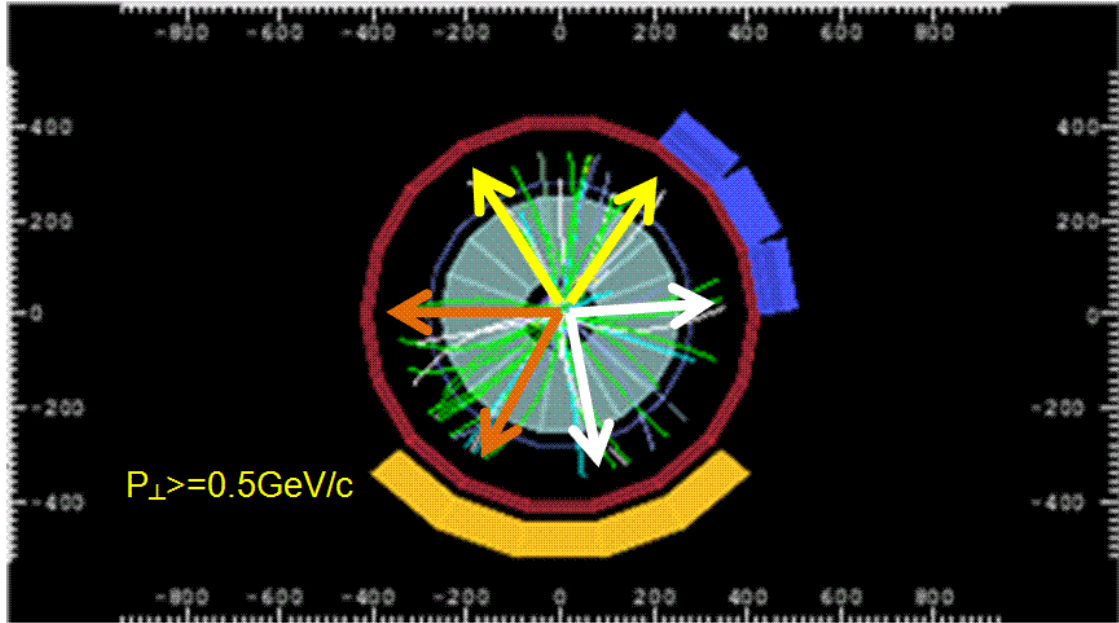


Figure 4.36: Scan of one event of region C. Particles which appear in the picture have: $p_t \geq 0.5 \text{ GeV}/c$.

There are many configurations of isotropic distributions that could lead to high τ values, however the scans of the events as shown in Fig. 4.36 for a typical event result in a clear three jets configurations. A small contribution from events with more than 3 jets can be found.

It is important to say that this class of events occurs completely inside the acceptance of our detector, we have to remind that this is controlled by the term r . For example, if we increase the range of r , the azimuthal distribution in the away side shows a shift of the two peaks because the calculation of the variables use incomplete information of the event.

In order to see the conservation of the transverse momentum in this class of events, we divided the azimuth into three regions:

Near side: formed by particles in the azimuthal range: $\pi/4 \text{ rad} \leq \Delta\phi \leq 3\pi/4 \text{ rad}$.

Away side: formed by the particles in the remainder of the azimuth.

As in the previous cases we have taken into account only primary charged particles with $p_t > 0.3 \text{ GeV}/c$. Fig. 4.37 shows the transverse momentum of each side. The agreement between both spectra is reasonable in the limits of the statistics.

We compute also event by event the ratio of the transverse momenta of the toward jet over the vectorial sum of the away jets as a function of r . The result of this analysis is shown in Fig. 4.38. Again these distributions reach their peaks at 1, suggesting the correct transverse momentum conservation.

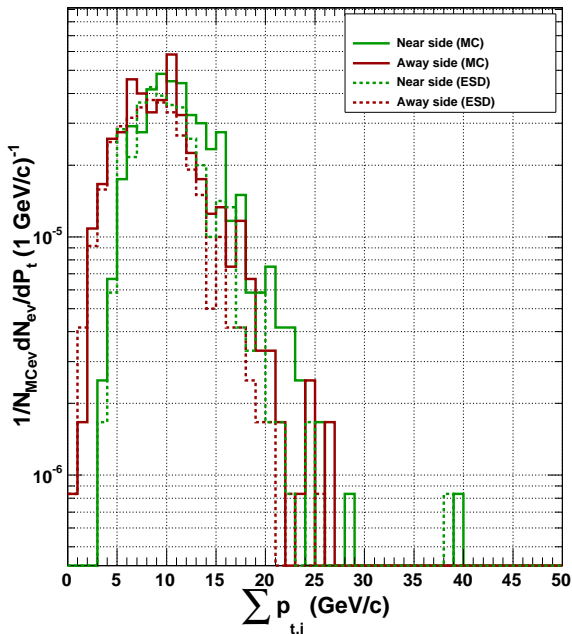


Figure 4.37: Transverse momentum spectra for three-jet events, the including charged particles with $p_t > 0.3$ GeV/c. Toward side (black line) corresponds to particles in the azimuthal region: $\pi/4 \text{ rad} \leq \Delta\phi \leq 3\pi/4 \text{ rad}$. Away side formed by particles in the remainder azimuth. The results at generator level (solid line) and reconstruction (dotted line) are shown.

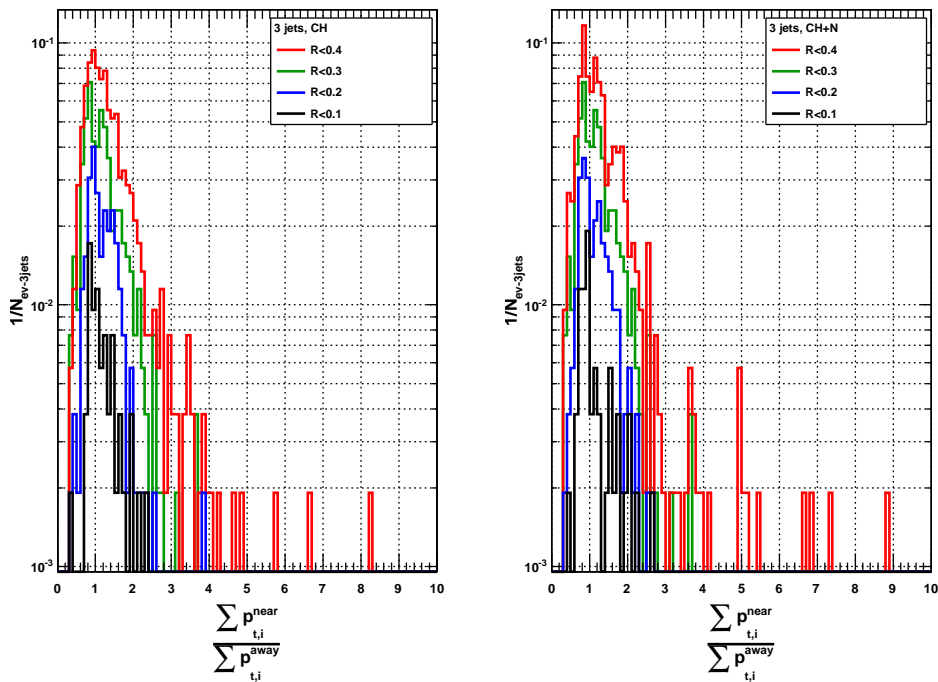


Figure 4.38: Mercedes events. Ratio of transverse momentum distributions of toward jet over transverse momenta of the away jets. The $\Delta\phi$ ranges used are the same as in the previous figure.

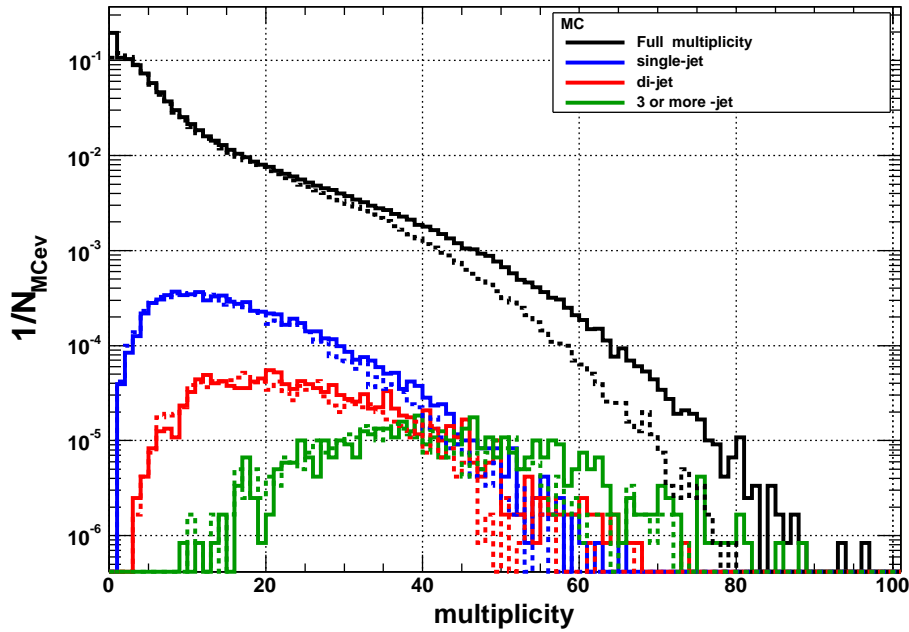


Figure 4.39: Multiplicity (charged particles with $p_t > 0.3$ GeV/c) distribution. In black is the full true spectrum. The different colored distributions correspond to the three classes of topologies which we discriminated using ESA.

The events with mercedes topology were found in MB simulation at 10 TeV in the c. m. as well as in MB simulations at 200 GeV [ACD⁺09].

Multiplicity in the context of ESA.

In this section we investigate the multiplicity of each event which we selected. In order to do this task we plotted the multiplicity spectra of the full sample (1 200 000 events), and we compared it with the multiplicities of the events with a given thrust value. The multiplicity is the number of primary charged particles in the acceptance $|\eta| \leq 1$ with $p_t > 0.3$ GeV/c. As we can see in the plots of Fig. 4.39, the conditions which we demanded to each event reduces the number of low multiplicity events. The events with are not related with any of the classes we studied belong to multi-jet events, and also are of high multiplicity. We observe that the mercedes events are generally of large multiplicities.

Chapter 5

Technical details of the analysis

The previous chapters were dedicated to the general considerations about the event structure variables and their sensitivity to the generator parameters. Now, we describe the technical details that were developed to measure one event shape variable, the transverse sphericity. The observable was linearized to guarantee it to be collinear safe and it was measured in the plane perpendicular to the beam direction using primary charged tracks. As well we will present the different corrections applied to the physical observables in function of the multiplicity.

5.1 Linearization of the transverse sphericity

The goal is to measure the transverse sphericity. As it was discussed in the previous chapter, at hadron colliders the event shapes are restricted to the transverse plane in order to avoid the bias from boost along the beam axis [ea04a]. The transverse sphericity is commonly defined in terms of the eigenvalues: $\lambda_1 > \lambda_2$ of the transverse momentum tensor:

$$\mathbf{S}_{xy}^Q = \sum_i \begin{pmatrix} p_{xi}^2 & p_{xi}p_{yi} \\ p_{xi}p_{yi} & p_{yi}^2 \end{pmatrix}$$

where $\vec{p}_{Ti} = (p_{xi}, p_{yi})$ is the transverse momentum of the particle i in a given acceptance, the transverse sphericity is defined as:

$$S_T \equiv \frac{2\lambda_2}{\lambda_2 + \lambda_1} \tag{5.1}$$

Since \mathbf{S}_{xy}^Q is quadratic in particle momenta, this sphericity is a non-collinear safe quantity in QCD perturbation theory. For instance, if a hard momentum along the x direction splits into two equal collinear momenta, then their combined contribution to $\sum_i p_{xi}^2$ will be half that of the original momentum. Therefore collinear splittings change the sphericity. To avoid this divergence, the transverse momentum tensor can be linearized as follows:

$$\mathbf{S}_{\mathbf{xy}}^{\mathbf{L}} = \frac{1}{\sum_i p_{Ti}} \sum_i \frac{1}{p_{Ti}} \begin{pmatrix} {p_{xi}}^2 & p_{xi}p_{yi} \\ p_{xi}p_{yi} & {p_{yi}}^2 \end{pmatrix}$$

And we can define a linearized sphericity as in 5.1. In both cases, the limits of the transverse sphericity are:

$$S_{\perp} = \begin{cases} = 0 & \text{"pencil-like" limit} \\ = 1 & \text{"isotropic" limit} \end{cases}$$

5.2 Event and Track Selection.

The selection of the events consists in the implementation of the following criteria:

- Off-line physics selection with background rejection. It guarantees the selection of physics collisions. In the next section it is discussed in detail.
- The reconstructed vertex along the beam axis must be in $|v_z| \leq 10$ cm.
- The pile up rejection is done through the identification of those events having more than one primary vertex reconstructed by the ITS.
- More than two primary particles with transverse momentum above 500 MeV/c in $|\eta| < 0.8$ [COP].

The events satisfying the above requirements conform the so-called “**bulk**” sample.

The observables are measured using global tracks. To guarantee the quality of the tracks, the following cuts were applied:

- At least 70 reconstructed points (clusters) in the TPC.
- The value of the χ^2 per TPC cluster used for the momentum fit must be less than 4.
- Rejection of kink daughters.
- We require a refit on TPC and ITS.

To select tracks from primaries the distance of closest approach of the tracks with respect to the reconstructed primary vertex in the plane perpendicular to the beam axis, d_0 , must satisfies $d_0 \leq 7(0.0350 + \frac{0.0420}{p_T^{0.9}})$ (p_T in GeV/c). It is tuned to select primary charged particles with high efficiency and to minimize the contributions from weak decays, conversions and secondary hadronic interactions in the detector material.

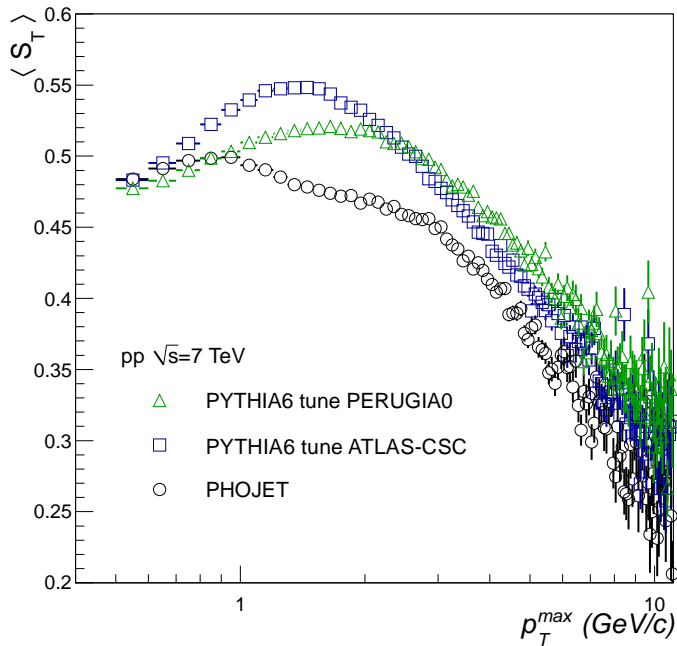


Figure 5.1: Mean transverse sphericity versus p_T^{\max} (of each event) for MC simulations at $\sqrt{s} = 7$ TeV. Results for PYTHIA6 (tunes ATLAS-CSC and PERUGIA-0) and PHOJET simulations are displayed, the events have more than 2 primary charged particles in $|\eta| \leq 0.8$ and transverse momentum above 0.5 GeV/c .

5.3 Separation in “soft” and “hard” events

We present the analysis for two categories of events defined by the maximum transverse momentum in each event. This method has been used often in an attempt to characterize events by separating the different modes of production. It aims to divide the sample into “soft” and “hard” events. Different experiments have shown marked differences between the two regimes [Col02b, Hua]. Fig. 5.1 shows the mean transverse sphericity *vs.* maximum p_T of the event. The plots were obtained from minimum bias simulations at $\sqrt{s} = 7$ TeV and following the cuts at particle and event level previously discussed. Note that PYTHIA6 simulations [Sjo94] (tunes: ATLAS-CSC [Mor] and PERUGIA-0 [Ska]) exhibit a maximum on $\langle S_T \rangle$ around 1.5-2.0 GeV/c . On the other hand, PHOJET [Eng95] shows an intermediate transition slope in $p_T^{\max} = 1 - 3$ GeV/c . This behavior on $\langle S_T \rangle$ motivated us to do the following separation cut. The “soft” events are defined as events that do not have a track above 2 GeV/c , while the “hard” events are all the others. Throughout the present work we will keep this distinction between “hard” and “soft” events and will also show the aggregate of both classes called “bulk”.

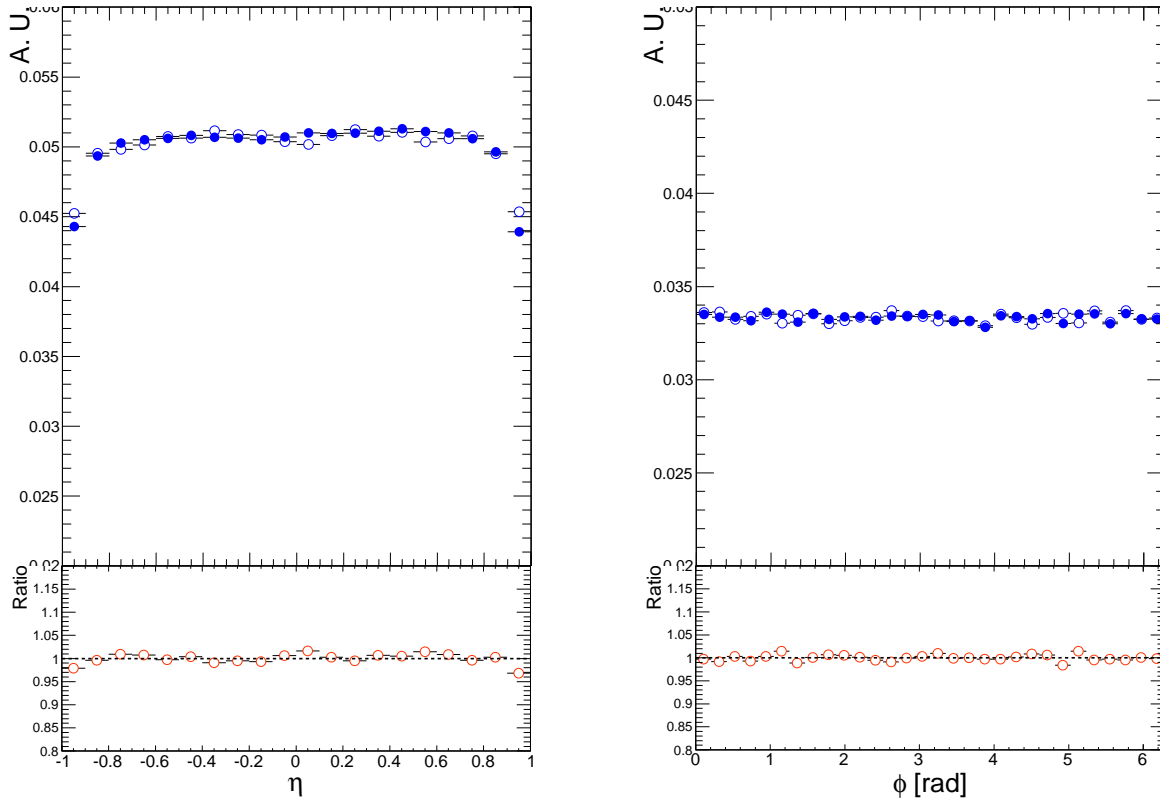


Figure 5.2: Pseudorapidity (left) and azimuthal distributions of TPC tracks: MC (empty points), real data (full points). Each plot show the nice agreement between data and MC.

5.4 Multiplicity estimator

The multiplicity estimator takes into account all primary tracks in the acceptance $|\eta| < 0.8$ and having $p_T \geq 0.5$ GeV/c. The correction of the multiplicity uses MC simulations which include the generation and the transport of the particles through the detector. So, the correct simulation of the ALICE detectors is crucial because on it depends the quality of the final results. To illustrate the good understanding of the TPC, Fig. 5.2 shows the pseudorapidity and azimuthal distributions of TPC tracks. The measured tracks are compared with MC tracks.

In this work, different MC productions were tested, all produce very similar results with negligible discrepancies ($< 1\%$). Fig. 5.3 shows the correlation between the true and reconstructed multiplicity. In this context, the adjective “true” means that the observable was computed using the MC primary charged particles¹ before the transport, *i. e.* at “generator”

¹Primary particles are defined as particles produced in the collision, including products of strong and electromagnetic decays, but excluding feed-down products from strange weak decays and particles produced in secondary interactions. In the simulation these are the final state particles created by the event generator,

level. The reconstructed observable is computed using the reconstructed tracks. From this distribution we get the response matrix, $R(N_t, N_m)$, which is the mathematical object which transforms the reconstructed observable into the true one. Fig. 5.3 displays the multiplicity response matrix obtained using PYTHIA6 for the generation of events.

To reach high multiplicity values the events were produced using PYTHIA6, tune ATLAS-CSC, MB proton-proton collisions at 7 TeV with flat multiplicity.

5.5 Correction of $\langle S_T \rangle$ vs N_{ch}

The correction of the mean sphericity as a function of multiplicity requires the unfolding² of the sphericity spectra in bins of measured multiplicity. The analysis flow goes as follows:

1. Correct the sphericity spectra in bins of measured multiplicity

The unfolding consists in the minimization of the function [GO09]:

$$\chi^2(U) = \sum_m \left(\frac{M_m - \sum_t R_{mt} U_t}{e_m} \right)^2 + \beta P(U) \quad (5.4)$$

which are then propagated (and decayed) by the subsequent detector simulation.

What is the unfolding?

One of the goals of experimental physics is to measure distributions $f(x)$ of a given physical variable x . In the experiment, the measured distribution $\hat{f}(x)$ differs from the true distribution $f(x)$ by statistical errors $\epsilon(x)$.

In high energy physics experiments often the variable x and its distribution can not be measured directly due to limited acceptance and resolution in the detector. So, instead of the variable x , a variable y and its distribution $g(y)$ are measured. In fact, for a one-dimensional variable x the variable y can be multidimensional.

For instance, if the distributions $f(x)$ ($a \leq x \leq b$) and $g(y)$ are related by the convolution integral:

$$g(y) = \int_a^b R(y, x) f(x) dx \quad (5.2)$$

where the function $R(y, x)$ describes the response of the detector including the transformation x to y . Actually, the measured distribution $\hat{g}(y)$ differs from the expected $g(y)$ by statistical errors $\epsilon(y)$.

$$\hat{g}(y) = g(y) + \epsilon(y) \quad (5.3)$$

So, an accurate determination of the response function R is essential for any meaningful analysis of the data. In practice it is determined using the full simulation of the detector including the interaction of the radiation with the matter.

The reconstruction of $f(x)$ from the measured distribution $\hat{g}(y)$ is called **unfolding**, and it is a statistical estimation problem [Blo].

Note that if the variables x and y are discrete variables then the integral of 5.2 must be replaced by a sum. Then the function $R(y, x)$ becomes the response matrix $R(y, x)$ of the detector.

So, the unfolding is the key to compare the measurements with theoretical models.

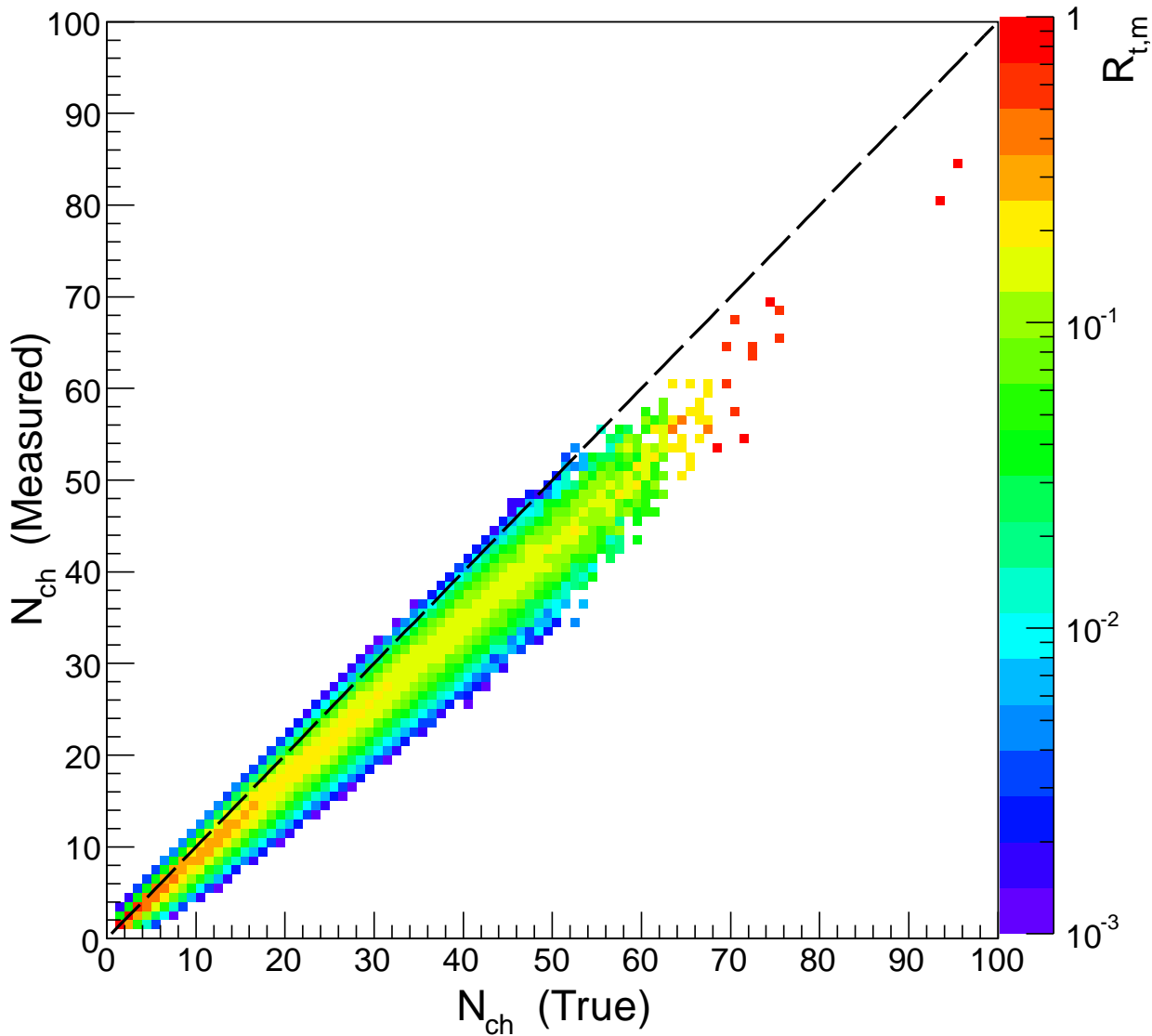


Figure 5.3: Multiplicity response matrix. Particles and tracks in $|\eta| \leq 0.8$ and $p_T \geq 0.5$ GeV/c are considered. The events were produced using PYTHIA6 tune ATLAS-CSC, pp minimum bias collisions at 7 TeV with flat multiplicity.

where M is the measured spectrum with error in the measurement e_m ; R_{mt} is the response matrix; U the guessed spectrum. To prevent the fluctuating solutions we add a regularization term $P(U)$ weighted by the parameter β . Different regularization functions and weights were tested [COP], our final election was to use a linear function and $\beta = 10^3$.

2. **Correct by the multiplicity** The result of the first step is $\langle S_T \rangle(N_m)$, now we follow the approach used in [KAea10c] to correct the multiplicity:

$$\langle S_T \rangle(N_t) = \sum_m \langle S_T \rangle^{\text{unf}}(N_m) R(N_t, N_m) \quad (5.5)$$

5.5.1 Extrapolation of the sphericity response matrices

The deconvolution of the sphericity spectra demands the knowledge of the respective response matrices at high multiplicity. With our available MC statistics we ignored the behavior of the observable at relative high multiplicity. Fig. 5.4 shows the response matrix for measured multiplicity = 42. In the picture, the third dimension is the number of entries, it is clear that the statistics is poor especially in the first bin of sphericity.

The first step is to understand the evolution of the sphericity resolution with multiplicity. The resolution is just the normalized distribution of the measured observable at a given true sphericity. The range of sphericity was divided in 20 bins, so, the bin size was 0.05. Fig. 5.5 displays the resolution at true sphericity = 0.075, and for measured multiplicities from 15 up to 34. Note the poorness of statistics at low S_T .

The situation becomes better for higher sphericities, for example Figs. 5.6 and 5.7 illustrate the cases $S_T = 0.525$ and 0.975 , respectively.

The distributions were fitted to a gaussian function, the quality of the fit is quantified through the factor $\chi^2/n.d.f.$, where $n.d.f.$ is the number of degrees of freedom, as an example, Fig. 5.8 shows the quality of the fit as a function of multiplicity for $S_T = 0.525 \pm 0.025$. Note that the quality of the fit is improved for high multiplicity.

Fig. 5.9 shows the sigma of the fit as a function of multiplicity for different bins of true sphericity: 0.075, 0.525 and 0.975. Each plot was fitted to a exponential function in order to extrapolate the values for larger multiplicities, the quality is quite good because as you can see $\chi^2/n.d.f. < 1$. The mean of the distribution versus multiplicity is plotted in Fig. 5.10 where the same bins of true sphericity are shown as well.

Almost we have all the available information to build the response matrices at high multiplicity. To cope the problem of statistics poorness at low S_T , the sigma of the resolution it was interpolated to $S_T = 0$. Fig. 5.11 displays the mean and the sigma of the sphericity resolution as a function of true sphericity at measured multiplicity 35. The mean shows a nice linear correlation with the true sphericity. In the case of sigma, the first two bins clearly are outliers, this is due to the statistics lacking in those bins, however, the next points show

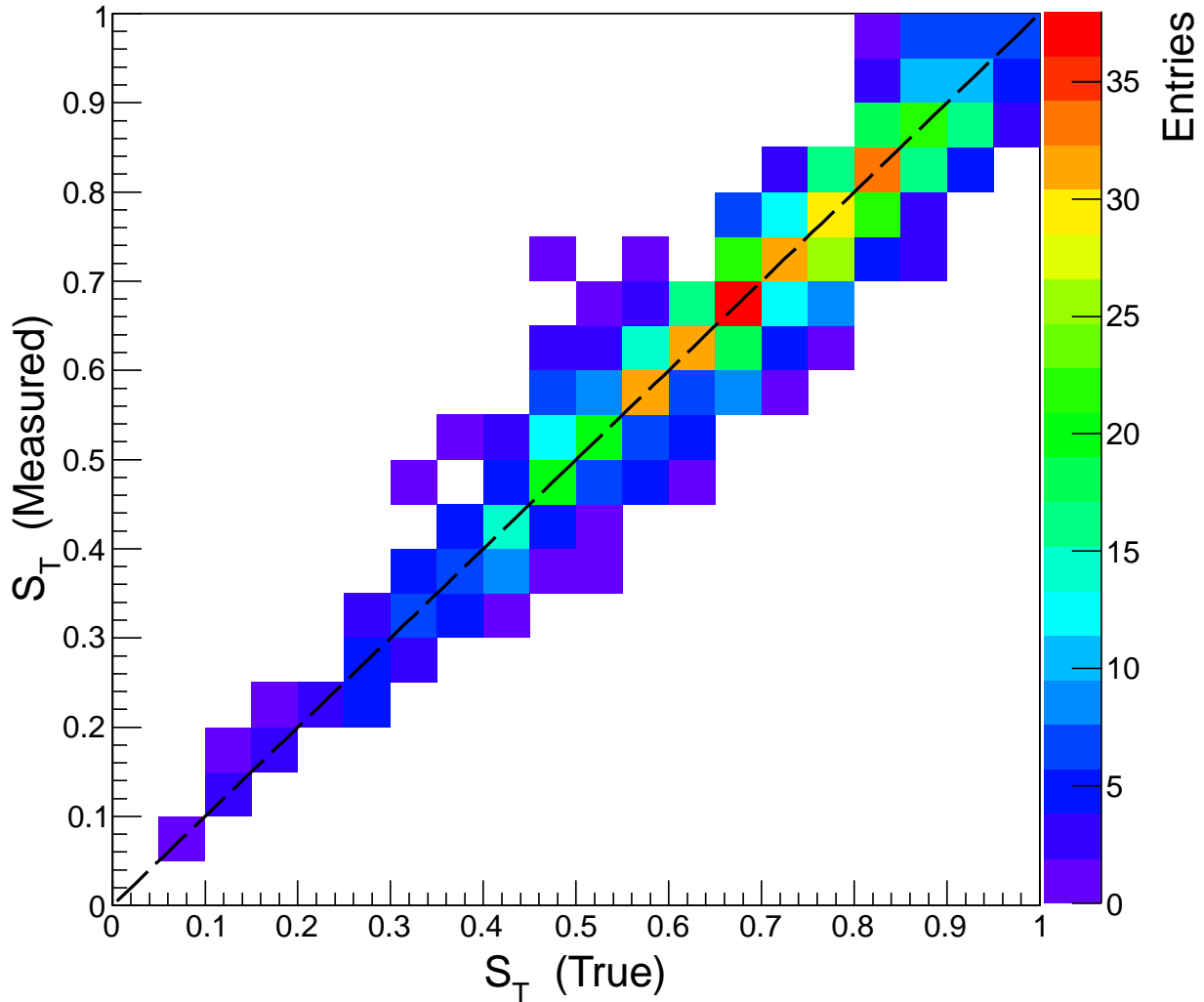


Figure 5.4: Sphericity response matrix. Particles and tracks in $|\eta| \leq 0.8$ and $p_T \geq 0.5$ GeV/c are considered. The events were produced using PYTHIA6 tune ATLAS-CSC, pp minimum bias collisions at 7 TeV with flat multiplicity.

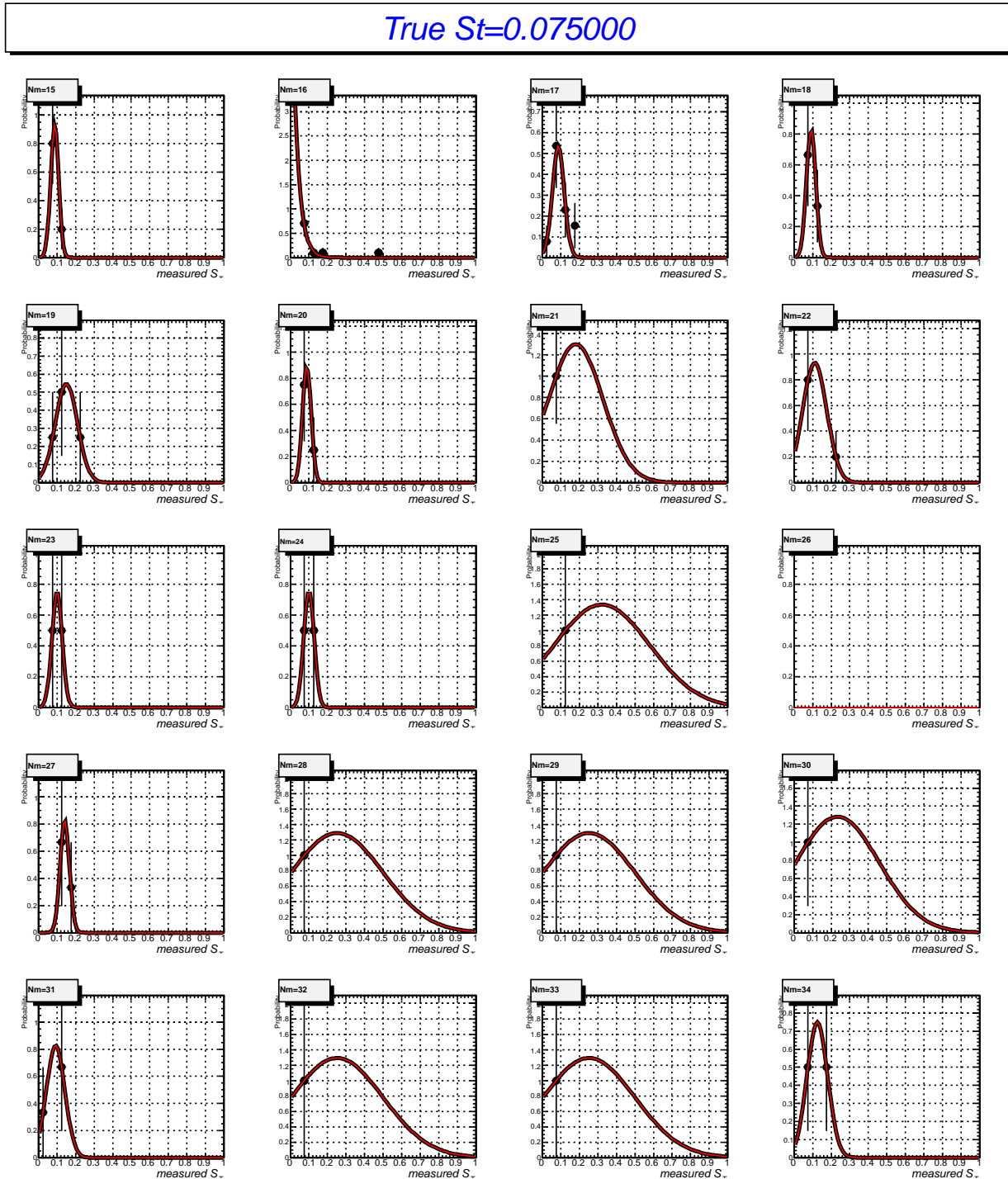


Figure 5.5: Resolution of the sphericity as a function of multiplicity. The true sphericity was fixed to 0.075 ± 0.025 .

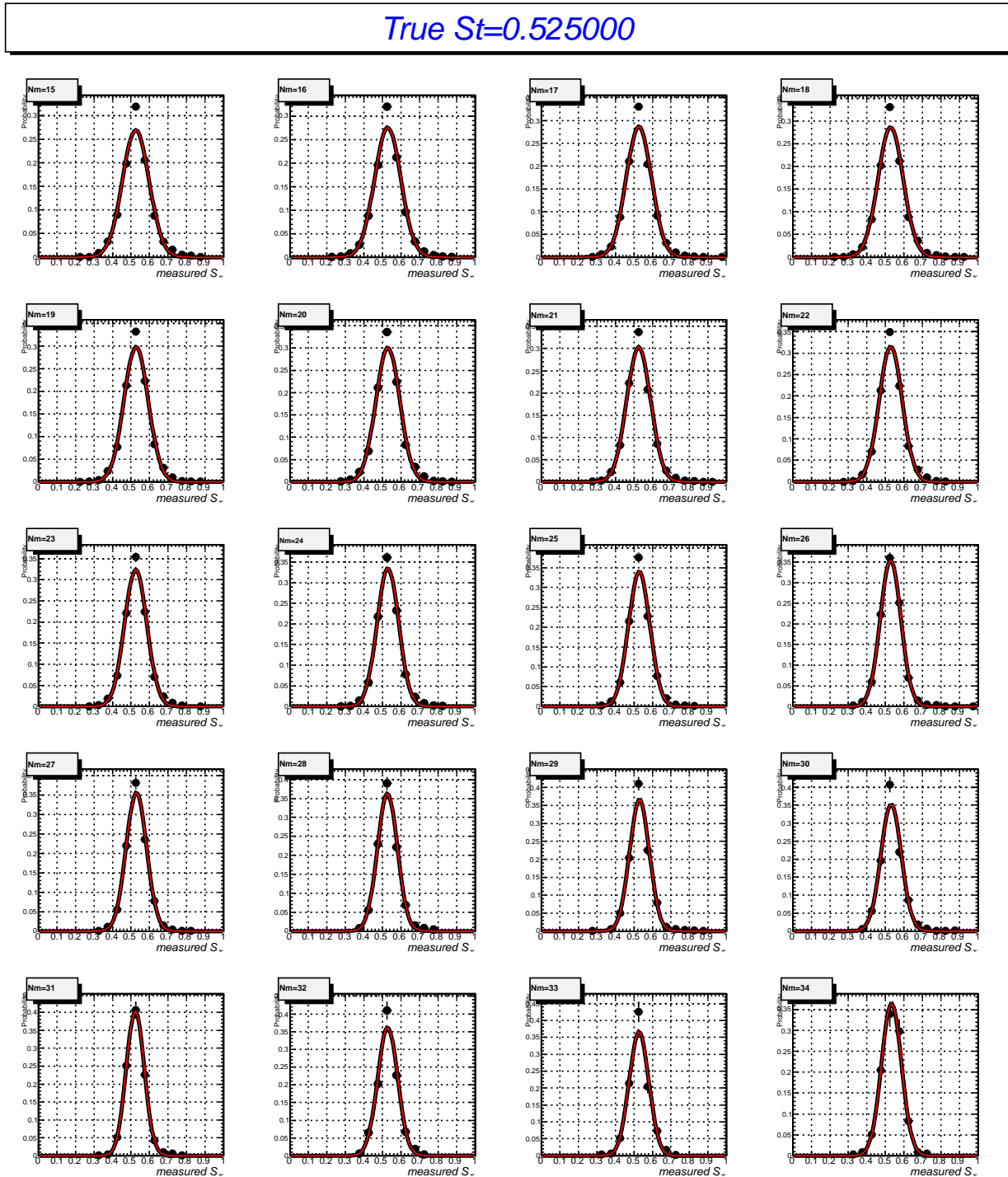


Figure 5.6: Resolution of the sphericity as a function of multiplicity. The true sphericity was fixed to 0.525 ± 0.025 .

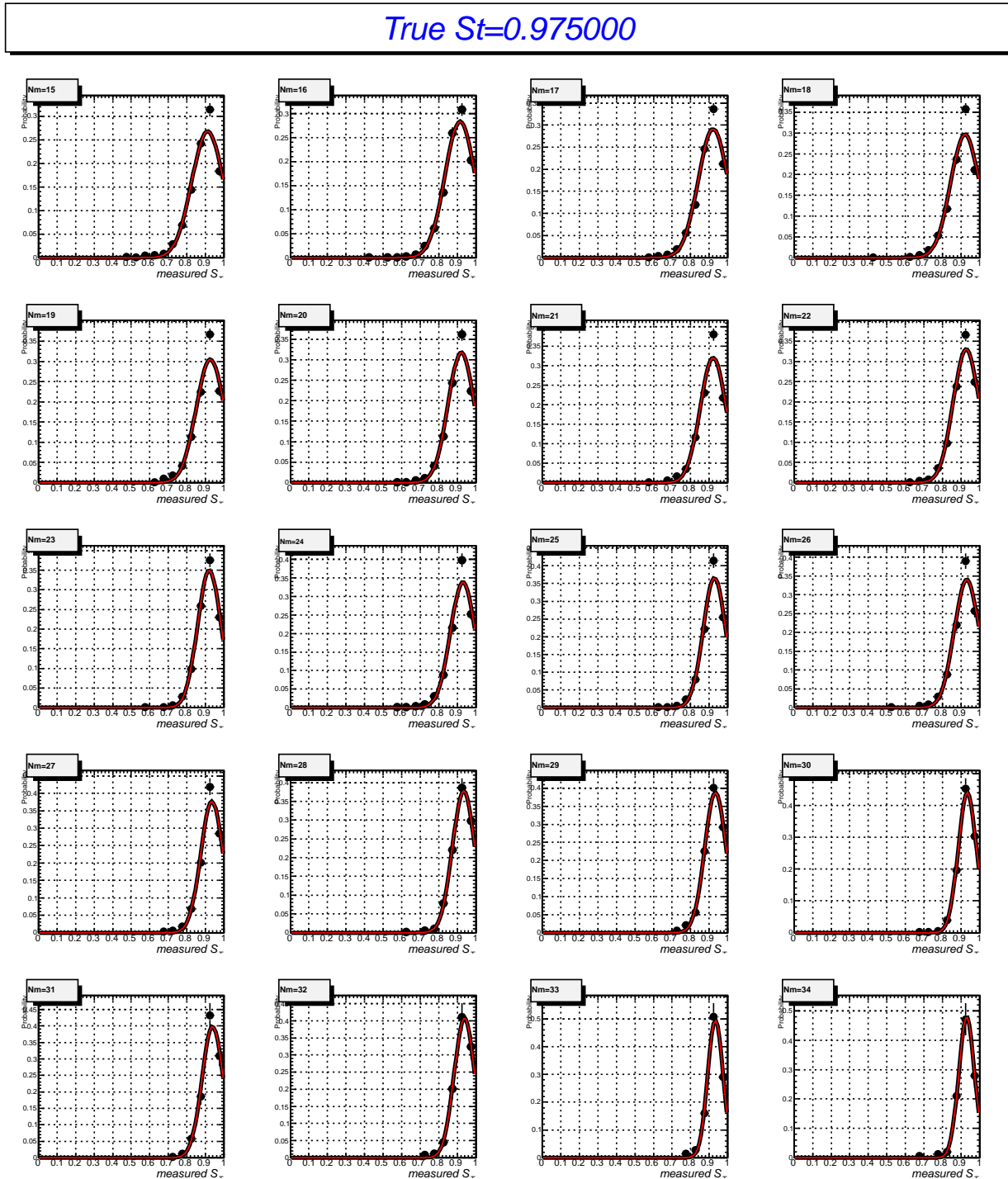


Figure 5.7: Resolution of the sphericity as a function of multiplicity. The true sphericity was fixed to 0.975 ± 0.025 .

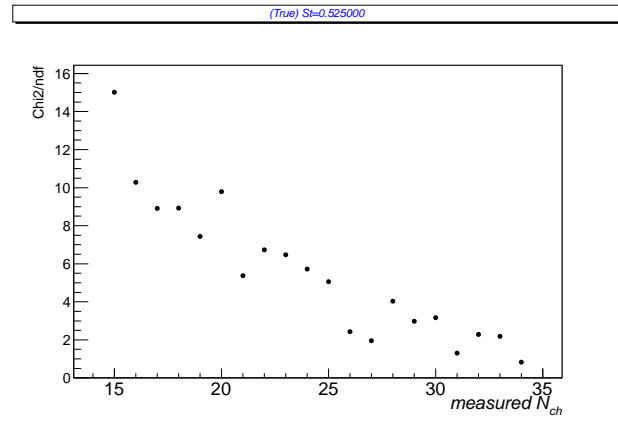


Figure 5.8: Gaussian fit quality of the sphericity resolution as a function of multiplicity. The true sphericity was fixed to 0.525 ± 0.025 .

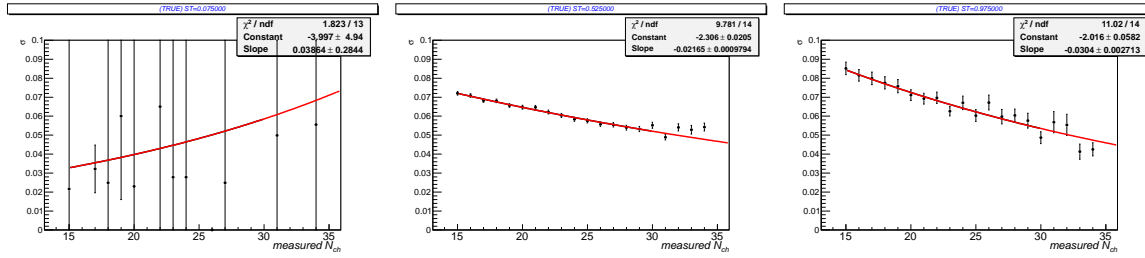


Figure 5.9: Sigma of the gaussian function versus multiplicity at $S_T = 0.075, 0.525$ and $0.975 (\pm 0.025)$. The red line indicates an exponential fit.

a clear increasing tendency with the sphericity, and then around $S_T \sim 0.7$ it reaches its maximum and then start to decrease. The outliers were “ignored”, the points were fitted to a linear function up to $S_T \sim 0.5$, in this manner we estimated the characteristics of the function at low sphericity.

Now we have enough information to construct the response matrices.

Fig. 5.12 shows an example of the sphericity response matrix with measured multiplicity =25. The MC used for the computations was based on the PYTHIA (version 6.4.21) event generator tune ATLAS-CSC[Mor] with flat multiplicity.

5.5.2 Test of the method

The response matrices were computed using simulations generated with PYTHIA[Sjo94] tune ATLAS-CSC[Mor], two production cycles were tested:

- **LHC10b6:** Early physics-2, measured SPD mean vertex and spread, pp, ATLAS CSC, flat multiplicity distribution 0.5T, 7 TeV, ID #170.

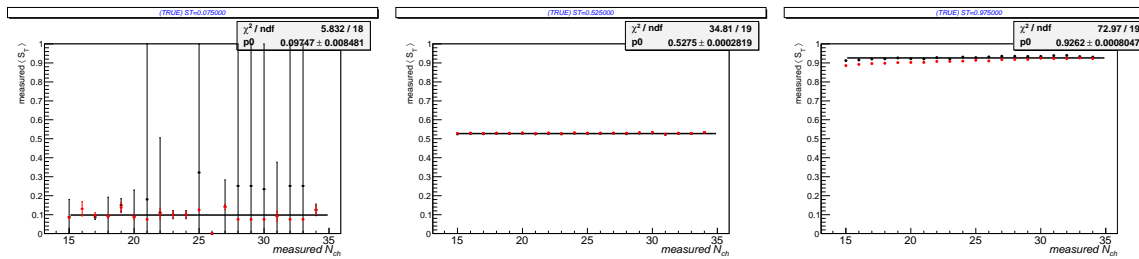


Figure 5.10: Mean of the gaussian function versus multiplicity at $S_T = 0.075, 0.525$ and $0.975 (\pm 0.025)$.

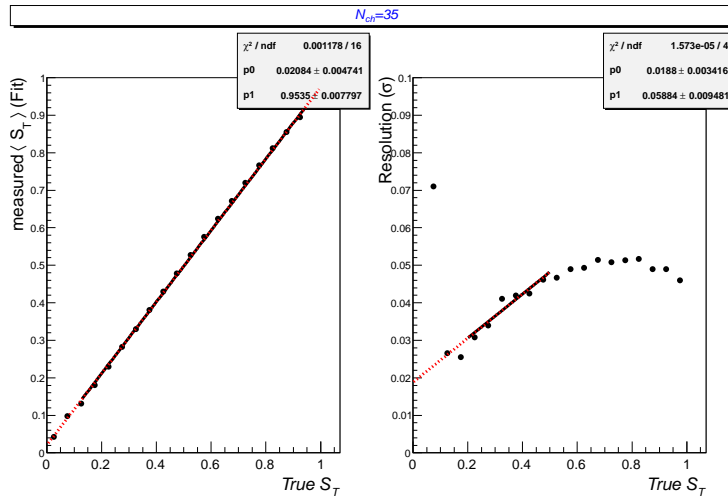


Figure 5.11: Mean and sigma of the fit as a function of true sphericity at measured multiplicity 35. For sigma, the two first bins are out of the tendency because they were computed with poor statistics. The sphericity was interpolated to $S_T = 0$ using a linear fit.

- **LHC10h16:** pp, ATLAS CSC, flat multiplicity distribution (range 0-100), 0.5T, 7 TeV, LHC10d anchors, ID #236.

The procedure was tested using simulations generated with PHOJET[Eng95], the input to the program is the sphericity spectra after the reconstruction. Different MC production cycles were tested:

- **LHC10d2:** pp, Phojet, 0.5T, 7000GeV, LHC10b anchor runs, ID #185.
- **LHC10e21:** pp, Phojet, 0.5T, 7 TeV, LHC10e anchor runs (10% statistics), ID #234

Both produce similar results. For instance, Fig. 5.13 shows a comparison between the corrected and the true points (average multiplicity *vs.* multiplicity at generator level³). In

³The results at generator level are gotten by counting all the events produced by the generator before of the transport through the detector. In the analysis we only count primary charged particles.

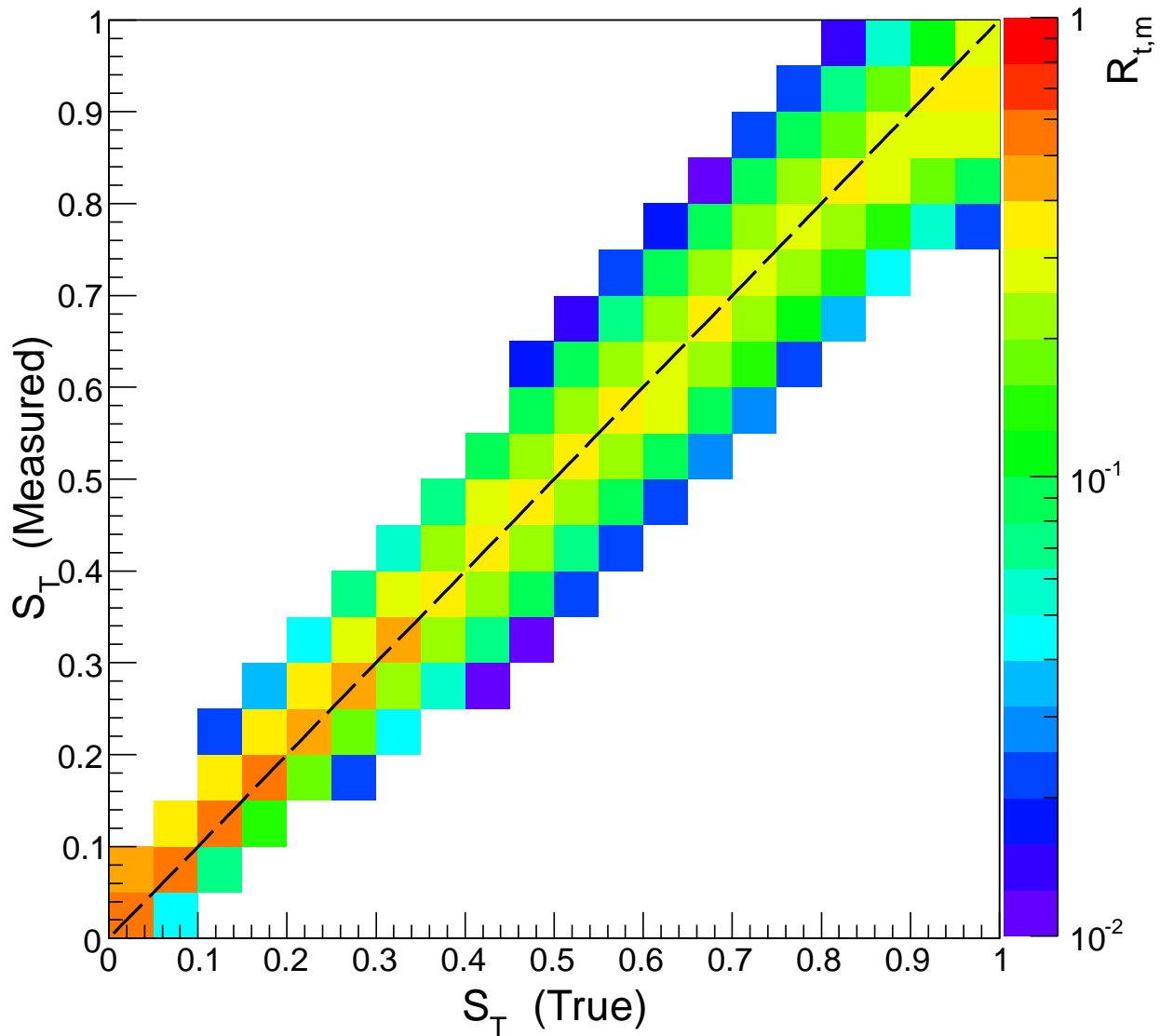


Figure 5.12: Example of the response matrix for the sphericity at reconstructed multiplicity of 25 primary tracks. PYTHIA event generator tune ATLAS-CSC[Mor] with flat multiplicity.

this case, the MC productions: LHC10b6 and LHC10d2 were used. The figure illustrates the results arising from the “bulk” and “hard” samples. The largest error in the method is in the “hard” sample at low multiplicity where it is $\sim 17\%$, but reaches around of $\sim 1 - 2\%$.

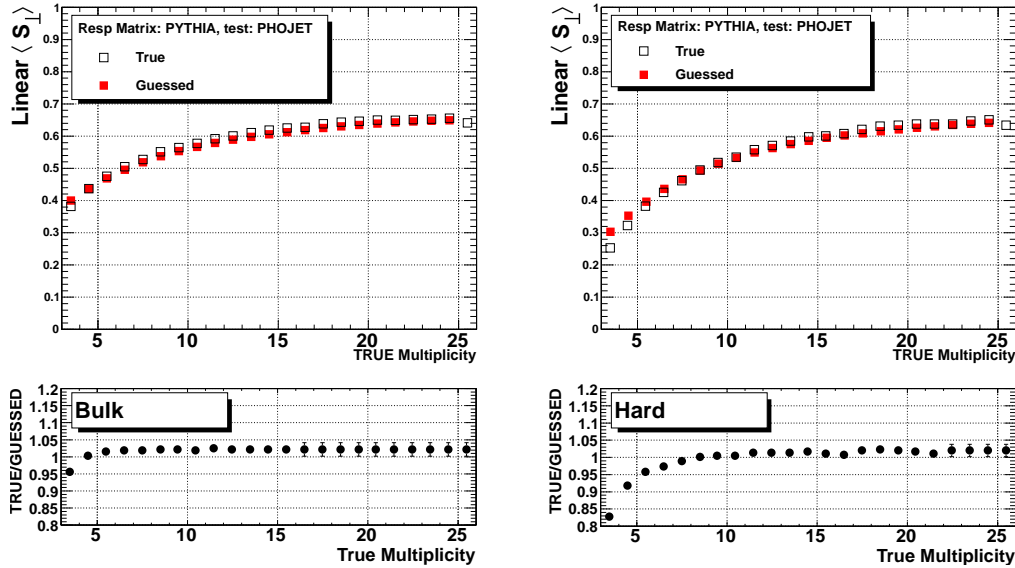


Figure 5.13: Test of the method to get the unfolded linearized sphericity as a function of the true multiplicity. The samples: “bulk” and “hard” are shown. The true points are gotten using primary charged particles produced at generator level.

5.6 Average transverse momentum versus multiplicity

The average transverse momentum was computed event-by-event by summing over all primary tracks in $|\eta| < 0.8$ and $p_T \geq 0.5$:

$$\langle p_T \rangle = \frac{\sum_i p_{Ti}}{N_{ch}} \quad (5.6)$$

One important remark is that if we change the definition to compute the average p_T , we can get quite different results (at least at 7 TeV). For instance, let consider the definition of multiplicity used in [KAea10c] and let's use two ways for the computation of $\langle p_T \rangle$, the first one applying an upper cut on p_T ($0.5 \leq p_T \leq 4$ GeV/c, as in [KAea10c]) and the other one without such upper cut. The results at generator level for three different models are shown in Fig.5.14. At high multiplicity, the average p_T differs in $\sim 13\%$, at least in events generated with PYTHIA8[eab].

For the event shape analysis we computed the mean p_T following the relation (5.6). In different bins of multiplicity, we compute the average p_T , the result is $\langle p_T \rangle^m(N_m)$. Then, to

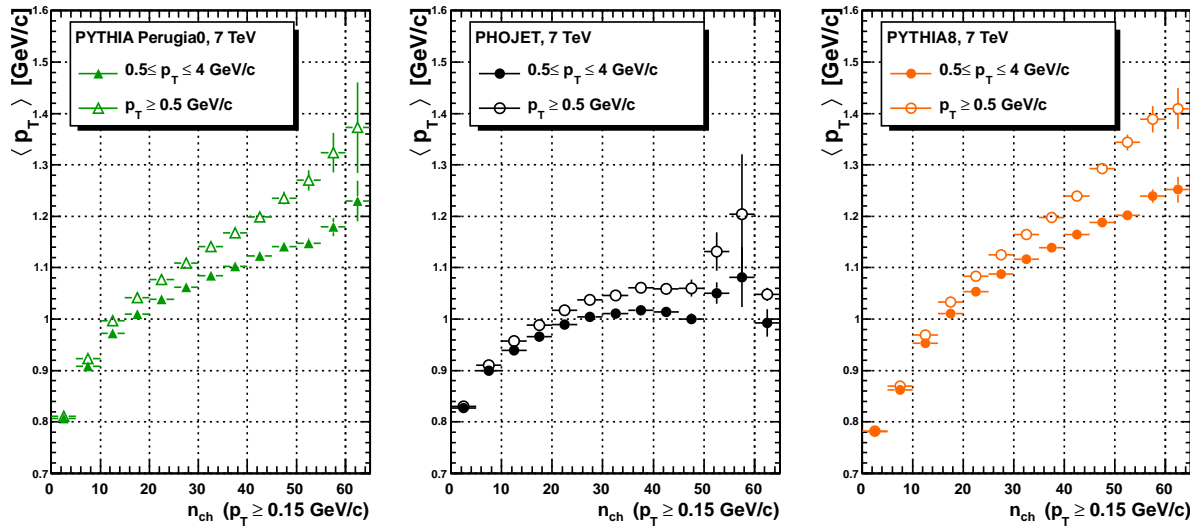


Figure 5.14: Average transverse momentum versus multiplicity. The results from three MC models are shown: PYTHIA6 (tune PERUGIA0), PHOJET and PYTHIA8. Two ways for the computation of the average were used: one with an upper cut on p_T , and the second one without such cut.

get $\langle p_T \rangle(N_t)$ we follows the approach:

$$\langle p_T \rangle(N_t) = \sum_m \langle p_T \rangle^m(N_m) R(N_t, N_m) \quad (5.7)$$

Fig. 5.15 shows the performance of the method. As in the sphericity case, the method was tested using PHOJET as input (production: LHC10d2), the corrections were computed using PYTHIA6. The figure illustrates the cases: “bulk” and “soft”. Note that the error associated to the method is below 3%.

In order to prove that our method reproduces well the published data at 900 GeV/c, Fig. 5.16 shows a comparison between the results gotten using the approach (5.7) and the results published in [KAea10c], of course, for the comparison we applied the cuts as are described in [KAea10c]. Inside the systematic uncertainty, we observe a good agreement between both results.

5.6.1 Sphericity spectra in bins of multiplicity

To get the normalized sphericity spectra in bins of multiplicity, a correction was applied bin-by-bin . The probability to find an event with sphericity S_T^{corr} in a given multiplicity bin (N_{ch}) is obtained as follows:

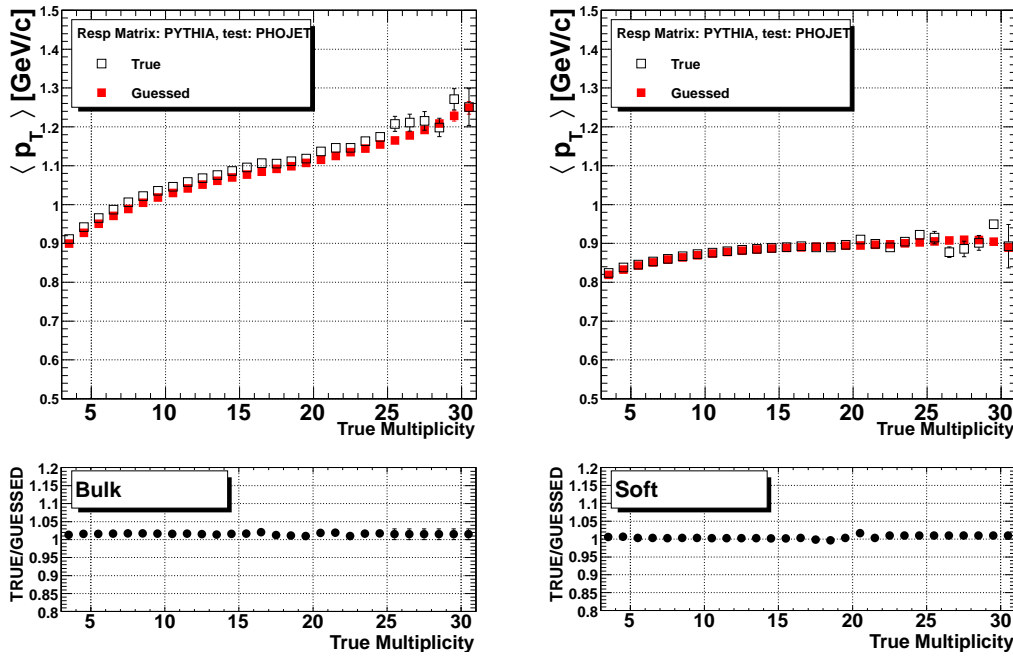


Figure 5.15: Test of the method to correct the average p_T versus multiplicity in events generated with PHOJET. The samples: “bulk” and “soft” are shown. The true points are gotten using primary charged particles produced at generator level. The analysis was done at 7 TeV, the corrections were computed using PYTHIA6.

$$P(S_T^{corr}) |_{atNch} = P(S_T^{raw}) |_{atNraw} \times C_1 \times C_2 \quad (5.8)$$

where $P(S_T^{raw}) |_{atN_{raw}}$ is the reconstructed probability to find an event with sphericity S_T in a bin of reconstructed multiplicity (N_{raw}). Such probability is corrected by C_1 and C_2 which are computed using MC. C_1 is the correction of the spectra for the chosen measured multiplicity bin.

$$C_1 = \frac{P(S_T^{unf})}{P(S_T^m)} |_{atNm} \quad (5.9)$$

On the other hand C_2 corrects the probability by the leak in multiplicity:

$$C_2 = \frac{P(S_T^t) |_{atNt}}{P(S_T^t) |_{atNm}} \quad (5.10)$$

In the expressions, $P(S_T^t)$ is the probability to find an event with true sphericity S_T^t , the symbols N_m and N_t are the measured and true multiplicities, “true” means that the information was gotten at generator level. S_T^t and S_T^{unf} are the true and unfolded sphericity spectra,

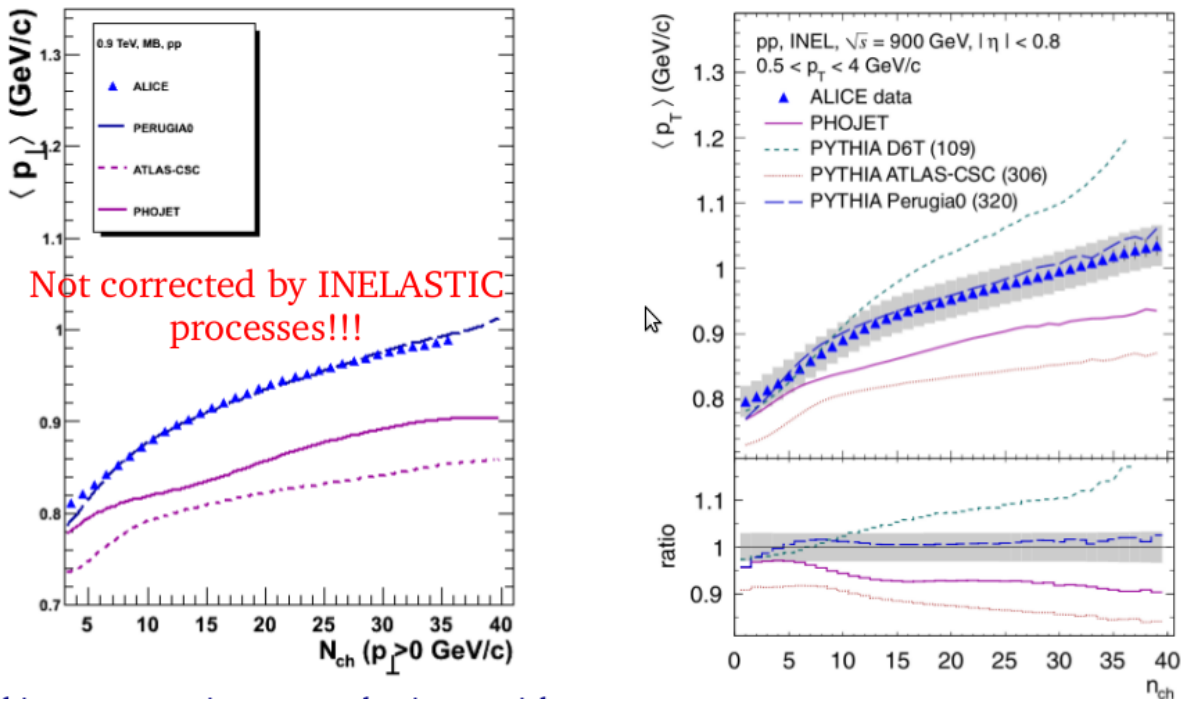


Figure 5.16: Average transverse momentum versus multiplicity at 900 GeV/c. The results for inelastic events published by ALICE (right side) are compared with the results which we got after applying our approach (5.7).

5.6. AVERAGE TRANSVERSE MOMENTUM VERSUS MULTIPLICITY 90

respectively. The latter are the results of the unfolding of the simulated measurements, *i.e.* PYTHIA6 (tune PERUGIA0) corrected by PHOJET and vice versa.

We worked in three bins of multiplicity:

- $3 \leq N_{ch} < 10$
- $10 \leq N_{ch} < 20$
- $20 \leq N_{ch} < 30$
- $N_{ch} \geq 30$

Fig. 5.17 illustrates the performance of the correction procedure. In each multiplicity container the true distribution is compared with the corrected one. Events generated with PHOJET (PYTHIA6) and then transported through the detector were reconstructed and subsequently corrected using PYTHIA6 (PHOJET). Both cases are displayed.

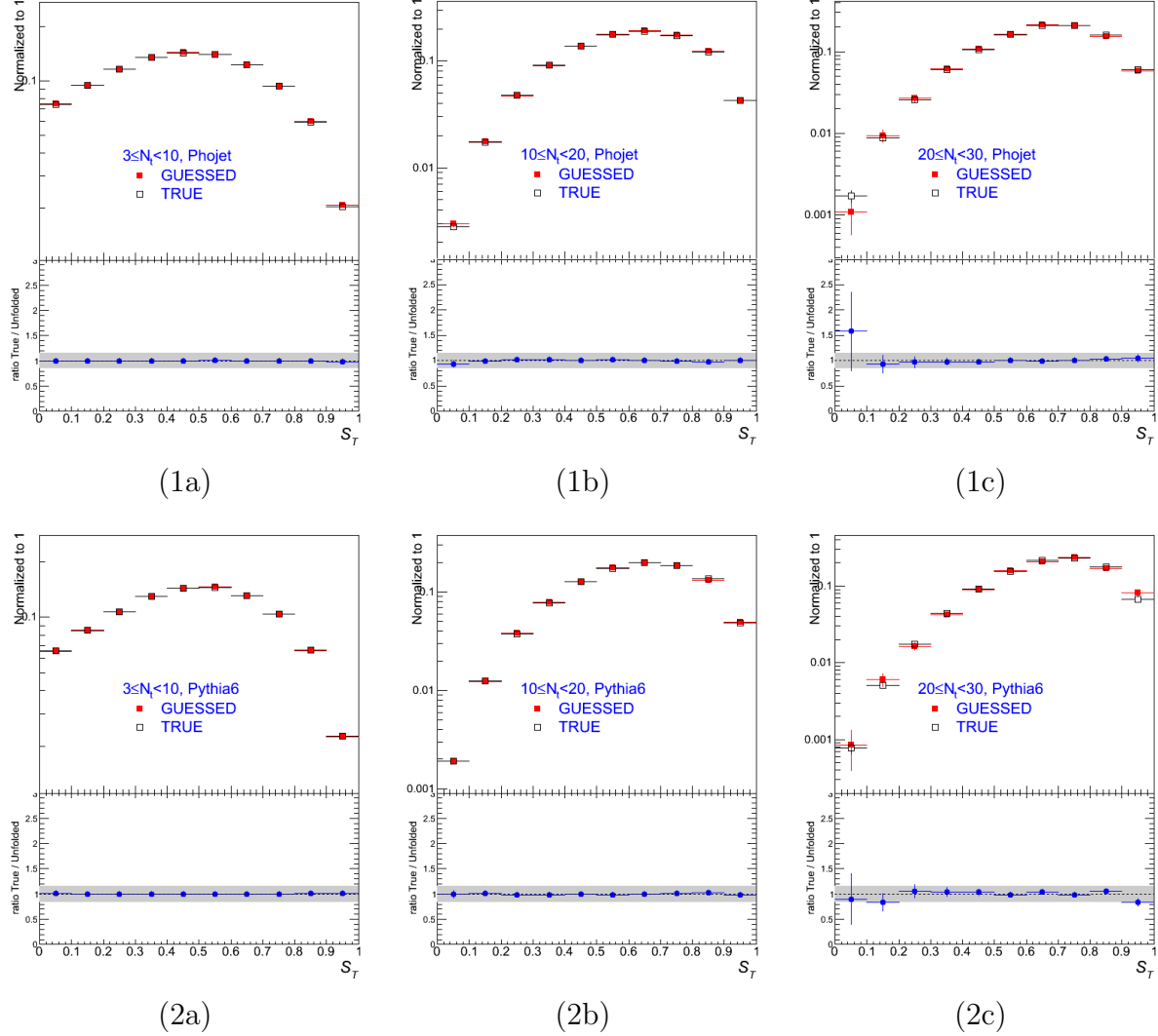


Figure 5.17: Performance of the procedure. (Upper) Reconstructed events generated with PHOJET are corrected using simulations generated with PYTHIA6 (tune PERUGIA-0). (Bottom) Reconstructed distributions generated with PYTHIA6 are corrected using simulations produced with PHOJET. Three different multiplicity bins are shown: $3 \leq N_{ch} < 10$, $10 \leq N_{ch} < 20$ and $20 \leq N_{ch} < 30$.

Chapter 6

Analysis in real data

In this chapter the results of the analysis are presented. The analysis was applied to real data corresponding to MB proton-proton collisions at $\sqrt{s} = 0.9, 2.76$ and 7 TeV. The reported measurements are: average transverse sphericity and average transverse momentum as a function of the multiplicity, and the sphericity spectra in multiplicity bins.

6.1 Data Analysis

ALICE recorded minimum bias (MB) triggered events at $\sqrt{s} = 0.9$ and 7 TeV (in 2010) and at $\sqrt{s} = 2.76$ TeV (in 2011). The overall number of analyzed events per energy is ~ 40 million events at each 7 and 2.76 TeV, and 3.6 millions at 0.9 TeV.

The position of the interaction vertex was reconstructed by correlating hits in the two silicon-pixel layers. The vertex resolution achieved depends on the track multiplicity, and is typically $0.1\text{-}0.3$ mm in the longitudinal (z) and $0.2\text{-}0.5$ mm in the transverse direction. The event is accepted if its longitudinal vertex position (z_v) satisfies $|z_v - z_0| < 10$ cm, where z_0 is the nominal position.

To get a good resolution on the transverse sphericity, only events with more than two primary tracks in $|\eta| < 0.8$ and $p_T > 0.5$ GeV/c are considered [COP]. This is because a non negligible amount of events with true multiplicity larger than two migrates due to inefficiencies to the first bins of measured multiplicity. These cuts reduce the statistics to ~ 9.1 , ~ 4.2 and ~ 0.42 million of MB events for the 7 TeV, 2.76 TeV and 0.9 TeV data, respectively.

The trigger and the beam-related background rejection is performed using the VZERO detector consisting of two forward scintillator hodoscopes. Each detector is segmented into 32 scintillator counters which are arranged in four rings around the beam pipe. They are located at distances $z = 3.3$ m and $z = -0.9$ m from the nominal interaction point and cover the pseudorapidity ranges: $2.8 < \eta < 5.1$ and $-3.7 < \eta < -1.7$ respectively. As an example,

Fig. 6.1 shows the arrival times of particles at the detector relative to the “time zero”. Note that in general several particles are registered for each event. Particles hitting one of the detectors before the beam crossing have negative arrival times and are typically due to interactions taking place outside the central region of ALICE.

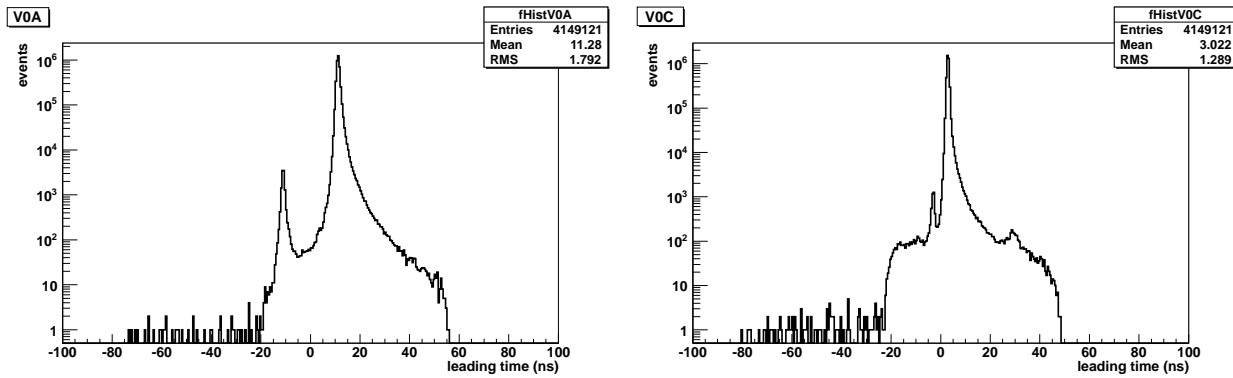


Figure 6.1: Arrival time of particles in the VZERO detectors relative to the beam crossing time (time zero). A number of beam-halo or beam-gas events are visible as secondary peaks in VZERO-A (left panel) and VZERO-C (right panel). This is because particles produced in background interactions arrive at earlier times in one or the other of the two counters.

The trigger required a hit in one of the VZERO counters or in the SPD detector. In addition a coincidence between the signals from two beam pickup counters, one on each side of the interaction region, indicating the presence of passing bunches was required [K Aeal0f].

6.1.1 Off-line physics selection

To select “physics” events an off-line selection was applied. Basically, it consists in selecting events having the correct event type (physics-flagged on-line) and interaction trigger (*i.e.* trigger on bunch crossings). Also, the events should fulfill the on-line trigger condition (replayed using off-line signals). They are not flagged as beam-gas by either V0A or V0C (or by the cut based on the SPD clusters vs tracklets correlation).

To monitor the beam-related background flagged by VZERO, Fig. 6.2 shows the fraction of such background as a function of time (run number). The MB trigger corresponds to “CINT1-B,” in order to compare the background level, also other triggers were included: the muon trigger (“CMUSH1-B”) and the high multiplicity trigger (“CSH1-B”). Note, that for MB events the level is $\sim 0.6\%$, the largest is reached by the high multiplicity trigger with about $\sim 10\%$. In the plot, the red points are the outliers. Outliers are flagged automatically, by computing the median of the sample and estimating the sigma as the median of the distance from the sample median (MAD), divided by ~ 0.6745 . We then look for points being more than 3 sigmas away from the median.

The fraction of events flagged as background by the correlation between the SPD clusters

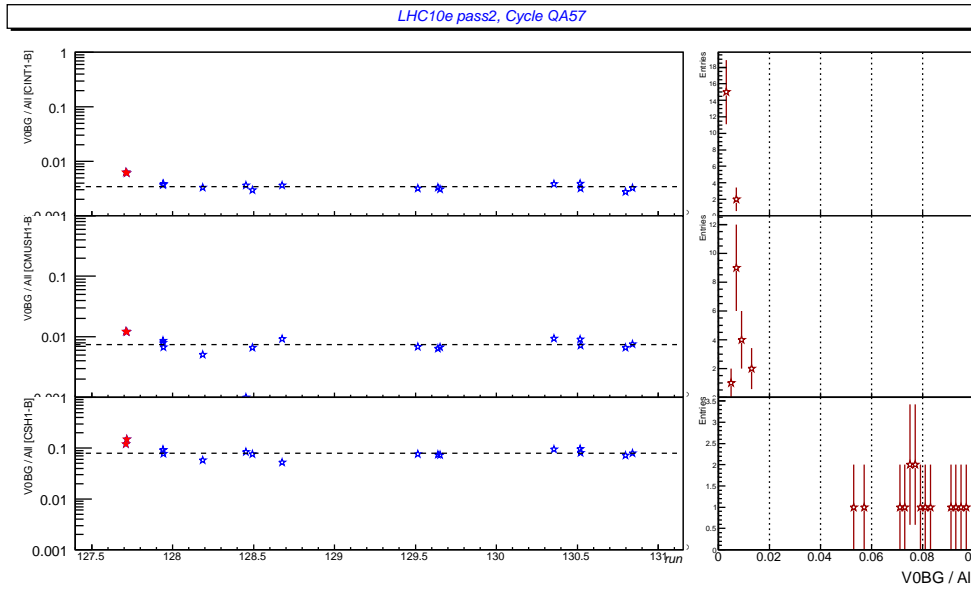


Figure 6.2: Monitoring of the beam-related background flagged by VZERO, the red points are the outliers, in the text the procedure to compute the outliers is explained.

and tracklets is plotted as a function of time in Fig. 6.3. The picture displays three different trigger configurations. Note that for MB trigger the fraction is $\sim 0.1\%$.

At the end, the percentage of accepted events after the off-line selection is $\sim 99\%$ for the MB trigger. This shows that the background level is very small, $< 1\%$, and it shows a very stable behavior with time. Fig. 6.4 shows the fraction of accepted events for the different event classes.

6.1.2 Selection of events due to their hardness

In the previous chapter we discussed the cuts at event and track levels, as well the approach to separate “soft” and “hard” events was presented. Table 6.1 shows the event ratio “soft” to “hard” for ALICE data and the generators: PYTHIA6, PHOJET and PYTHIA8 [eab]. The fraction of “soft” events is different between MC and ALICE data, for example, at 7 TeV the data look softer than PERUGIA-0 but harder than ATLAS-CSC. Even among the different MC’s the ratios exhibit a noticeable disagreement especially at 0.9 TeV.

6.1.3 Systematic uncertainties on $\langle S_T \rangle(N_{ch})$

In order to estimate the systematic uncertainties on the average sphericity, the results of the analysis were evaluated changing different conditions.

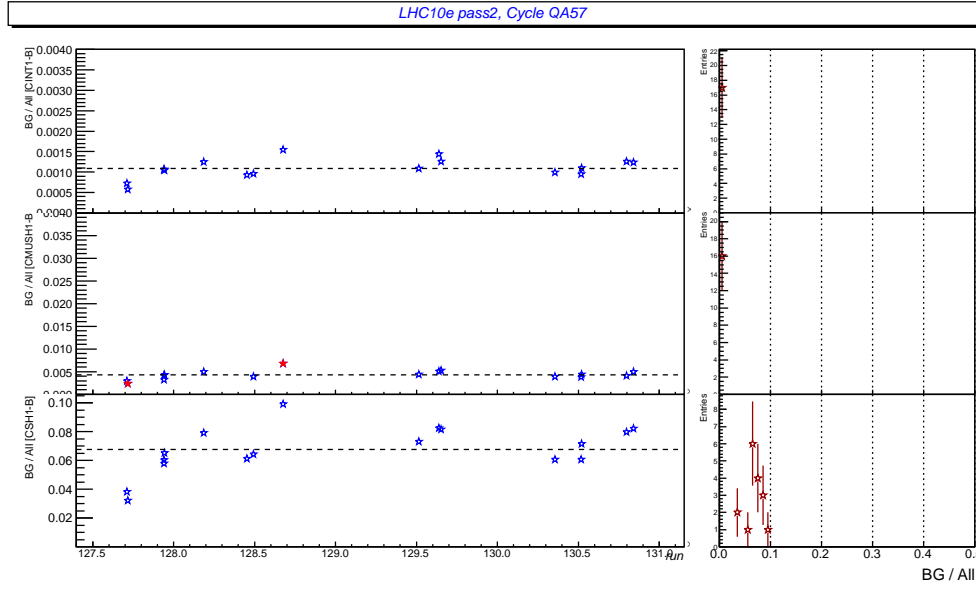


Figure 6.3: Monitoring of the beam-gas background flagged by the correlation between the number of SPD clusters and the number of tracklets. The red points are the outliers, in the text the procedure to compute the outliers is explained.

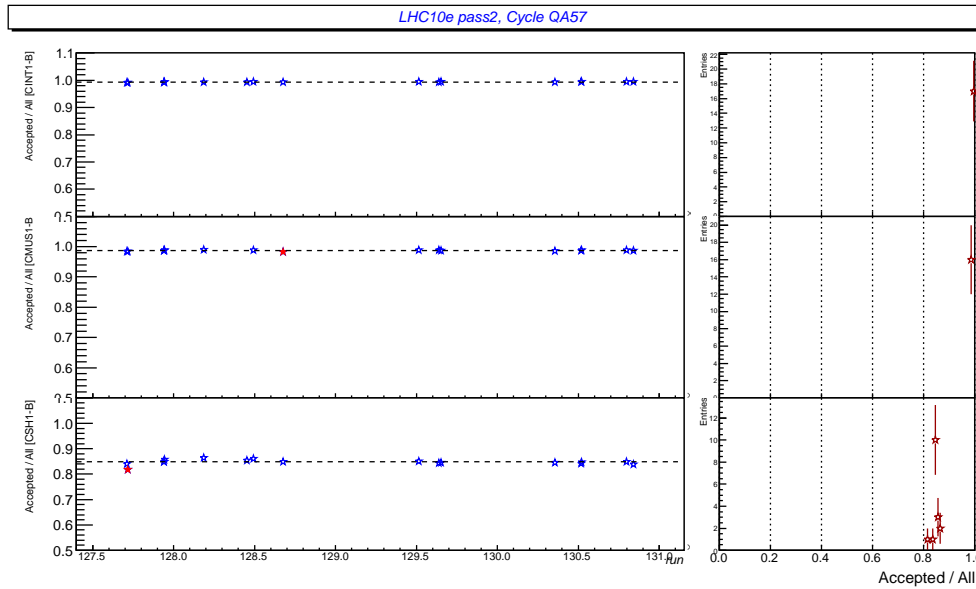


Figure 6.4: Fraction of accepted events after the off-line physics selection. For the MB trigger it is $> 99\%$, this tells us that the background level is negligible.

Table 6.1: Ratio of the number of “soft” to “hard” events. In the present analysis, more than two primary particles in $|\eta| < 0.8$ and $p_T > 0.5$ GeV/c are required. The corrections for reconstruction were made.

\sqrt{s}	0.9 TeV	7 TeV
Data	$R_{S/H}$	$R_{S/H}$
ALICE	5.7	2.36
PERUGIA-0	5.6	2.06
ATLAS-CSC	10.95	3.41
PHOJET	8.53	2.52
PYTHIA8	7.28	2.37

First of all, the contribution due to pile up. By construction, the probability to have n interactions reconstructed as a single event can be described by a Poisson distribution:

$$P(n, \mu) = \frac{\mu^n e^{-\mu}}{n!} \quad (6.1)$$

where μ is the median. If N^{CBEAMB} is the number of triggers indicating the presence of beams from both sizes and N^{CINT1B} the number of interactions with beam-beam from both sizes, then the probability to have at least 1 interaction is given by:

$$\frac{N^{CINT1B}}{N^{CBEAMB}} = 1 - P(0, \mu) \quad (6.2)$$

Therefore:

$$\mu = \ln(N^{CBEAMB}) - \ln(N^{CBEAMB} - N^{CINT1B}) \quad (6.3)$$

The samples which were analyzed have an average μ of ~ 0.05 . The aim of this section is to compare the result using a “typical” sample ($\mu \sim 0.06$) with those using the events with the largest μ of the sample ($0.07 < \mu < 0.35$). This is the maximum pile up which is present in my samples. Also, these results are compared with an extreme case of very high pile up: $0.6 < \mu < 3$.

Fig. 6.5 displays the behavior of the average S_T versus multiplicity, the data are not corrected, in all the cases the correction factors should be the same. As you can see the effect on the average is very small even in the sample with very high pile up. The ratio between the reference points and the high pile up ($0.07 < \mu < 0.35$) is also plotted. For the three event categories, the effect is smaller than 0.2%.

The event generator dependence was estimated by changing the MC generator used to compute the correction factors, *i.e.*, PYTHIA6 and PHOJET. The results for “bulk” and “hard” events are shown in Fig.6.6. In the first case the uncertainty is smaller than 1% while in the second is below 2%.

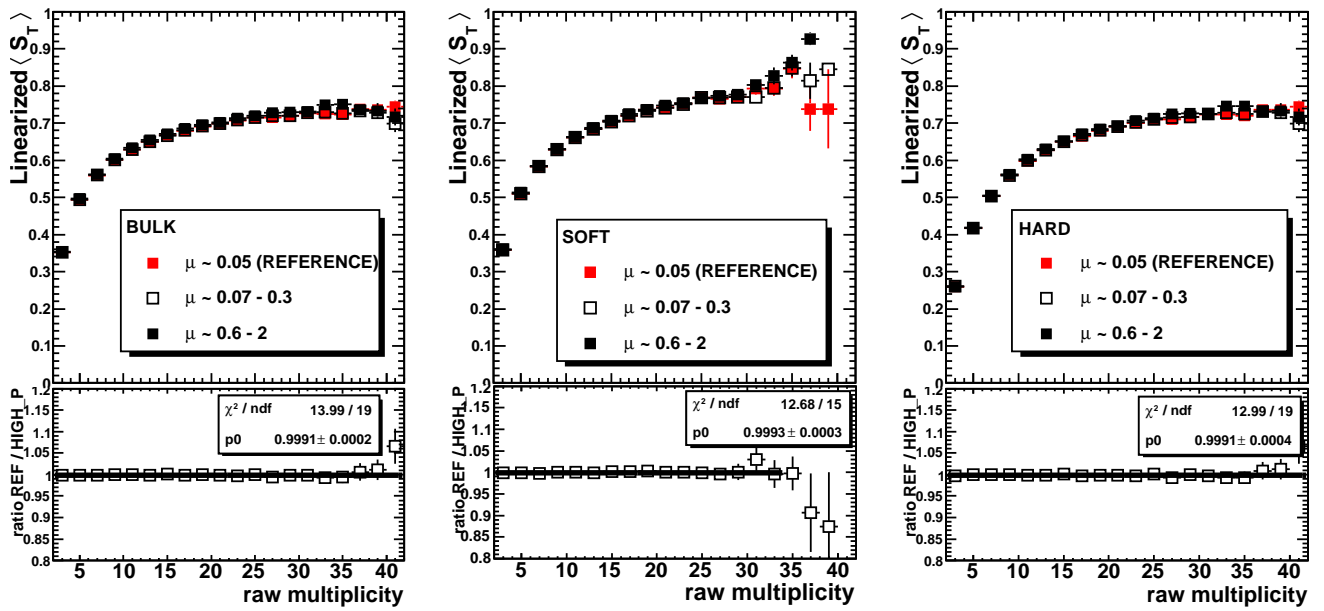


Figure 6.5: Effect of the pile up on the average S_T . Data from the period LHC10d (pass2) were analyzed. The reference data were taken from a sample with typical μ around 0.05. The high pile up sample includes events having $0.07 < \mu < 0.35$, this are the maximum values which can be reached in a typical sample of the period LHC10e. An extreme case is also shown where the μ is between 0.4 and 2. The effect on $\langle S_T \rangle$ is small even in the very extreme case.

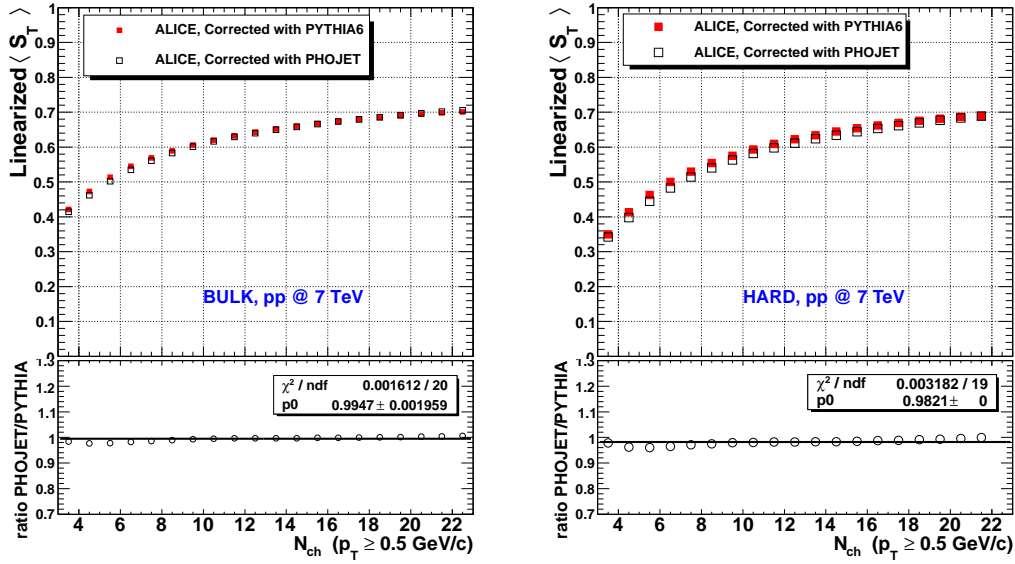


Figure 6.6: Event generator dependence of the $\langle S_T \rangle$. The MB data of the period LHC10e are corrected using the response matrices from PYTHIA6 and PHOJET.

The systematic uncertainty due to the rejection of secondaries was done by increasing the contribution of them up to $\sim 8\%$. This is attained when the condition $d_0 > N(0.0182 + \frac{0.035}{p_T^{1.01}})$ (p_T in GeV/c) is varied, d_0 is the distance of closest approach in the plane perpendicular to the beam. The default value is $N = 7$. Fig. 6.7 illustrates how the contribution from secondaries is increased as a function of N ($\sqrt{s} = 7$ TeV). According with MC, the values $N = 7, 35, 70, 105$ and 175 correspond to contaminations $\sim 2.2\%$, $\sim 4.9\%$, $\sim 6.3\%$, $\sim 7.3\%$, and $\sim 8.1\%$ respectively.

Fig. 6.8 shows the effect on the quadratic $\langle S_T \rangle$ when the amount of secondaries is increased. The effect on the linearized sphericity is expected to be the same as in the quadratic observable.

Added to the preceding studied other checks were done to ensure the quality of the measurements, for instance, the analysis was applied to mixing events, since the results are very different then we concluded that the observed systematics cannot be understood from randomized events. Also, the analysis was applied to events with sphericity axis in different regions of the TPC, the results were invariant under such conditions. For example, Fig. 6.9 shows the mean sphericity versus charged tracks multiplicity for: all charged tracks, positive and negative charged tracks. As expected, the results indicate that the value of sphericity computed using positive or negative charged tracks is the same. This behavior is also reproduced by MC.

Finally, the Table 6.2 summarizes the systematic uncertainties on the mean sphericity for the different event classes.

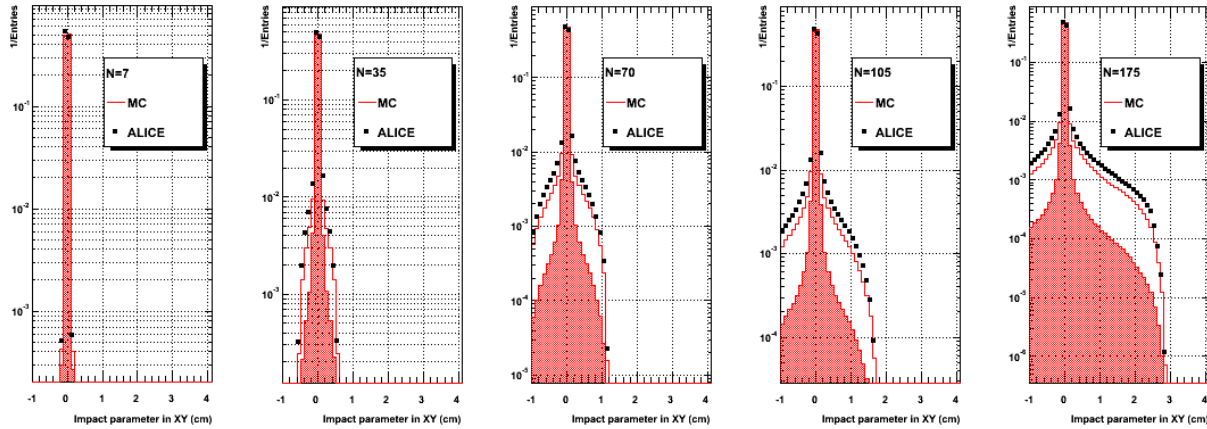


Figure 6.7: Effect of the cut on the distance of closest approach (DCA). The DCA on the plane perpendicular to the beam is plotted for “primary” tracks. The MC distribution (line) is compared with the ALICE measurements (points). The shaded area correspond to the true primary MC tracks, so, the difference between the line and the shaded area is the contamination of secondaries.

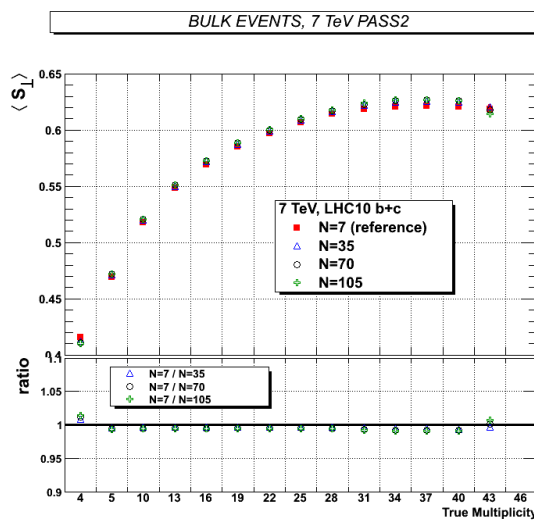


Figure 6.8: Effect of the secondaries on the (quadratic) sphericity. The standard value $N = 7$ correspond to a contamination of about 2% while $N = 175$ to $\sim 8\%$.

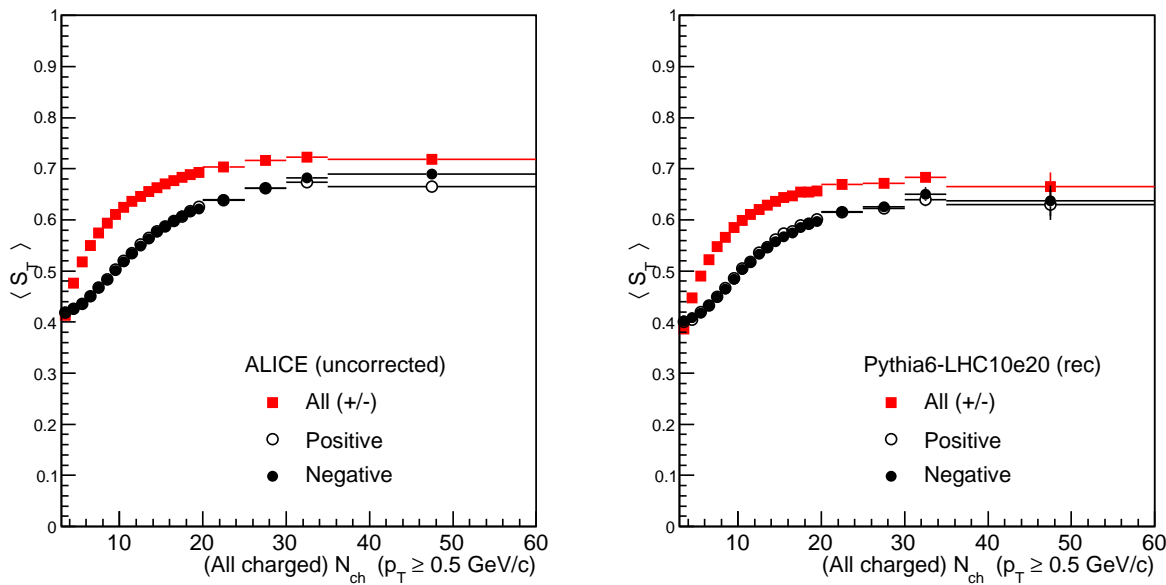


Figure 6.9: Mean sphericity versus charged tracks multiplicity for: all charged tracks, positive and negative charged tracks. As is expected, the result for positive and negative charged tracks is the same.

Table 6.2: Contributions to the systematic uncertainties on the average transverse sphericity $\langle S_T \rangle$.

Contribution	Bulk	Soft	Hard
Track selection cuts	0.3%	0.3%	0.3%
Event generator dependence	0.1%	0.1%	0.1%
Different run conditions	1.0%	1.0%	1.0%
Secondary track rejection	0.8	0.8	0.8
Pile up events	0.2%	0.2%	0.2%
Method ($N_t < 5$)	< 4.0%	< 4.0%	< 8.0%
Method ($N_t \geq 5$)	$\sim 3.0\%$	$\sim 1.0\%$	3.4%
Run conditions	1.0%	1.0%	1.0%
Detector misalignment	negl.	negl.	negl.
ITS efficiency	negl.	negl.	negl.
TPC efficiency	negl.	negl.	negl.
Beam-gas events	negl.	negl.	negl.
Total ($N_t < 5$)	< 4.3%	< 4.3%	< 8.2%
Total ($N_t \geq 5$)	< 2.6%	< 1.7%	< 3.8%

Table 6.3: Systematic uncertainties on the sphericity spectra.

Multiplicity range	3-9	10-19	20-29
Method	< 0.1%	< 2.0%	< 5.0%
Event generator dependence	< 5.0%	< 1.0%	< 1.0%
Pile-up events	< 1.0%	< 1.0%	< 4.0%
Total	< 5.1%	< 2.4%	< 6.5%

6.1.4 Systematic uncertainties on the sphericity spectra

The most significant systematic uncertainties on the sphericity spectra are discussed in this subsection. To address the question concerning to pile up, we investigated the effect on the spectra considering events with different μ values. We took the samples discussed in the previous section, *i. e.* $\langle \mu \rangle \sim 0.05$ (reference with μ up to 0.3), $\mu = 0.07 - 0.3$, and $\mu > 0.3$. In Fig. 6.10, the spectra in the multiplicity containers: $3 \leq N_{ch} < 10$, $10 \leq N_{ch} < 20$, $20 \leq N_{ch} < 30$ and $N_{ch} \geq 30$ are plotted. The effect of the pile up is small at low multiplicity (< 1%), and it is a bit higher for multiplicities larger than 20 (< 4%). The points are not corrected because the factors are the same for all the samples.

The model dependence is shown in Fig. 6.11 for the first three bins of multiplicity. While, in Fig. 6.12, the total systematic uncertainty in the different multiplicity ranges is shown. Table 6.3 summarizes the systematic uncertainties.

6.1.5 Systematic uncertainties on the mean p_T

In the case of the mean transverse momentum as a function of multiplicity the systematic uncertainties are taken from [KAea10c], the only difference being the method of correction. The estimation of the uncertainty was done applying the correction algorithm to reconstructed events that were generated with PYTHIA6, the correction matrices were computed using events generated with PHOJET. The final distributions were compared with the results at generator level. For the “bulk” sample the uncertainty reaches $\sim 1.5\%$, while for “soft” and “hard” they reach $\sim 1.0\%$ and $\sim 5.1\%$, respectively.

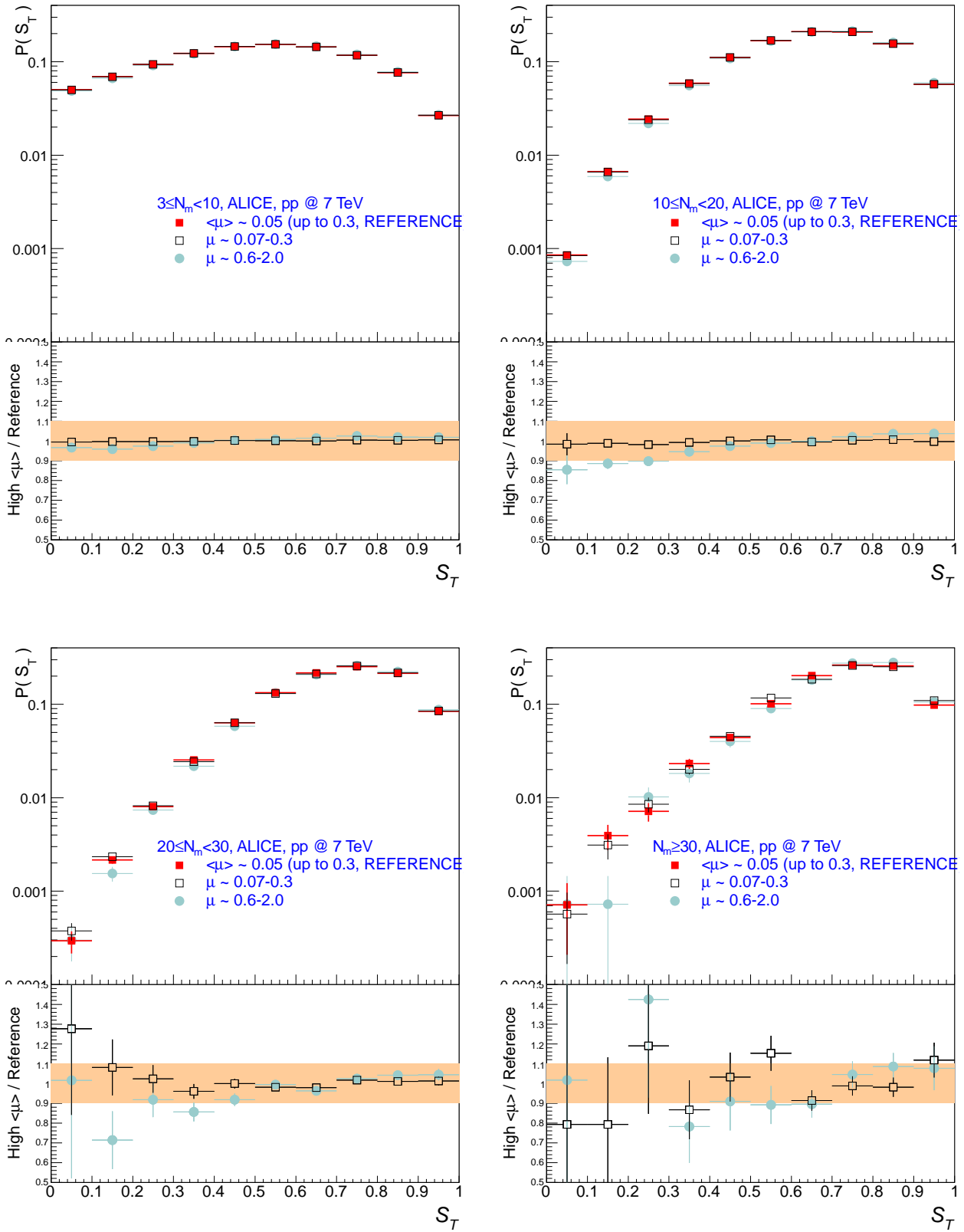


Figure 6.10: Effect of the pile up on the sphericity spectra. The multiplicity bins are displayed in the panels.

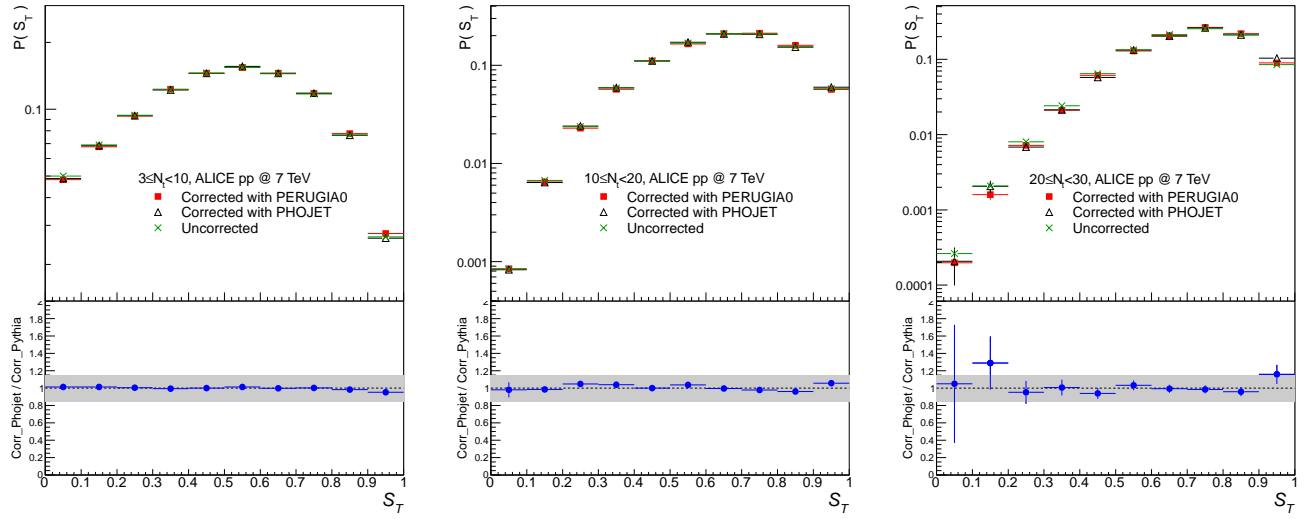


Figure 6.11: Model dependence on the sphericity spectra. The multiplicity bins are displayed in the panels.

6.2 Results

In this section the results of the analysis are presented along with the predictions of different models: PYTHIA6 [Sjo94] (tunes: ATLAS-CSC [Mor] and PERUGIA-0 [Ska]), PHOJET [Eng95] and PYTHIA8 [eab].

6.2.1 $\langle S_T \rangle$ in 0.9 TeV data

The mean transverse sphericity plots for $p - p$ collisions at $\sqrt{s} = 900$ GeV are shown in Figs. 6.13, 6.14 6.15 for “bulk”, “soft” and “hard” events, respectively. The different event classes are displayed.

Within the statistical and systematic uncertainties, the “bulk” events exhibit a good agreement with the models: PHOJET and the various tunes of PYTHIA6. The data points lie $\sim 15\%$ above PYTHIA8 over the entire range of multiplicity.

Looking at the “soft” events, the four models are in accordance with the ALICE measurements for the multiplicity up to 13, but for the PYTHIA8 prediction which is $\sim 5\%$ off. The fact that ALICE points stop at $N_{ch} = 13$ is due to lack of statistics to perform the unfolding.

For the “hard” events, there is a noticeable difference between ALICE and all the models. The differences are larger than the systematic and statistical uncertainties. The lowest sphericity is predicted by PYTHIA8 as in the other classes of events.

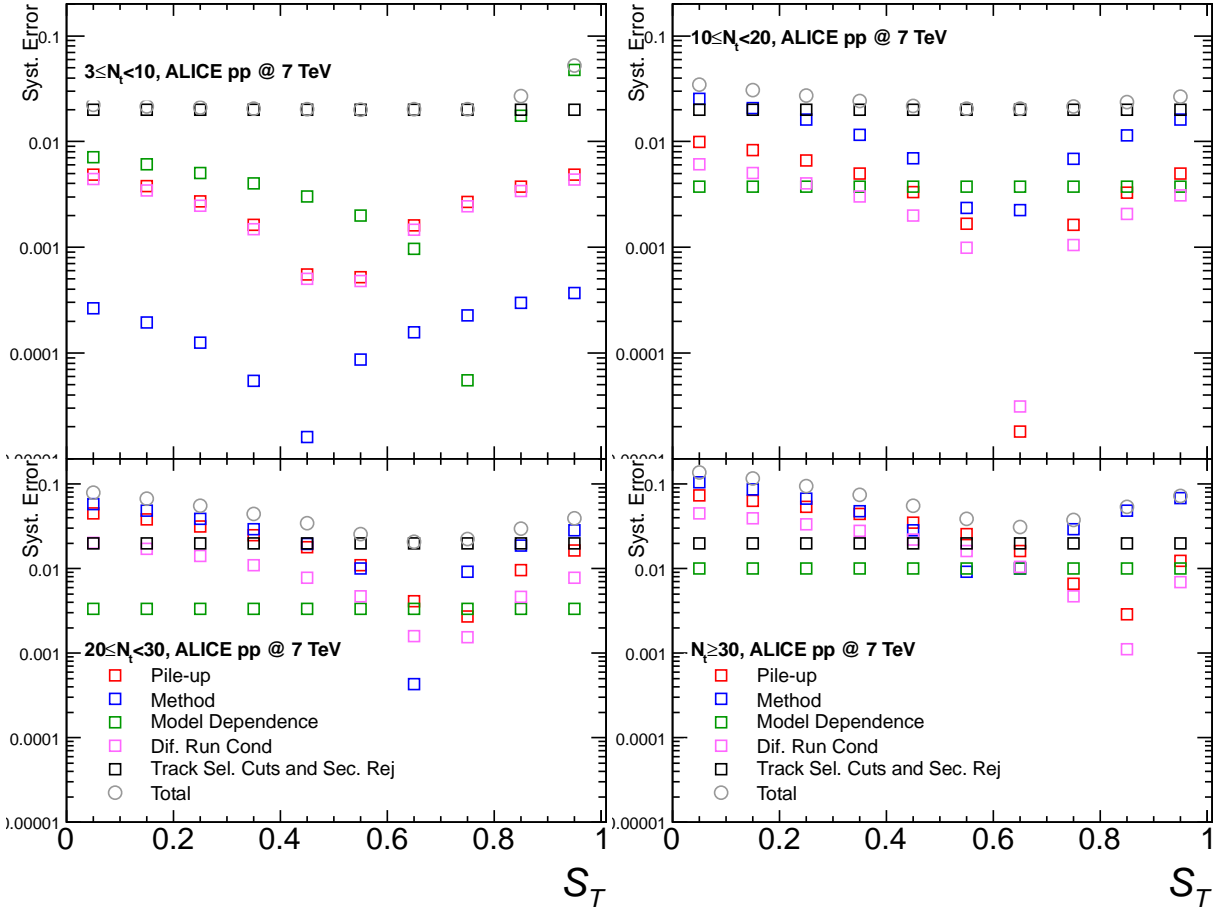


Figure 6.12: Decomposition of the systematic uncertainty on the sphericity spectra for the different multiplicity ranges.

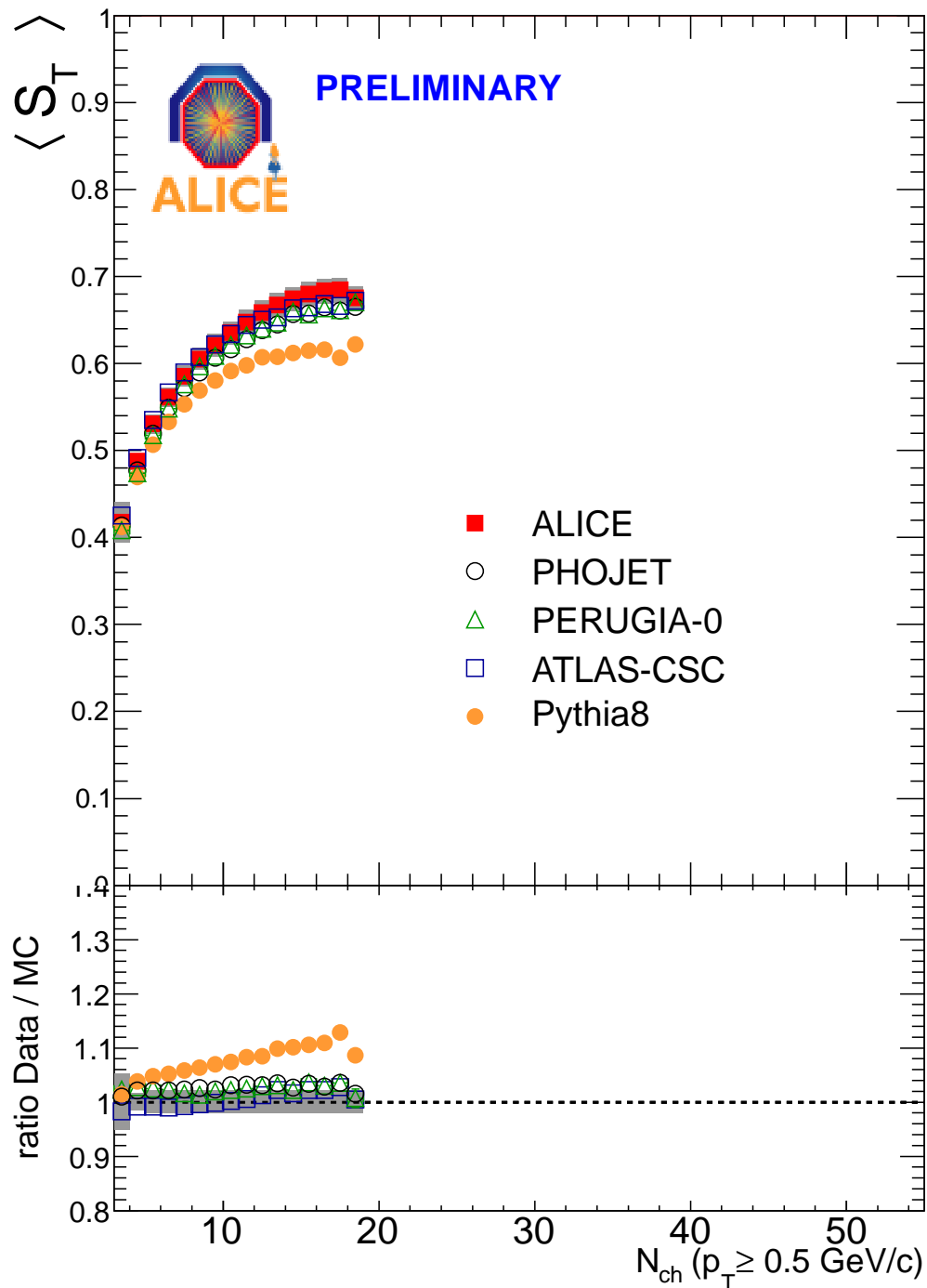


Figure 6.13: Mean transverse sphericity as a function of charged particle multiplicity for $p - p$ collisions at $\sqrt{s} = 0.9$ TeV. The statistical errors are displayed as error bars and the systematic uncertainties as the shaded area. Symbols for data points and model predictions are presented in the legend. The results are shown for “bulk” events

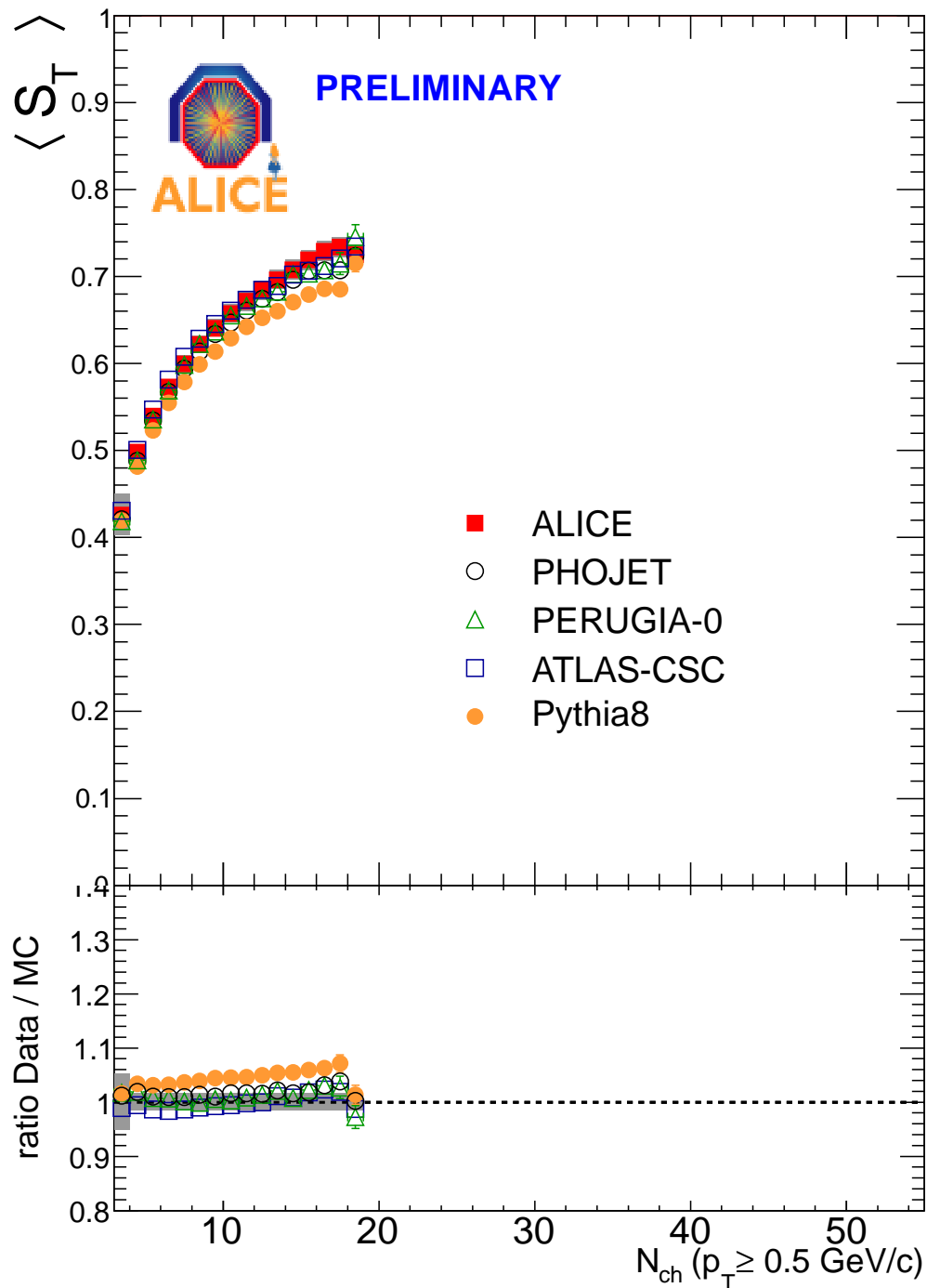


Figure 6.14: Mean transverse sphericity as a function of charged particle multiplicity for $p - p$ collisions at $\sqrt{s} = 0.9 \text{ TeV}$. The statistical errors are displayed as error bars and the systematic uncertainties as the shaded area. Symbols for data points and model predictions are presented in the legend. The results are shown for “soft” events

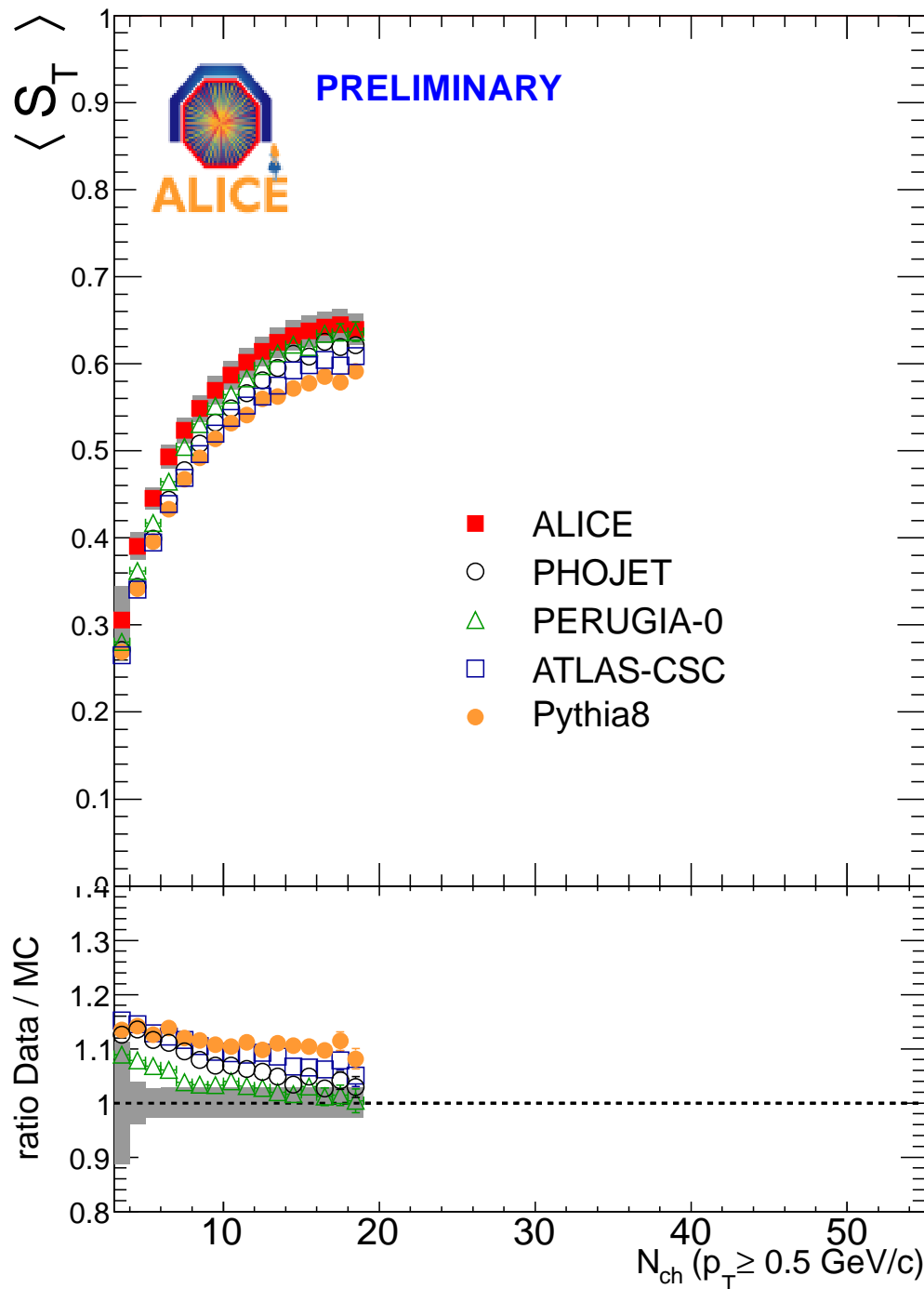


Figure 6.15: Mean transverse sphericity as a function of charged particle multiplicity for $p - p$ collisions at $\sqrt{s} = 0.9 \text{ TeV}$. The statistical errors are displayed as error bars and the systematic uncertainties as the shaded area. Symbols for data points and model predictions are presented in the legend. The results are shown for “hard” events

6.2.2 Results on $\langle S_T \rangle$ in 7 TeV data

Figs. 6.16, 6.17 and 6.18 shows the mean sphericity as a function of charged multiplicity for “bulk”, “soft” and “hard” events, respectively at 7 TeV. The behavior of the “bulk” events are in disagreement with the models, except in the range $N_{ch} = 3 - \sim 10$, where ATLAS-CSC reproduces the shape of the measurements. However, for highest multiplicities, PYTHIA simulations reach a value $\langle S_T \rangle \sim 0.7$ and then, around $N_{ch} \sim 25$ they present a slight fall. For PHOJET a most dramatic fall at multiplicities around 25 is observed. The rest of the MCs look similar at both energies. In contrast ALICE data exhibit a more isotropic behavior for events having multiplicities larger than 20.

For the “soft” data, the four models describe reasonably well the trend of the measurements; over the whole range of multiplicity we have an offset of less than 10% in the ratios. So, the differences observed in the “bulk” are caused by the events of “hard” nature. By looking at the “hard” events, the mean the sphericity predicted by the models is smaller than the measured one in the complete range of multiplicity. The fall in PHOJET for this event class is present as well.

Comparing Figs. 6.13 and 6.16 it is seen that the predictions of various models have a larger spread at 7 TeV than at 0.9 TeV. Specifically, at 0.9 TeV the values $\langle S_T \rangle$ of PYTHIA8 is the smallest while at 7 TeV it is closer to the other predictions.

6.2.3 Mean transverse momentum

Fig. 6.19 displays $\langle p_T \rangle$ as a function of charged multiplicity. For “bulk” events, at 0.9 TeV, Fig. 6.19 shows that PERUGIA-0 reproduces best the data, while PYTHIA8 is in good agreement for multiplicities up to 12, beyond which its slope increases noticeably compared to the measurements. PHOJET and ATLAS-CSC are softer than data. For the data at 7 TeV the slope of the data is smaller than that of the MC with the exception of the ATLAS-CSC MC result. Generally we observe that, the slope of the generators tends to increase significantly around 30. This behavior is consistent with our observations of sphericity since at these multiplicities, the $\langle S_T \rangle$ of generators reaches a maximum and then decreases sharply at higher values. In contrast, for lower multiplicities, PHOJET more closely approximates the data. PERUGIA-0 is harder than the data over the full range of multiplicity and ATLAS-CSC is softer. This behavior in terms of multiplicity dependence implies that PERUGIA-0 contains more jets than the data.

Considering the “soft” events, at 0.9 TeV PERUGIA-0 and PYTHIA8 describe the data well. At 7 TeV for multiplicities smaller than 20, PERUGIA-0, PHOJET and PYTHIA8¹, are in good agreement with data while at higher multiplicities differences are observed. For the “hard” events the difference with generators above a multiplicity of 20 is even more noticeable. The measurements imply that the generators seem to build the high multiplicity

¹In the next paragraph it will be demonstrated that the agreement is fortuitous.

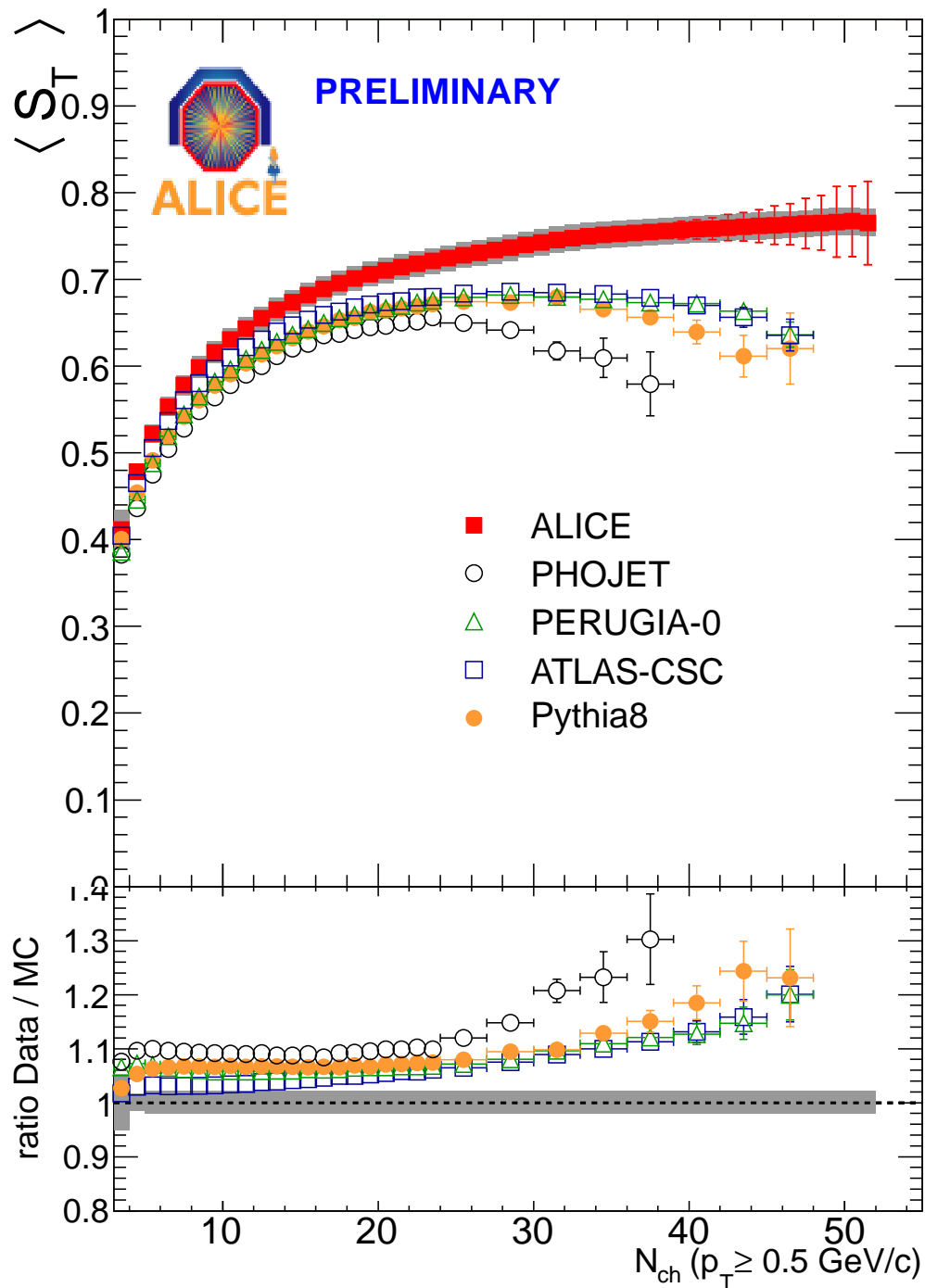


Figure 6.16: Mean transverse sphericity as a function of charged particle multiplicity for $p - p$ collisions at $\sqrt{s} = 7 \text{ TeV}$. The statistical errors are displayed as error bars and the systematic uncertainties as the shaded area. Symbols for data points and model predictions are presented in the legend. The results are shown for “bulk” events.

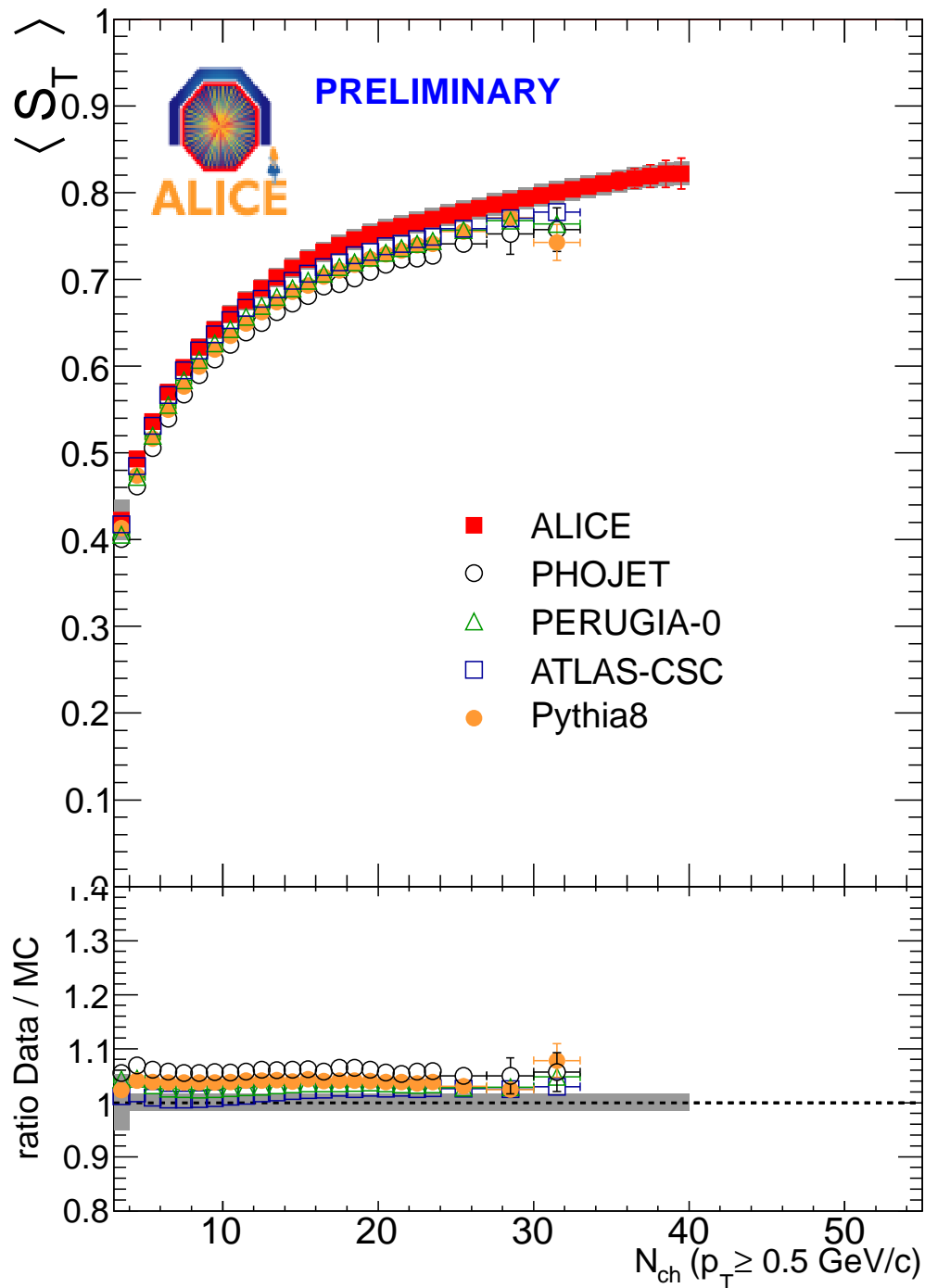


Figure 6.17: Mean transverse sphericity as a function of charged particle multiplicity for $p - p$ collisions at $\sqrt{s} = 7 \text{ TeV}$. The statistical errors are displayed as error bars and the systematic uncertainties as the shaded area. Symbols for data points and model predictions are presented in the legend. The results are shown for “soft” events.

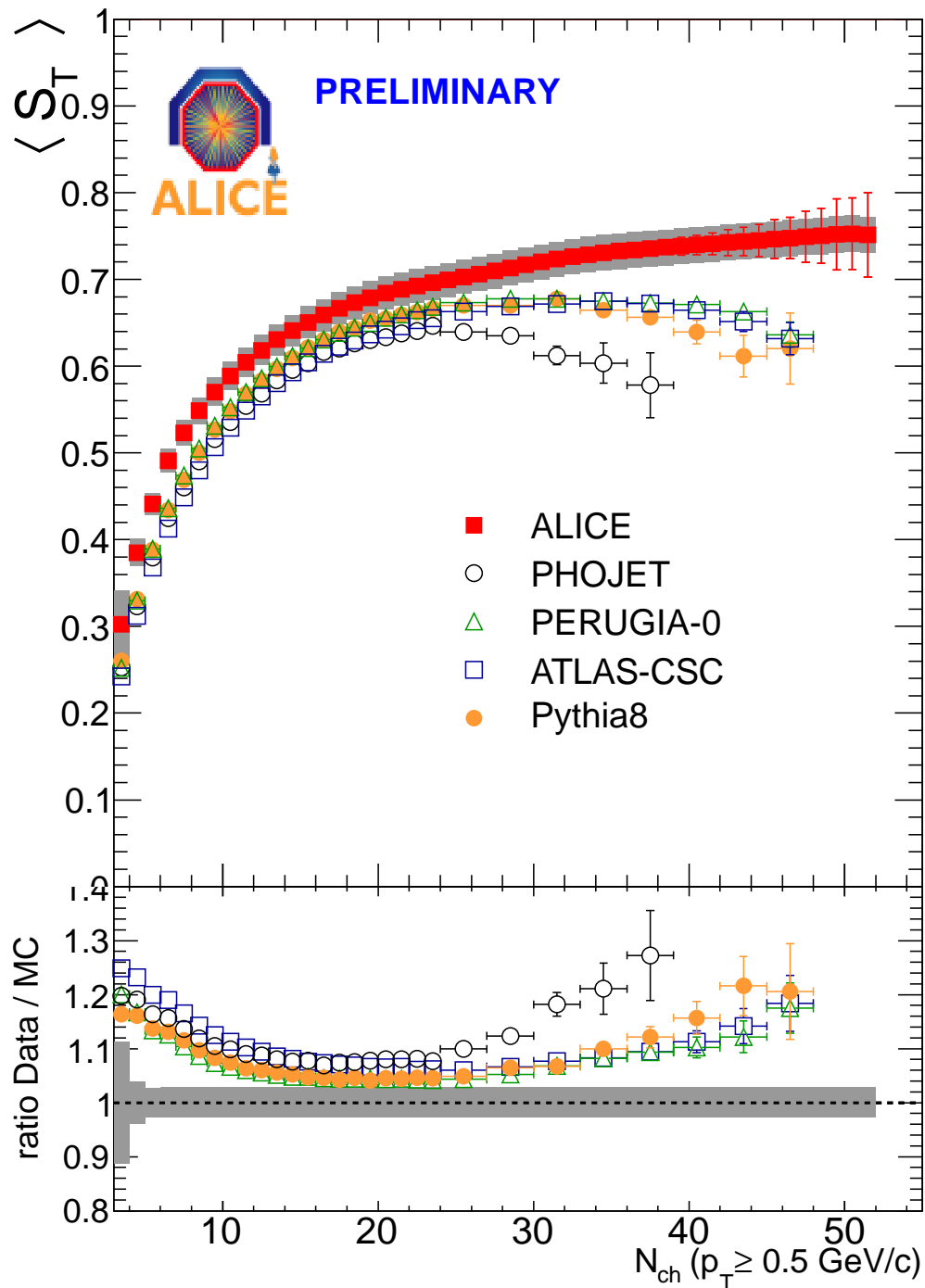


Figure 6.18: Mean transverse sphericity as a function of charged particle multiplicity for $p - p$ collisions at $\sqrt{s} = 7 \text{ TeV}$. The statistical errors are displayed as error bars and the systematic uncertainties as the shaded area. Symbols for data points and model predictions are presented in the legend. The results are shown for “hard” events.

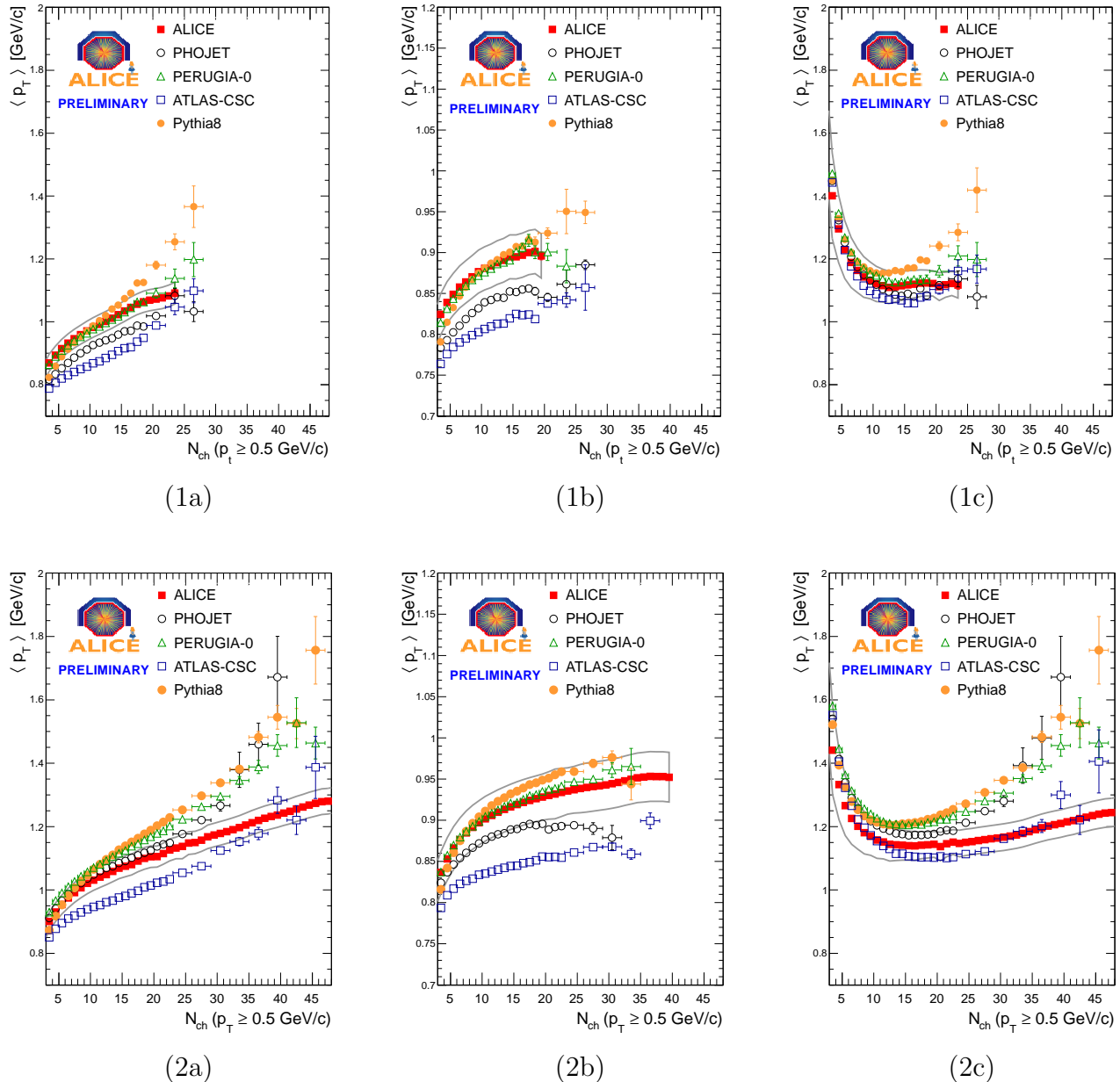


Figure 6.19: Mean transverse momentum versus multiplicity. The ALICE data are compared with four models: PHOJET [Eng95], PYTHIA6 (tunes: ATLAS-CSC [Mor] and PERUGIA-0 [Ska]) and PYTHIA8 [eab]. Results at $\sqrt{s} = 0.9$ and 7 TeV are shown in the rows 1 and 2 respectively. Different event classes are presented: “bulk” (a), “soft” (b) and “hard” (c).

events by augmenting the $\langle p_T \rangle$ of the events.

6.2.4 S_T spectra in multiplicity bins

To disentangle the ambiguities between $\langle p_T \rangle$, $\langle S_T \rangle$ and multiplicity we extracted also the normalized transverse sphericity spectra (plotting the probability of having events of different transverse sphericity in a given multiplicity bin) were computed for four different bins of multiplicity: $N_{ch} = 3 - 9$, $10 - 19$, $20 - 29$ and > 30 . These are shown in Figs. 6.20, 6.21, 6.22 and 6.23 along their ratios to the corresponding MC. In the first multiplicity bin, the agreement between data and MC is good, but in the next bin ($N_{ch} = 10 - 19$) the ratio data to MC reaches 0.3. In the last bin of multiplicity the overproduction of “jetty” events reaches a factor of 3, and the underestimation of the isotropic events is up to a factor 2.

In order to investigate the interplay between the mean transverse momentum, sphericity and multiplicity we did an exercise consisting in to extract the $\langle p_T \rangle$ in bins of multiplicity and sphericity. Remember that one of our arguments in the event shape analysis is that low S_T events are harder than the high S_T ones, so, it is interesting to see the effect of the sphericity spectra in the mean p_T analysis. This study has been done using MC generators at $\sqrt{s} = 7$ TeV, but the conclusion is general. Fig. 6.24 shows $\langle p_T \rangle$ as a function of S_T for two multiplicities (upper panels) alongside the contribution of each sphericity bin (lower panel) to the final mean p_T , *i. e.* the mean p_T weighted by the value $P(S_T)$ from Fig. 6.20. There are two points to emphasize. Firstly, in the upper panel we observe a very large dependence of p_T on sphericity for high multiplicities and secondly, we observe that for identical p_T predictions their contributions can be very different in function of S_T . For instance at $S_T = 0.4$ PHOJET and ATLAS-CSC have about the same value, while the contribution to the mean p_T is twice larger for PHOJET. Hence, without the reproduction of the sphericity it might be very difficult to tune the generators.

6.2.5 Evolution of the transverse sphericity with multiplicity at 0.9, 2.76 and 7 TeV

The last part of this thesis is dedicated to a comparison of the mean sphericity at the three energies. Figs. 6.25, 6.26 and 6.27 show the results for “bulk,” “soft” and “hard” events, respectively. The ALICE data are compared with PYTHIA8 and PHOJET. In real data we see that the functional form of the mean sphericity as a function of N_{ch} is the same at all three energies except for the last bins. On the other hand, the MCs exhibit a dependence different from that of the data and also differ among themselves for “bulk” and “hard” events. On the contrary, the predictions for “soft” events describe quite good the data, this was seen in the previous section.

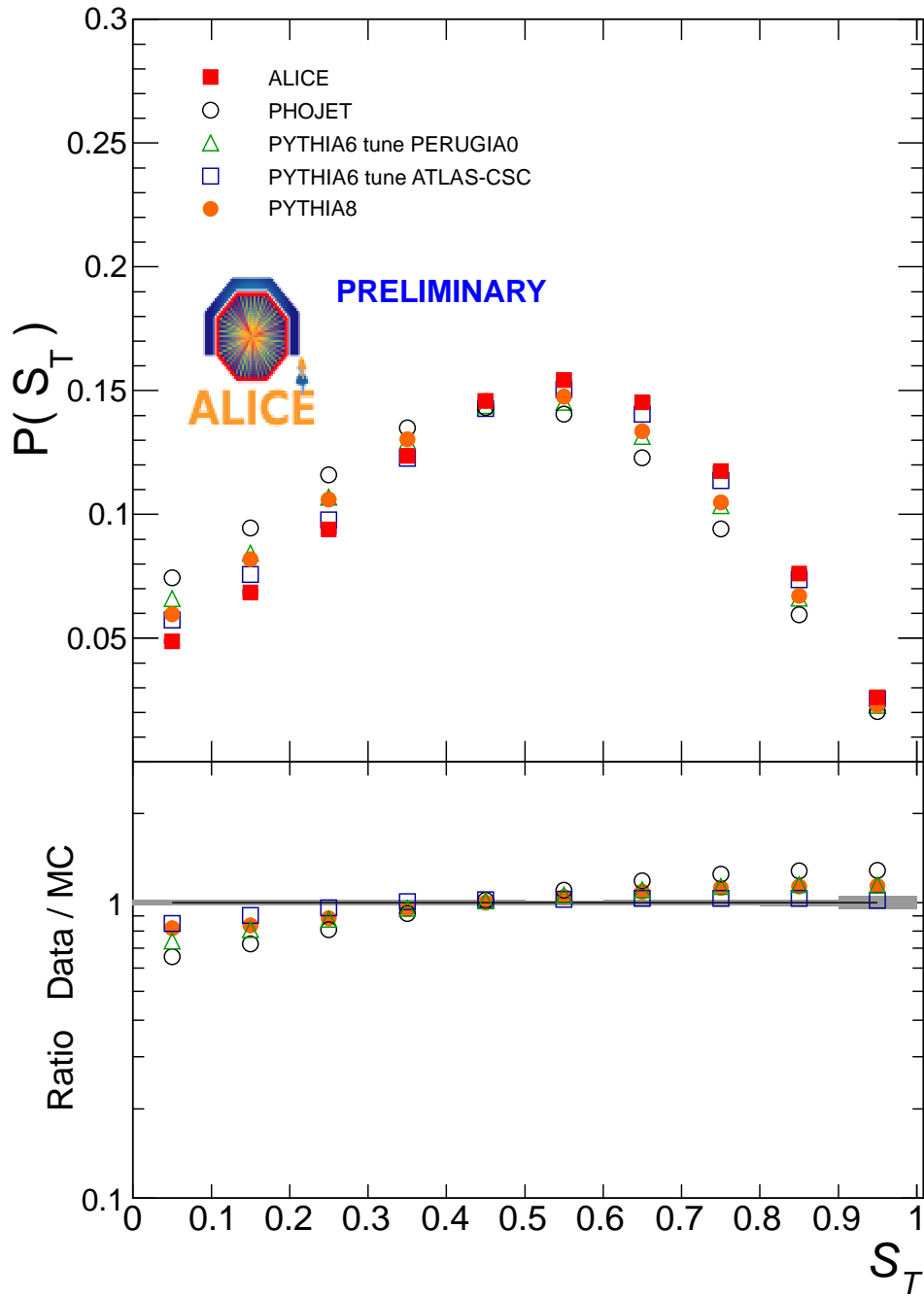


Figure 6.20: Sphericity spectrum in the bin of multiplicity: $3 \leq N_{ch} < 10$. The result is for $p - p$ collisions at $\sqrt{s} = 7$ TeV. The statistical errors are displayed as error bars and the systematic uncertainties as the shaded area. Symbols for data points and model predictions are presented in the legend. The results are shown for “hard” events.

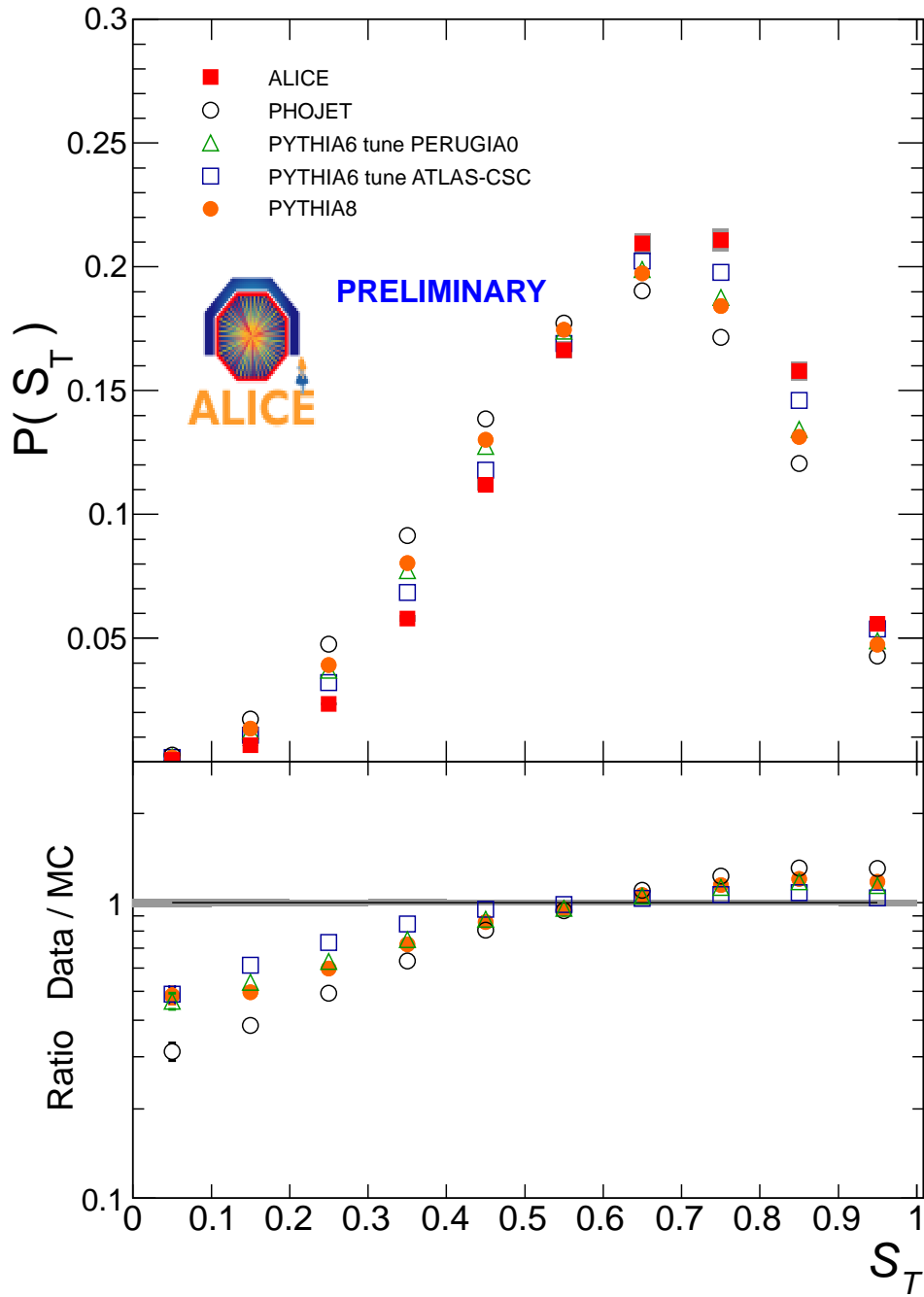


Figure 6.21: Sphericity spectrum in the bin of multiplicity: $10 \leq N_{ch} < 20$. The result is for p – p collisions at $\sqrt{s} = 7$ TeV. The statistical errors are displayed as error bars and the systematic uncertainties as the shaded area. Symbols for data points and model predictions are presented in the legend. The results are shown for “hard” events.

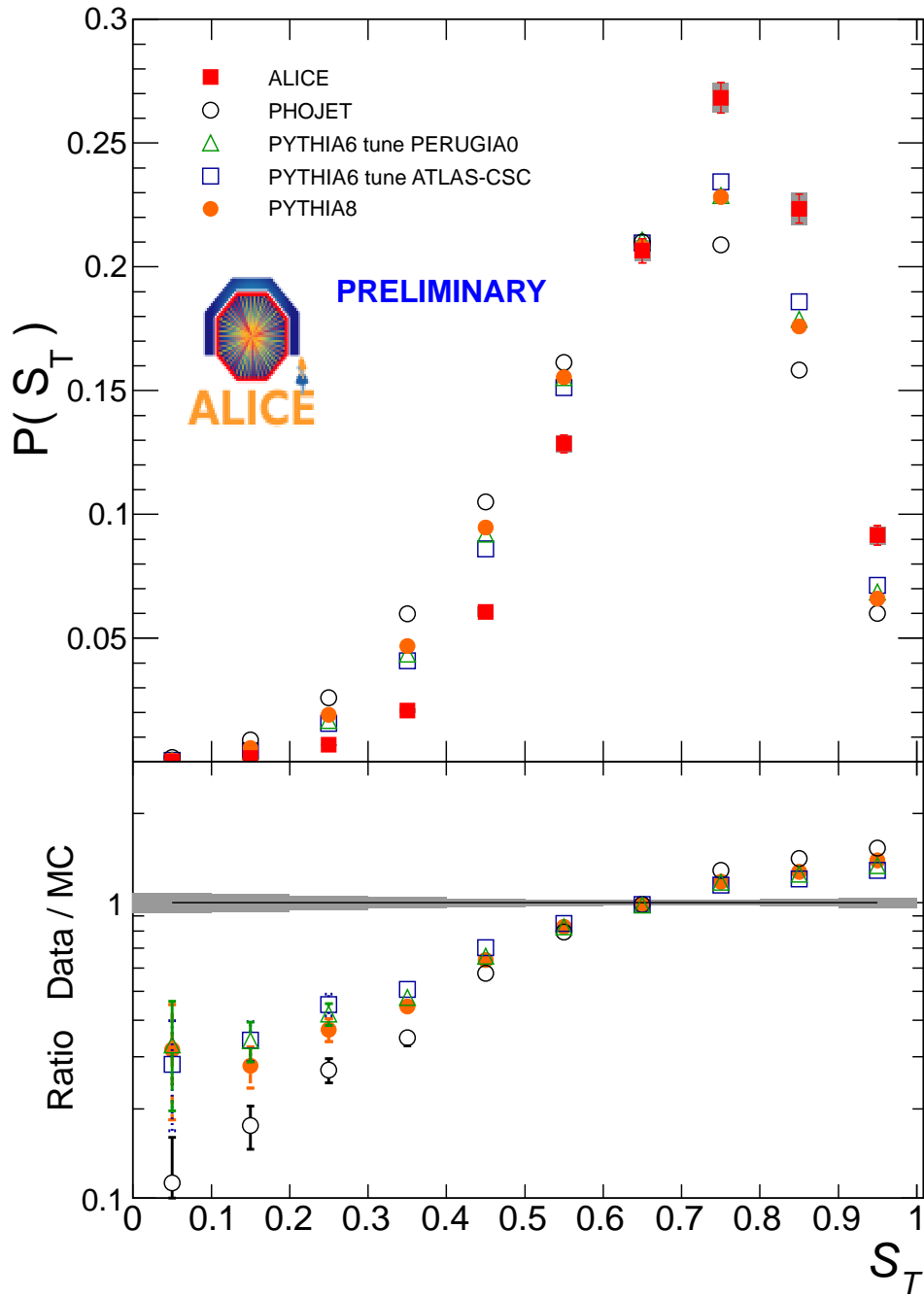


Figure 6.22: Sphericity spectrum in the bin of multiplicity: $20 \leq N_{ch} < 30$. The result is for p – p collisions at $\sqrt{s} = 7$ TeV. The statistical errors are displayed as error bars and the systematic uncertainties as the shaded area. Symbols for data points and model predictions are presented in the legend. The results are shown for “hard” events.

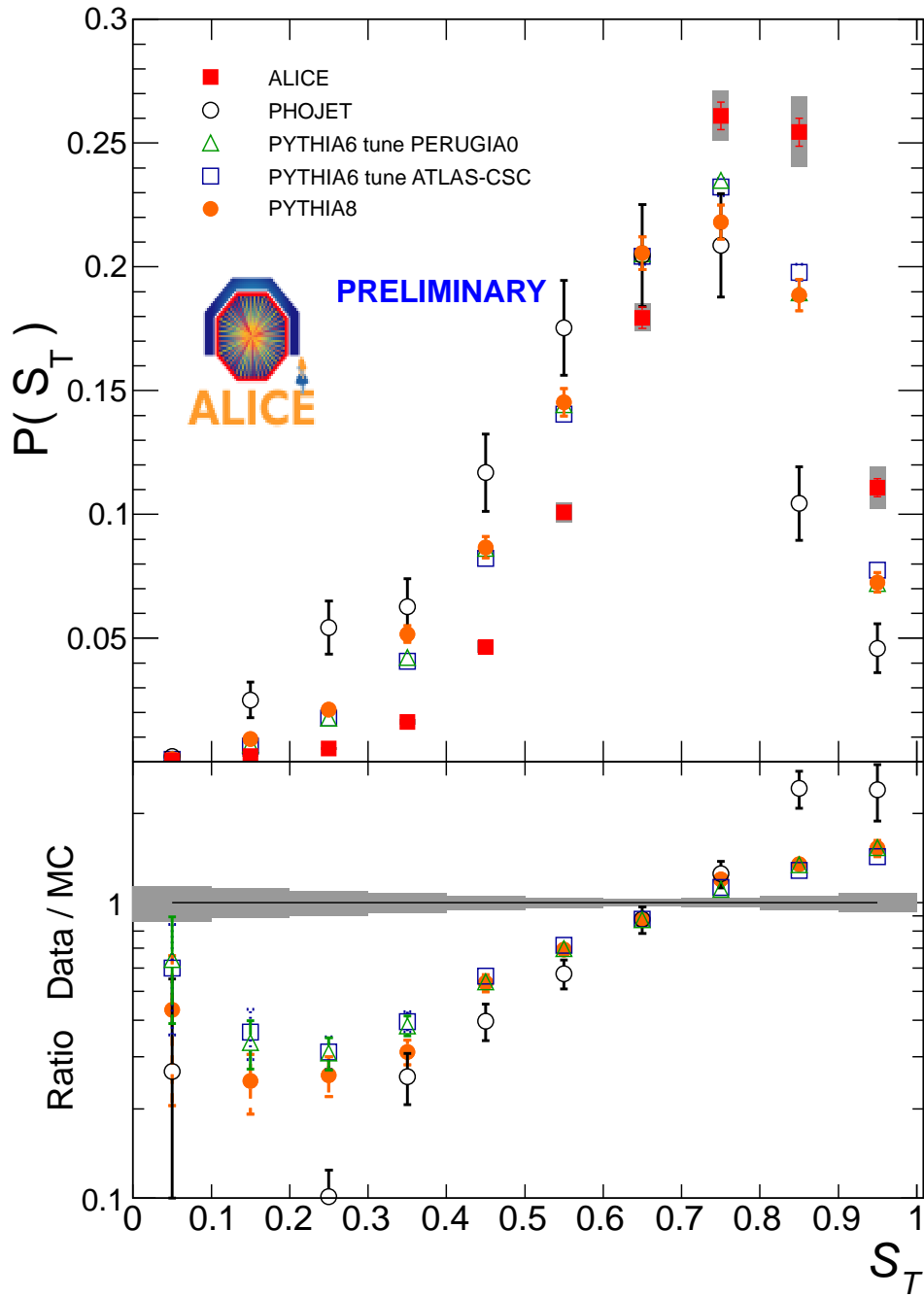


Figure 6.23: Sphericity spectrum in the bin of multiplicity: $N_{ch} \geq 30$. The result is for p – p collisions at $\sqrt{s} = 7$ TeV. The statistical errors are displayed as error bars and the systematic uncertainties as the shaded area. Symbols for data points and model predictions are presented in the legend. The results are shown for “hard” events.

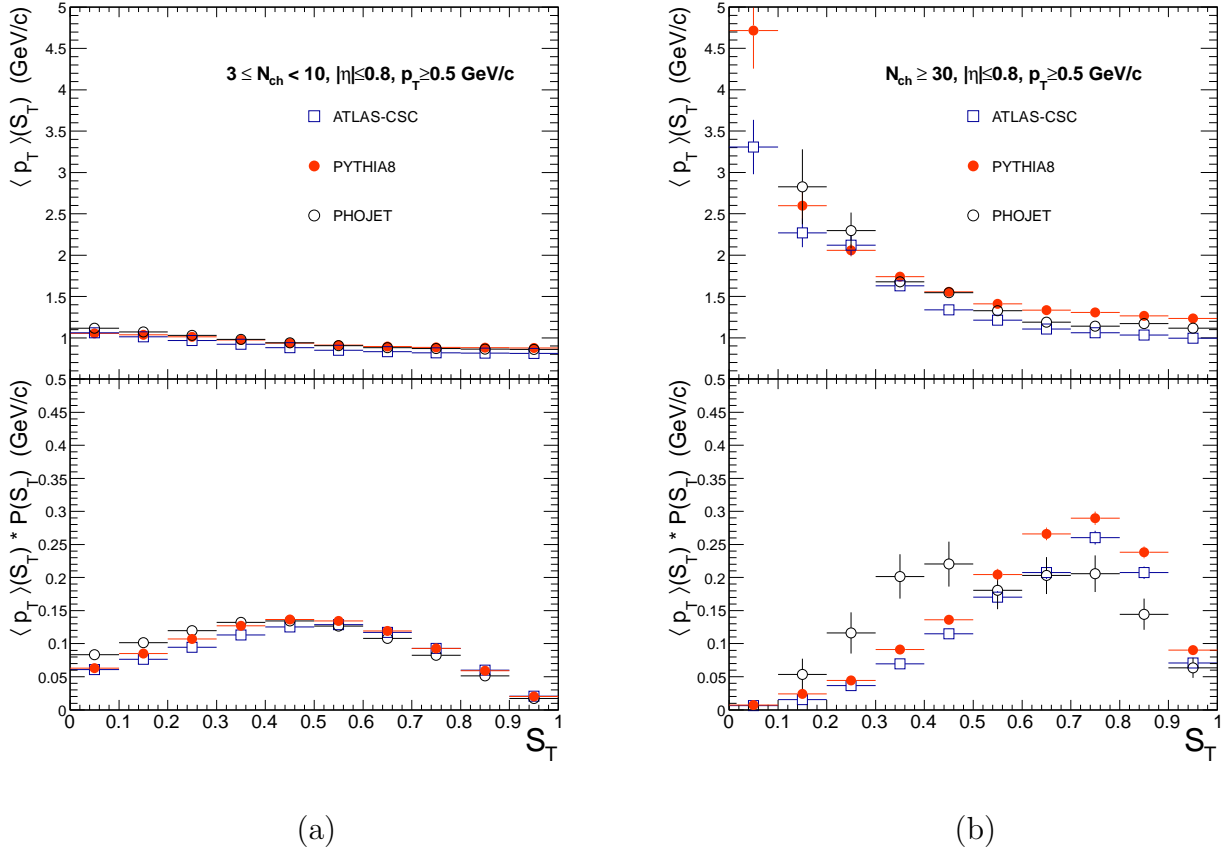


Figure 6.24: Mean p_T as a function of sphericity for two multiplicity bins: (a) $3 \leq N_{ch} < 10$ and (b) $N_{ch} \geq 30$. The plots were obtained using MB pp collisions at $\sqrt{s} = 7$ TeV simulated with three different MC generators: PYTHIA6 (tune ATLAS-CSC), PYTHIA8 and PHOJET. Also the contributions of the different event topologies to the averaged mean p_T is presented.

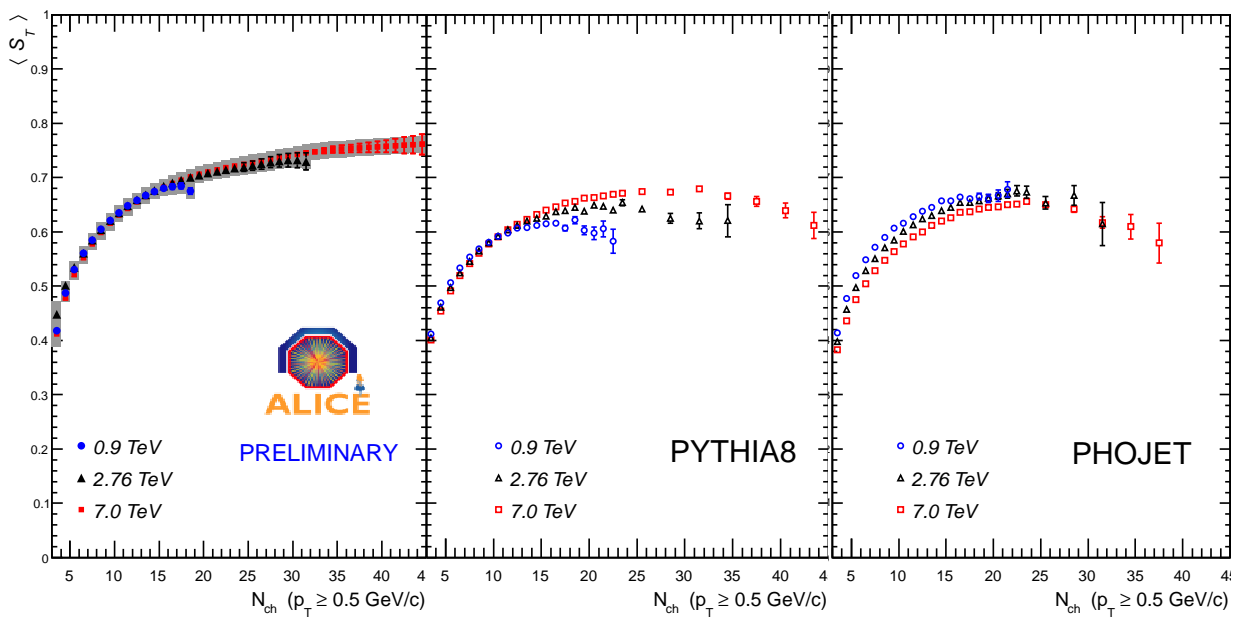


Figure 6.25: Mean sphericity versus multiplicity for “bulk” events. Three samples at different energies were analyzed: $\sqrt{s} = 0.9$, 2.76 and 7 TeV. ALICE data are compared with PYTHIA8 and PHOJET.

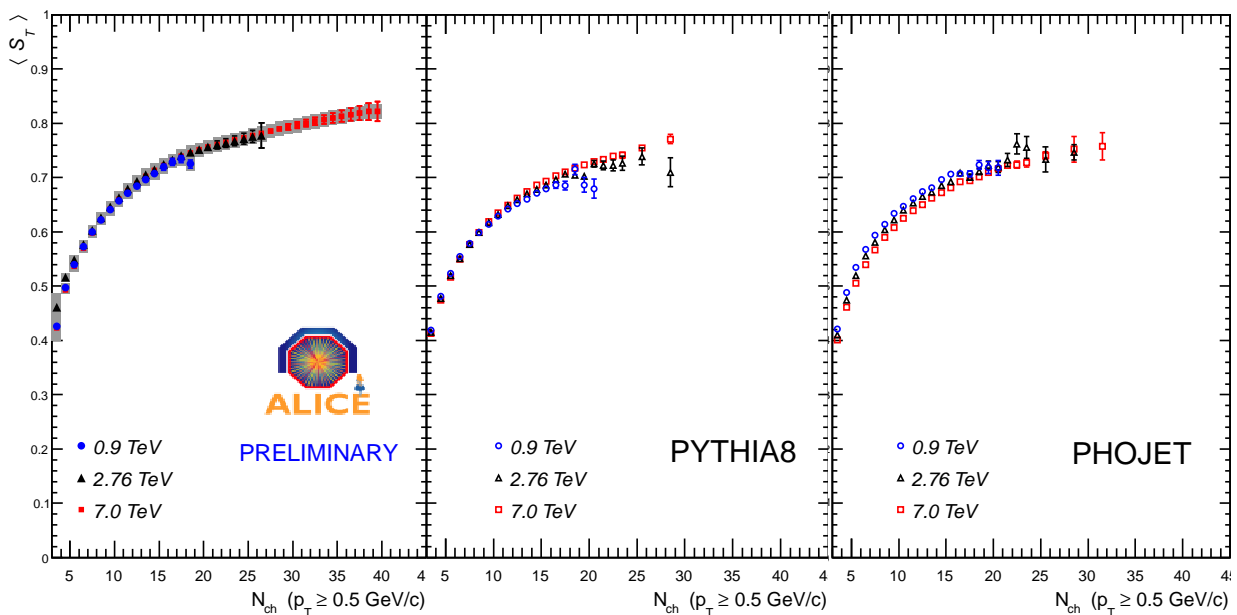


Figure 6.26: Mean sphericity versus multiplicity for “soft” events. Three samples at different energies were analyzed: $\sqrt{s} = 0.9$, 2.76 and 7 TeV. ALICE data are compared with PYTHIA8 and PHOJET.

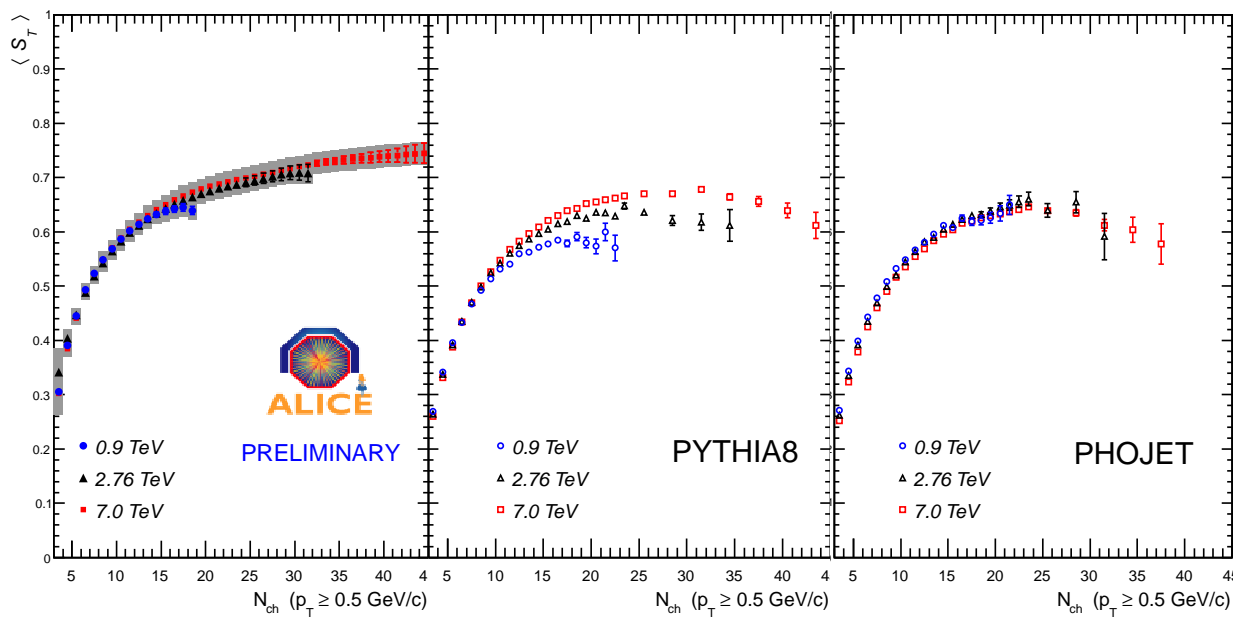


Figure 6.27: Mean sphericity versus multiplicity for “hard” events. Three samples at different energies were analyzed: $\sqrt{s} = 0.9$, 2.76 and 7 TeV. ALICE data are compared with PYTHIA8 and PHOJET.

6.3 Discussion

In the present paper we have studied the behavior of the (linearized) transverse sphericity and of the mean transverse momentum as a function of the charged particle multiplicity in MB proton-proton interactions at $\sqrt{s} = 0.9, 2.76$ and 7 TeV. The data samples were split in two categories: “soft” ($p_T^{\max} < 2$ GeV/c) and “hard” ($p_T^{\max} \geq 2$ GeV/c), but also the entire sample was analyzed, “bulk”. The selection of 2 GeV/c was not arbitrary since is the general accepted limit between soft and hard processes [ea11]. For parton-parton interactions the differential cross section is divergent for $p_T \rightarrow 0$, so that a lower cut-off has to be introduced in order to regularize the divergence, for example in PYTHIA6 the default cut-off is 2 GeV for $2 \rightarrow 2$ processes [Sjo94]. With a different approach, CDF and STAR [Col02b, Hua] have addressed the problem, they demonstrated that the mean p_T as a function of multiplicity does not evolve much from RHIC energy (0.2 TeV) to the CDF energy (0.63 TeV and 1.8 TeV) for the “soft” part while the “hard” part exhibits an evolution towards larger values. This information was paramount in our decision to split the samples.

Throughout the thesis we have seen that the differences between the generators and the data are generally small for “soft” events, suggesting that by considering only the “bulk” events one reduces the differences between the generators and in comparison to the data. The main features observed in the present analysis are:

1. Looking at Table 6.1 we observe firstly that the predictions in the ratio soft to hard exhibits very different behavior at the two energies reported. While at 0.9 TeV the generators predict a much softer spectrum where the ratio reaches up to twice the measured value, at 7 TeV the predictions are more grouped and generally much closer to the measurements except for ATLAS-CSC.
2. The transverse sphericity was studied in two ways: extracting the mean S_T as a function of multiplicity, and in a more differential manner plotting the S_T spectra for different multiplicity bins. The analysis has revealed important features. The first observation is that the generators exhibit a decrease of $\langle S_T \rangle$ at high multiplicity with a simultaneous steep rise of $\langle p_T \rangle$. On the contrary, in ALICE data $\langle S_T \rangle$ stays approximately constant or even slightly rising accompanied with a mild increase in $\langle p_T \rangle$ (Fig. 6.19). In both cases the differences between predictions and data are clearly outside the systematic uncertainties. The observation of the “coupling” of the mean p_T and mean sphericity prompted us to investigate the sphericity spectra in different bins of multiplicities. The results shown in Fig. 6.20 clarified considerably the situation. For instance, it is clear that at high multiplicity ($N_{ch} \geq 30$) the generators underestimate the production of isotropic events and overestimate the production of jetty-like events. This points to a flaw in the approach of the generators. Namely, the generators tend to “produce” large multiplicity events by favoring the production of high p_T jets (low S_T) more so than in nature.
3. The separation in two hardness classes has demonstrated that the nature of the agree-

ment or disagreement between the generators and with data are different for soft and hard events.

4. The functional form of $\langle S_T \rangle$ as a function of N_{ch} is the same at all three energies in the overlapping region. The MC generators show a different behavior.

Chapter 7

Conclusions

The event shape analysis opens many possibilities of studies in the perturbative and non-perturbative QCD regimens in high energy hadronic interactions. The main results based on the Monte Carlo event generators: PYTHIA and PHOJET are:

- The event shapes allow to discriminate events with specific jet topologies, *vis.* single-jet, di-jet and multi-jet. This is attained cutting on the variables thrust and recoil which define the so-called “thrust-map.”
- The PYTHIA parameters which control the underlying activity, in specific the multi-parton interaction, they show large effects on thrust, thrust-minor and transverse sphericity spectra and on their correlations with the multiplicity and mean p_T . It was demonstrated that high multiplicity events mostly come from hard processes, so, the multiplicity correlations were proposed to be used as a test of pQCD at extreme multiplicity, where many generators show substantial differences.

From the ESA applied to MB pp collisions at $\sqrt{s} = 0.9$ and 7 TeV we can conclude:

- The analysis of the mean transverse sphericity of “hard” and “soft” events shows that the later are well reproduced by the existing generator codes, while for the “hard” events we observe a substantial difference in the behavior of the S_T . The highest multiplicity events show a substantial difference with respect to the generator prediction.
- There is a marked difference in the behavior of the “hard” and “soft” events in the sphericity parameter up to rather important multiplicities - at low multiplicities the difference is of a factor of 2 diminishing to a value of 1.2 at the highest multiplicities.
- The $\langle S_T \rangle$ shows a saturation in the data at high multiplicity while the generators indicate a fall in the sphericity. Studies of systematic errors like: rejection of secondaries pile-up, track cuts, model dependence do not allow to explain the discrepancy in trend.

- The analysis of the S_T spectra exhibit two clear features: a lack of low sphericity events in the data at moderate multiplicities and an excess over at high sphericity compared with models. The results are comparable for all the generators.
- The $\langle p_T \rangle$ distribution for “hard” events shows a much slower rise in the case of data especially at 7 TeV than is predicted by the generators.

The above findings lead us to resume the present work as an indication that the treatment of MB events in pp collisions in the generators is actually not adequate especially for the high multiplicity events. It seems that the generators favor the production of high momentum emissions (multi-jets?) while the data show a tendency of isotropic lower p_T emission.

Bibliography

- [AAAJea08] [LHCb Collaboration] A. Augusto Alves Jr. et. al. *JINST*, 3:S08005, 2008.
- [ACD⁺09] A. Ayala, E. Cuautle, I. Domínguez, A. Ortiz, and G. Paic. *Eur. Phys. J.*, C62:535–540, 2009.
- [aDVS95] M. E. Peskin and D. V. Schroeder. *An Introduction To Quantum Field Theory*. Reading, USA: Addison-Wesley, 1995.
- [Alb10] S. Albino. *Rev. Mod. Phys.*, 82:2489–2556, 2010.
- [aLR] W. Blum and L. Rolandi. *Particle Detection with Drift Chambers*. Springer.
- [aPS11] K. Wraight and P. Skands. *Eur.Phys.J.*, C71:1628, 2011.
- [Bet03] S. Bethke. *Nucl. Phys.*, 121:74, 2003.
- [Blo] V. Blobel. “Unfolding Methods in High-Energy Physics Experiments”, DESY 84/118 (1984).
- [BSZ] A. Banfi, Gavin P. Salam, and G. Zanderighi. Arxiv:1001.4082v1.
- [Col77] P. D. B. Collins. *An Introduction to Regge Theory and High-Energy Physics*. Cambridge University Press, 1977.
- [Col79a] MARK-J Collaboration. *Phys. Rev. Lett.*, 43:830, 1979.
- [Col79b] PLUTO Collaboration. *Phys. Rev.*, B86:418, 1979.
- [Col79c] TASSO Collaboration. *Phys. Rev.*, B86:243, 1979.
- [Col80] JADE Collaboration. *Phys. Rev.*, B91:142, 1980.
- [Col02a] CDF Collaboration. *Phys. Rev.*, D65:092002, 2002.
- [Col02b] [CDF Collaboration]. *Phys. Rev.*, D65:072005, 2002.
- [Col03] D0 Collaboration. *Phys. Rev.*, D67:0520001, 2003.

- [Col10] CMS Collaboraction. *JHEP*, 09:1009.4122, 2010.
- [Col11a] CDF Collaboration. *Phys. Rev.*, D83:112007, 2011.
- [Col11b] CMS Collaboration. *Phys. Lett.*, B699:48–67, 2011.
- [COP] E. Cuautle, A. Ortiz, and G. Paic. ALICE note, ALICE-INT-2010-013.
- [CSTV94] A. Capella, U. Sukhatme, C. I. Tan, and J. Tran Thanh Van. *Phys. Rept.*, 236:225, 1994.
- [DS04] M. Dasgupta and G. P. Salam. *J. Phys.*, G30, 2004.
- [eaa] E. Cuautle et al. Sensitivity of the parameters measured in pp collisions on the gluon PDF, arXiv:1001.0613 [hep-ph].
- [eab] T. Sjstrand et al. CERN-LCGAPP-2007-04 LU TP 07-28.
- [ea75] G. Hanson et al. *Phys. Rev. Lett.*, 35:1609, 1975.
- [ea84] A. Breakstone et al. *Phys. Rev.*, D30:528, 1984.
- [ea87a] G. J. Alner et al. *Phys. Rep.*, 154:247, 1987.
- [ea87b] T. Akesson et al. *Z. Phys.*, C34:163, 1987.
- [ea90] F. Abe et al. *Phys. Rev.*, D41:2330, 1990.
- [ea91] J. Alitti et al. *Phys. Lett.*, B268:145, 1991.
- [ea94] G. A. Schuler et al. *Phys. Rev.*, D49:2257, 1994.
- [ea96] H. L. Lai et al. *Phys. Rev.*, D55:1280–1296, 1996.
- [ea97] F. Abe et al. *Phys. Rev.*, D56:3811, 1997.
- [ea98] T. Alexopoulos et al. *Phys. Lett.*, B435:453, 1998.
- [ea99] S. G. Matinyan et al. *Phys. Rev.*, D59:034022, 1999.
- [ea00] H. L. Lai et al. *Eur. Phys. J.*, C12-3:375–392, 2000.
- [ea02] J. Pumplin et al. *JHEP*, 07:1126–6708, 2002.
- [ea04a] A. Banfi et al. *JHEP*, 0408:062, 2004.
- [ea04b] F. Carminati et. al. *J. Phys.*, G30, 2004.
- [ea06] B. Alessandro et. al. *J. Phys.*, G32, 2006.
- [ea08a] A. Moraes et al. *Eur. Phys. J.*, C50:435–466, 2008.

- [ea08b] C. Amsler et al. *Phys. Lett.*, B667, 2008.
- [ea08c] L. Evans et. al. *JINST*, 3:S08001, 2008.
- [ea11] Wei-Tian Deng et al. *Phys. Rev.*, C83:014915, 2011.
- [eaPC08] A. Adare et al. [PHENIX Collaboration]. *Phys. Rev.*, C78:014901, 2008.
- [eaZC05] S. Chekanov et al. [ZEUS Collaboration]. *Eur. Phys. J.*, C42-1:1–16, 2005.
- [Eng95] R. Engel. *Z. Phys.*, C66:203, 1995.
- [Fer92] R. C. Fernow. *Introduction to Experimental Particle Physics*. Cambridge University Press, 1986/1989/1992.
- [FFF78] R. P. Feynman, R. D. Field, and G. C. Fox. *Phys. Rev.*, D18:3320–3343, 1978.
- [Fie] R. Field. http://www.phys.ufl.edu/rfield/cdf/chgjet/chgjet_intro.html.
- [Fie89] R. D. Field. *Frontiers in physics*, 77. Addison-Wesley, 1989.
- [ftAC11] A. Ortiz for the ALICE Collaboration. *AIP Conf. Proc.*, 1348:111–117, 2011.
- [GAea08] [ATLAS Collaboration] G. Aad et. al. *JINST*, 3:S08003, 2008.
- [GM64] M. Gell-Mann. *Phys. Lett.*, 8:214, 1964.
- [GO09] J. F. Grosse-Oetringhaus. *Measurement of the Charged-Particle Multiplicity in Proton-Proton Collisions with the ALICE Detector*. PhD thesis, 2009. CERN-THESIS-2009-033.
- [GOE] J. F. Grosse-Oetringhaus and C. Ekman. ALICE note ALICE-INT-2007-005.
- [Gri08] D. Griffiths. *Introduction to Elementary Particles*. Wiley-VCH, 2nd edition, 2008.
- [Hig64] P. W. Higgs. *Phys. Lett.*, 12:132, 1964.
- [Hua] S. Huang. arXiv:0403038v1 [nucl-ex].
- [Jam68] F. James. Monte Carlo Phase Space. *CERN 68-15*, 1968.
- [JFD92] E. Golowich and B. R. Holstein J. F. Donoghue. *Dynamics of the standard model*, volume 2. Cab. Monogr. Part.Phys. Cosmol., 1992.
- [KAea10a] [ALICE collaboration] K. Aamodt et. al. *Phys. Rev. Lett.*, 105:252301, 2010.
- [KAea10b] [ALICE collaboration] K. Aamodt et. al. *Eur. Phys. J.*, C68:345–354, 2010.
- [KAea10c] [ALICE collaboration] K. Aamodt et. al. *Phys. Lett.*, B693:53–68, 2010.

- [KAea10d] [ALICE Collaboration] K. Aamodt et. al. *Phys. Rev. Lett.*, 105, 2010.
- [KAea10e] [ALICE Collaboration] K. Aamodt et. al. *JINST*, 5:P03003, 2010.
- [KAea10f] [ALICE collaboration] K. Aamodt et. al. *Eur. Phys. J.*, C65:111–125, 2010.
- [Kai94] A. B. Kaidalov. *Phys. Atom. Nucl.*, 66:2003, 1994.
- [Mor] A. Moraes. ATLAS Note ATL-COM-PHYS-2009-119, ATLAS CSC (306) tune.
- [OP] A. Ortiz and G. Paic. ALICE note ALICE-INT-2009-015.
- [P.84] Billoir P. *Nucl. Instrum. Meth.*, A225:352, 1984.
- [PA96] et al. P. Abreu. *Z. Physik*, C73:11, 1996.
- [Pau40] W. Pauli. *Phys. Rev.*, 58:716–722, 1940.
- [Per00] D. H. Perkins. *Introduction to High-Energy Physics*. Cambridge University Press, 4th edition, 2000.
- [SCea08] [CMS Collaboration] S. Chatrchyan et. al. *JINST*, 3:S08004, 2008.
- [SGM99] W. D. Walker S. G. Matiyan. *Phys. Rev.*, D59:034022, 1999.
- [Sjo94] T. Sjöstrand. *Comput. Phys. Commun.*, 82:74, 1994.
- [SK01] et al. S. Kluth. *Eur. Phys. J.*, C21:199, 2001.
- [Ska] P. Z. Skands. Presented in Multi-Parton Interaction Workshop, Perugia, Italy, 28-31 Oct. 2008. arXiv:0905.3418 [hep-ex] (2009), Perugia-0 (320) tune.
- [SLM01] T. Sjöstrand, L. Lonnblad, and S. Mrenna. *Comput. Phys. Commun.*, 135:238, 2001.
- [YLD91] A. Mueller and S. Troyan Y. L. Dokshitzer, V. Khoze. *Basics of Perturbative QCD*. Editions Frontières, 1991.

List of Figures

1	Medición de la distribución de multiplicidad en $ \eta < 1$ para eventos inelásticos. Las barras de error de los datos representan el error estadístico mientras que las zonas sombreadas representan la incertidumbre sistemática. Los datos a $\sqrt{s} = 7$ TeV son comparados con los generadores Monte Carlo PHOJET y PYTHIA.	ix
2	Espectro de momento transverso de partículas primarias cargadas en colisiones $p - p$ a $\sqrt{s} = 7$ TeV medido con ALICE en el LHC. La figura muestra el espectro en el rango de 0.15 a 100 GeV/c además de la comparación con los generadores de eventos Monte Carlo PYTHIA y PHOJET así como la razón MC/Datos.	x
3	Distribución en dos dimensiones del número de pares de hadrones cargados correlacionados por trigger en función de $\Delta\eta$ y $\Delta\phi$ con un corte en el pico del jet para una mejor visibilidad del “ridge”. El estudio se hace para eventos de multiplicidad mayor a 110 hadrones cargados en colisiones $p - p$ a $\sqrt{s} = 7$ TeV. Dos casos son mostrados: (a) $2 < p_T^{trig} < 3$ GeV/c y $1 < p_T^{assoc} < 2$ GeV/c, (b) $5 < p_T^{trig} < 6$ GeV/c y $1 < p_T^{assoc} < 2$ GeV/c.	xii
4	Estructura de un evento de alta multiplicidad y baja esfericidad transversal en el espacio η - ϕ . El evento corresponde a una colisión de protones a $\sqrt{s} = 7$ TeV reconstruida por ALICE. Las trazas usadas para el cálculo son de partículas primarias con momento transverso mayor que 500 MeV/c en $ \eta < 0.8$	xiv
5	Estructura de un evento de alta multiplicidad y alta esfericidad transversal en el espacio η - ϕ . El evento corresponde a una colisión de protones a $\sqrt{s} = 7$ TeV reconstruida por ALICE. Las trazas usadas para el cálculo son de partículas primarias con momento transverso mayor que 500 MeV/c en $ \eta < 0.8$	xv
6	Distribución de la observable τ para eventos generados con PYTHIA6 modelo ATLAS-CSC[Mor] en los que se hacen diferentes cortes en la partícula de más alto momento transverso del evento.	xvi

7	Correlación a dos hadrones normalizada al número de partículas líder en el rango: $2 \leq p_T \leq 15$ GeV/c. Los eventos son generados con PYTHIA6 modelo ATLAS-CSC. Se muestran tres casos: todos los parámetros del modelo están activados, sin radiación de estado inicial (MSTP(61)=0), sin radiación de estado final (MSTP(71)=0). Los eventos tienen una multiplicidad mayor de dos partículas primarias cargadas con $p_T \geq 0.5$ GeV/c en $ \eta \leq 0.8$. Para ver la estructura de los eventos de acuerdo al valor de su esfericidad, se muestran tres tipos de selección: (izquierda) todo el rango de S_T , (en medio) $0 \leq S_T \leq 0.1$ y (derecha) $0.5 \leq S_T \leq 0.6$	xvii
8	Velocidad de deriva <i>vs.</i> intensidad del campo eléctrico en un detector de gas.	xx
9	Segmentación de los arreglos V0A/V0C.	xxiii
10	Prueba del funcionamiento del procedimiento de corrección del momento transverso promedio en función de la multiplicidad para los eventos “bulto”. En esta prueba, datos MC reconstruidos generados con PHOJET son corregidos usando PYTHIA6. En la gráfica se muestran los puntos corregidos y los puntos obtenidos directamente del generador (TRUE).	xxvii
1.1	Idealization of a large p_\perp hadronic interaction producing four jets.	5
1.2	Environment of the high energy hadron collisions.	6
1.3	Schematic view of: a) elastic, b) single-diffractive, c) double-diffractive and d) non-diffractive hadron interactions in the $\eta - \phi$ space.	7
2.1	ALICE schematic view.	14
2.2	Layout of the ITS and his orientation with respect to the ALICE global reference system.	15
2.3	Schematic view of the TPC.	17
2.4	Arrival time of particles in the V0 detectors relative to the beam crossing time. A number of beam-halo or beam-gas events are visible as secondary peaks in V0A (left panel) and V0C (right panel). This is because particles produced in back-ground interactions arrive at earlier times in one or the other of the two counters. The data correspond to the first $p - p$ collisions reconstructed by ALICE at $\sqrt{s} = 900$ GeV/c on November 2009 [KAea10f].	18
3.1	Geometrical sketch of the algorithm used to correlate the points in the two pixel layers.	21
3.2	Resolution and efficiency of the vertex reconstruction along the beam direction using the SPD as a function of dN_{ch}/dy for the case of pp interactions.	22

3.3	Efficiency and resolutions for the primary vertex reconstructed in 3D from tracks as a function of dN_{ch}/dy for the case of pp events.	22
4.1	For events with $\alpha = \frac{p_\perp^l}{p_\perp^a}$ equal to 1 (left) and 10 (right). The function $f(\phi_n)$ is shown for different configurations given in terms of ϕ	29
4.2	The function $r(\tau)$ for two classes of events: when the associated particle is in the hemisphere of the leading (left) and when the associated particle is in the away hemisphere (right).	31
4.3	Left panel corresponds to $r(\tau)$ function for different values of α . Right panel, shows τ vs. r weighted by $\langle\alpha\rangle$, for p-p collisions at 0.9 TeV simulated with PYTHIA. Only events with two charged particles in $ \eta \leq 0.8$ and $p_\perp \geq 0.5$ GeV/c were considered.	32
4.4	τ spectra for simulations based on an isotropic phase-space and PYTHIA models (left). Mean τ as a function of the multiplicity for both models (right).	33
4.5	S_\perp spectra for simulations based on an isotropic phase-space and PYTHIA models (left). Mean S_\perp as a function of the multiplicity for both models (right).	34
4.6	r (recoil) spectra for simulations based on an isotropic phase-space and PYTHIA models (left). Mean r as a function of the multiplicity for both models (right).	34
4.7	τ spectra as a function of $p_{\perp min}$ (left). Mean multiplicity of primary charged particles versus τ for different cuts on $p_{\perp min}$ (right).	37
4.8	τ versus mean transverse momentum for different values of $p_{\perp min}$ (left). Thrust minor spectra as a function of $p_{\perp min}$ (right).	38
4.9	Analysis of the “soft” component of the sample, <i>i. e.</i> , events with leading particle with $p_\perp < 2$ GeV/c. (τ spectra as a function of $p_{\perp min}$ (left). Mean multiplicity of primary charged particles versus τ for different cuts on $p_{\perp min}$ (right)).	39
4.10	Analysis of the “hard” component of the sample, <i>i. e.</i> , events which leading particle has $p_\perp \geq 2$ GeV/c. τ spectra as a function of $p_{\perp min}$ (left). Mean multiplicity of primary charged particles versus τ for different cuts on $p_{\perp min}$ (right).	40
4.11	Thrust minor spectra for the “soft”(left) and “hard”(right) samples. The value of $p_{\perp min}$ was varied starting from 1.7 up to 1.9.	41
4.12	Average multiplicity of primary charged particles as a function of τ . The analysis was done in the central barrel of rapidity $ \eta \leq 0.9$, and using particles with $p_\perp \geq 500$ MeV/c. “soft” component (left) with $p_\perp^l \leq 2$ GeV/c of the leading particle, while “hard” component with $p_\perp^l \geq 2$ GeV/c (right). Different values of core size: $a_2/a_1 = 0.2, 0.4$ and 0.5 (default value for the ATLAS-TDR tune). The core density is fixed at $\beta = 0.5$	42

4.13 τ spectra as a function of the core size. The analysis was done in the central barrel of rapidity $ \eta \leq 0.9$, and using particles with $p_\perp \geq 500$ MeV/c. “soft” component (left) with momentum of the leading particle $p_\perp^l \leq 2$ GeV/c, while “hard” component (right) with $p_\perp^l \geq 2$ GeV/c are shown. Different values of core size: $a_2/a_1 = 0.2, 0.4$ and 0.5 (default for ATLAS tune).	43
4.14 τ at 900 GeV for two cases. “soft” (left) events, with leading particle $p_t < 2$ GeV/c, and “hard” (right) events, with leading $p_t \geq 2$ GeV/c. The τ spectrum is shown for different values of PARP(85), which is associated with the probability that an additional interaction in the old multiple- interaction formalism that gives two gluons(see text).	44
4.15 Correlations on Sphericity at 900 GeV. Average transverse momentum per event versus τ (left); the average multiplicity per bin of τ (right). Both cases are shown for different values of PARP(85), which is associated with the probability that an additional interaction in the old multiple- interaction formalism gives two gluons.	45
4.16 Sphericity at 900 GeV for the cases: “soft” events (left), leading particle has $p_t < 2$ GeV/c and “Hard” events, with leading $p_t \geq 2$ GeV/c (right).	46
4.17 T_{min} at 900 GeV for the cases: “soft” events, leading particle has $p_t < 2$ GeV/c (left); “Hard” events, with leading $p_t \geq 2$ GeV/c (right).	47
4.18 Some correlations at 900 GeV: mean transverse momentum of the charged particles per event as a function of the Sphericity (left). Mean multiplicity as a function of Sphericity (right). Three different values of k_\perp were considered: 0.5, 2.5 and 5.5 GeV/c.	48
4.19 Average multiplicity of primary charged particles as a function of Sphericity. The analysis was done at $ \eta \leq 0.9$, and using particles with $p_\perp \geq 500$ MeV/c. “soft” component (left), leading particle with $p_\perp^l \leq 2$ GeV/c and “hard” (right) component, $p_\perp^l \geq 2$ GeV/c. Different Parton Distribution Functions were used: CTEQ4L, CTEQ5L (default of ATLAS tune) and CTEQ6L.	49
4.20 Sphericity spectra for different PDF’s: CTEQ4L, CTEQ5L and CTEQ6L. “soft” (left) component and “hard” (right) component.	50
4.21 Plot: η vs. $\Delta(\phi - \pi/2)$ vs. p_t for a typical event. The leading particle is placed at $\pi/2$ rad. Different radii are shown.	51
4.22 Illustration of the distribution of the momenta in the transverse plane for two classes of events. (left) Dijet event, (right) monojet event. In both cases the thrust axis is very close to the direction of the leading particle.	53
4.23 Thrust map: a) generator level (upper), in this case we use primary charged MC particles; and b) reconstruction level (bottom), in this case we used tracks associated to primaries from TPC+ITS information.	54

4.24 Correlation between the quantity τ computed from MC information and from TPC+ITS information.	55
4.25 Correlation between the quantity r computed from MC information and from TPC+ITS information.	56
4.26 Sensitivity of the azimuthal correlation of the away side peak on the thrust variable range. Fixed τ interval and variation of the r range (right panel). Fixed r and modification of the range τ (left panel)	57
4.27 Azimuthal correlation for particles with $p_t \geq 1.5$ GeV/c: dijets (red-region A), mono jets (blue-region B) and the mercedes events (green-region C). True spectrum (solid line), measured spectrum (dotted line). The leading particle is not shown.	58
4.28 Transverse momentum vs. $\Delta(\phi - \pi/2)$ for the associated particles: dijets (top), mono jets (middle) and the mercedes events (bottom). True distribution (left plots), measured distribution (right plots). The leading particle is shown, and you can note the cut $p_t \geq 1.5$ GeV/c which we imposed.	59
4.29 Visualization of one dijet event from the region A. The lines are primary Monte Carlo tracks with $p_t \geq 0.5$ GeV/c. The superimposed arrows separate each jet for a better visualization.	61
4.30 Distribution of the sum of the transverse momenta of particles with $p_t > 0.3$ GeV/c in the toward and away regions for dijet events. The toward region (black, leading jet) is formed by primary charged particles in the azimuthal range: $\pi/4$ rad $\leq \Delta\phi \leq 3\pi/4$ rad while the away region (red line) corresponds to particles with: $5\pi/4$ rad $\leq \Delta\phi \leq 7\pi/4$ rad. The plot shows two cases: reconstruction (dotted line) and generation (solid line).	62
4.31 Ratio of the transverse momenta of the toward jet over transverse momenta of the away jet as a function of r for dijet events. The participants have $p_t \geq 0.3$ GeV/c. The near side corresponds to the azimuthal range: $\pi/4$ rad $\leq \Delta\phi \leq 3\pi/4$ rad. For the away side: $5\pi/4$ rad $\leq \Delta\phi \leq 7\pi/4$. Charged component (right), (left) including the neutral component.	63
4.32 Multiplicity distribution of particles with transverse momenta: $p_t > 0.3$ GeV/c for dijet events. The particles belonging to the leading jet (black line) consist of primary charged particles in the azimuthal range: $\pi/4$ rad $\leq \Delta\phi \leq 3\pi/4$ rad. The away side (red line) corresponds to particles with: $5\pi/4$ rad $\leq \Delta\phi \leq 7\pi/4$ rad. The plot shows two cases: reconstruction (dotted line) and generation (solid line).	64
4.33 Visualization of a mono-jet event. The lines are mctracks with $p_t \geq 0.8$ GeV/c. The arrows contain the particles associated with the jet.	65

4.34 The distribution of the total charged transverse momenta of the identified mono-jets. The particles which were counted are within the azimuthal range: $\pi/4 \text{ rad} \leq \Delta\phi \leq 3\pi/4 \text{ rad}$; and they have: $p_t > 0.3 \text{ GeV/c}$. The generated (solid line) and the reconstructed (dotted line) are shown.	66
4.35 Multiplicity of primary charged particles ($p_t > 0.3 \text{ GeV/c}$) of mono-jet events. The azimuthal range is: $\pi/4 \text{ rad} \leq \Delta\phi \leq 3\pi/4 \text{ rad}$. The results of generation (solid line) and the reconstruction (dotted line) are compared.	67
4.36 Scan of one event of region C. Particles which appear in the picture have: $p_t \geq 0.5 \text{ GeV/c}$	68
4.37 Transverse momentum spectra for three-jet events, the including charged particles with $p_t > 0.3 \text{ GeV/c}$. Toward side (black line) corresponds to particles in the azimuthal region: $\pi/4 \text{ rad} \leq \Delta\phi \leq 3\pi/4 \text{ rad}$. Away side formed by particles in the remainder azimuth. The results at generator level (solid line) and reconstruction (dotted line) are shown.	69
4.38 Mercedes events. Ratio of transverse momentum distributions of toward jet over transverse momenta of the away jets. The $\Delta\phi$ ranges used are the same as in the previous figure.	70
4.39 Multiplicity (charged particles with $p_t > 0.3 \text{ GeV/c}$) distribution. In black is the full true spectrum. The different colored distributions correspond to the three classes of topologies which we discriminated using ESA.	71
5.1 Mean transverse sphericity versus p_T^{\max} (of each event) for MC simulations at $\sqrt{s} = 7 \text{ TeV}$. Results for PYTHIA6 (tunes ATLAS-CSC and PERUGIA-0) and PHOJET simulations are displayed, the events have more than 2 primary charged particles in $ \eta \leq 0.8$ and transverse momentum above 0.5 GeV/c	74
5.2 Pseudorapidity (left) and azimuthal distributions of TPC tracks: MC (empty points), real data (full points). Each plot show the nice agreement between data and MC.	75
5.3 Multiplicity response matrix. Particles and tracks in $ \eta \leq 0.8$ and $p_T \geq 0.5 \text{ GeV/c}$ are considered. The events were produced using PYTHIA6 tune ATLAS-CSC, pp minimum bias collisions at 7 TeV with flat multiplicity.	77
5.4 Sphericity response matrix. Particles and tracks in $ \eta \leq 0.8$ and $p_T \geq 0.5 \text{ GeV/c}$ are considered. The events were produced using PYTHIA6 tune ATLAS-CSC, pp minimum bias collisions at 7 TeV with flat multiplicity.	79
5.5 Resolution of the sphericity as a function of multiplicity. The true sphericity was fixed to 0.075 ± 0.025	80
5.6 Resolution of the sphericity as a function of multiplicity. The true sphericity was fixed to 0.525 ± 0.025	81

5.7	Resolution of the sphericity as a function of multiplicity. The true sphericity was fixed to 0.975 ± 0.025	82
5.8	Gaussian fit quality of the sphericity resolution as a function of multiplicity. The true sphericity was fixed to 0.525 ± 0.025	83
5.9	Sigma of the gaussian function versus multiplicity at $S_T =$, 0.075, 0.525 and 0.975 (± 0.025). The red line indicates an exponential fit.	83
5.10	Mean of the gaussian function versus multiplicity at $S_T =$, 0.075, 0.525 and 0.975 (± 0.025).	84
5.11	Mean and sigma of the fit as a function of true sphericity at measured multiplicity 35. For sigma, the two first bins are out of the tendency because they were computed with poor statistics. The sphericity was interpolated to $S_T = 0$ using a linear fit.	84
5.12	Example of the response matrix for the sphericity at reconstructed multiplicity of 25 primary tracks. PYTHIA event generator tune ATLAS-CSC[Mor] with flat multiplicity.	85
5.13	Test of the method to get the unfolded linearized sphericity as a function of the true multiplicity. The samples: “bulk” and “hard” are shown. The true points are gotten using primary charged particles produced at generator level.	86
5.14	Average transverse momentum versus multiplicity. The results from three MC models are shown: PYTHIA6 (tune PERUGIA0), PHOJET and PYTHIA8. Two ways for the computation of the average were used: one with an upper cut on p_T , and the second one without such cut.	87
5.15	Test of the method to correct the average p_T versus multiplicity in events generated with PHOJET. The samples: “bulk” and “soft” are shown. The true points are gotten using primary charged particles produced at generator level. The analysis was done at 7 TeV, the corrections were computed using PYTHIA6.	88
5.16	Average transverse momentum versus multiplicity at 900 GeV/c. The results for inelastic events published by ALICE (right side) are compared with the results which we got after applying our approach (5.7).	89
5.17	Performance of the procedure. (Upper) Reconstructed events generated with PHOJET are corrected using simulations generated with PYTHIA6 (tune PERUGIA-0). (Bottom) Reconstructed distributions generated with PYTHIA6 are corrected using simulations produced with PHOJET. Three different multiplicity bins are shown: $3 \leq N_{ch} < 10$, $10 \leq N_{ch} < 20$ and $20 \leq N_{ch} < 30$. . .	91

6.1	Arrival time of particles in the VZERO detectors relative to the beam crossing time (time zero). A number of beam-halo or beam-gas events are visible as secondary peaks in VZERO-A (left panel) and VZERO-C (right panel). This is because particles produced in background interactions arrive at earlier times in one or the other of the two counters.	93
6.2	Monitoring of the beam-related background flagged by VZERO, the red points are the outliers, in the text the procedure to compute the outliers is explained.	94
6.3	Monitoring of the beam-gas background flagged by the correlation between the number of SPD clusters and the number of tracklets. The red points are the outliers, in the text the procedure to compute the outliers is explained.	95
6.4	Fraction of accepted events after the off-line physics selection. For the MB trigger it is $> 99\%$, this tells us that the background level is negligible.	95
6.5	Effect of the pile up on the average $\langle S_T \rangle$. Data from the period LHC10d (pass2) were analyzed. The reference data were taken from a sample with typical μ around 0.05. The high pile up sample includes events having $0.07 < \mu < 0.35$, this are the maximum values which can be reached in a typical sample of the period LHC10e. An extreme case is also shown where the μ is between 0.4 and 2. The effect on $\langle S_T \rangle$ is small even in the very extreme case.	97
6.6	Event generator dependence of the $\langle S_T \rangle$. The MB data of the period LHC10e are corrected using the response matrices from PYTHIA6 and PHOJET.	98
6.7	Effect of the cut on the distance of closest approach (DCA). The DCA on the plane perpendicular to the beam is plotted for “primary” tracks. The MC distribution (line) is compared with the ALICE measurements (points). The shaded area correspond to the true primary MC tracks, so, the difference between the line and the shaded area is the contamination of secondaries.	99
6.8	Effect of the secondaries on the (quadratic) sphericity. The standard value $N = 7$ correspond to a contamination of about 2% while $N = 175$ to $\sim 8\%$	99
6.9	Mean sphericity versus charged tracks multiplicity for: all charged tracks, positive and negative charged tracks. As is expected, the result for positive and negative charged tracks is the same.	100
6.10	Effect of the pile up on the sphericity spectra. The multiplicity bins are displayed in the panels.	102
6.11	Model dependence on the sphericity spectra. The multiplicity bins are displayed in the panels.	103
6.12	Decomposition of the systematic uncertainty on the sphericity spectra for the different multiplicity ranges.	104

6.13 Mean transverse sphericity as a function of charged particle multiplicity for $p - p$ collisions at $\sqrt{s} = 0.9$ TeV. The statistical errors are displayed as error bars and the systematic uncertainties as the shaded area. Symbols for data points and model predictions are presented in the legend. The results are shown for “bulk” events	105
6.14 Mean transverse sphericity as a function of charged particle multiplicity for $p - p$ collisions at $\sqrt{s} = 0.9$ TeV. The statistical errors are displayed as error bars and the systematic uncertainties as the shaded area. Symbols for data points and model predictions are presented in the legend. The results are shown for “soft” events	106
6.15 Mean transverse sphericity as a function of charged particle multiplicity for $p - p$ collisions at $\sqrt{s} = 0.9$ TeV. The statistical errors are displayed as error bars and the systematic uncertainties as the shaded area. Symbols for data points and model predictions are presented in the legend. The results are shown for “hard” events	107
6.16 Mean transverse sphericity as a function of charged particle multiplicity for $p - p$ collisions at $\sqrt{s} = 7$ TeV. The statistical errors are displayed as error bars and the systematic uncertainties as the shaded area. Symbols for data points and model predictions are presented in the legend. The results are shown for “bulk” events.	109
6.17 Mean transverse sphericity as a function of charged particle multiplicity for $p - p$ collisions at $\sqrt{s} = 7$ TeV. The statistical errors are displayed as error bars and the systematic uncertainties as the shaded area. Symbols for data points and model predictions are presented in the legend. The results are shown for “soft” events.	110
6.18 Mean transverse sphericity as a function of charged particle multiplicity for $p - p$ collisions at $\sqrt{s} = 7$ TeV. The statistical errors are displayed as error bars and the systematic uncertainties as the shaded area. Symbols for data points and model predictions are presented in the legend. The results are shown for “hard” events.	111
6.19 Mean transverse momentum versus multiplicity. The ALICE data are compared with four models: PHOJET [Eng95], PYTHIA6 (tunes: ATLAS-CSC [Mor] and PERUGIA-0 [Ska]) and PYTHIA8 [eab]. Results at $\sqrt{s} = 0.9$ and 7 TeV are shown in the rows 1 and 2 respectively. Different event classes are presented: “bulk” (a), “soft” (b) and “hard” (c).	112
6.20 Sphericity spectrum in the bin of multiplicity: $3 \leq N_{ch} < 10$. The result is for $p - p$ collisions at $\sqrt{s} = 7$ TeV. The statistical errors are displayed as error bars and the systematic uncertainties as the shaded area. Symbols for data points and model predictions are presented in the legend. The results are shown for “hard” events.	114

6.21 Sphericity spectrum in the bin of multiplicity: $10 \leq N_{ch} < 20$. The result is for p – p collisions at $\sqrt{s} = 7$ TeV. The statistical errors are displayed as error bars and the systematic uncertainties as the shaded area. Symbols for data points and model predictions are presented in the legend. The results are shown for “hard” events.	115
6.22 Sphericity spectrum in the bin of multiplicity: $20 \leq N_{ch} < 30$. The result is for p – p collisions at $\sqrt{s} = 7$ TeV. The statistical errors are displayed as error bars and the systematic uncertainties as the shaded area. Symbols for data points and model predictions are presented in the legend. The results are shown for “hard” events.	116
6.23 Sphericity spectrum in the bin of multiplicity: $N_{ch} \geq 30$. The result is for p – p collisions at $\sqrt{s} = 7$ TeV. The statistical errors are displayed as error bars and the systematic uncertainties as the shaded area. Symbols for data points and model predictions are presented in the legend. The results are shown for “hard” events.	117
6.24 Mean p_T as a function of sphericity for two multiplicity bins: (a) $3 \leq N_{ch} < 10$ and (b) $N_{ch} \geq 30$. The plots were obtained using MB pp collisions at $\sqrt{s} = 7$ TeV simulated with three different MC generators: PYTHIA6 (tune ATLAS-CSC), PYTHIA8 and PHOJET. Also the contributions of the different event topologies to the averaged mean p_T is presented.	118
6.25 Mean sphericity versus multiplicity for “bulk” events. Three samples at different energies were analyzed: $\sqrt{s} = 0.9, 2.76$ and 7 TeV. ALICE data are compared with PYTHIA8 and PHOJET.	119
6.26 Mean sphericity versus multiplicity for “soft” events. Three samples at different energies were analyzed: $\sqrt{s} = 0.9, 2.76$ and 7 TeV. ALICE data are compared with PYTHIA8 and PHOJET.	120
6.27 Mean sphericity versus multiplicity for “hard” events. Three samples at different energies were analyzed: $\sqrt{s} = 0.9, 2.76$ and 7 TeV. ALICE data are compared with PYTHIA8 and PHOJET.	121

List of Tables

1	Incertidumbres sistemáticas en los espectros de esfericidad	xxix
1.1	Basic blocks of matter (quarks and leptons) in the Standard Model [ea08b]. . .	2
1.2	Fundamental forces [Per00]. All forces, except gravitation, are described by the Standard Model. Their strength is given relative to the strength of the strong force for two protons at a distance of about 0.5 fm. The gravitons, the gauge bosons of gravity, are postulated but have not been found yet.	2
2.1	Trigger efficiency in percent at $\sqrt{s} = 10$ TeV (Pythia) (see [GO09]).	19
4.1	Parameters of tune ATLAS-TDR.	36
4.2	τ and r parameters used for the present analysis.	57
4.3	Number of events with particular topologies in the analyzed sample of 1.2 million of events.	60
6.1	Ratio of the number of “soft” to “hard” events. In the present analysis, more than two primary particles in $ \eta < 0.8$ and $p_T > 0.5$ GeV/c are required. The corrections for reconstruction were made.	96
6.2	Contributions to the systematic uncertainties on the average transverse sphericity $\langle S_T \rangle$	100
6.3	Systematic uncertainties on the sphericity spectra.	101